ON THE LUMINOUS AND DARK MATTER DISTRIBUTION IN EARLY-TYPE GALAXIES

Dottorando
LORENZO POSTI

Relatore
Dr. **CARLO NIPOTI**

Correlatori
Prof. **LUCA CIOTTI**
Dr. **MASSIMO STIAVELLI**

Coordinatore
LAURO MOSCARDINI

Contents

Chapter 1

Introduction

1.1 Mass distribution in galaxies

1.1.1 Baryons and dark matter

A long standing problem in Astrophysics is that large bound structures such as galaxies and galaxy clusters appear to have more mass than what can be accounted for by the stars and gas which emits the observed radiation. Even though not unique, the most popular solution to this conundrum is that galaxies and galaxy clusters are embedded within haloes much larger than the host stellar system, which are made of non-emitting matter interacting only gravitationally with gas and stars: this additional source of mass, which lives outside of the Standard Model of Particle Physics, is called *dark matter*. If it does exist, such invisible matter must be composed of weakly self-interacting and very massive elementary particles with respect to ordinary baryonic particles such as electrons and protons (see Fermi-LAT Collaboration, 2015). The Planck Collaboration et al. (2014) gave probably the most convincing argument for the existance of such non-emitting dark matter with observations of the cosmic microwave background: the amount of baryonic matter (i.e., stars, gas, dust, compact objects) that is in the Universe is about 16% of the total amount of gravitationally interacting matter. This ratio is usually called cosmological *baryonic fraction.*

In general, the fraction of baryonic over total mass is a function of both i) time, since it is not constant over the lifetime of a bound structure, and ii) position in the Universe, i.e., it is different in general from object to object. In the so-called *hierarchical clustering scenario* (see White & Rees, 1978) dark matter structures started collapsing before the baryon-radiation decoupling. Galaxy formation starts when baryons fall into the potential well of such dark haloes: at the centre of the halo, where the gravity

is stronger, the gas dissipates efficiently, cools and eventually forms stars. How many baryons w.r.t. dark matter particles are present in a given structure at a given time depends on the evolutionary history of the system: violent processes, such as feedback from supernovae and from the central Active Galactic Nucleus (AGN), can expel some of the gas out of the potential well; while encounters and mergers with other structures bring in new material that becomes gravitationally bound to the system. The major source of uncertainty in determining what is the baryonic fraction of a given object at a given time is that while the evolution of the dark matter content is solely influenced by gravity, for which sophisticated and accurate models exist (see e.g., Mo & White, 1996; Springel, Frenk, & White, 2006), the evolution of the baryonic component is strongly dependent on many details of gas physics, which are still poorly modeled and understood.

1.1.2   Mass as a driver for evolution

The largest bound structures that are in the Universe today, i.e., the galaxy clusters, are embedded in coronae of very hot gas ($10^7 - 10^8$ K) which can be detected from its X-ray or Sunyaev & Zeldovich (1970) emission (see e.g., Sarazin, 1986; Birkinshaw, 1999). Such hot and diffuse gas typically amounts to about 90% of the total baryonic content of the cluster, leaving just about 10% of the baryonic mass in stars, which are mostly confined in galaxies (Voit, 2005). This is likely not going to change much in time since the very deep potential wells of the clusters (with masses around $10^{14} - 10^{15} M_\odot$) make the cooling time of the hot atmospheres much longer than the Hubble time, implying that gas condensation is very unlikely and therefore star formation is negligible (except at the cluster's centre). The potential well of a typical galaxy is instead of the order of $10^{12} - 10^{13} M_\odot$, which typically allows for efficient conversion of gas into stars (at least in the absence of *quenching mechanisms*, i.e. processes that stop star formation. e.g., Peng et al., 2010). This, in the lifetime of a galaxy, ultimately leads to a stellar content dominating over the gaseous content: typically the gas-to-stellar mass fraction in elliptical galaxies is up to about $\sim 10 - 20\%$ (see e.g., Binney & Merrifield, 1998) and also in late-types with stellar mass $\gtrsim 10^9 M_\odot$ the stellar mass dominates over the gas mass (see e.g., Papastergis et al., 2012).

The mass distribution of cosmological structures is most likely the major driver of its evolution. Galaxies have largely assembled by mergers, which are more likely for more massive dark haloes (e.g., Fakhouri, Ma, & Boylan-Kolchin, 2010), and their mass, size and other structural properties have been following very different evolutionary tracks depending on how matter is distributed in them. Also star-formation and other complex baryonic processes are strongly influenced by the total mass of the system: in very massive galaxies, star formation tends to be strong, episodic, short-lasting and taking place when the Universe was young; for galaxies with smaller mass, star formation tends to be mild, long-lasting and accompanying most of the galaxy lifetime. So, how much luminous and dark matter there is in a galaxy is a direct tracer of the galaxy evolution.

The distribution of matter in galaxies and galaxy clusters can also be used to probe cosmological models of structure formation on different scales. Since the total mass of such stellar systems is typically dominated by their dark matter haloes, whose evolution

is mainly driven by gravity and not by complex gas physics phenomena, measurements of the total mass of galaxies and galaxy clusters are fundamental for a statistical comparison with an analogous populations predicted by a given model. For instance, the number of galaxies of given mass per unit volume of the Universe gives constraints on the baryonic and non-baryonic mass functions on large scale; while the number of Milky Way satellites of given mass gives constraints on the cosmological models on smaller scales.

1.1.3 Galaxy mass estimators

Many techniques have been developed in order to measure the mass of galaxies in the Universe. The three most used approaches are i) inferring the mass distribution only from the light distribution, usually using stellar population models, ii) deriving the gravitational field from strong and/or weak graviational-lensing observations and iii) using the Doppler shifts and broadenings of stellar and/or gaseous lines to trace the underlying potential well (see e.g., the review by Courteau et al., 2014). The first measures only the mass in stars and not the total mass of the system, but is the easiest and faster method and has been applied extensively also at high redshift. However, it has some uncertainties and the results vary significantly if the stellar population model's details are varied. While the second is the most accurate in measuring the mass within a fixed radius, but the lensing signal can be detected only for special geometrical configurations. The third method, on the other hand, is by far the most popular since it can be applied to all galaxies for which spectroscopical observations are available and it is sufficiently accurate in recovering the mass distribution of the system. The analysis of the spectral lines provides information on the motion of the objects which emitted the lines. This allows for the reconstruction of their motion using a *kinematical* model, which characterizes e.g., the galaxy's rotation velocities and velocity dispersion in a parametric way. On top of that, one can seek for a *dynamical* model in which the system's gravitational potential is modeled and it is responsible for the observed kinematics. With the latter it is possible to characterize the system's orbital distribution and hence give robust estimates of the dynamical, i.e., total, mass distribution.

1.2 Early-type galaxies

The distribution of galaxies in the Universe appears to be bimodal in many aspects: the optical morphology (either disc-like or elliptical), the colour (either blue or red), the amount of warm/cold gas (either rich or poor), the amount of hot gas (either poor or rich), the age of their stellar populations (either young or old), the star-formation activity (either star-forming or passive), the environment in which the galaxy lives (either low-density or high-density), the tendency of hosting an AGN (either moderate or significant). Elliptical, red, warm/cold-gas-poor, hot-gas-rich, old, passive, with high probability of being clustered and of hosting an AGN are called *early-type* galaxies, as opposed to the *late-type* galaxies. These galaxies have typically assembled most of their stellar mass very early-on and their subsequent evolution, either quiescent or driven by episodic
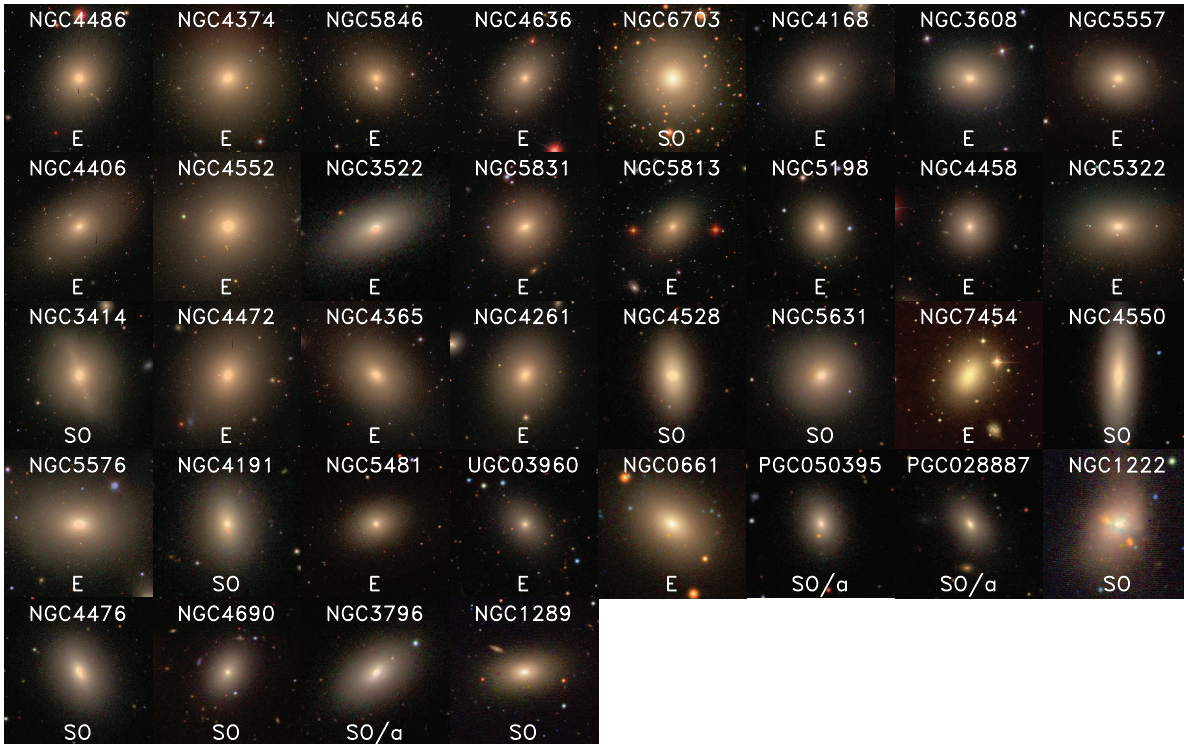
Figure 1.1: Sample of 36 early-type galaxies drawn from the ATLAS^{3D} survey. The images are red-green-blue composites from observations with the Isaac Newton Telescope and the Sloan Digital Sky Survey Data Release 7 (SDSS DR7, Abazajian et al., 2009). The name of the galaxy and the morphological classification from the HyperLeda database (at `http://leda.univ-lyon1.fr/`) are shown respectively on top and bottom of each image. The scale of each panel is $10R_\mathrm{e} \times 10R_\mathrm{e}$, where R_e is the effective radius. Figure adapted from Cappellari et al. (2011a).

mergers, is characterized by a mild growth stellar mass and by star formation or AGN activity triggered by occasional gas accretion. Most of the early types that we observe in the local Universe appear to be smooth and not disturbed both in optical, where the stars dominate the light, and in X-ray, where their hot ($10^6 - 10^7$ K) gaseous atmospheres emit via bremsstrahlung. This indicates that they have likely not experienced a violent evolution in the last billion years, but instead they have gone through a quiescent evolutionary phase. Figure 1.1 shows some local Universe early types (taken from the ATLAS^{3D} sample; Cappellari et al., 2011a) as they appear in optical wavelenghts.

1.2.1 Mass from tracers of the gravitational potential

1.2.1.a Cold and warm gas as a tracer

In the local Universe, for those early-types for which no lensing signal can be detected (see e.g., the Sloan Lens ACS Survey, for some cases in which strong lensing features are present, Bolton et al., 2006) the total mass distribution is best measured by analysing the motion of some visible objects in the galaxy's potential. The objects on which one studies the action of the potential are usually called *tracers*. For late-type galaxies the obvious choice is the cold neutral gas, which is ubiquitus and conspicuous and whose kinematics can be probed with 21 cm observations of the hyperfine transition of the nautral hydrogen atoms with radio telescopes. Such emission line has proved to be ideal to study the dynamics of spiral galaxies and over the years improved radio telescopes have helped in shedding some light in how their luminous and dark mass is distributed (see e.g., de Blok et al., 2008). Gaseous discs extend typically much more than optical discs and easily reach the regions where the dark matter is expected to dominate the mass budget, therefore these measurements are of great importance if one is willing to decompose the matter distribution in dark and luminous (see e.g., van Albada et al., 1985). Similarly, bright emission lines such as the Hα Balmer recombination line can be used to probe the kinematics of the warm phase of ionised hydrogen at high redshift, where the 21 cm can not be detected (see e.g., Förster Schreiber et al., 2009).

1.2.1.b Planetary nebulae, globular clusters and hot gas as tracers

Emission lines of cold and/or warm gas are not present in early-types, hence the tracers of the potential must be of some other kinds. Planetary nebuale produce bright emission lines that can be typically observed out to the very outskirts of an elliptical galaxy (out to about $5-8$ effective radii, see e.g., Cortesi et al., 2013; Gerhard, 2013). The planetary nebula is a phase in the final stages of the life of old stars ($1M_\odot \leq M \lesssim 8M_\odot$) and it is characterized by extremely bright emission lines produced by the expanding stellar envelope, especially a forbidden line of the doubly-ionised oxygen (in visual bands). The radial velocities of such stars can be accurately determined by these bright lines and typically used to probe the galaxy's net rotation. If no bright emission line is available, absorption line produced by the atmospheres of stars can be used to derive the kinematics. Similarly to planetary nebulae, globular clusters appear as point-like objects in the halo of early types and can be observed out to about 4 effective radii. In typical nearby

early-types, the radial velocities of some hundreds of star clusters can be estimated from the ionised calcium triplet (in near-infrared bands, see e.g., Romanowsky et al., 2009). Dealing with discrete kinematic information can be more difficult w.r.t. the continuous information coming from, e.g., gas emission lines (for instance, the determination of the velocity dispersion along the line-of-sight is often difficult with those tracers), indeed ad-hoc discrete dynamical models have been developed to efficiently deal with such data (see Section 2.4). Planetary nebulae have proved to be essential tracers of the potential of early types in the outskirts, since they naturally trace the dynamics of the stars in the galaxy (being them old stars) and since they are visible even where the galaxy's surface brightenss is faint. Converseley, globular clusters do not trace the stellar kinematics equally well since those on orbits plunging closer to the galactic centre are likely to be tidally disrupted, leaving intact only clusters with lesser radial excursion. Therefore, the orbits of the observed globular clusters will be more biased towards circular orbits and typically also a simultaneous determination of their (completeness-corrected) density profile is needed. Another noteworthy approach for recovering the dynamical mass of early types up to several effective radii ($\sim 2-4$) is by measuring the X-ray emission from their hot gaseous coronae. With some assuptions on the geometry of the system, one can generate a dynamical model for the galaxy by assuming that the hot gas is in hydrostatic equilibrium in the galactic gravitational potential (e.g., Das et al., 2010). Two main drawbacks can be associated with this technique: first, the X-ray luminosity can be dominated by point sources (e.g., X-ray binaries) so the measured temperatures do not necessarily trace the underlying potential and second, inflow and outflows often disturb the hot corona so that the assumption of hydrostatic equilibrium is questionable.

1.2.1.c   Stars as tracers

Stars are, however, the tracers most often used to determine the mass distribution in early-type galaxies. From long-slit spectra along the major axis (see e.g., Davies et al., 1983) to modern Integral Field Spectrographs which spatially resolve the galaxy stellar kinematics on the plane of the sky (see e.g., Cappellari et al., 2011a; Sánchez et al., 2012), the analysis of absorption lines produced by unresolved stars within the galaxy (typically in the visual bands encompassing the H and K lines of ionised calcium) has a long history in characterizing the dynamics of early types. Their mass is measured studying how the stars move through the system along a given line-of-sight, i.e., recovering the line-of-sight velocity distribution (LOSVD) from the observed stellar absorption lines. In these systems the stellar surface brightness falls off rapidly from the centre (approximately as $I \sim \exp(-R^{1/4})$, where I is the surface brightenss and R is the distance from the centre, see de Vaucouleurs, 1948) and the signal-to-noise of the stellar spectrum becomes too small for any reliable determination of the kinematics at about $1-3$ effective radii. Where the signal-to-noise is large enough, the galaxy's line-of-sight velocity distribution (LOSVD) can be determined from the integrated stellar spectra. At a given position on the sky, the observed spectrum is given by the luminosity-averaged sum of the spectra of each star that falls into the resolution element of the instrument, which is Doppler-shifted according to the star's line-of-sight (LOS) velocity. If the intrinsic emission of all the stars in that position of the sky is known, then the observed integrated spectrum is
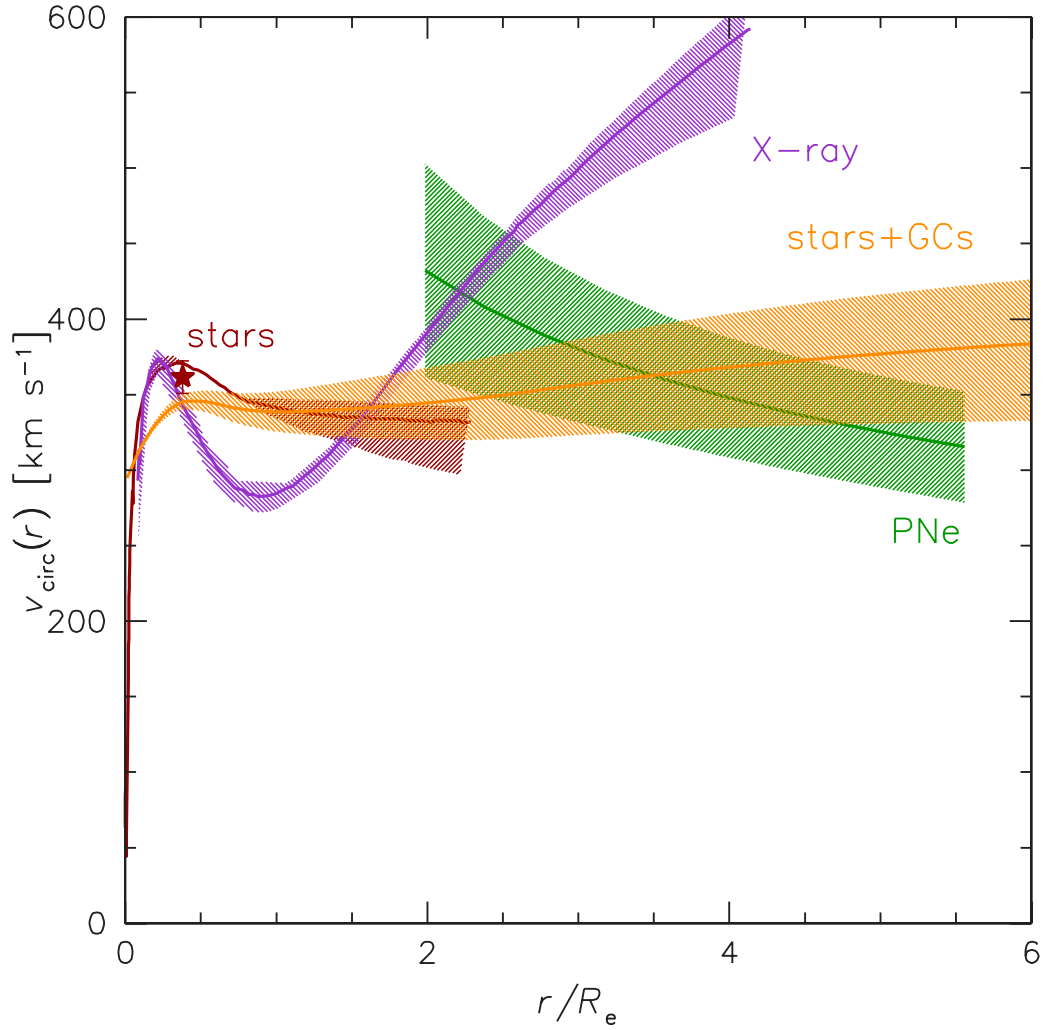
Figure 1.2: Circular velocity profile for the elliptical galaxy NGC 5846 with different methods. Stellar kinematics from Kronawitter et al. (2000, red band) and Cappellari et al. (2013, red star), X-ray dynamical model in hydrostatic equilibrium from Das et al. (2008, violet band), dynamical model constrained with planetary nebulae from Deason et al. (2012, green band) and constrained with stars+globular clusters in the SAGES Legacy Unifying Globulars and GalaxieS (SLUGGS) survey from Napolitano et al. (2014, yellow band). Figure adapted from Napolitano et al. (2014).

the convolution between such intrinsic emission and the LOSVD, so that one can hope to recover the latter by solving an inversion problem. Such inverse problem is far from easy to resolve and it is often ill-conditioned (since deconvolutions tend to amplify the noise). However, many methods have been developed to solve this crucial problem: the method that is currently the most popular consists of the following steps

(i) assume some given templates for the stellar intrinsic emission (usually templates for single stellar populations)

(ii) parametrize the LOSVD, typically with an expansion in Gauss-Hermite functions up to order 4 or more (see Gerhard, 1993; van der Marel & Franx, 1993)

(iii) use a penalized likelihood recovery algorithm (see Merritt, 1997) to invert the convolution problem, so that for large signal-to-noise also the higher moments of the expansion are important, whereas for small signal-to-noise one effectively fits a Gaussian (only the order $0, 1$ and 2 of the Gauss-Hermite expansion are fitted).

An optimal and very popular implementation of this scheme was proposed by Cappellari & Emsellem (2004).

In Figure 1.2 an example of comparison among estimates of the circular velocity curve (which can be readily translated into total mass profile since $v_{\mathrm{circ}}^2(r) = GM(r)/r$) is presented for the elliptical galaxy NGC 5846. All the methods indicate that this galaxy is dominated by dark matter already within the effective radius (e.g., the ATLAS$^{\mathrm{3D}}$ collaboration estimates a mass-to-light ratio in r-band of ~ 8.1, see Cappellari et al., 2013). Also, the two methods which probe the outermost regions of the galaxy agree in indicating that this dominance increases with radius (by roughly a factor of ~ 2 in mass-to-light ratio from 1 to 5 effective radii, see e.g., Napolitano et al., 2014). Some discrepancies in the innermost part can be ascribed to different calibrations and sensible differences in the modeling techniques used, while the peculiar shape of the circular velocity curve inferred from the hot X-ray halo probably suggests that such atmosphere is not in hydrostatic equilibrium and maybe that unresolved X-ray binaries are responsible for a significant fraction of the observed X-ray flux. However, the various methods describe the total mass distribution of the galaxy in qualitative agreement.

1.2.2   Shape and internal dynamics

As Figure 1.1 illustrates, many early-type galaxies appear flat on the sky. The shape of their isophotes, i.e., curves of equal surface brightness, is to first order elliptical and one may wonder what are the intrinsic shapes of such galaxies.

The problem of understanding the intrinsic shape of galaxies from the observations is not easy to solve, since the flattening of the observed isophotes ($\xi = b/a$, where a and b are, respectively, the semi-major and semi-minor axis of the isophote) is due both to an intrinsic flattening of the stellar system[1] q and to the inclination of the line-of-sight i, which for axisymmetric galaxies is the angle between the line-of-sight and the symmetry axis. Such degeneracy between q and i is difficult to break and typically one derives results on one with some reasonable assumptions on the other. If the galaxy is oblate, then

$$\xi = \cos^2 i + q^2 \sin^2 i. \tag{1.1}$$

The probability distribution of observed axis ratios $P(\xi)$ will be given by integrating over all the possible intrinsic axis ratios q and inclinations i, hence

$$P(\xi) = \int \mathrm{d}q\, P(q) P(\xi|q), \tag{1.2}$$

---

[1] I assume here that galaxies are axisymmetric for simplicity, but the results can be generalized to triaxial systems (see Lambas, Maddox, & Loveday, 1992)

where $P(\xi|q)$ is the conditional probability of observing a projected axial ratio ξ given that a galaxy is intrinsically flattened by q. $P(\xi|q)$ is a function of the inclination angle i. Following Lambas, Maddox, & Loveday (1992, see also Binney & Merrifield 1998 §4.3.3) one can invert (1.2) and determine $P(q)$ from the observed $P(\xi)$ by assuming that galaxies are seen at random angles. The main result from a large sample ($\simeq 20000$) of diverse galaxies, is that the observed distribution of disc galaxies' shapes is produced by a homogeneous population of very thin stellar discs (axial ratio < 0.2). Lenticular galaxies are somewhat similar to spirals, while ellipticals have a broader q distribution with a peak at about $q \simeq 0.6$

Since the observed distribution of early-type shape is not consistent with discs randomly oriented on the sky, it is natural to ask whether the physical mechanism that makes their shape flattened and long-lived is the same as for late-types. For the latter, we know that a significant net rotation is present and is supporting the galaxies against gravity: in fact most stars in the stellar disc are on nearly circular orbits. For a long time before the mid '70s, also ellipticals where thought to be fast-rotating spheroidal objects, whose shape is due to a flattening by rotation (see e.g., Gott, 1973; Larson, 1975). Our understanding of such objects changed drastically when the first observations of stellar rotation curves in ellipticals showed that they rotate significantly less than expected (see Bertola & Capaccioli, 1975; Illingworth, 1977). Binney (1978) proposed that the flattening of the ellipticals' shape is due to an anisotropy of the velocity dispersion tensor, rather than to the net streaming motion. This implies that the support against gravity in these system is not given by rotation, but it is given by a dynamical pressure term, coming from the random motion of stars, whose magnitude is different in different directions.

Illingworth (1977) and Binney (1978) introduced the V/σ-ϵ diagram, where $\epsilon \equiv 1-\xi$ is the observed *ellipticity*, to study ratio of the amount of rotational kinetic energy to that in random motions. Traditionally V/σ was measured from observations as $V/\sigma \equiv V_{\mathrm{max}}/\sigma_0$, where V_{max} is the peak of the rotation curve and σ_0 is the central velocity dispersion. However, Binney (2005) introduced a new definition, based on the Tensor Virial Theorem (e.g., Binney & Tremaine, 2008, §4.8.3), in which both the streaming velocity and the velocity dispersion are light-averaged on the sky (see Section 4.4.2.c and in particular equation 4.15). Figure 1.3 shows a collection of such data taken from the ATLAS$^{\mathrm{3D}}$ sample of early-types (see Emsellem et al., 2011). Roughly all galaxies have $V/\sigma < 1$, whereas spiral galaxies have $V/\sigma > 2$, so for these objects rotation is not the most important factor in determining the observed ellipticity. A substantial fraction of them lies below the curve in which rotating, oblate galaxies with isotropic velocity tensor sit. When seen edge-on, systems with anisotropic velocity dispersions are found below that curve (see e.g., Cappellari et al., 2007).

1.3   Scaling relations

Early-type galaxies are known to closely follow some well-defined, empirical scaling laws such as luminosity-velocity dispersion (Faber & Jackson, 1976), size-surface brightness (Kormendy, 1977), Fundamental Plane (Djorgovski & Davis, 1987; Dressler et al.,
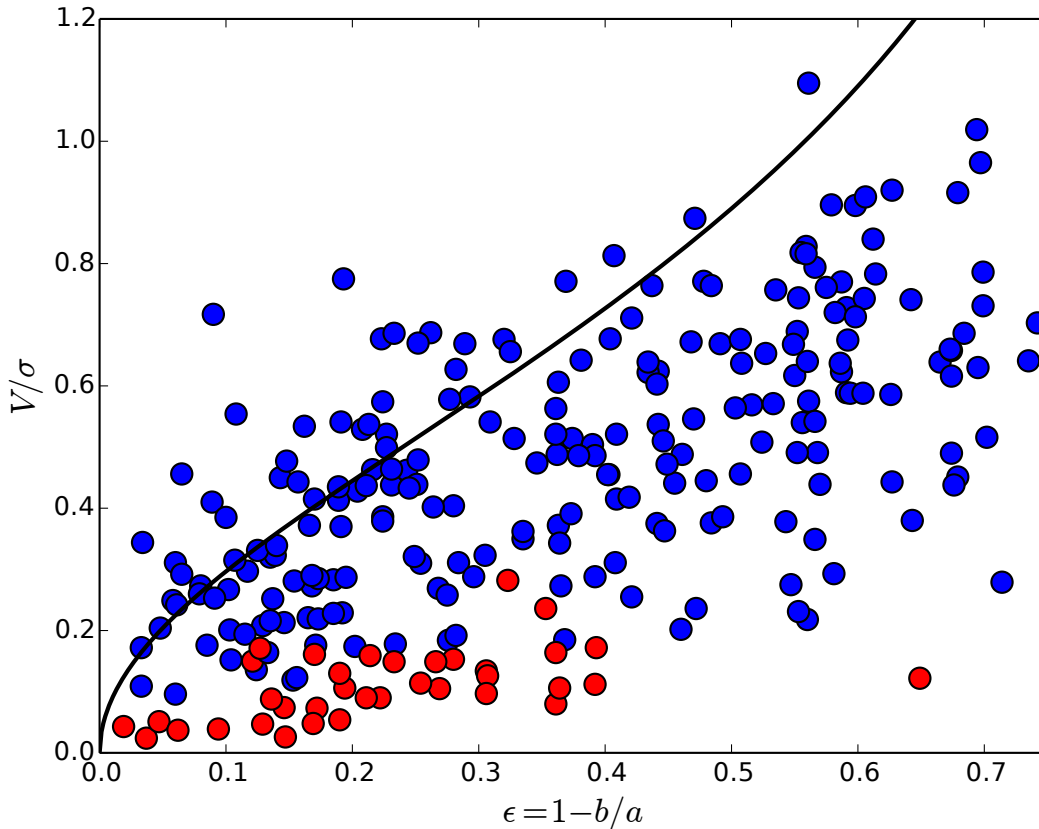
Figure 1.3: The ATLAS^{3D} sample of early-type galaxies in the rotational support plane: V/σ versus ellipticity $\epsilon = 1 - b/a$. Points in red are for galaxies classified as slow rotators, while those in blue are for fast rotating galaxies (see Emsellem et al., 2007). The black solid curve is the locus of points occupied by oblate isotropic rotators seen edge-on as in Binney (2005). I acknowledge the ATLAS^{3D} collaboration for making their data publicly available at `http://www-astro.physics.ox.ac.uk/atlas3d`.

1987), central black-hole mass-bulge mass (Magorrian et al., 1998), central black-hole mass-velocity dispersion (Ferrarese & Merritt, 2000; Gebhardt et al., 2000) and central black-hole mass-Sérsic index (Graham et al., 2001) relations. Such correlations hold on a large dynamical range, from dwarf ellipticals and bulges of normal galaxies to giant ellipticals. Therefore, the picture of early-types appear to be that of a very homogeneous population, in which large systems are self-similar scaled-up versions of smaller ones. In this respect, all these scaling laws set very tight constraints on any proposed galaxy formation model and can be exploited to give clues about how galaxies form and evolve. For instance, in the hierarchical structure formation scenario, galaxies form by subsequent mergers of smaller systems, though it is still unclear how such hierarchy of mergers can produce such an homogeneous class of objects with respect to their global structure, dynamics and properties of the stellar populations (see e.g., Nipoti, Londrillo, & Ciotti, 2003). In the following I will focus on the global properties of early-types as stellar systems and therefore I shall not consider the presence of the central supermassive black-hole (see e.g., Ciotti, 2009, for an extensive discussion).

From the Scalar Virial Theorem (see e.g., Binney & Tremaine, 2008, §4.8.3) it follows that for a galaxy in a steady-state, whose dynamical mass is M, effective radius is R_e and the central stellar velocity dispersion is σ_0,

$$M = K\frac{R_\mathrm{e}\sigma_0^2}{G}, \tag{1.3}$$

where G is the gravitational constant and the factor K is often called *virial coefficient*, which varies from galaxy to galaxy and depends on the the system's internal dynamics, velocity anisotropy and geometry (see e.g., Ciotti, 2009). The Fundamental Plane is a correlation between the effective radius R_e, central velocity dispersion σ_0 and the total luminosity L in some band. From (1.3), this can be interpreted as

$$L = \frac{K}{\Upsilon}R_\mathrm{e}\sigma_0^2, \tag{1.4}$$

where $\Upsilon \equiv M/L$ is the total *mass-to-light ratio* in some given band in which L is measured. Whereas for any virialized galaxy its structural properties will be related as in equations (1.3)-(1.4), every galaxies would have a different constant K and a different value for the mass-to-light ratio Υ in general. Indeed the ratio K/Υ varies systematically with the galaxy's luminosity (the so-called *tilt* of the FP; see e.g., Ciotti, 2009), but still early types lie very close to the plane. This is remarkable coincidence since, in principle, the scatter of the FP could be arbitrarily large.

Recently Cappellari et al. (2013) gave important new insights on the FP by showing that a large sample of early-type galaxies (the ATLAS[3D] sample) adhere to an even tighter correlation, i.e., the Mass Plane, which is essentially equation (1.3) where K is similar for all galaxies. In their study, they estimated the total mass from the stellar kinematics by generating state-of-the-art dynamical models (see Section 2.3.1). Figure 1.4 shows the distribution of that sample of early-types in the Mass Plane $M \propto \sigma_\mathrm{e}^2 R_\mathrm{e}$, where σ_e is the velocity dispersion within the effective radius. Each galaxy is coloured by its mass-to-light ratio Υ which, however, is not observed and is model-dependent, as well as the dynamical mass M. Nonetheless, Figure 1.4 shows that different galaxies with different Υ still lie on the same scaling law, which could be indicative of an homologous population of objects with different Initial Stellar Mass functions (IMF, see Ciotti, 2009; Cappellari et al., 2012).

The FP and other scaling relations are observed to evolve with redshift only in their normalization and not in their slope (see e.g., La Barbera et al., 2003; Jørgensen et al., 2006). The evolution in normalization is such that, at fixed stellar mass, galaxies at higher z are more compact. The scaling relations are actually observed to evolve very similarly to the expectations of simple cosmological models (see e.g., Mo, Mao, & White, 1998; Mo, van den Bosch, & White, 2010). The evolution of a population of galaxies initially on the FP will evolve on sequences parallel to the FP, so to mantain its slope, but not parallel to the FP at any time, since e.g., the galaxies' average size grows. Whether this picture is completely consistent with current formation scenarios is still matter of debate, since hierarchical dry (i.e., gas-less) mergers tend to disrupt some observed scaling relations (e.g., the luminosity-velocity dispersion and size-surface brightness;
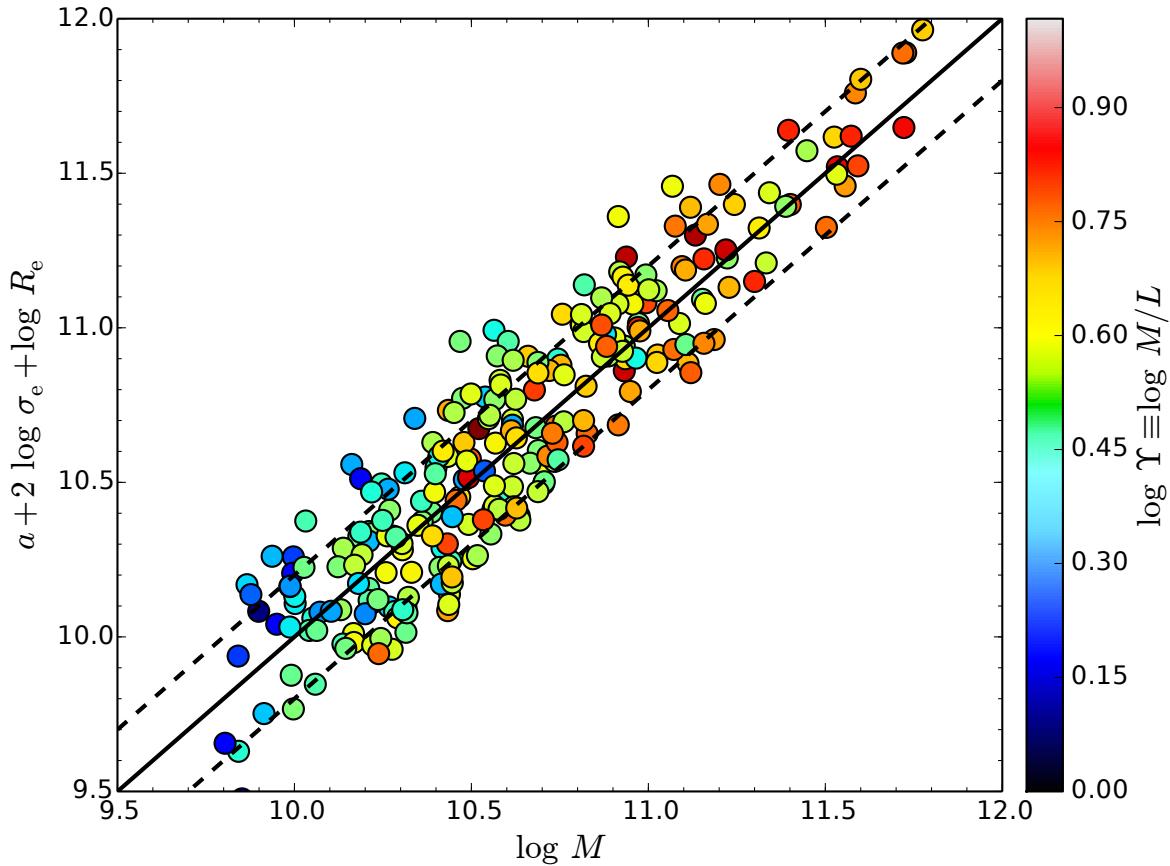
Figure 1.4: The ATLAS^{3D} sample of early-type galaxies in the Mass Plane: $a + 2\log \sigma_{\mathrm{e}} + \log R_{\mathrm{e}}$ versus dynamical mass $\log M$. Here σ_{e} is the stellar velocity dispersion measured within the effective radius and a is a constant. Each galaxy is coloured accordingly to its mass-to-light ratio. The black solid line is the one-to-one relation with ± 0.2 dex (black dashed lines). I acknowledge the ATLAS^{3D} collaboration for making their data publicly available at `http://www-astro.physics.ox.ac.uk/atlas3d`.

Nipoti, Londrillo, & Ciotti, 2003). A key ingredient to reconcile the hierarchical scenario with the persistence of the scaling laws could be the presence of dark matter haloes. For instance, Mo, Mao, & White (1998) argued that they are responsible for building and maintaining the scaling laws of disc galaxies (such as the Tully & Fisher, 1977, relation) and there are also some important clues on the imprint of the dark matter haloes on the scaling relations of galaxy clusters (see Lanzoni et al., 2004) and on evolutionary trends of galaxies (see e.g., Stringer et al., 2014).

1.4   Integral Field Spectroscopy

The advent of Integral Field Spectroscopy (IFS) has recently rejuvenated the study of the internal dynamics of galaxies. When an IFS is attached to an optical (or near-infrared) telescope, it allows to obtain simultaneously multiple spectra at different locations on the

sky, so that the time-cost of an observation where many spectra have to be recorded is greatly reduced. The advantage of IFS with respect to older Multi-Object Spectrographs is that their design driver is to have the best possible spatial resolution when the multiple spectra are taken at adjacent regions on the sky, so that the final image will actually be a cube in $x - y$ on the sky plane and z as spectral dimension (much like a common data-cube of a 21 cm radio observation). The three main technologies used to realize such instruments are

(i) *lenslet array*: the field of view is focused on the lenslet array, which performs the spatial sampling. Each lens produces an image which is later dispersed by a grism. Examples of this technique are the "Traitment Intégral des Galaxies par l'Etude de leurs Raises" (TIGER, Bacon et al., 1995) and the "Spectroscopic Areal Unit for Research on Optical Nebulae" projects (SAURON, Bacon et al., 2001).

(ii) *image slicer*: an array of mirrors is placed on the field of view, each mirror reflects different slices of the image onto different pupil mirrors which re-image such slices into several classical long-slits from which the spectra are extracted. Examples of this technique are the K-band Multi-Object Spectrograph (KMOS, Sharples et al., 2013) and the Multi Unit Spectroscopic Explorer project (MUSE, Bacon et al., 2010).

(iii) *fibre bundles*: the field of view is populated with a bundle of optical fibres, which separately collect the light and send it to a dispersing element. Example of this techniques are the PMAS/PPaK instrument used in the "Calar Alto Legacy Integral Field Area" survey (CALIFA, Verheijen et al., 2004; Sánchez et al., 2012), the "Sydney-AAO Multi-object Integral field spectrograph" (SAMI, Croom et al., 2012) and the "Mapping nearby Galaxies at Apache Point Observatory" survey (MaNGA, Bundy et al., 2015).

Having spectra at different adjacent locations on the sky allows for the study of spatially resolved galaxy properties, at a spatial resolution determined by the size of the so-called *spaxel*, i.e., single resolution element. For instance, such instruments allows for the detailed study of the spatially resolved stellar and gas kinematics and star formation, gradients in element abundances, ages and other stellar population properties. In particular, the determination of the stellar kinematics on entire images of early-type galaxies is fundamental in the study of their internal dynamics, since it gives an unprecedented number of kinematic constraints on the models which would take an unreasonable amount of time to obtain with classical slit spectroscopy.

The SAURON and ATLAS^{3D} projects (Cappellari et al., 2011a) have exploited the power of such IFS and designed a new extensive picture of early-type galaxies. Amongst their important results there are: i) early-types can be subdivided into two main kinematic classes of fast-rotators and slow-rotators, depending on their total angular momentum; ii) the stellar kinematics within the effective radius is consistent with a constant mass-to-light ratio and a small dark matter fraction; iii) axisymmetric, one-component dynamical models in which the vertical velocity dispersion is everywhere equal to that in the radial direction provides a good representation of the stellar kinematics within the effective radius; iv) the ratio between the stellar mass, derived from

stellar population models with fixed parameters, and the dynamical mass, derived from the observed stellar kinematics, systematically increases as the dynamical mass-to-light ratio increases (this was interpreted by Cappellari et al., 2012, as an indication of a variation of the stellar initial mass function as the dynamical mass increases). Their results have been obtained with dynamical models based on the Jeans (1919) equations and their observations trace the galaxy's dynamics out to $\sim R_{\mathrm{e}}$. Moreover, the spectral range sampled is quite limited (about $\sim 500\mathrm{aa}$), while modeling a stellar population would benefit also from a larger spectral coverage. An obvious way to improve and cross-check their results would be employing an Integral Field Unit with a much wider spatial and spectral coverage (e.g., PMAS/PPaK instrument) and by using more general and predictive models (e.g., distribution function models; see Section 2.2).

From the wide panorama of Integral Field Spectroscopic surveys, CALIFA stands out for having released data for the larger sample of diameter-selected galaxies of all Hubble types (about 600, see Sánchez et al., 2012, however MaNGA will enlarge the sample to about 10000) and larger field of view w.r.t. ATLAS$^{\mathrm{3D}}$, SAMI and MaNGA for instance. The CALIFA galaxy sample is ideal to study the internal dynamics of local galaxies, since the spectral range probed covers the whole optical domain (unlike e.g., ATLAS$^{\mathrm{3D}}$) which allows for the analysis of many different spectral features. Moreover for the diameter-selected galaxies, high-quality stellar kinematics can be extracted out to typically $2 - 3R_{\mathrm{e}}$, which is currently unprecedented.

1.5   Action-angle variables

In this Section I will briefly report some classical notions about integrable dynamical systems and angle-action coordinates. The formalism and notions here introduced are going to be extensively used in Chapters 3-4, where I present a novel family of dynamical models and I present applications to early-type galaxies in the nearby Universe. The most inspirational textbook, where all the following propositions can be found, is Arnold (1978), while most of the notations are taken from Binney & Tremaine (2008).

The time evolution of an N-dimensional dynamical system is governed by *Hamilton's equations*

$$\begin{aligned}
\frac{\mathrm{d}\mathbf{p}}{\mathrm{d}t} &= -\frac{\partial H}{\partial \mathbf{q}}, \\
\frac{\mathrm{d}\mathbf{q}}{\mathrm{d}t} &= \frac{\partial H}{\partial \mathbf{p}},
\end{aligned} \tag{1.5}$$

where $H = \frac{1}{2}||\mathbf{p}||^2 + \Phi$ is the Hamiltonian, $(\mathbf{p}, \mathbf{q})$ are a generic set of canonical momenta and positions and Φ is the gravitational potential[2]. Any function $I : \mathbb{R}^{2N} \longrightarrow \mathbb{R}$ such that

$$\frac{\mathrm{d}I}{\mathrm{d}t} = 0, \tag{1.6}$$

---

[2] Where I adopted the convention in which the mass is unity.

is said to be an *integral of motion*. For any functions $f, g : \mathbb{R}^{2N+1} \longrightarrow \mathbb{R}$ their *Poisson bracket* is

$$\{f, g\} := \frac{\partial f}{\partial \mathbf{q}} \cdot \frac{\partial g}{\partial \mathbf{p}} - \frac{\partial f}{\partial \mathbf{p}} \cdot \frac{\partial g}{\partial \mathbf{q}}. \tag{1.7}$$

Obviously, $\{f, f\} = 0$ for any $f : \mathbb{R}^{2N+1} \longrightarrow \mathbb{R}$. If I_1, I_2 are integrals of motion and $\{I_1, I_2\} = 0$, then I_1, I_2 are said to be *in involution*. Suppose there exist N integrals of motion $I_1, \ldots, I_N$ in involution, i.e., so that all their mutual Poisson brackets vanish, then the dynamical system is said to be *integrable* and viceversa. Each of the integrals in involution reduce the dimensionality of the space accessible to the motion by one, i.e., orbits are confined to a manifold in $\mathbb{R}^6$ in which N functions are constant. Because of this property, such integrals are also said to be *isolating integrals*.

The only set of N integrals of motion in involution that can be completed with a set of conjugate positions are called *actions* $\mathbf{J}$ and their conjugate positions are called *angles* $\boldsymbol{\theta}$. It can be shown that i) the angle variables are 2π-periodic, ii) the canonical transformation from the original $(\mathbf{p}, \mathbf{q})$ to the action-angle coordinates $(\mathbf{J}, \boldsymbol{\theta})$ is unique and iii) that the space where the orbits are confined is diffeomorphic to an N-torus in $\mathbb{R}^{2N}$ on which $(\mathbf{J}, \boldsymbol{\theta})$ are the natural coordinate frame. In action-angle coordinates Hamilton's equations read

$$\begin{aligned} \frac{d\mathbf{J}}{dt} &= -\frac{\partial H}{\partial \boldsymbol{\theta}} = 0, \\ \frac{d\boldsymbol{\theta}}{dt} &= \frac{\partial H}{\partial \mathbf{J}} \equiv \boldsymbol{\Omega}(\mathbf{J}), \end{aligned} \tag{1.8}$$

because the actions are integrals of motion. From the former it follows that the Hamiltonian is a function of the actions only $H = H(\mathbf{J})$, from the latter it follows that the angles increase linearly with time at a rate $\boldsymbol{\Omega}$ which is a function of tha actions only, i.e., $\boldsymbol{\theta}(t) = \boldsymbol{\theta}(0) + \boldsymbol{\Omega}(\mathbf{J})t$. Ω_i for each $i = 1, \ldots, N$ are the so-called *characteristic frequencies* or simply frequencies associated with the corrsponding angle and action (θ_i, J_i).

On the N-torus, the Poincarè invariant $\mathcal{P}$ vanishes

$$\mathcal{P} = \int_\Sigma d\boldsymbol{\theta} \cdot d\mathbf{J} = 0, \tag{1.9}$$

since each action J_i is constant on each 2-surface Σ on the N-torus. Hence, the N-torus is said be a *null* torus. The line integral $\oint_{\gamma_i} \mathbf{p} \cdot d\mathbf{q}$ performed on a curve $\gamma_i \subset \mathbb{R}^6$ on which the i-th angle varies in the range $0 \le \theta_i \le 2\pi$ while all the other are constants, is

$$\oint_{\gamma_i} \mathbf{p} \cdot d\mathbf{q} = J_i \int_{\gamma_i} d\theta_i = 2\pi J_i. \tag{1.10}$$

This result is insensitive to which path γ_i is actually used to perform the integration and depends only on the topology of the torus. This is because if one selects another path τ_i on which $\theta_i \in [0, 2\pi]$, the difference of the two integrals is equal to the integral of the closed line $\gamma_i - \tau_i$ which is equal to a surface integral by Green's theorem that vanishes for the same reason equation (1.9) does. For this reason in principle one could always

choose to integrate along an invariant curve parametrized by $t \mapsto \lambda(t)$ in the original $(\mathbf{p}, \mathbf{q})$ space so that

$$J_i = \frac{1}{\pi} \int_{\lambda_{\min}}^{\lambda_{\max}} p_i \, \mathrm{d}q_i, \tag{1.11}$$

where $\lambda_{\min}$ and $\lambda_{\max}$ are the minumum and maximum of the curve parametrization. Lastly, one of the most important properties of the action integrals is that they are *adiabatic invariants*, meaning that they do not change when the potential is stressed on timescales longer than the dynamical time. This property, which derives from the fact that $(\mathbf{J}, \boldsymbol{\theta})$ are canonical, makes the action integrals even more unique w.r.t. all the other isolating integrals of motion. In the study of the dynamics of galaxies this characteristic can be crucial if one wishes to study perturbed or multi-component systems.

For axisymmetric integrable potentials, one of the three actions quantifies the extent of the orbit's oscillation in the radial direction and I shall call it J_{r}; another one quantifies the extent of the orbit's excursion orthogonal to the equatorial plane and I shall call it J_{z}; finally, the last one is the component of the angular momentum about the symmetry axis and I shall call it $J_\phi \equiv L_{\mathrm{z}}$. Throughout this Thesis I will adopt this convention.

1.6 Overview of this Thesis

This Thesis discusses how the distribution of luminous and dark matter in early-type galaxies affects their evolution and dynamics. The main goals of the research conducted in the present Thesis are two: i) introducing a novel approach to the generation of equilibrium dynamical models to understand the detailed distribution of mass in nearby early-type galaxies and ii) investigating the role of dark-matter haloes in driving the time-evolution of the structural parameters of a population of early-types such as mass, size and velocity dispersion. For the first task, analytic computations together with numerical integrations are used to build the models and to project them in the observable space to be compared with observations of galaxies with photometry from the Sloan Digital Sky Survey (SDSS) and spectroscopy from the CALIFA collaboration. For the second task, numerical N-body models of the formation and evolution of a dark matter halo population in a cosmological context are used; then, the haloes are populated with galaxies with analytic prescriptions and such model galaxies are compared with a collection of diverse observations of early-type galaxies in the redshift range $0 \leq z \leq 2.5$ (galaxy sizes come from many surveys including SDSS and Great Observatories Origins Deep Survey[3], while the velocity dispersions at high redshift come from high-resolution spectrographs mounted on 8m-class telescopes).

In Chapter 2 a brief general introduction to collisionless dynamics is provided. The basic mathematical tools and notations used to characterize the dynamical state of a stellar system are introduced. Continuous and discrete models are described and their differences are discussed. Finally, numerical models for the time evolution of stellar systems are introduced.

---

[3] GOODS, see Giavalisco et al. (2004).

1.6.1 Action-based distribution function models

In Chapter 3 I present a novel approach to the design of distribution functions of spheroidal galaxy components. The distribution functions depend on the positions and velocities through the action integrals (Section 1.5) and are tailored for spherical and axisymmetric potentials. The models are three-integral, so that they represent general equilibrium configurations for axisymmetric systems. They are built on simple mathematical ansatz on the distribution function (i.e., that is a two-power law of the actions), which is motivated by robust dimensional arguments. We demonstrate the flexibility of our approach by designing distribution functions which yield potential-density pairs remarkably similar to that of classical models such as the Hernquist (1990), Jaffe (1983) and Navarro, Frenk, & White (1996) spheres.

Dynamical models for galaxies are easily generated and observables computed via integration in phase-space (Section 2.2.1) can readily be fitted to observations of stellar systems. Generalization to flattened and rotating models is trivial in the formalism of Binney (2014).

1.6.2 Dynamical models for nearby early-type galaxies

In Chapter 4 I apply the self-consistent action-based distribution function models of Chapter 3 to a sample of three early-type galaxies in the CALIFA survey. This serves as a proof-of-concept of the applicability of such newly developed dynamical models to galaxies observed with Integral Field Spectrographs. CALIFA is an ideal galaxy survey from which to draw the small sample of interest since, for each galaxy, high-quality velocity maps are measured up to typically $2-3R_{\mathrm{e}}$, where the dark matter component is expected to dominate the mass budget. The selected sample is heterogeneous in Hubble type (two ellipticals and one lenticular) and on the amount of rotational over random motion (one slow rotator and two fast rotators). The models are a generalization of those described in Chapter 3 to include adjustable flattening and rotation. Each model is self-consistent and axisymmetric and is specified by eight free parameters. For simplicity, the presentation is limited to models in which the dark matter follows the light profile, i.e., the mass-to-light ratio is constant with radius.

I establish a connection between the model's parameters and the physical observables, such as the surface brightness and the kinematics. Of the eight free parameters, two specify the model's surface brightness; four govern the model's orbital anisotropy and the flattening of its isophotes close to the centre and in the outskirts; finally, two vary the amplitude and steepness of the model's rotation curve. Additionally, two parameters are used to scale the model in physical units, while the inclination angle of the line-of-sight is estimated directly from the photometry of the galaxies. The free parameters are then adjusted so that the models are tailored to reproduce simultaneously the surface brightenss, from r-band SDSS images, and the velocity and velocity dispersion maps of each galaxy, from the CALIFA survey.

1.6.3   Size and velocity dispersion evolution of early-types and their dark matter haloes

In Chapter 5 I study the evolution of a population of early-type galaxies and their dark-matter haloes in a cosmological N-body simulation. This technique is ideal to study the statistical properties of a homogeneous population of collisionless systems and, in particular, I focus on their mass, size and velocity dispersion. Since there is growing observational evidence that the stellar density of early-types scales with the mean density of the Universe at the time of galaxy formation, I investigate the possible imprint that the cosmological evolution of dark matter haloes has left on galaxy evolution.

Since early-types are observed to adhere to tight scaling laws as well as the dark-matter haloes are expected to do, it is natural to ask whether the observed evolution of the galaxies' scaling laws is somehow driven by that of the haloes. To address this question, I analyse the mass-size and mass-velocity dispersion correlations for the dark haloes and accurately derive parametrizations for their evolution. The haloes follow well-defined evolutionary tracks on the mass-size and mass-velocity dispersion planes from $z \simeq 2.5$ to $z = 0$ and I study whether those tracks can be explained by analytic models in which the halo growth is due to dry mergers.

The implications for galaxy evolution are then investigated by populating the haloes with galaxies under simple, but justified prescriptions. I use models for the so-called stellar-to-halo mass relation from the literature which I integrate with expectations from simple cosmological models (see Mo, Mao, & White, 1998) for e.g., the stellar-to-halo size relation. This model allows to follow the average size and velocity dispersion of the model galaxy population from $z \simeq 2.5$ to $z = 0$ in the simulation. I compare the expectations of this models with a collection of photometric and spectroscopic observations of passive and massive galaxies from $z \simeq 2.5$ to $z = 0$.

Chapter 2

Dynamical models

In this Chapter I will briefly introduce the methods by which the dynamics of an early-type galaxy can be characterized. I will summarize the theoretical foundations of the methods I will be using to model galaxies in the next Chapters, then I will introduce both the modeling techniques used in Chapters 3-5 and other popular ones to which one can compare. The discussion is arranged as follows: first, steady-state models are presented and I first focus on those that model continuously the mass density and the gravitational potential and then on those which generate model galaxies as superposition of a finite number of discrete elements; finally, I briefly introduce a class of non-stationary models which follow the galaxy evolution.

2.1 Introduction

2.1.1 Collisionless dynamics

A system composed of many stars orbiting in the same potential well would have an internal dynamics different depending on whether the motion of a star is influenced by the short-range collisions with other stars. If the cumulative effect of all the encounters is that of changing significantly the orbit that the star would have had in a smooth gravitational field, then the system is called *collisional* and its properties are completely insensitive to the initial conditions, since the many collisions have completely changed the structure of the system. In astronomy, dense star clusters are an example of such systems. On the other hand, if encounters do not alter significantly the motion of a star, then the orbits of each star are governed not by the exact locations of the other stars in the system, but instead by the overall gravity field made by those stars. These systems are called *collisionless* of which galaxies are a perfect astronomical example.

23

To quantify the importance of collisions in the dynamical evolution of a stellar system, one usually computes the time that it takes for a star of mass m, orbiting in the system of N other stars at velocity $\mathbf{v}$, to change its speed by $||\Delta\mathbf{v}|| \sim ||\mathbf{v}||$, i.e., the time to change its speed by of the order itself. Such time will be called *two-body relaxation time* or simply *relaxation time* and can be shown to be (see e.g., Binney & Tremaine, 2008, §1.2.1)

$$t_{\mathrm{relax}} \sim \frac{N}{8\ln N} t_{\mathrm{cross}}, \tag{2.1}$$

where $t_{\mathrm{cross}} \sim R/V$ is the crossing time, i.e., the typical time required to pass through the system, and R and V are some system's characteristic length and velocity scales. For a galaxy whose length and velocity scales are $R \sim 5$ kpc and $V \sim 220$ km/s and which contains some 10^{11} stars, the relaxation time is $t_{\mathrm{relax}} \simeq 2.5 \times 10^6 \, t_{\mathrm{H}}$, where t_{H} is the Hubble time. Hence, stellar encounters are not driving the galaxy dynamics and the galaxy itself is said to be a collisionless gravitational system.

While it seems to be un-practical to follow each stars' orbit in the galaxy's potential, it is customary to adopt a probabilistic approach at the problem and to focus on the probability of finding a star orbiting around a given position $\mathbf{x}$, in the three dimensional configuration space, and a given velocity $\mathbf{v}$, in the three dimensional velocity space[1]. Since any orbit's domain is the six dimensional *phase space*, i.e.,

$$\Gamma \subseteq \mathbb{R}^6 : \ \forall \boldsymbol{\gamma} \in \Gamma, \ \exists (\mathbf{x}, \mathbf{v}) \in \mathbb{R}^3 \times \mathbb{R}^3 : \boldsymbol{\gamma} = (\mathbf{x}, \mathbf{v}), \tag{2.2}$$

and given that the phase-space volume element is $\mathrm{d}\Gamma = \mathrm{d}\mathbf{x}\,\mathrm{d}\mathbf{v}$, I define the system's *distribution function* (hereafter DF) as

$$f : \Gamma \times \mathbb{R} \longrightarrow \mathbb{R}^+, \tag{2.3}$$

so that $f(\mathbf{x}, \mathbf{v}, t)\,\mathrm{d}\mathbf{x}\,\mathrm{d}\mathbf{v}$ is the probability of finding a star in a given phase-space volume element $\mathrm{d}\mathbf{x}\,\mathrm{d}\mathbf{v}$ at time t. In order to be a meaningful representation of such a probability, the DF must be positive-definite and normalized so that the probability that the star can be found in the whole phase-space volume is the total mass of the system M:

$$\int_\Gamma f(\mathbf{x}, \mathbf{v}, t)\,\mathrm{d}\mathbf{x}\,\mathrm{d}\mathbf{v} = M. \tag{2.4}$$

The time evolution of the DF is regulated by Liouville (1838) theorem, which encapsulates the conservation of volumes in phase space:

$$\frac{\partial f}{\partial t} + \frac{\partial f}{\partial \mathbf{x}} \cdot \dot{\mathbf{x}} + \frac{\partial f}{\partial \mathbf{v}} \cdot \dot{\mathbf{v}} = 0, \tag{2.5}$$

i.e., the *total derivative* $\mathrm{d}f(\mathbf{x}, \mathbf{v}, t)/\mathrm{d}t$ (often called Lagrangian derivative, see e.g., Binney & Tremaine, 2008, §F.1.2) vanishes along an orbit in phase space. Equation (2.5) is also referred as the *collisionless Boltzmann equation* (hereafter CBE) or Vlasov equation and using Hamilton's equations it can be re-arranged as:

$$\frac{\partial f}{\partial t} + \frac{\partial f}{\partial \mathbf{x}} \cdot \mathbf{v} - \frac{\partial f}{\partial \mathbf{v}} \cdot \frac{\partial \Phi}{\partial \mathbf{x}} = 0, \tag{2.6}$$

where $H = ||\mathbf{v}||^2/2 + \Phi(\mathbf{x}, t)$ is the Hamiltonian and $\Phi(\mathbf{x}, t)$ is the gravitational potential.

---

[1] For the purpose of this introduction I can assume, without loss of generality, that the star's mass is unity and hence that the usual Lagrangian canonical coordinates $(\mathbf{q}, \mathbf{p}) = (\mathbf{x}, \mathbf{v})$.

2.1.2   Equilibrium

A particular class of solutions to the CBE are the *configurations of dynamical equilibrium* (or steady-state or stationary solutions), in which the phase-space density f does not depend explicitly on time t, i.e., $f = f(\mathbf{x}, \mathbf{v})$. It can be shown that any stady-state solution of the CBE is constant along all the orbits in phase space, so it is an integral of motion (1.6), and therefore the dynamical equilibrium configurations are those in which also the DF itself is an integral of motion.

It is unclear whether galaxies can effectively be represented by stationary configurations: complex phenomena involving baryonic physics (such as dissipation, star-formation, winds and spiral arms) and not (such as mergers, tidal interactions and rotating bars) are very likely to push a stellar system away from a steady-state. Even so, equilibrium models have a fundamental role to play in the dynamics of galaxies, the main reason being that out-of-equilibrium configurations, e.g., in which the potential is also a function of time $\Phi = \Phi(\mathbf{x}, t)$, are best studied via perturbing equilibrium states (e.g., Arnold, 1978).

Collisionless systems are driven to dynamical equilibrium states by phenomena such as *phase mixing* (see e.g, Binney & Tremaine, 2008, §4.10.2) and *violent relaxation* (see Lynden-Bell, 1967): the former is able to "diffuse" clumps in phase space as time goes by, so that averages of the DF computed within fixed and finite volumes of phase space decrease with time before reaching a (almost) constant value; the latter can alter the energies of the stars widening the range of allowed orbits. These processes have net effects analogous to those produced by collision-induced relaxation in an ordinary gas (even if gravitational systems do not tend to maximum-entropy steady-states[2]) as they make the galaxy reach an almost stationary configuration.

A fundamental tool in the attempt to build steady-state models of galaxies is the following theorem due to Jeans (1915).

Theorem (Jeans). *$f : \Gamma \times \mathbb{R} \longrightarrow \mathbb{R}^+$ is a steady-state solution of the CBE (2.6) if and only if it depends on the phase-space coordinates only through integrals of motion, i.e., $f(\mathbf{x}, \mathbf{v}, t) = f[I_1(\mathbf{x}(t), \mathbf{v}(t)), \cdots, I_N(\mathbf{x}(t), \mathbf{v}(t))]$, where $\mathrm{d}I_j/\mathrm{d}t = 0, \forall j = 1, \cdots, N$.*

Proof. If f is a steady-state solution, then it is also an integral of motion (1.6). Conversely, if $f(\mathbf{x}, \mathbf{v}, t) = f[I_1(\mathbf{x}(t), \mathbf{v}(t)), \cdots, I_N(\mathbf{x}(t), \mathbf{v}(t))]$, where I_j is an integral of motion (1.6) for all $j = 1, \cdots, N$, then

$$\frac{\mathrm{d}f}{\mathrm{d}t} = \sum_{j=1}^{N} \frac{\partial f}{\partial I_j} \frac{\mathrm{d}I_j}{\mathrm{d}t} = 0. \tag{2.7}$$

$\square$

Since any function of only integrals of motion is also another integral of motion, Jeans' theorem would be unhelpful in the study of galaxies if it wasn't for a more

---

[2] Unlike ideal gases, for which from first principles it is to be expected that the system is inclined towards a (unique) maximum entropy state, for a gravitational system such a maximum entropy configuration does not exists, since for any stellar system with finite mass and total energy it is always possible to find re-distribution of stars with larger entropy (see e.g., Binney & Tremaine, 2008, §4.10.1).

restrictive result that directly derives from it. I shall call the following Lynden-Bell (1962b) theorem, but it is also known as Strong Jeans theorem (Binney 1982a and also Binney & Tremaine, 2008, §4.2).

Theorem (Lynden-Bell). *The* DF *of any integrable stellar system depends on phase-space coordinates only through isolating integrals of motion.*

A system with N degrees of freedom (dof) for which all the orbits are regular (quasi-periodic[3]) admits N isolating integrals of motion and it is therefore integrable[4]. Galaxies are three-dof systems, but in general it is difficult to determine whether the nature of the orbits of its stars is regular or chaotic. For instance, stars living on stellar discs are on (nearly) circular orbits which are regular, though the presence of resonances, due e.g., to the rotation speed of the galaxy, can induce chaotic behaviour on the stars' orbits (e.g., resonant trapping, see Binney & Tremaine, 2008, §3.7.2). Hence, a typical approach one can follow is assuming that all the motion of stars in a galaxy is on regular orbits and studying to what extent such integrable systems resemble real galaxies in observable space. More general configurations in which not all orbits are regular are best studied either numerically (e.g., Binney & Spergel, 1982) or by perturbation theory starting from a known integrable configuration (e.g., Laskar, 1990; Gerhard & Saha, 1991; Binney & Tremaine, 2008, §3.7.1).

In the following Sections I will describe methods for generating dynamical equilibrium models focusing on systems that are integrable and self-consistent, i.e., such that the distribution of the luminous matter (the tracers) contributes to the total potential. However, globular clusters (e.g., Côté et al., 2003), planetary nebulae (e.g., Méndez et al., 2001) and also extended X-ray haloes (Humphrey et al., 2006) have extensively been used as (almost) mass-less tracers of the potential of massive ellipticals and several works have proved it to be a successful method to estimate the total distribution mass in such galaxies (see Section 1.2.1). The models developed below can also be applied to these non self-gravitating systems.

2.1.3   Symmetries in galactic potentials and classical integrals

Even if galaxies are fairly complex systems they usually possess evident spatial symmetries that can be exploited when looking for a (stationary) potential $\Phi = \Phi(\mathbf{x})$ that characterizes them. For instance, disc galaxies are to first order axisymmetric about the axis orthogonal to the disc plane, while globular clusters and clusters of galaxies are to first order spherically symmetric. Elliptical and lenticular galaxies appear to have nearly spheroidal or ellipsoidal isodensity surfaces (e.g., Binney & Merrifield, 1998, §4.3). For these objects, which have likely undergone some relaxation process, it seems to be adequate to adopt potentials stratified on ellipsoidal surfaces (see Binney & Tremaine, 2008, §2 for a comprehensive review of galactic potentials).

---

[3] An orbit is *quasi-periodic* if the trajectory is a quasi-periodic function: a function $f : \Gamma \times \mathbb{R} \longrightarrow \mathbb{R}$ is quasi-periodic if for any sequence $\beta_n \in \mathbb{R}^n$, there is a subsequence $\alpha_n \subset \beta_n$ such that the sequence of functions $f_n(x) = f(x + \alpha_n)$ for $n \in \mathbb{N}$ converges uniformly in the limit $n \to +\infty$.

[4] The Hamilton-Jacobi equation for that system is separable is some coordinates.

An isolated system where the total potential is time-independent, $\Phi = \Phi(\mathbf{x})$, conserves its energy: $H = H(\mathbf{x}, \mathbf{v}) = E$, where E is a constant. Any symmetry of time and space under which the potential is invariant implies a conservation law for the system[5]. So, any equilibrium configuration of interest in galactic dynamics with a time-invariant potential will have at least one isolating integral of motion, the energy H. Other isolating integrals can be readily obtained for systems with special symmetries.

The simplest class of potentials is that of central potentials $\Phi = \Phi(||\mathbf{x}||)$, for which equipotential and corresponding isodensity surfaces are stratified on spheres. In this case the motion is restricted onto a plane, since the angular momentum vector $\mathbf{L} = \mathbf{x} \times \mathbf{v}$ is conserved. This gives three additional isolating integrals of motion that are the three components of $\mathbf{L}$. Axisymmetric potentials where $\Phi = \Phi(R, z)$ in cylindrical coordinates (R, ϕ, z) being z in the direction of the symmetry axis, admit only another isolating integral which is the component of the angular momentum about the symmetry axis L_z. For these systems, the equipotential surfaces are stratified on spheroids flattened on the z direction, in contrast with triaxial potentials which are stratified on ellipsoids in three dimensions and have all the three semi-axes different. Such systems do not posses any spatial symmetry and therefore no other isolating integral except H is known in general.

Isolating integrals such as the energy, the components of the angular momentum or their combinations are usually referred as *classical integrals*. This is because they are the isolating integral that one can promptly derive from geometrical symmetries of the system. Non-classical integrals are, on the other hand, conserved quantities that are not directly related to time- or rotation-invariance of the potential. With this classification the action integrals would be in general considered non-classical.

2.1.4 Third integral of motion

2.1.4.a Clues from orbit integration

The phase space Γ is six-dimensional as well as the configuration space and, therefore, the number of degrees of freedom is three for such systems. Any isolating integral reduces by one the dimensions of the surface in phase space on which the orbits lives. The maximum number of isolating integrals for stellar system is hence five, so that the orbit is confined to a one-dimensional curve in phase space. The minimum number of isolating integrals is, instead, one: the energy H.

Integrable systems have at least three isolating integrals, so that the orbit is diffeomorphic to a torus in phase space. However, for axisymmetric potentials, which play a special role of interest in galactic dynamics, only two classical isolating integrals are known, so one wonders if these systems are in general integrable or not. While the most general configuration is that of a non-integrable system, for which orbits are higher-dimensional manifolds in phase space, it is natural to ask whether for some potentials of interest in galactic dynamics there are integrable configurations. In that case, there must be an additional *third non-classical integral of motion* I_3 that makes the Hamilton-

---

[5] From a more formal point of view: if the Lagrangian $\mathcal{L}$ admits a *cyclic variable*, i.e., any generalized coordinate q_i such that $\partial \mathcal{L}/\partial q_i = 0$, then the quantity $\partial \mathcal{L}/\partial \dot{q}_i$, where $\dot{q}_i = \mathrm{d}q_i/\mathrm{d}t$, is an integral of motion (see e.g., Landau & Lifshitz, 1969).

Jacobi equation separable together with H and L_z. One way to address that question is by numerically integrate orbits in a given potential and then characterize them in either regular or chaotic. The seminal works by Contopoulos (1963) and Ollongren (1962) were the first to establish that axisymmetric galactic potentials possess regular orbits which can not be completely specified by their values of energy and angular momentum and Contopoulos (1960) gives an analytic expression of the third integral in the form of an ansymptotic power series. For instance, Figure 2.1 shows two orbits in the meridional plane of an axisymmetric logarithmic potential (see Binney & Tremaine, 2008, §2.3.2) which have been integrated for several dynamical times. These two orbits have the same values of the classical integrals of motion H and L_z, yet they look very different. In particular, one seems to have a larger radial excursion, i.e. $R_{max} - R_{min}$, while the other has a much larger vertical excursion z_{max}. Hence, specifying only H and L_z does not uniquely characterize the orbit. Nevertheless, the two orbits appear regular and not chaotic and, as a matter of fact, they do not fill the whole region available for their motion, defined by the zero-velocity curve on the meridional plane, because they are confined by their respective invariant curves[6] (see Richstone, 1982; Binney & Tremaine, 2008, §3.2.1). This suggests that a third isolating non-classical integral of motion is conserved by these orbits, since only for a three-integral system all the orbits are regular. Their Poincarè surfaces of section, for (R, v_R) at $z = 0$ and $v_z > 0$, are shown in Figure 2.2. The series of the consequents[7] for both orbits lie on two smooth invariant curves, which is the intersection of the two orbital torii with the (R, v_R) plane.

2.1.4.b Clues from observations

The most convincing argument which favors the introduction of a third isolating integral of motion from observations of both the Milky Way and external galaxies is that of the velocity ellipsoids (see e.g., Binney & Tremaine, 2008, §4.1.2 for a definition of velocity ellipsoids). The old stars in the solar neighbourhood are known from a very long time to have a different kinematics in the radial and vertical directions (Kapteyn, 1922; Oort, 1932). From modern measurements with dedicated surveys, we know now that the radial velocity dispersion of giant stars distant from the Sun less than than 2.5 kpc is roughly two times that in the vertical direction (Sharma et al., 2014; Binney et al., 2014). Conversely, in external galaxies the velocity ellipsoids are not directly observables, since the lack of proper motion measurements does not allow to estimate the velocity dispersion in directions other than that of the line-of-sight. Nonetheless, they can be reasonably inferred from e.g., line-of-sight velocity dispersion measurements along the major and minor axis: van der Marel (1991) computed the ratio of the line-of-sight velocity dispersion at distance r along the major and minor axis both for the observed galaxies and for some oblate two-integral models. The main result is that those two-integral models are inconsistent with observations and the measured discrepancy is larger for flatter galaxies. Another technique that has been used to assess the geometry

---

[6] A curve $\gamma \subset \Gamma$ is said to be an *invariant curve* if the orbit through a point in γ remains in γ at all times.

[7] The consequents are the intersections of the orbit's trajectory with the plane of the surface of section at $z = 0$ when the orbit is rising along the z-axis, i.e., $v_z > 0$.
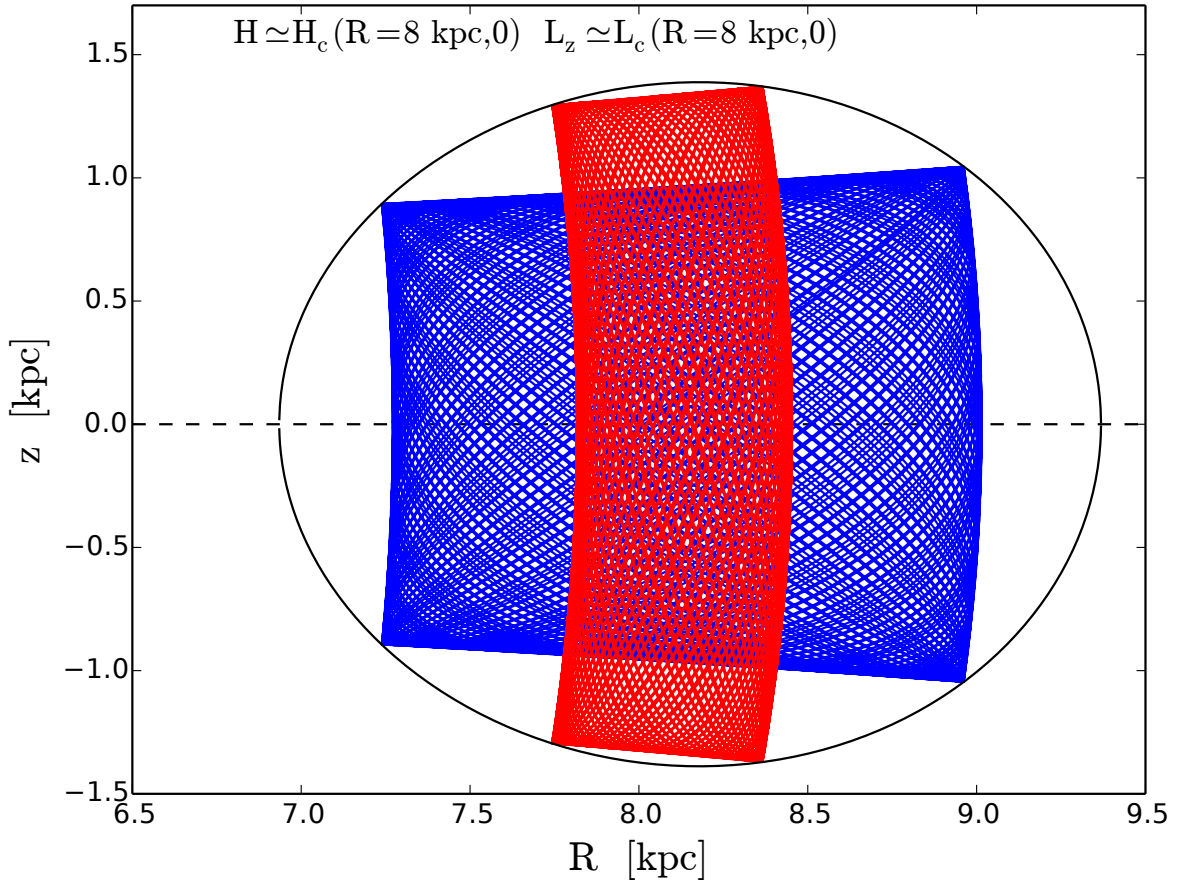
Figure 2.1: Two orbits in the meridional plane for a logarithmic potential $\Phi(R, z) = \frac{v_c^2}{2} \ln(R^2 + z^2/q^2)$ with $v_c = 220$ km/s and $q = 0.8$ integrated for about 10 Gyr. The two orbits share the same energy H and vertical component of the angular momentum L_z which are equal to those of the circular orbit H_c and L_c at $R = 8$ kpc in the equatorial plane. Despite having two equal classical integrals of motion, the two orbits appear much different. None of them fills entirely the region allowable for motion defined by the zero-velocity curve (black line), meaning that they are both confined within a well-defined invariant curves (see also Richstone, 1982).

of the velocity ellipsoids is inferring them by fitting accurate two- and three-integral dynamical models to spectroscopic data (see e.g., Emsellem, Dejonghe, & Bacon, 1999; Cappellari et al., 2007): the overall results is that they are far from spherical.

2.2   Continuous models: distribution function

Spherical, axisymmetric or triaxial stellar systems can be described with appropriate choices for the DF. A system with three integrals of motion would admit only quasi-periodic orbits, since a canonical transformation to angle-action coordinates is always possible (see Section 1.5). That is, any orbit is diffeomorphic to a three-dimensional torus in phase space which can be described by means of angle-action coordinates.
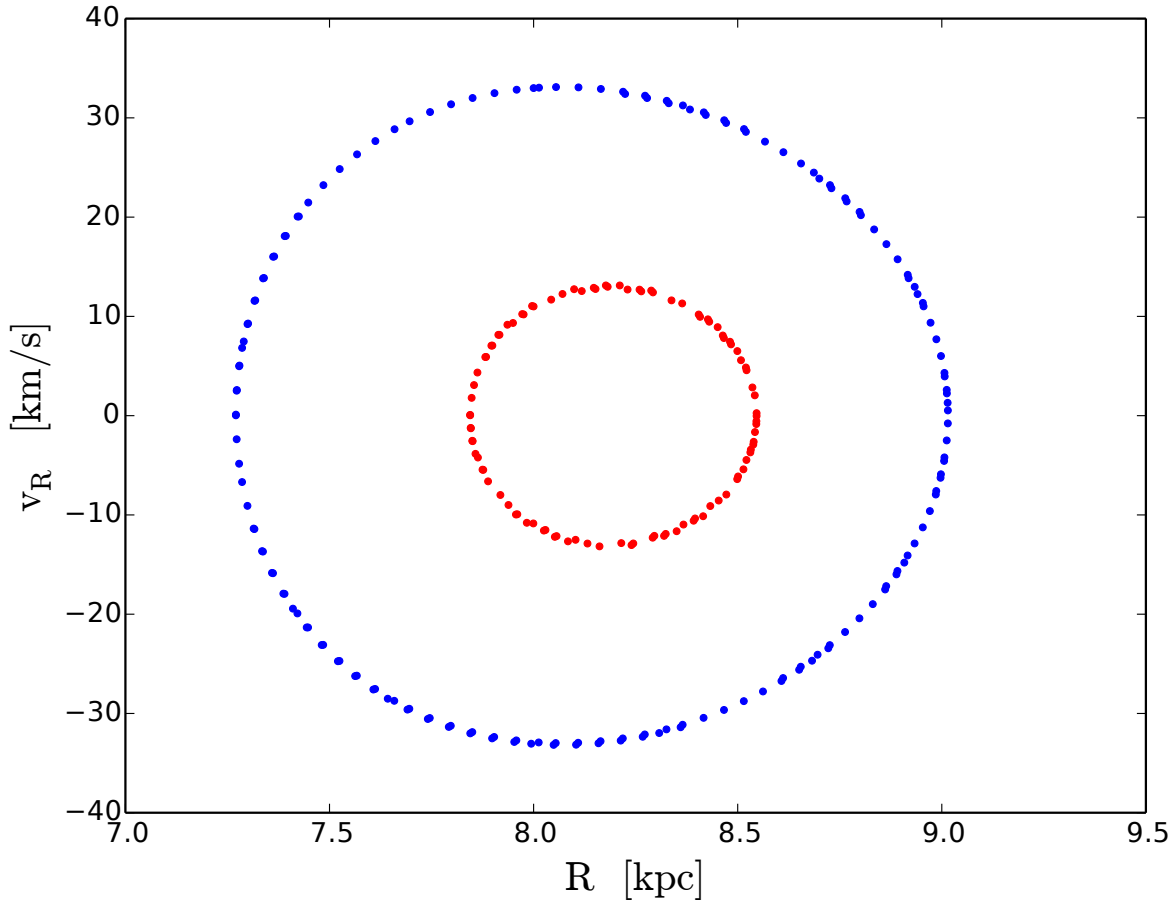
Figure 2.2: Surfaces of section for the same orbits as in Figure 2.1. The consequents of the two orbits lie on two different smooth invariant curves, indicating the conservation of an additional integral of motion w.r.t. H and L_z.

Further isolating integrals exist if any ratio between the characteristic frequencies Ω_i (see equation 1.8 and Section 1.5) is commensurable like, for instance, in the case of Kepler's potential $\Phi \propto r^{-1}$ (see Binney, 1982b).

2.2.1   Observables

The DF completely specifies the dynamical state of a stellar system since it gives access to the probability of finding a star at a given position in phase space. Typical observable quantities such as the mass- or luminosity-density, the mean velocity of stars along a given line-of-sight or their velocity dispersion along the same line-of-sight are readily computed by integration in phase space (e.g., Binney & Tremaine, 2008, §4.1.2).

   The mass density at any fixed position $\mathbf{x}$ is given by the integral

$$\rho(\mathbf{x}) = \int \mathrm{d}^3\mathbf{v}\, f(\mathbf{x}, \mathbf{v}), \qquad (2.8)$$

the mean velocity $\overline{\mathbf{v}}$ is

$$\overline{\mathbf{v}}(\mathbf{x}) = \frac{1}{\rho(\mathbf{x})} \int \mathrm{d}^3\mathbf{v}\, \mathbf{v}\, f(\mathbf{x}, \mathbf{v}), \tag{2.9}$$

and the components of the velocity-dispersion tensor σ_{ij} for $i, j = 1, 2, 3$ are given by

$$\sigma_{ij}^2(\mathbf{x}) = \frac{1}{\rho(\mathbf{x})} \int \mathrm{d}^3\mathbf{v}\, (v_i - \overline{v}_i)(v_j - \overline{v}_j)\, f(\mathbf{x}, \mathbf{v}), \tag{2.10}$$

which can be also written as $\sigma_{ij}^2 = \overline{v_i v_j} - \overline{v}_i \overline{v}_j$. Spectroscopy can be used to probe the target's *line-of-sight velocity distribution* by carefully analyzing the shift of the spectral lines w.r.t. rest frame laboratory lines. Typically, the first and second velocity-moments of the DF can be inferred by high-quality spectra. In principle, the observed line-of-sight velocity distribution can be used to probe the probability distribution of the velocity of the stars $\mathbf{v}$ at the position $\mathbf{x}$

$$P_{\mathbf{x}}(\mathbf{v}) = \frac{f(\mathbf{x}, \mathbf{v})}{\rho(\mathbf{x})}. \tag{2.11}$$

2.2.2 Spherical systems

The first attempts of modeling stellar systems by seeking a functional form for the DF were made under assumptions of spherical symmetry about a hundred years ago. Two approaches can be followed:

(i) make an ansatz on the functional form of the DF, derive observables and compare with observations,

(ii) or derive a density-potential pair (ρ, Φ) from observations and then invert equation (2.8) to get f.

The energy H is an isolating integral of motion, therefore models for which the DF depends solely on H, i.e., $f = f(H)$, are physically plausible and are called *ergodic models* (see Binney & Tremaine, 2008, §4.2.1 and §4.3). To this category belong popular models such as Plummer (1911) and King (1966) which have proved to be very successful in the field of modeling globular clusters. $f = f(H)$ systems with $H = ||\mathbf{v}||^2/2 + \Phi(r)$, where the potential Φ is central (r is the spherical radial coordinate), have equi-phase-space-density surfaces that overlap with equi-energetic surfaces, which are spheres since the system is spherical. Defining $v \equiv ||\mathbf{v}||$, we then have that the density distribution is also spherical[8]

$$\rho(r) = 4\pi \int \mathrm{d}v\, v^2\, f(H) = 4\pi \int_0^{-\Phi} \mathrm{d}H\, f(H) \sqrt{2(H - \Phi)}. \tag{2.12}$$

Models in which the DF is ergodic can not have streaming motions since f depends only on the absolute values of the velocities and not on their sign, therefore the integrals (2.9)

---

[8] Here I have implicitly assumed that the system extends to infinity and that the potential is zero at infinity.

always vanish. For the same reasoning also the off-diagonal terms of the velocity dispersion tensor vanish and the only terms which survive are those in which the integrand in (2.10) are even functions of the velocities, i.e., only the diagonal terms. Moreover, the diagonal terms are also equal to each other, since in the DF the three velocities all appear on the same footing:

$$\sigma_{ij}^2(r) = \sigma^2(r)\delta_{ij}, \quad \text{where} \quad \sigma^2(r) = \frac{4\pi}{3\rho(r)} \int_0^{-\Phi} \mathrm{d}H \, f(H) \, [2(H - \Phi)]^{3/2} \qquad (2.13)$$

Such spherically symmetric, non-rotating and isotropic models are of theoretical interest since $f = f(H)$ can be chosen so that the integrals in (2.12)-(2.13) are analytically tractable.

The dependence of the DF on another isolating integral of motion in spherical symmetry, i.e., the magnitude of the angular momentum L, generalizes spherical models to be anisotropic, i.e., so that the velocity dispersion is not the same in all directions[9]. Then, the DF would be $f = f(H, L)$. For a spherical galaxies to be also spherically symmetric in all its properties (e.g., $\sigma_{ij}(\mathbf{x})$), the DF can not depend on any component of $\mathbf{L}$ along a preferred direction, therefore two-integral models of the kind $f = f(H, L)$ are the most general for completely spherically symmetric systems[10]. Models of this type are for instance the Michie (1963) and Osipkov-Merritt models (Osipkov, 1979; Merritt, 1985). For anisotropic models one usually defines the *anisotropy parameter* β which quantifies the model's bias towards more radial or more circular orbits:

$$\beta \equiv 1 - \frac{\sigma_\theta^2 + \sigma_\phi^2}{2\sigma_r^2}, \qquad (2.14)$$

where I have abbreviated $\sigma_i = \sigma_{i,i}$ for the three diagonal components of σ_{ij}. With this definition, isotropic models have $\beta = 0$, models with $\beta = 1$ have all radial orbits and models with $\beta \to -\infty$ have purely circular orbits. How the DF depends on the angular momentum L determines the behaviour of the anisotropy parameter as a function of radius $\beta = \beta(r)$. For instance, DFs of the type $f(H, L) = L^{-2\beta}F(H)$ generate systems with constant anisotropy β; Osipkov-Merritt models have, instead, anisotropy increasing from $\beta \to 0$ at the centre to $\beta \to 1$ at the system's outskirts (e.g., Binney & Tremaine, 2008, §4.3.2b).

Instead of deriving observables given a specific DF, one can try to infer f from the observed luminosity density by inverting equation (2.8). With the assumption of spherical symmetry one can deproject the observed luminosity density of a given stellar system and compute the intrinsic three-dimensional luminosity density $\nu(r)$. If the system's mass-to-light ratio $\Upsilon \equiv M/L$ is constant with radius, then the mass density is $\rho(r) = \Upsilon\nu(r)$. The system is also self-consistent if the gravitational potential is

$$\Delta\Phi = 4\pi G\rho, \qquad (2.15)$$

---

[9] σ_{ij} has at least two different eigenvalues, which makes the three-dimensional velocity ellipsoid non-spherical.

[10] As a counter-example of a three-integral $f = f(H, L, L_z)$ that generates a system with a spherical density $\rho(r)$ which has a net rotation about the z axis see Lynden-Bell (1960).

being G the gravitational constant and Δ the Laplace operator. A classical and very important result in galaxy dynamics is the following: under certain conditions, it is possible to find an ergodic DF that generates the self-consistent potential-density pair (ρ, Φ). Eddington (1916) proved that using an Abel (1826) transform on equation (2.12) one can solve for the ergodic DF

$$f(\mathcal{E}) = \frac{1}{\sqrt{8}\pi^2} \frac{\mathrm{d}}{\mathrm{d}\mathcal{E}} \int_0^{\mathcal{E}} \frac{\mathrm{d}\Psi}{\sqrt{\mathcal{E} - \Psi}} \frac{\mathrm{d}\rho}{\mathrm{d}\Psi}, \qquad (2.16)$$

where $\mathcal{E} \equiv -H$ and $\Psi \equiv -\Phi$ are the relative energy and potential, respectively[11]. The condition which must be satisfied so that the DF is positive-definite is that $\int_0^{\mathcal{E}} \mathrm{d}\Psi (\mathcal{E} - \Psi)^{-1/2} \rho'(\Psi)$ is an increasing function of $\mathcal{E}$. Given self-consistent potential-density pairs such as that of the Hénon (1959) isochrone, the Jaffe (1983) and the Hernquist (1990) models, it is possible to solve equation (2.16) analytically to yield corresponding positive-definite ergodic DFs (e.g., Binney & Tremaine, 2008, §4.3.1a). A generalization of equation (2.16) to spherical anisotropic systems is not trivial, but in some cases of interest, such as constant-anisotropy models $f(H, L) = L^{-2\beta} F(H)$ and Osipkov-Merritt models, analytical expressions for the two-integral DF which generates an given (ρ, Φ) can be derived (e.g., Binney & Tremaine, 2008, §4.3.2).

2.2.3 Axisymmetric systems

If the potential $\Phi(\mathbf{x})$ is non-spherical, but symmetric around the z-axis, then $L_z = Rv_\phi$ is an isolating integral of motion, while L is not. For these systems the DF must depend on at least the energy and the z-component of the angular momentum.

Galaxies that appear axisymmetric in projection are often found to have a dynamically-important net rotation around their symmetry axis. The disc of spiral galaxies is mostly made by stars on nearly circular orbits with a coherent sense of rotation and recently it was shown that dynamically-important streaming motions are present also in most axisymmetric early-type galaxies (e.g., Emsellem et al., 2004). Hence, models with non-vanishing mean rotation around their symmetry axis are of great interest. For any axisymmetric potential the DF of the system will generally be a function of L_z and H, i.e., $f = f(H, L_z)$, which can be always separated in an odd f_- and an even component f_+ with respect to the argument L_z

$$f(H, L_z) = f_+(H, L_z) + f_-(H, L_z) \qquad (2.17)$$

where

$$f_+(H, L_z) = \frac{f(H, L_z) + f(H, -L_z)}{2}$$
$$f_-(H, L_z) = \frac{f(H, L_z) - f(H, -L_z)}{2}. \qquad (2.18)$$

---

[11] The relative energy and potential of a system which does not extend to infinity would be $\mathcal{E} \equiv -H + \Phi_0$ and $\Psi \equiv -\Phi + \Phi_0$, where Φ_0 is an arbitrary additive constant.

The mass density is readily obtained as

$$\rho(R, z) = \frac{4\pi}{R} \int_0^{-\Phi} \mathrm{d}H \int_0^{R\sqrt{2(H-\Phi)}} \mathrm{d}L_\mathrm{z}\, f_+(H, L_\mathrm{z}). \qquad (2.19)$$

The odd part f_- does not contribute to the mass density (equation 2.8) since f_- is odd v_ϕ and hence $\int \mathrm{d}^3\mathbf{v}\, f_- = 0$. Conversely, the even part f_+ does not contribute to the net streaming motion in the azimuthal direction, which is

$$\overline{v}_\phi = \frac{1}{\rho} \int \mathrm{d}^3\mathbf{v}\, v_\phi\, f(H, L_\mathrm{z}) = \frac{1}{\rho} \int \mathrm{d}v_\mathrm{R} \int \mathrm{d}v_\mathrm{z} \int \mathrm{d}v_\phi\, v_\phi\, f_-(H, L_\mathrm{z}). \qquad (2.20)$$

The mean velocities along the radial and vertical directions, $\overline{v}_\mathrm{R}$ and $\overline{v}_\mathrm{z}$ respectively, vanish also for $f = f(H, L_\mathrm{z})$ models. Moreover, their second velocity-moments would be equal in the radial and vertical directions, i.e., $\sigma_\mathrm{R}=\sigma_\mathrm{z}$, while that on the azimuthal direction would generally differ from the previous two, i.e.,

$$\sigma_\phi^2 = \frac{1}{\rho} \int \mathrm{d}v_\mathrm{R} \int \mathrm{d}v_\mathrm{z} \int \mathrm{d}v_\phi\, (v_\phi - \overline{v}_\phi)^2\, f_+(H, L_\mathrm{z}). \qquad (2.21)$$

For such two-integral axisymmetric models, the pressure acting on any direction of the meridional plane (R, z) is the same and it is different from that acting in the azimuthal direction. All their mixed velocity moments, i.e., the off-diagonal terms of σ_{ij}^2, vanish since the DF is even in both v_R and v_z, therefore the sections of the velocity ellipsoids in the meridional plane are circles everywhere on the plane. For these systems the velocity ellipsoid is said to be aligned with the cylindrical coordinates, since σ_{ij}^2 is diagonal in that coordinate frame. Popular two-integral $f = f(H, L_\mathrm{z})$ models are, for instance, the Fricke (1952) and Evans (1994) power-law galaxies.

Amongst the observables of interest in galaxy dynamics, only the odd part f_- affects the system's rotation and viceversa. This is one of the most useful properties of two-integral DFs for axisymmetric galaxies: in pronciple the observed rotation pattern completely determines f_-, while f_+ is unaffected by the galaxy's streaming motion and can be constrained using the observed light and velocity dispersion distribution. Many authors attempted to generalize Eddington's inversion formula (2.16) to the axisymmetric case[12] (see e.g., Lynden-Bell, 1962a; Hunter, 1975; Dejonghe, 1986; Hunter & Qian, 1993) and others have constructed realistic galaxy models fully exploiting observations to constrain the even and odd parts two-integral models (see e.g., Binney, Davies, & Illingworth, 1990; van der Marel et al., 1994; Dehnen, 1995): typically a model is fitted to the (de-)projected luminosity density and the potential of the stellar component is computed via Poisson's equation (2.15), while the observed velocity dispersions give constraints only on the mass implied by f_+ and not on its functional form; then, the odd part f_- is fitted to the observed streaming velocities. Despite being a very successful approach, one of the major cons of such method is that it is unable to rule-out more general solutions such as three-integral $f = f(H, L_\mathrm{z}, I_3)$ model, where I_3 is the third isolating non-classical integral of motion.

---

[12] The most general solution to the problem of inverting equation (2.19) is that of Hunter & Qian (1993), which gives $f(H, L_\mathrm{z})$ via a contour-integration of $\rho(R, \Phi)$ on the complex plane.

Moreover, another issue of axisymmetric two-integral models is that since $\sigma_{\mathrm{R}} = \sigma_{\mathrm{z}}$, flattened oblate models can be made only via large azimuthal velocities, hence implying a bias towards large-L_{z} orbits (because of the tensor virial theorem, see e.g., Binney & Tremaine, 2008, §4.8.3). Conversely, generating very prolate galaxies would require a suppression of large-L_{z} orbits, which eventually breaks the DF positive-definiteness.

2.2.4 Three-integral DFs

2.2.4.a Classical integrals

General finite analytical expressions of a third isolating integral of motion (see Section 2.1.4) for axisymmetric potentials do not exist, however there are some specific and useful cases in which it is possible to work them out. For instance, Lynden-Bell (1962c) uses the separability of the Hamilton-Jacobi equation in several coordinate frames for a limited set of potentials and he is able to derive analytical formulae for three isolating integrals. Later, several attempts have been made at modeling galaxies employing Lynden-Bell's potentials with remarkable success (e.g., for massive round ellipticals, see Stiavelli & Bertin, 1985; Bertin, Saglia, & Stiavelli, 1988). The most general result about separability is that of Stäckel (1890), who showed that the most general coordinate frame which separates the Hamilton-Jacobi equation is the confocal ellipsoidal coordinates. Hence, if a potential is separable in confocal ellipsoidal coordinates, it is said to be of the Stäckel form. In his seminal paper, de Zeeuw (1985) studied in detail galaxy potentials of the Stäckel form and constructed both axisymmetric and triaxial three-integral models. The Stäckel separability can be used both to generate self-consistent axisymmetric and triaxial three-integral models by specifying the DF (e.g., Dejonghe & de Zeeuw, 1988; Evans, de Zeeuw, & Lynden-Bell, 1990) and by generalizing Eddington's formula (2.16) to $f = f(H, L_{\mathrm{z}}, I_3)$ models (see Dejonghe & Laurent, 1991). Also numerical approximations of the DF constrained by observables, such as those obtained via *quadratic programming* (see Dejonghe, 1989), have had some success in modeling elliptical galaxies (e.g., Emsellem, Dejonghe, & Bacon, 1999).

2.2.4.b Action integrals

If the system is integrable, three action integrals exist (see Section 1.5). They are special isolating integrals of motion and so it is tempting to generate dynamical models whose distribution function depends on action integrals. Historically, though, actions have always been cumbersome to compute for generic axisymmetric potentials, but several recent works have drastically changed the situation giving modellers many reliable methods to accurately estimate actions in axisymmetric and triaxial potentials (see Section 4.1).

The two main advantages of using actions as arguments for the DF, i.e., $f = f(\mathbf{J})$ where $\mathbf{J} = (J_{\mathrm{r}}, J_{\phi}, J_{\mathrm{z}})$, are the following:

(i) actions are adiabatic invariants. This implies that they are independent on slow changes of the potential and, therefore, that a given orbit will be weighted with the same probability by $f(\mathbf{J})$ even if the potential slowly changes.
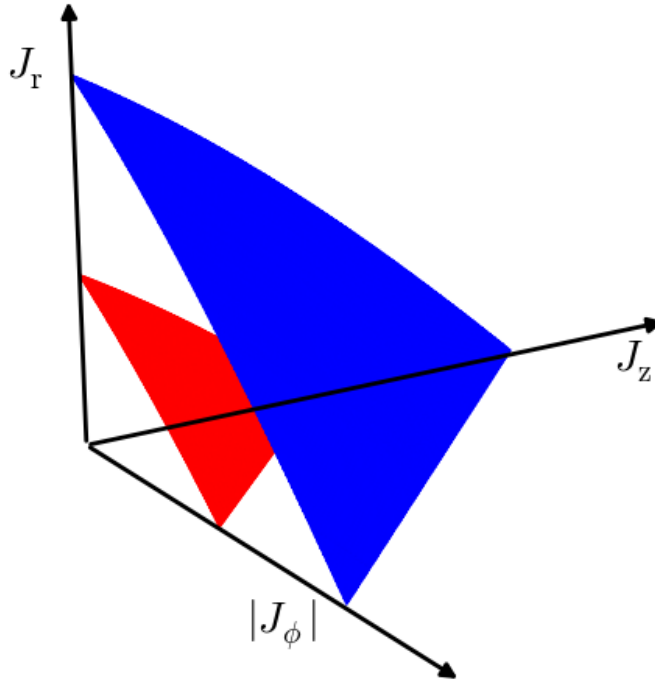
Figure 2.3: Two surfaces of constant energy in action space $(J_{\rm r}, |J_\phi|, J_{\rm z})$ for an isochrone potential. The three axes are in units of $\sqrt{GMb}$, where M is the mass and b is the scale radius of the isochrone. The bigger surface (blue) is at higher energy $(E = -GM/10b)$ and farther from the centre, the smaller (red) is at lower energy $(E = -GM/5b)$ and closer to the centre.

(ii) the mass of the system can be computed at the outset. The volume occupied by a subset of phase space $\Omega \subseteq \Gamma$ is $\int_\Omega {\rm d}^3\mathbf{x}{\rm d}^3\mathbf{v} = (2\pi)^3 \int_\Omega {\rm d}^3\mathbf{J}$, hence the total mass of the system with DF $f(\mathbf{J})$ is $M = (2\pi)^3 \int {\rm d}^3\mathbf{J}\, f(\mathbf{J})$ where, for axisymmetric systems, $J_{\rm r}, J_{\rm z} \in [0, +\infty[$ and $J_\phi \in\,]-\infty, +\infty[$.

The second property, for instance, makes it convenient to use action-based DFs to generate multi-component models, since the mass of each component is immediately computed even without knowledge of the total potential of the system[13].

A general procedure to build DFs which depend on action integral is that proposed by Binney (1987, see also Binney & Tremaine 2008 §4.6). Given $f = f(\mathbf{J})$, the mass of stars with energy between E and $E + {\rm d}E$ is

$$ {\rm d}m(E) = (2\pi)^3 {\rm d}E \int_\Theta \frac{{\rm d}J_\phi {\rm d}J_{\rm z}}{\Omega_{\rm r}}\, f(\mathbf{J}), \qquad (2.22) $$

where $\Theta = \{(J_{\rm r}, J_\phi, J_{\rm z}) \in [0, +\infty[\times[-\infty, +\infty[\times[0, +\infty[: H(\mathbf{J}) = E\}$ and $\Omega_{\rm r} = \partial H/\partial J_{\rm r}$.

---

[13] When energy and angular momentum are used, this can not be accomplished since the integration volume of the mass integral depends on the potential.

If there exist a function $s = s(\mathbf{J})$ so that

$$f(\mathbf{J}) = s(\mathbf{J})F(E), \tag{2.23}$$

where $F(E)$ is an ergodic DF and $s(\mathbf{J})$ is a *shift function* which redistributes the probability of orbits on the same surface of constant energy in action-space, then the mass of stars $dm(E)$ given by (2.22) would be the same as that of $F(E)$ (see Binney & Tremaine, 2008, §4.3.1) if

$$\int_{\Theta} \frac{dJ_{\phi}dJ_{\mathrm{z}}}{\Omega_{\mathrm{r}}} = \int_{\Theta} \frac{dJ_{\phi}dJ_{\mathrm{z}}}{\Omega_{\mathrm{r}}} \, s(\mathbf{J}). \tag{2.24}$$

Equation (2.24) formally states that the redistribution of orbits happens on surfaces of constant energy.

Figure 2.3 shows two surfaces of constant energy in action space for an isochrone sphere (Hénon, 1959), for which the energy is an analytic function of the actions (see Gerhard & Saha, 1991). In the spherical limit, $L = J_{\mathrm{z}} + |J_{\phi}|$ and the surfaces are almost triangular. The shift function $s(\mathbf{J})$ redistributes the probability of the orbits on those surfaces leaving, therefore, unchanged the density profile. Binney (2014), for instance, used a linear action-rescaling to act as a shift function on equal-energy surfaces and, starting from the ergodic $F(E)$ for the isochrone (Hénon, 1960), he is able to generate self-consistent flattened, anisotropic rotating models.

2.3   Continuous models: Jeans equations

Observations of galaxies can only give constraints on the projected luminosity density and on the line-of-sight velocity distribution at some location on the plane of the sky. Thus, comparisons of theoretical models with observations of real galaxies typically involve only the velocity moments of the DF. Given a DF, it is straightforward to compute the velocity moments via integration on the velocity space (see Section 2.2.1), while given observed moments such as $\rho(\mathbf{x})$ and $\overline{\mathbf{v}}(\mathbf{x})$ it is not easy to compute a positive-definite DF which is a stationary solution of the CBE (see Sections 2.2.2- 2.2.3). Even if a DF can be found by an inversion similar to Eddington's (2.16), the solution is typically not unique and it is often problematic to show its positive-definiteness (see Dejonghe, 1986, for a review).

Jeans (1919) was the first to apply to stellar dynamics the equations that James Clerk Maxwell had derived in the context of fluid dynamics. For that reason I shall call the following the *Jeans equations* or equations of stellar hydrodynamics. To derive them, one has to take the velocity-moments of the CBE (2.6). The zeroth moment is obtained by integrating equation (2.6) over the velocity space[14], which yields

$$\frac{\partial \rho}{\partial t} + \sum_{i} \frac{\partial (\rho \overline{v}_i)}{\partial x_i} = 0. \tag{2.25}$$

---

[14] $\dfrac{\partial}{\partial t} \displaystyle\int d^3\mathbf{v} \, f + \sum_{i} \left(\displaystyle\int d^3\mathbf{v} \, v_i \frac{\partial f}{\partial x_i} - \frac{\partial \Phi}{\partial x_i} \displaystyle\int d^3\mathbf{v} \frac{\partial f}{\partial v_i} \right) = 0$ where the partial time-derivative can safely be taken outside the integration as well as the potential since it is independent of v_i. The last term vanishes because of the divergence theorem and the fact that $f \to 0$ for $|\mathbf{v}| \to +\infty$ (e.g., Binney & Tremaine, 2008, §4.8 and Appendix B).

The first-order velocity-moments of the CBE are instead obtained by multiplying equation (2.6) by v_j and then integrating over the velocity space[15]

$$\frac{\partial(\rho\overline{v}_j)}{\partial t} + \sum_i \frac{\partial\left(\rho\overline{v_i v_j}\right)}{\partial x_i} + \rho\frac{\partial\Phi}{\partial x_j} = 0. \tag{2.26}$$

The above three equations for $j = 1, 2, 3$ can be rearranged by subtracting equation (2.25) multiplied by $\overline{v}_j$ and using $\sigma_{ij}^2 = \overline{v_i v_j} - \overline{v}_i\overline{v}_j$

$$\rho\frac{\partial\overline{v}_j}{\partial t} + \sum_i \left[\rho\overline{v}_i\frac{\partial\overline{v}_j}{\partial x_i} + \frac{\partial\left(\rho\sigma_{ij}^2\right)}{\partial x_i}\right] + \rho\frac{\partial\Phi}{\partial x_j} = 0. \tag{2.27}$$

Equations (2.25)-(2.27) define an incomplete set of equations since four equations do not uniquely determine the nine unknowns $\overline{v}_j$ and σ_{ij}, even assuming that (ρ, Φ) are known. From this it follows that in general the Jeans equations can not be used directly to infer the DF from (ρ, Φ). The *closure* of this system of differential equations can be achieved though, provided that some assumptions are made on the DF itself: e.g., for ergodic $f = f(H)$ (see Binney & Mamon, 1982), for axisymmetric two-integral $f = f(H, L_z)$ (see Magorrian & Binney, 1994; Arnold, 1995) and, more generally, for any Stäckel potential (see van de Ven et al., 2003).

Typically equations (2.25)-(2.27) are used to construct dynamical models as follows: some assumptions must be made on the system's geometry (inclination and symmetries) and on anisotropy (shape and orientation of the velocity ellipsoid and arguments of the DF) in order to get expressions for the line-of-sight first and second velocity-moments as a function of (ρ, Φ); one de-projects the galaxy's surface brightness taken from photometric observations (with the assumed geometry) to infer the three-dimensional luminosity density and then, with a further assumption on the mass-to-light ratio, one is able to recover the mass density and the potential by solving Poisson's equation (2.15). With this procedure one recovers the model's line-of-sight velocity distribution up to, typically, second-order. This provides enough information to fit the model to the observations and if the quality of the fit is not considered sufficiently good, then one can vary the model's inclination or mass-to-light ratio and compute a new model.

The success of such an approach is due to the fact that it is relatively easy to generate a dynamical model given any photometric observation of a galaxy. This is because the method is able to find a solution for any given light profile and potential (see e.g., Emsellem, Monnet, & Bacon, 1994). Though, there is no guarantee that such solution is physical, since in general there is no positive-definite DF which generates the wanted velocity-moments with the given potential-density pair. The check of the positivity of the inferred DF should be always made a posteriori with an independent method (e.g., the Hunter & Qian 1993 inversion). Although fast and relatively easy to compute, the major drawback of this kind of modeling is that when a satisfactory fit is found it is

---

[15] $\frac{\partial}{\partial t}\int \mathrm{d}^3\mathbf{v}\, v_j f + \sum_i \left(\int \mathrm{d}^3\mathbf{v}\, v_i v_j \frac{\partial f}{\partial x_i} - \frac{\partial\Phi}{\partial x_i}\int \mathrm{d}^3\mathbf{v}\, v_j \frac{\partial f}{\partial v_i}\right) = 0.$ Then by applying the divergence theorem the last term can be rearranged as $\partial\Phi/\partial x_i \int \mathrm{d}^3\mathbf{v}\, f\, \partial v_j/\partial v_i = \partial\Phi/\partial x_i\, \delta_{ij}\rho$ (e.g., Binney & Tremaine, 2008, §4.8 and Appendix B).
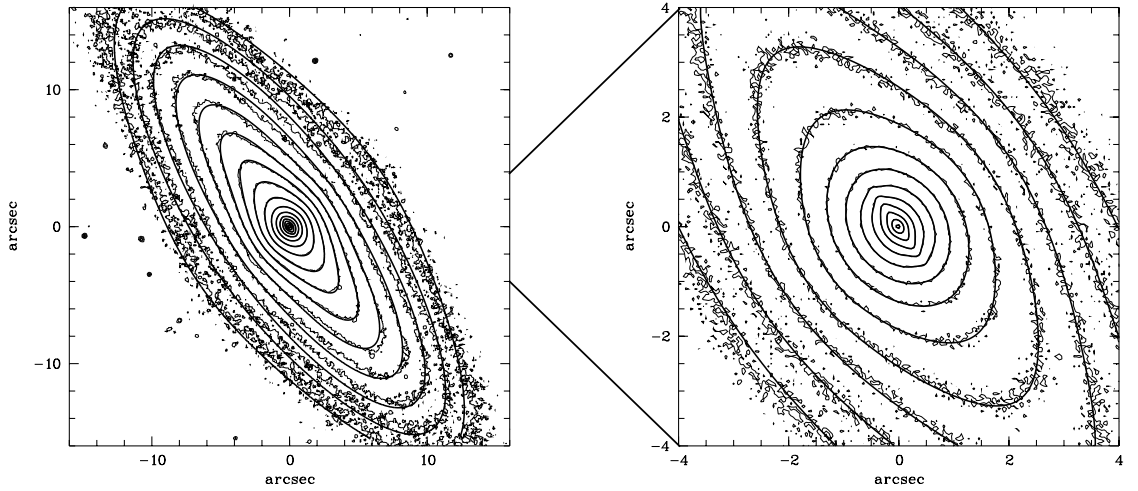
Figure 2.4: *I*-band photometric contours of NGC 4342, taken with Hubble Space Telescope, at two different scales: 32×32 (left panel) and 8×8 (right panel) arcseconds. Superimposed are the (smooth) MGE contours convolved with the proper Point Spread Function. In this case, the position angle is the same for all the Gaussian components, which implies that the galaxy model is axisymmetric. Figure adapted from Cretton & van den Bosch (1999).

not possible to rule out more general models with different geometry or anisotropy, and also in the cases where a reasonably good fit is not achieved it is difficult to say which models with less restrictive assumptions would provide a better representation to the data.

2.3.1 Multi-gaussian expansions and Jeans anisotropic models

One of the most successful application of the Jeans equations in generating dynamical models is that of the *Multi-Gaussian Expansion* (MGE) method of Emsellem, Monnet, & Bacon (1994, see also Cappellari 2002). The basic idea, which is however due to Bendinelli (1991), is expanding the observed projected surface brightness of a galaxy in a series of two-dimensional Gaussians. This set of (non-orthogonal) basis functions is of particular interest in astronomy since de-projections and especially convolutions with the Point Spread Function are computed analytically. The galaxy surface brightness Σ is expanded as

$$\Sigma(x, y) = \sum_{k=1}^{n} \frac{L_k}{2\pi\sigma_k^2 q_k} \exp\left[-\frac{x_k^2 + y_k^2/q_k^2}{2\sigma_k^2}\right], \tag{2.28}$$

where (x, y) is the position on the sky, L_k, σ_k and q_k are the total luminosity, standard deviation and observed flattening of the k-th Gaussian. Assuming that the Point Spread Function can be written as a sum of circular Gaussians $\Pi(R) \propto \sum_j \exp(-2R^2/\sigma_j)$, the convolution $\Sigma_c \equiv \Sigma * \Pi$ is written in an analogous way to (2.28) (see e.g., Emsellem, Monnet, & Bacon, 1994).

For each k-th Gaussian component of the MGE, the three-dimensional luminosity density $\nu(\mathbf{x})$ can be analytically derived by assuming that $\nu(\mathbf{x})$ is stratified on triaxial

ellipsoids and the total potential is computed using Poisson's equation with a constant mass-to-light ratio Υ (see e.g., Monnet, Bacon, & Emsellem, 1992; Emsellem, Monnet, & Bacon, 1994; Cappellari, 2002).

With a sufficiently large number of Gaussians it is possible to achieve fits of any desired accuracy to the surface brightness of different kinds of galaxies, from round ellipticals, to flat lenticulars to triaxial ellipticals with isophotal twist (e.g., Cappellari, 2002). Figure 2.4 shows, as an example, a comparison between the *I*-band photometry of the S0 galaxy NGC 4342 with a MGE with up to eleven Gaussians from Cretton & van den Bosch (1999). In their MGE, they assumed that the position angle of every Gaussian component is the same, leading, therefore, to an axisymmetric model with a two-integral DF. With this choice the density and the potential will be axisymmetric, the radial and vertical dispersion would be equal $\sigma_{\rm R} = \sigma_{\rm z}$ and the velocity ellipsoids will be aligned with the cylindrical coordinates, i.e., $\overline{v_{\rm R} v_{\rm z}} = 0$. The equations (2.27) reduce to a system of two differential equations with two unknowns[16]. The only variable left undetermined is how $\overline{v_\phi^2}$ divides in streaming motion $\overline{v_\phi}^2$ and azimuthal pressure σ_ϕ^2. The most popular approach is to decompose the two contribution with an additional parameter as was introduced by Satoh (1980): by comparing to the isotropic rotator case, in which $\sigma_{\rm R} = \sigma_{\rm z} = \sigma_\phi$, he introduced the parameter $0 \leq k \leq 1$ as

$$\overline{v_\phi}^2 = k^2 \left(\overline{v_\phi^2} - \overline{v_{\rm R}^2} \right), \tag{2.30}$$

where $\sigma_{\rm R}^2 = \overline{v_{\rm R}^2} = \sigma_{\rm z}^2 = \overline{v_{\rm z}^2}$. For $k = 1$, the model reduces to the isotropic rotator since equation (2.30) implies $\overline{v_\phi}^2 - \overline{v_\phi^2} = \sigma_\phi^2 = \sigma_{\rm R}^2$; if $k = 0$, the model has no streaming motions, but only azimuthal anisotropy.

Motivated by observational indications that the velocity ellipsoids of the majority of the (fast-rotating) ellipticals are flattened in the meridional plane and mostly aligned as the spheroidal coordinates (see Figure 2.5 and Cappellari et al., 2007), Cappellari (2008) generalized the axisymmetric MGE formalism to generate dynamical models with constant anisotropy in the meridional plane[17]. The assumptions of alignment of the principal axes of the velocity ellipsoids with the *R*- and *z*-axes and that $\overline{v_{\rm R}^2} = b\overline{v_{\rm z}^2}$, where $b > 0$ is a constant, allow to generate models with more radial pressure than vertical along the model's major and minor axes. Together with an MGE model for the photometry and an assumption on the total mass of the system (e.g., a constant mass-to-light ratio), the so-called *Jeans Anisotropic Multi-gaussian expansion* (JAM)

---

[16]

$$\frac{\partial(\rho\sigma_{\rm R}^2)}{\partial R} + \rho \left(\frac{\sigma_{\rm R}^2 - \overline{v_\phi^2}}{R} + \frac{\partial\Phi}{\partial R} \right) = 0,$$
$$\frac{\partial(\rho\sigma_{\rm z}^2)}{\partial z} + \rho \frac{\partial\Phi}{\partial z} = 0, \tag{2.29}$$

where $\sigma_{\rm R}(= \sigma_{\rm z})$ and $\overline{v_\phi^2}$ are the two unknowns.

[17] If there exists a DF consistent with such a Jeans models, it must depend on three isolating integrals since $\sigma_{\rm z} \neq \sigma_{\rm R}$.
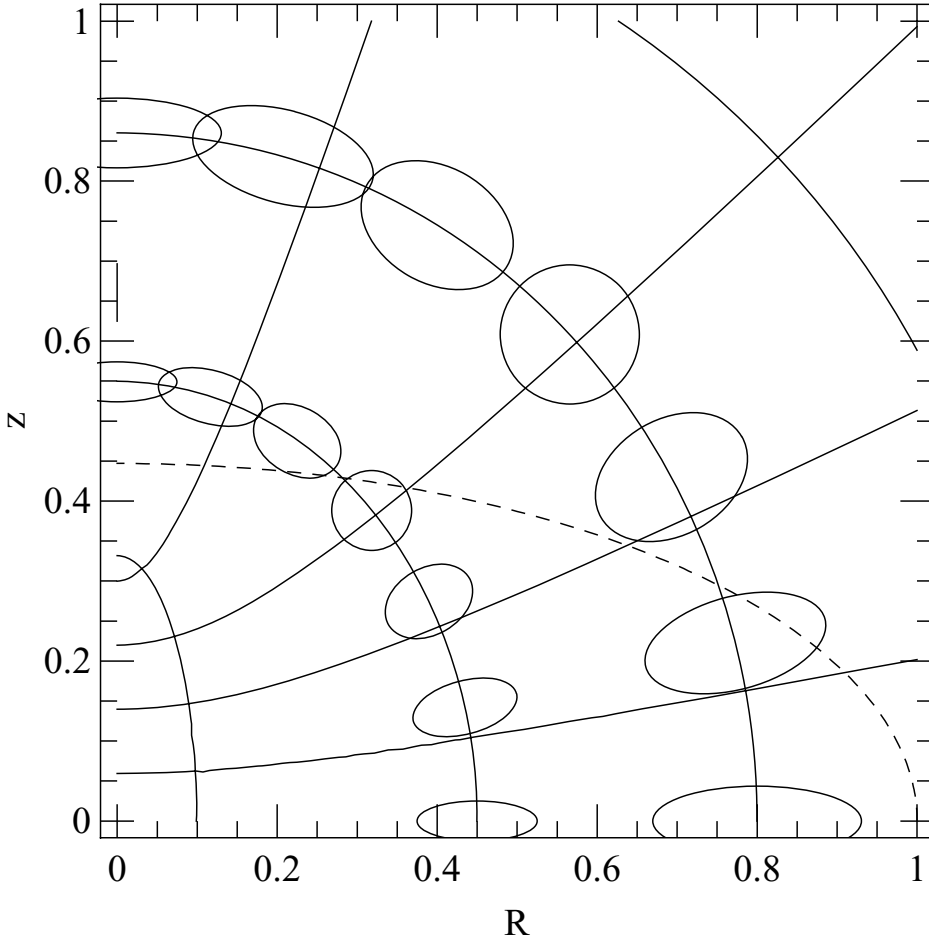
Figure 2.5: Schematic representation of the obervations of Cappellari et al. (2007). The velocity ellipsoids of the majority of (fast-rotating) early-type galaxies i) tend to be aligned with the ellipsoidal coordinates and ii) tend to be flattened in the vertical direction both along the model's major and minor axis. Figure adapted from Cappellari (2008).

models can be used to constrain the galaxy's inclination and vertical anisotropy

$$\beta_z \equiv 1 - \frac{\sigma_z^2}{\sigma_R^2}, \tag{2.31}$$

by comparing the observed line-of-sight second velocity-moment with the quantity

$$v_{\mathrm{RMS}} \equiv \sqrt{v_\parallel^2 + \sigma_\parallel^2}, \tag{2.32}$$

where $v_\parallel$ and $\sigma_\parallel$ are respectively the line-of-sight mean velocity and velocity dispersion. Once the line-of-sight second velocity-moment is fitted to the data, the Satoh (1980) decomposition allows to determine the amount of streaming motion w.r.t. the azimuthal pressure.

2.4   Discrete models

So far I have considered continuous dynamical models. In this Section I will briefly describe an alternative approach that treats the DF as a superposition of discrete components. The two major branches of this approach are i) the models in which the DF is recovered as a superposition of discrete DFs for individual orbits, i.e., orbit-based methods, and ii) those in which particles are assigned to trace the probability distribution of stars.

Briefly, both methods have the advantage w.r.t. continuous models that they are more flexible in constructing equilibrium configurations also for non-axisymmetric and triaxial potentials. Moreover, unike Jeans models, the final outcome will always be physical in the sense that the underlying (unknown) DF is assured to be nowhere negative. The major drawback of discrete models is that the number of free parameters which must be constrained is of the order of the number of orbits/particles, i.e., typically $10^5 - 10^6$. Other than the observables, some further constraints are usually added in order to reduce such enormous freedom, but for typical applications the number of free parameters actually fitted by the routines is no less than a few hundreds. Since marginalizations over so many dimensions is unfeasible, it is extremely difficult to study the possible degeneracies on such parameters.

Both of these two methods typically involve computation of many orbits, which can be efficiently done numerically. However, the computational cost of such approaches normally exceeds that of DF or Jeans models by orders of magnitude.

2.4.1   Orbit-based models

Finding a DF consistent with a given set of observables such as luminosity density and velocity-moments is often a prohibitive task. The inversion of a (multi-dimensional) integral equation is involved and the range of known analytical solution is limited. Numerical schemes have helped in expanding such range: for instance, Kuijken (1995) linearizes the inversion problem by discretizing (ρ, Φ) on a grid and then computing f on that grid (though, smoothing is typically needed because of the noisy nature of the discretization, but see also Merritt, 1993, 1996).

An alternative approach is characterizing the DF as a finite set of orbits which are to be populated with as many stars as required to give a successful representation of the observations. This approach was introduced by Schwarzschild (1979) and has pioneered the field of *orbit-based* models, which was born with his work. Essentially the idea is to seek a numerical configuration of equilibrium, given a potential-density pair, which is consistent with the observed kinematics. Such configuration is constructed by adding a certain number of discrete orbits, accurately integrated numerically in the given potential, and then fitting the line-of-sight kinematics by adjusting the number of stars on each orbit. The advantage of this approach w.r.t. DF modeling is that it makes no assumptions on how many integrals of motion exist, which, instead, can be verified a posteriori once the model has been computed.

Schwarzschild (1979) seminal paper can be summarized in the following five steps.

(i) A target luminosity density must be assumed. It can be, for instance, derived from the galaxy's photometry using the MGE formalism (see Section 2.3.1).

(ii) Assume a given potential Φ. For instance, it can be computed with Poisson's equation (2.15) assuming that mass-follows-light.

(iii) Different intial conditions are spanned and large library of orbits are computed. Each orbit in the library is integrated for many oscillations in the potential (at least a hundred) and the time each orbit spends in a given grid-cell of the discretized configuration space is stored. The time spent on each grid-cell can be interpreted as the density distribution produced by each orbit when averaged over a long time.

(iv) At this stage the orbits in the library can be characterized in terms of third-integral: orbits that do not pass in each grid-cell available to its motion are quasi-periodic and, therefore, admit three isolating integrals of motion.

(v) Seek how many stars are needed on each orbits so that the target luminosity density distribution and kinematics are reproduced. The non-negative number of stars on each orbits are actually parameters that *weight* the probability of the given orbit in the system

If no acceptable solution is found, then one must proceed first, by increasing the orbit library and seeking a new solution with the larger library and second, by rejecting the assumed potential and start again with a new Φ. This can be effectively used to give constraints on the total potential of the observed stellar system and hence to infer the mass distribution of dark components such as a dark halo (see e.g., Rix et al., 1997) or a central black hole (see e.g., van der Marel et al., 1998). Of course, if the potential was chosen to be the self-consistent one, i.e., with no other external components, in the case where no acceptable solution is found one concludes that no equilibrium configuration exists for the given density distribution.

For orbit-based models one can interpret the orbital weights, which are fitted to the data, as the coefficients for an effective discrete DF

$$f_{\text{Schw}}(\mathbf{I}) = \sum_{\zeta} w_{\zeta}(\mathbf{I}_{\zeta})\delta(\mathbf{I} - \mathbf{I}_{\zeta}), \qquad (2.33)$$

where $\mathbf{I} = (I_1, I_2, I_3)$ is a triple of generic integrals of motion, ζ is an orbit in the library whose best fitting weight is w_{ζ}, $\mathbf{I}_{\zeta}$ is the value of the integrals of motions on that orbit and δ is the Dirac-δ distribution. Having a discrete representation of the DF, it is interesting to compare models with known DF and equation (2.33) of an orbit-based one which produce roughly the same observables (see e.g., Thomas et al., 2004). Figure 2.6 shows the comparison of an axisymmetric two-integral Abel model[18] of Dejonghe & Laurent (1991) with a Schwarzschild's model tailored to reproduce the same observables.

---

[18] In general, *Abel models* are those in which the mass density and the DF are related by an Abel (1826) inversion. The most general case in which such an inversion can be computed is for systems with triaxial Stäckel (1890) potentials (see Dejonghe & Laurent, 1991).
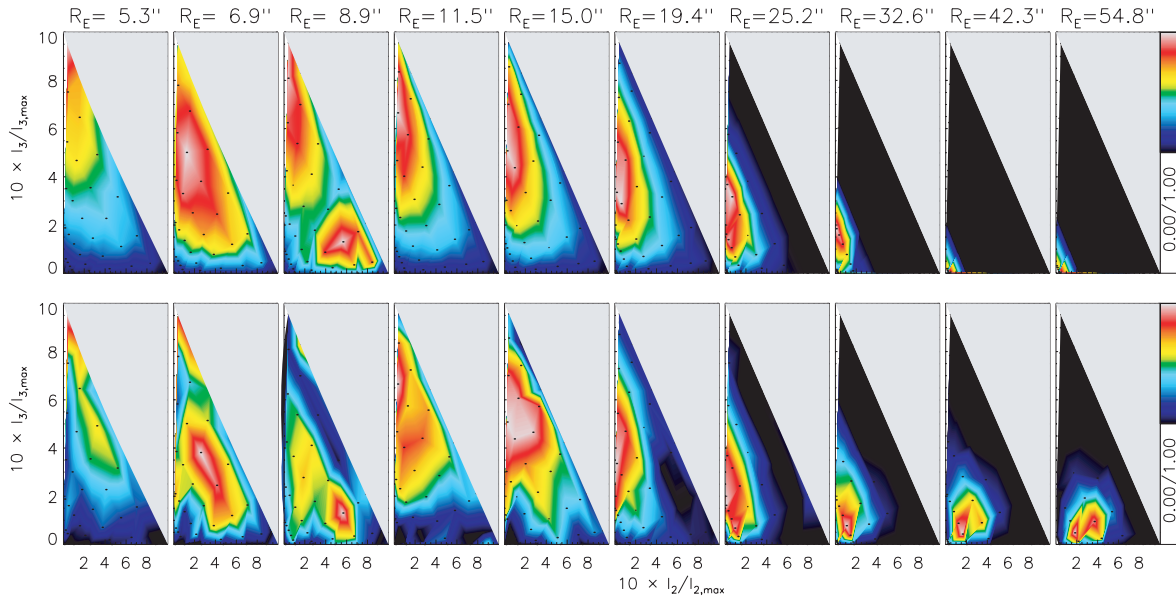
Figure 2.6: Orbital weights distribution for an oblate axisymmetric Abel model (top row, see Dejonghe & Laurent, 1991) and for an orbit-based Schwarzschild's model (bottom row) in the (I_2, I_3) plane, where $I_2 = L_z^2/2$, which produce a very similar set of observables such as line-of-sight velocity and velocity dispersion. The panels show sections of the three-dimensional space of the integrals of motion (H, L_z, I_3) at constant energy H, which increases from left to right as well as the average distance of the orbit from the system's centre (expressed by the radius of the thin short-axis tube orbit R_E in arcseconds, see van de Ven, de Zeeuw, & van den Bosch, 2008, for details). Colour-coded is the orbital weight of the Schwarzschild's model for each orbit (colour-bar is on the right), while the grey areas are those prohibited to the motion for that energy. Figure adapted from van de Ven, de Zeeuw, & van den Bosch (2008).

In the panels are shown some comparisons of sections of the integral space at constant energy. Equation (2.33) gives a reasonable approximation to the analytic DF.

Modern versions of the Schwarzschild (1979) method have been extensively used by different authors to model the dynamics of different objects (see e.g., Cretton & van den Bosch, 1999; Cappellari et al., 2006; van den Bosch et al., 2008).

2.4.2 Particle-based models

An alternative approach conceptually very similar to that of orbit-based models is seeking a representation of the DF not by assigning weights to orbits in phase space, but populating orbits with particles and so effectively constructing an N-body model. This approach was pioneered by Syer & Tremaine (1996): given a potential Φ, any observable Y of the stellar system is given by an integration over the phase space

$$Y = \int_\Gamma \mathrm{d}\boldsymbol{\gamma}\, K(\boldsymbol{\gamma}) f(\boldsymbol{\gamma}), \tag{2.34}$$

where $\boldsymbol{\gamma} = (\mathbf{x}, \mathbf{v})$ is a phase-space element, $K = K(\boldsymbol{\gamma})$ is a known kernel and f is the DF. For a system of N particles moving in a given potential, the observable would be

$$y(t) = \sum_{i=0}^{N} w_i \, K[\boldsymbol{\gamma}_i(t)], \tag{2.35}$$

where w_i are some positive weights assigned to each particle and the time dependence reflect the fact that the particles are moving in the potential. The goal of the method is to determine a set of weights w_i so that the time average of the model observable $\langle y(t) \rangle$ is equal to the target Y. The more the observables Y, the more the constraints one uses to seek the particle weights.

The core of the algorithm is that as time runs and the orbital integration proceeds, the value of $y(t)$ changes as well as that of $\langle y(t) \rangle$, in general. The model is often called *Made-to-Measure* (M2M) because Syer & Tremaine (1996) developed a method to evolve the weights w_i so that the time-averaged observable $\langle y(t) \rangle$ gets closer to the target Y. The equation that at each time-step computes $\mathrm{d}w_i/\mathrm{d}t$ is called *force-of-change* (FOC) equation, which generally takes the form (see Syer & Tremaine, 1996)

$$\frac{\mathrm{d}w_i}{\mathrm{d}t} = -\epsilon w_i G(w_i), \tag{2.36}$$

where $\epsilon > 0$ is a small constant and $G(w_i)$ is a function that depends on the flavour of the M2M method (see e.g., de Lorenzi et al., 2007; Dehnen, 2009; Long & Mao, 2010). Typically, $G(w_i) \propto [y(t) - Y]/Y$ so that the rate of change of w_i is proportional to the distance between the target observable and that of the model at the time t. For instance, if the target observable is the mass density at location $\mathbf{x}$, then the kernel in equation (2.34) is $K(\mathbf{x}, \mathbf{v}) = \delta(\mathbf{x})$ and the weight of each particle would be interpreted as their masses. In this case, the FOC equation governs the variation in time of the mass of each particle.

The system of differential equations (2.36) is, however, typically ill-conditioned since the number of particles exceeds that of observables. If one does not impose additional constraints on the weights, the FOC equation will make the model observable to converge towards the targets, but w_i will continue to vary even after the convergence is reached. To remove the ill-conditioning one maximizes over a given *profit function*, which typically takes the form of an entropy

$$S = \sum_i w_i \log \frac{w_i}{m_i}, \tag{2.37}$$

where m_i are some given priors on the weights w_i. The higher the number of observables Y, the higher the number of constraints on $G(w_i)$ and hence on the weights. The orbits of the particles are integrated for a long timescale, much longer than that on which they typically converge i.e., ϵ^{-1}.

Such data-constrained N-body model must be specified at the outset with some prescription for the initial conditions. Typically such initial conditions are chosen so to have a density profile similar to what is expected for the final equilibrium, while it is rather arbitrary how to set the initial particle velocities. Fortunately Syer & Tremaine

([1996](#)) argue that the final equilibrium should not be affected by the specific choice of the initial conditions (modulo that the priors are resonable, e.g., uniform for all particles).

Some of the evident advantages of M2M models w.r.t. orbit-based ones are that, given the same level of accuracy in representing the observations, i) the particle-based method has the nice outcome of having a full N-body realization of the model, which can in principle be used for purposes other than fitting the data and ii) one can use the final stage of an N-body simulation as initial conditions, for the M2M algorithm, so that one effectively *steers* an N-body model to a better representation of a given set of observables (see e.g., Bissantz, Debattista, & Gerhard, 2004).

2.5 Time evolution: N-body simulations

The study of equilibrium models is of vital importance in order to understand the dynamics of stellar systems in the Universe and, in particular, to understand how mass is distributed in them. However, equilibrium configurations are by definition steady-states and therefore give us no insight on the galaxy evolution, i.e., on its deviations from equilibrium and on how such state was reached in the first place. The evolution of a galaxy is primarily determined by its surroundings: interactions with neighbouring bound structures and continuous accretion of matter determine the mass accretion history of galaxies in a statistical sense (see e.g., van den Bosch, 2002), while the detailed evolution of the galaxy's stellar component can be strongly influenced by the environment in a non-trivial manner (see e.g., Peng et al., 2010). While studying the dynamical evolution of a single model galaxy can be hard (probably the only physically meaningful way is by applying perturbation theory on some given equilibrium; see e.g., Kaasalainen, 1994), the dynamical evolution of the statistical properties of a galaxy population can be studied in detail by means of sophisticated numerical algorithms. Since both stars and dark matter behave as a collisionless fluid, their evolution from some specified initial conditions and under their own gravity is a problem well suited to be addressed with N-body numerical simulations.

N-body algorithm have revolutionized our understanding of how galaxies form and evolve over the last $3 - 4$ decades. They are normally implemented in sophisticated computer codes that run on massively-parallel supercomputers. These codes take as input an initial configuration of a large number of particles and follow the particle motion under their mutual gravitational attraction. For relevant applications in the study of galaxies the maximum number of particles that a current supercomputer can efficiently represent (about $\sim 10^{10} - 10^{11}$) is typically much smaller than the number of stars involved in the galaxy's formation and evolution process. Therefore, one simulates the evolution of a very large number of stars with a much smaller number of massive particles. The idea of an N-body model of a galaxy is that of following the motion of some (possibly large) number of test particles in the field of a smooth mass density $\rho(\mathbf{x}, t)$. In this sense, the N particles that are used to represent such a continuous density field act simply as Monte-Carlo samples of the underlying DF. Hence, the individual positions and velocities of a particle have no particular physical interst, while the whole statistical distribution of their positions and velocities does.

This is possible since galaxies and larger systems in the Universe are collisionless, because their two-body relaxation time is much longer than their age (equation 2.1). Galaxies, with a typical crossing times of tens or hundreds of Myrs, have relaxation times that are $(\sim 6 - 7)$ orders of magnitude larger than the age of the Universe. Hence, it makes sense to study the evolution of galaxies with models that follow the motion of test particles that move on trajectories given by the smooth potential of their own mutual gravity. Such collisionless N-body codes simulate the evolution of galaxies for times much shorter than relaxation time of either the real galaxy or the simulated N-body system. These simulations can be used only to study phenomena on scales shorter than the two-body relaxation time, e.g., on the violent relaxation (Lynden-Bell, 1967; van Albada, 1982) or the merging (White, 1978) timescale.

At each timestep, the gravitational potential of the system is computed from the particles configuration at that timestep using a Poisson solver (e.g., a Barnes & Hut 1986 oct-tree or a particle-mesh Hockney & Eastwood 1981), then the gravitational forces acting on each particle are computed and are used to update the positions and momenta of each particle up to the next timestep.

The time-dependent potential $\Phi(\mathbf{x}, t)$ of the smooth density distribution $\rho(\mathbf{x}, t)$ is related to the underlying phase-space density distribution of the system $f(\boldsymbol{\gamma}, t)$ by

$$\Phi(\mathbf{x}, t) = -GM \int \mathrm{d}\boldsymbol{\gamma}' \frac{f(\boldsymbol{\gamma}', t)}{|\mathbf{x} - \mathbf{x}'|}, \tag{2.38}$$

where $\boldsymbol{\gamma}' = (\mathbf{x}', \mathbf{v}')$ and M the system's total mass. Given N test particles randomly extracted from the DF with phase-space coordinates $\boldsymbol{\gamma}_i$ at the beginning of the timestep $t = 0$, one can define a sampling probability as $f_{\mathrm{s}} \equiv f(\boldsymbol{\gamma}_i, 0)$ and therefore write (see Binney & Tremaine, 2008, §4.7.1)

$$\Phi(\mathbf{x}, t) = -\frac{GM}{N} \sum_{i=1}^{N} \frac{f(\boldsymbol{\gamma}_i, t)/f_{\mathrm{s}}}{|\mathbf{x} - \mathbf{x}_i|} = -\frac{GM}{N} \sum_{i=1}^{N} \frac{f(\boldsymbol{\gamma}_i, t)/f(\boldsymbol{\gamma}_i, 0)}{|\mathbf{x} - \mathbf{x}_i|}. \tag{2.39}$$

This is the potential generated by N point masses distributed at locations $\boldsymbol{\gamma}_i$ in phase space and having mass

$$m_i(t) = \frac{M}{N} \frac{f(\boldsymbol{\gamma}_i, t)}{f(\boldsymbol{\gamma}_i, 0)}. \tag{2.40}$$

Actually, since the sampling points are on orbits, the right-hand side is time-independent and therefore the test particles will have the same mass at each timestep. For instance, in M2M models the masses of the test particles are varying with time according to (2.40), where the denominator is a sampling probability f_{s} which is $f_{\mathrm{s}} \neq f$.

An important caveat that must be stressed when interpreting results from collisionless N-body models is that no physical sense is attached to the particles. Since by equation (2.40) one can always choose the sampling probability as $f_{\mathrm{s}} \equiv f(\boldsymbol{\gamma}_i, 0)$ so that the masses are constant with time, one might interpret the N particles as stars or as clusters of stars moving through the system, instead the test particles are simply used to probe the underlying probability density and their motion is conceptually closer to representing the characteristic curves of the CBE (2.6), where the potential is given by (2.39).

Undoubtably the biggest success of N-body mothods are cosmological simulations of structure formation, where the prescription for the initial conditions is given phenomenologically by the observations of the Cosmic Microwave Background (see e.g., Frenk et al., 1988). These simulations brought many new insights on how galaxies and dark haloes form and evolve in the Universe (see e.g., Mo, van den Bosch, & White, 2010, for an extensive review). The main advantage of such simulations is that they trace extermely well the statistical properties of galaxies and haloes as a population, whereas the interpretation of the results when a single system is considered can be tricky since the discreteness noise can cover much of the results. In this sense, N-body simulations such as that in Figure 2.7 can be used as an extremely powerful tool to trace the global properties of galaxies and haloes as a whole population.
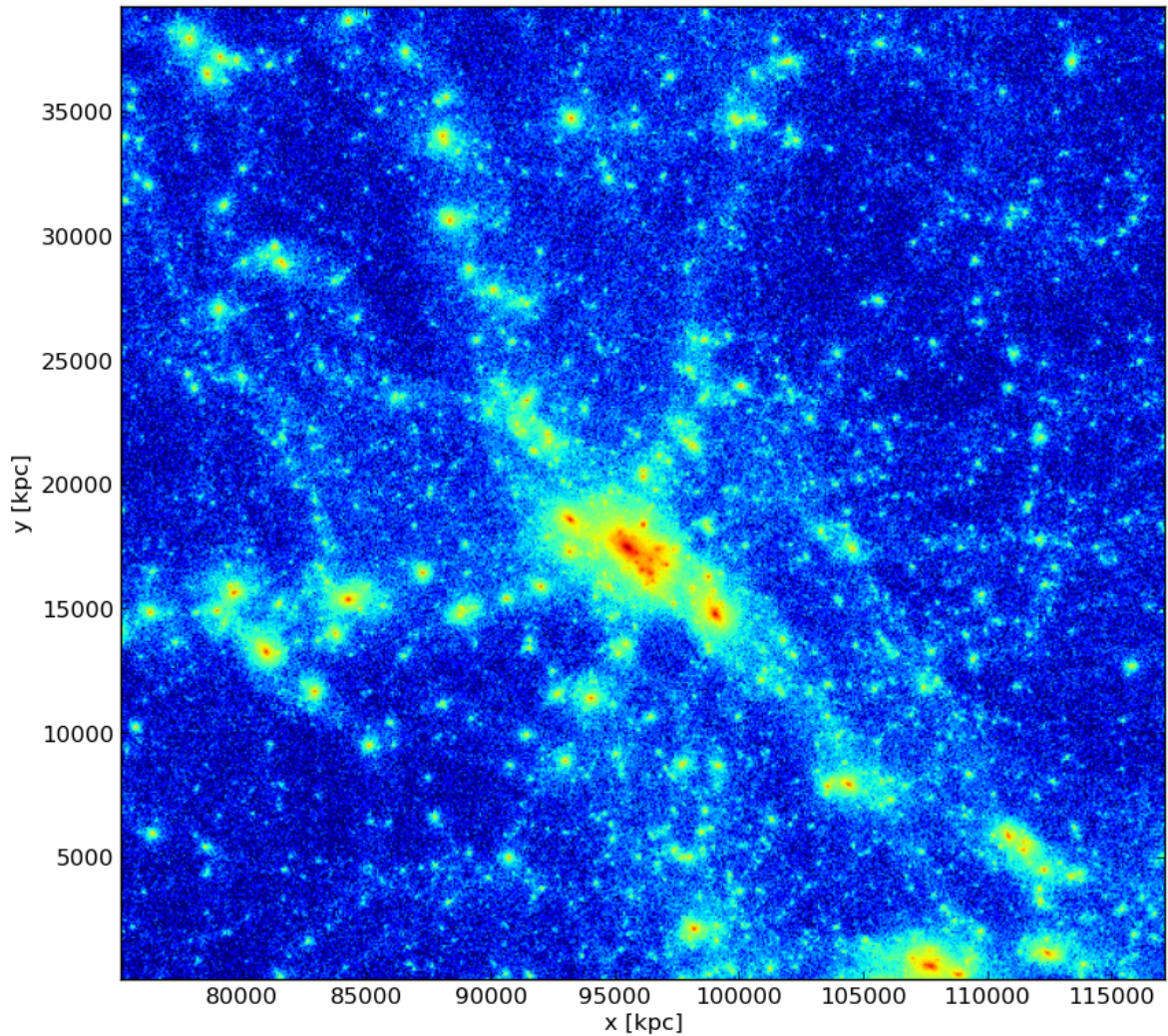
Figure 2.7: Projected dark matter density of a $5 \times 10^{13} M_\odot$ halo in a cosmological, dark-matter only, N-body simulation along an arbitrary line-of-sight. The image has been made by dividing the projected field into regular cells, counting how many particles are in that cell and assigning a density to the cell as the total mass in particles divided by the area of the cell. The density contrast between the highest (dark red) and the smallest density (dark blue) is of about 6 orders of magnitude. The N-body simulation is that used in Chapter 5 to study the evolution of early types and their dark matter haloes.

Chapter **3**

Action-based distribution functions for spheroids: the $f(\mathbf{J})$ models

Abstract

We present an approach to the design of distribution functions that depend on the phase-space coordinates through the action integrals. The approach makes it easy to construct a dynamical model of a given stellar component. We illustrate the approach by deriving distribution functions that self-consistently generate several popular stellar systems, including the Hernquist, Jaffe, and Navarro, Frenk and White models. We focus on non-rotating spherical systems, but extension to flattened and rotating systems is trivial. Our distribution functions are easily added to each other and to previously published distribution functions for discs to create self-consistent multi-component galaxies. The models this approach makes possible should prove valuable both for the interpretation of observational data and for exploring the non-equilibrium dynamics of galaxies via N-body simulations.

3.1   Introduction

Axisymmetric equilibrium models are extremely useful tools for the study of galaxies. A real galaxy will never be in perfect dynamical equilibrium – it might be accreting dwarf satellites, or being tidally disturbed by the gravitational field of the group or cluster to which it belongs, or displaying spiral structure – but an axisymmetric equilibrium model will usually provide a useful basis from which a more realistic model can be constructed by perturbation theory.

By Jeans (1915) theorem (see Section 2.1.2), every equilibrium model can be described by a distribution function (DF) that depends on the phase-space coordinates $(\mathbf{x}, \mathbf{v})$ only through isolating integrals of motion. In an axisymmetric potential, most orbits prove to be quasiperiodic, with the consequence that they admit three isolating integrals (Arnold, 1978). Consequently, a generic DF for an axisymmetric equilibrium galaxy is a function of three variables.

The major obstacle to exploiting this insight is that we have analytic expressions for only two isolating integrals of motion in a general axisymmetric potential, namely the energy $E = \frac{1}{2}v^2 + \Phi(\mathbf{x})$ and the component of the angular momentum about the symmetry axis, $J_\phi = (\mathbf{x} \times \mathbf{v})_z$. Several authors have examined model galaxies with DFs of the two-integral form $f(E, J_\phi)$ (Prendergast & Tomer, 1970; Wilson, 1975; Rowley, 1988; Evans, 1994), but in such models the velocity dispersions σ_R and σ_z in the radial and vertical directions are inevitably equal. This condition is seriously violated in our Galaxy and we have no reason to suppose that the condition is better satisfied in any external galaxy. Hence it is mandatory to extend the DF's argument list to include a "non-classical" integral, I_3, for which we do not have a convenient expression.

Since any function $J(E, J_\phi, I_3)$ of three isolating integrals is itself an isolating integral, we actually have an enormous amount of freedom as to what integrals to use as arguments of the DF. Given that we must use at least one integral for which we lack an expression for its dependence on $(\mathbf{x}, \mathbf{v})$, there is a powerful case for making the DF's arguments action integrals. These integrals are alone capable as serving as the three momenta J_i of a canonical coordinate system – this property makes them the bedrock of perturbation theory. Their canonically conjugate variables, the angles θ_i, have two remarkable properties: (i) along any orbit they increase linearly with time at rates $\Omega_i(\mathbf{J})$, so

$$\theta_i(t) = \theta_i(0) + \Omega_i(\mathbf{J})\, t, \tag{3.1}$$

and (ii) they make the ordinary phase-space coordinates periodic functions

$$\mathbf{x}(\boldsymbol{\theta} + 2\pi\mathbf{m}, \mathbf{J}) = \mathbf{x}(\boldsymbol{\theta}, \mathbf{J}) \quad \text{(integer } m_i). \tag{3.2}$$

The actions J_i also have nice properties. In particular, (i) any triple of finite numbers (J_r, J_ϕ, J_z) with $J_r, J_z \geq 0$ corresponds to a bound orbit with the orbit $\mathbf{J} = 0$ being that on which a star is stationary at the middle of the galaxy, and (ii) the volume of phase space occupied by orbits with actions in $\mathrm{d}^3\mathbf{J}$ is $(2\pi)^3\mathrm{d}^3\mathbf{J}$. Consequently, any non-negative function $f(\mathbf{J})$ that tends to zero as $|\mathbf{J}| \to \infty$ and has a finite integral $\int \mathrm{d}^3\mathbf{J}\, f(\mathbf{J})$ specifies a valid galaxy model of mass

$$M = (2\pi)^3 \int \mathrm{d}^3\mathbf{J}\, f(\mathbf{J}). \tag{3.3}$$

The actions are defined by integrals

$$J_i = \frac{1}{2\pi} \oint_{\gamma_i} \mathrm{d}\mathbf{x} \cdot \mathbf{v}, \tag{3.4}$$

where γ_i is a closed path in phase space. If we require that the first action J_r quantifies the extent of a star's radial excursions and the third action J_z quantifies the extent of its excursions either side of the potential's equatorial plane, then the actions are unambiguously defined. What we here call J_r is sometimes called J_R or J_u, and what we call J_z is sometimes called J_ϑ or J_v, but no significance attaches to these different notations. In a spherical potential $J_z = L - |J_\phi|$, where L is the magnitude of the angular momentum vector.

To obtain the observable properties of a model defined by $f(\mathbf{J})$, for example its density distribution $\rho(\mathbf{x}) = \int \mathrm{d}^3\mathbf{v}\, f(\mathbf{J})$ and its velocity dispersion tensor $\sigma_{ij}^2(\mathbf{x})$, one has to be able to evaluate $\mathbf{J}(\mathbf{x}, \mathbf{v})$ in an arbitrary gravitational potential. Recently a number of techniques have been developed for doing this (Binney, 2012a; Sanders & Binney, 2014, 2015). Consequently, while the last word on action evaluation has likely not yet been written, we now have algorithms that enable one to extract the observables from a DF $f(\mathbf{J})$ with reasonable accuracy.

DFs $f(\mathbf{J})$ that depend on the phase-space coordinates only through the actions were first used to model the disc of our Galaxy in an assumed gravitational potential (Binney, 2010, 2012b). Recently Binney (2014) showed how to derive the self-consistent gravitational potential that is implied by a given $f(\mathbf{J})$ by exploring a family of flattened, rotating models that he derived from the "ergodic" DF of the isochrone model: that is the DF $f(H)$ that depends on the phase-space coordinates only through the Hamiltonian $H = \frac{1}{2}v^2 + \Phi(\mathbf{x})$. Hénon (1960) derived the isochrone's ergodic DF, and in the case of the isochrone potential explicit expressions are available for $\mathbf{J}(\mathbf{x}, \mathbf{v})$ and $H(\mathbf{J})$ (Gerhard & Saha, 1991). Substituting $H(\mathbf{J})$ in $f(H)$ Binney (2014) obtained the DF $f(\mathbf{J})$ of the isotropic isochrone model. In this Chapter we present simple analytic functions $f(\mathbf{J})$ that generate nearly isotropic models of other widely used models, such as the Hernquist (1990), Jaffe (1983), and Navarro, Frenk, & White (1996, hereafter NFW) models.

Once a DF of the form $f(\mathbf{J})$ is available for a spherical, non-rotating model, the procedure Binney (2014) used to flatten the isochrone sphere and to set it rotating can be used to flatten and/or set rotating one's chosen model. So DFs for spherical models in the form $f(\mathbf{J})$ are valuable starting points from which quite general axisymmetric models are readily constructed.

Galaxies are generally considered to consist of a number of components, such as a disc, a bulge, and a dark halo, that cohabit a single gravitational potential. If we represent each component by a DF of the form $f(\mathbf{J})$, it is straightforward to find the gravitational potential in which they are all in equilibrium (e.g., Piffl et al., 2014; Piffl, Penoyre, & Binney, 2015). An analogous composition using DFs of the form $f(E, J_\phi, I_3)$ has never been achieved and may be impossible, because when components are added, their potentials must be added, and the energies of physically similar orbits in a given component are quite different before and after we add in the potential of another component. For example, the orbit on which a star sits at the centre of the galaxy will have different energies before and after addition. If E is used as an argument of the DF, the

change in E will change the density of stars on the given orbit, which is contrary to the fundamental idea of building up the galaxy by adding components. By contrast, the actions of the orbit on which a star sits at the galactic centre vanish in any potential, and if a component is defined by $f(\mathbf{J})$, it contributes the same density of stars to this orbit regardless of the external potential in which that component finds itself. This fact is a major motivation for discovering what DF of the form $f(\mathbf{J})$ is required to generate each component of a galaxy.

The DF of an isotropic spherical model must depend on the actions only via the Hamiltonian $H(\mathbf{J})$. The dependence of f on H is readily obtained from the inversion formula of Eddington (1916), but an exact expression for $H(\mathbf{J})$ is only available for the isochrone potential and its limiting cases, the harmonic oscillator and Kepler potentials. Our ignorance of $H(\mathbf{J})$ for potentials other than the isochrone amounts to a barrier to the extension of the approach of Binney (2014) to model building. One way to break through this barrier is to devise numerical approximations to $H(\mathbf{J})$ and some success has been had in this direction by Fermani (2013) and Williams, Evans, & Bowden (2014). In this Chapter we pursue a slightly different strategy, which is to develop simple algebraic expressions for DFs $f(\mathbf{J})$ that generate self-consistent models that closely resemble popular spherical systems. We also show that a very simple form of $f(\mathbf{J})$ generates a model that is almost identical to the isochrone sphere and we give a useful analytic expression for the radial action as a function of energy and angular momentum for a Hernquist sphere.

This Chapter is organised as follows. In Section 3.2 we use analytic arguments to infer $f(\mathbf{J})$ for scale-free models. These models are not physically realisable as they stand, so in Section 3.3 we consider models that consist of two power-law sections joined at a break radius. In Section 3.4 we extract realisable models from scale-free models by the alternative strategy of adding a core to the system and/or tidally truncating the model. Section 3.5 sums up.

3.2 Power-law models

Consider a gravitational potential that scales as a power of the distance from the galactic centre, i.e. $\Phi(\xi\mathbf{x}) \propto \xi^a \Phi(\mathbf{x})$ with $a \neq 0$: in the limit $a \to 0$ the gravitational potential tends to a logarithmic potential, which is an interesting special case that we will treat in Section 3.2.1.

An orbit in a power-law potential has time-averaged kinetic and potential energies, K and W respectively, that are related by the virial theorem: $2K = aW$. The instantaneous total energy, given by the sum of the instantaneous kinetic and potential energies, is conserved along the orbit and consequently is given by

$$E = K + W = \left(\frac{a}{2} + 1\right) W. \tag{3.5}$$

In any power-law potential we need only to study orbits of one arbitrarily chosen energy E because each of these orbits can be rescaled to a similar orbit at any given energy E'. Indeed, if an orbit is rescaled by a spatial factor, i.e., $\mathbf{x} \to \mathbf{x}' = \xi\mathbf{x}$, then the orbit's

total energy scales as

$$E \to E' = \xi^a E, \tag{3.6}$$

since obviously $W \to W' = \xi^a W$. Further $v^2 \propto K = \frac{1}{2}aW$, so under rescaling $\mathbf{v} \to \mathbf{v}' = \xi^{a/2}\mathbf{v}$.

Given the scalings derived above for $\mathbf{x}$ and $\mathbf{v}$ it follows that

$$\mathbf{J} \to \mathbf{J}' = \xi^{1+a/2}\mathbf{J}. \tag{3.7}$$

Thus both the energy and the actions of an orbit that is rescaled by the spatial factor ξ are rescaled by powers of this factor.

From equations (3.6) and (3.7) we deduce that the Hamiltonian is of the form

$$H(\mathbf{J}) = [h(\mathbf{J})]^{a/(1+a/2)}, \tag{3.8}$$

where $h(\mathbf{J})$ is a homogeneous function of degree one, i.e. $h(\zeta\mathbf{J}) = \zeta h(\mathbf{J})$ for every constant ζ. In particular, H is itself a homogeneous function of the three actions of degree $a/(1 + a/2)$. It is easy to check that equation (3.8) gives the correct scalings $H \propto |\mathbf{J}|$ and $H \propto |\mathbf{J}|^{-2}$ for the harmonic oscillator ($a = 2$) and Kepler ($a = -1$) potentials. Williams, Evans, & Bowden (2014) derive a closely related result in which a specific form is proposed for $h(\mathbf{J})$.

The homogeneous function h is strongly constrained by the orbital frequencies. Indeed

$$\frac{\Omega_i}{\Omega_j} = \frac{\partial H/\partial J_i}{\partial H/\partial J_j} = \frac{\partial h/\partial J_i}{\partial h/\partial J_j}. \tag{3.9}$$

In a scale-free model the frequency ratio on the left is a homogeneous function of degree zero, i.e., scale-independent, in agreement with the right side. A natural choice for h that we will use extensively is

$$h(\mathbf{J}) = J_r + \frac{\Omega_\phi(\mathbf{J})}{\Omega_r(\mathbf{J})}|J_\phi| + \frac{\Omega_z(\mathbf{J})}{\Omega_r(\mathbf{J})}J_z. \tag{3.10}$$

In a scale-free model this is homogeneous of degree one, as required. Moreover so long as the frequency ratios do not change rapidly within a surface of constant energy in action space, the derivatives of h satisfy equation (3.9) to good precision.

In the definition (3.10) of $h(\mathbf{J})$ the modulus of the angular momentum J_ϕ appears because we are concerned with the construction of the part of the DF that is even in J_ϕ. If we wish to set the model rotating, we will add to this even part an odd part as discussed by Binney (2014).

Consider now the density distribution that generates a power-law potential. In the

spherical case [1] we have

$$\frac{\mathrm{d}\Phi(r)}{\mathrm{d}r} = \frac{\partial \Phi(\xi r)}{r \partial \xi}\bigg|_{\xi=1} = \frac{a}{r}\Phi(r). \tag{3.12}$$

Hence

$$4\pi G\rho = \frac{1}{r^2}\frac{\mathrm{d}}{\mathrm{d}r}\left(r^2\frac{\mathrm{d}\Phi}{\mathrm{d}r}\right) = \frac{1}{r^2}\frac{\mathrm{d}}{\mathrm{d}r}\left(ar\Phi\right) = \frac{a+a^2}{r^2}\Phi. \tag{3.13}$$

If $a = -1$ we recover the expected result $\rho = 0$, but for $a \neq 0$ we obtain the polytropic relation for index $n = 1 - 2/a$ (e.g Binney & Tremaine, 2008, §4.3.3a):

$$\rho \propto |\Phi|^{1-2/a}. \tag{3.14}$$

From this relation it is easy to derive the ergodic DF

$$f(E) \propto E^{-(4+a)/2a} \tag{3.15}$$

from Eddington's formula (e.g. Evans, 1994). From equations (3.8) and (3.15) it follows that the distribution function of a power-law model is

$$f(\mathbf{J}) = [h(\mathbf{J})]^{-(4+a)/(2+a)}. \tag{3.16}$$

The DF of a power-law model is itself a power-law of the three actions and the exponent is completely determined by that of $\Phi(\mathbf{x})$.

3.2.1   Logarithmic potentials

Now consider the limit $a \to 0$ when the scaling of Φ becomes additive

$$\Phi(\xi\mathbf{x}) = \Phi(\mathbf{x}) + v_{\mathrm{c}}^2 \log(\xi), \tag{3.17}$$

where v_{c} is a constant that one can easily show is the circular speed. Since galaxies have quite flat circular-speed curves, potentials of this form are very useful.

The kinetic energy K does not change on rescaling, while the potential energy $W \to W' = W + v_{\mathrm{c}}^2 \log(\xi)$, so

$$E \to E' = E + v_{\mathrm{c}}^2 \log(\xi). \tag{3.18}$$

The invariance of K implies invariance of $\mathbf{v}$ under orbit rescaling, so the scaling of the actions is

$$\mathbf{J} \to \mathbf{J}' = \xi\mathbf{J} = \exp\left(\frac{E'-E}{v_{\mathrm{c}}^2}\right)\mathbf{J}. \tag{3.19}$$

---

[1]In the non-spherical case

$$4\pi G\rho(\xi\mathbf{R}) = \frac{a+a^2}{\xi^2 r^2}\Phi(\xi\mathbf{R})$$

$$+ \frac{1}{\xi^2 r^2 \sin\theta}\frac{\partial}{\partial\theta}\left(\sin\theta\frac{\partial\Phi(\xi\mathbf{R})}{\partial\theta}\right) + \frac{1}{\xi^2 r^2 \sin^2\theta}\frac{\partial^2\Phi(\xi\mathbf{R})}{\partial\phi^2} \tag{3.11}$$

$$= 4\pi G\xi^{a-2}\rho(\mathbf{R}).$$

Consequently ρ and Φ have simple scalings with r but they are not necessarily functions of each other.

We now use each side of this equation as the argument of a homogeneous function of degree one, $h(\mathbf{J})$, and obtain

$$h(\mathbf{J}') = \exp\left(\frac{E' - E}{v_{\mathrm{c}}^2}\right) h(\mathbf{J}), \tag{3.20}$$

or on rearrangement

$$E' = E + v_{\mathrm{c}}^2 \log[h(\mathbf{J}')/h(\mathbf{J})]. \tag{3.21}$$

Here E' and E are the energies of any two orbits whose actions $\mathbf{J}'$ and $\mathbf{J}$ are proportional to each other. We can choose to make $\mathbf{J}$ an orbit with vanishing energy, and we can choose h to be the homogeneous function that satisfies $h(\mathbf{J}) = 1$ as $\mathbf{J}$ moves over the surface $E = 0$ in action space. With these choices, we have

$$H(\mathbf{J}') = v_{\mathrm{c}}^2 \log[h(\mathbf{J}')]. \tag{3.22}$$

The ergodic DF that self-consistently generates the spherical logarithmic potential is well known to be

$$f(H) = \exp\left(\frac{E_0 - H}{\sigma^2}\right), \tag{3.23}$$

where $\sigma^2 = v_{\mathrm{c}}^2/2$ and E_0 is a constant (e.g. Binney & Tremaine, 2008, §4.3.3b). Using equation (3.22) it follows that the ergodic DF is

$$f(\mathbf{J}) = \text{constant} \times [h(\mathbf{J})]^{-2}. \tag{3.24}$$

This result is consistent with the limit $a \to 0$ of equation (3.16) for a power-law model.

Note that equation (3.24) implies that the phase-space density diverges as $\mathbf{J} \to 0$. It follows that this DF unambiguously specifies the singular isothermal sphere, in contrast to the DF (3.23), from which one can derive both cored and singular isothermal spheres (e.g. Binney & Tremaine, 2008, §4.3.3b). It is characteristic of DFs of the form $f(\mathbf{J})$ that they uniquely and transparently specify the phase-space density both at the centre of the model ($\mathbf{J} = 0$) and for marginally bound orbits ($\mathbf{J} \to \infty$). From a DF that depends on energy, by contrast, the phase-space density at the centre of the model is implicitly specified by the boundary condition adopted at $r = 0$ when solving Poisson's equation for the self-consistent potential.

The considerations of the last paragraph apply equally to the power-law DFs (3.16): although we used the standard form (3.15) of the energy-based DF of the polytropes to derive this DF, it implies infinite phase-space density at the system's centre, so it is inconsistent with familiar cored polytropes, such as the Plummer model.

3.3   Two-power models

Any power-law model is problematic in the sense that the mass interior to radius r diverges as $r \to \infty$ if the density declines as r^{-b} with $b \leq 3$, and the mass outside radius r diverges as $r \to 0$ when $b \geq 3$. Hence there is no value of b for which the model is physically reasonable at both large and small r. One way we can address this problem

is to assume that ρ scales as different powers of radius at small and large radii. A widely used family of models of this type is given by the density profile

$$\rho(r) = \frac{\rho_0}{(r/r_{\mathrm{b}})^{\alpha}(1 + r/r_{\mathrm{b}})^{\beta-\alpha}}, \qquad (3.25)$$

where r_{b} is the break radius (e.g., Binney & Tremaine, 2008). Three particular cases of importance are the Jaffe (1983) model $(\alpha, \beta) = (2, 4)$, the Hernquist (1990) model $(\alpha, \beta) = (1, 4)$, which belong to the family of Dehnen (1993) models $(\beta = 4)$, and the NFW model $(\alpha, \beta) = (1, 3)$ (Navarro, Frenk, & White, 1996). The ergodic DFs of the Jaffe and Hernquist models are known analytic function, but that of the NFW model is not. Our goal in this section is to find analytic functions $f(\mathbf{J})$ that generate models that closely resemble these three classic models.

In the regime $r \ll r_{\mathrm{b}}$ the mass $M(r)$ enclosed by the sphere of radius r is $M \propto r^{3-\alpha}$, so the gravitational acceleration is $\mathrm{d}\Phi/\mathrm{d}r \propto r^{1-\alpha}$ and thus the potential drop between radius r and the centre is

$$\Phi(r) - \Phi(0) \propto r^{2-\alpha} \quad \text{or} \quad \log(r) \text{ when } \alpha = 2. \qquad (3.26)$$

Setting $a = 2 - \alpha$ we can now employ the results we derived above for power-law potentials to conclude that

$$f(\mathbf{J}) = [h(\mathbf{J})]^{-(6-\alpha)/(4-\alpha)}. \qquad (3.27)$$

The Hernquist and NFW models both have $\alpha = 1$ so we expect their DFs to have asymptotic behaviour

$$f(\mathbf{J}) = [h(\mathbf{J})]^{-5/3} \text{ as } |\mathbf{J}| \to 0. \qquad (3.28)$$

A Jaffe model has $\alpha = 2$, so the asymptotic behaviour of the Jaffe model's DF as $\mathbf{J} \to 0$ is given by equation (3.24).

Consider now the asymptotic behaviour of a two-power model as $r \to \infty$. If the model has finite mass, the potential will asymptote to the Kepler potential, $\Phi \propto r^{-1}$, so $\rho \propto |\Phi|^{\beta}$. In the Kepler regime the dependence of the Hamiltonian on the actions is (e.g. Binney & Tremaine, 2008, eq. 3.226a)

$$H(\mathbf{J}) = [g(\mathbf{J})]^{-2}, \qquad (3.29)$$

where $g(\mathbf{J})$ is a homogeneous function of degree one. Although ρ is a simple power of $|\Phi|$ we cannot employ the polytropic formula (3.15), because that rests on Poisson's equation, which does not apply in this case: the model's envelope is a collection of test particles that move in the Kepler potential generated by its core. We instead go back to Eddington's formula

$$f(\mathcal{E}) \propto \frac{\mathrm{d}}{\mathrm{d}\mathcal{E}} \int_0^{\mathcal{E}} \frac{\mathrm{d}\Psi}{\sqrt{\mathcal{E}-\Psi}} \frac{\mathrm{d}\rho}{\mathrm{d}\Psi}, \qquad (3.30)$$

where $\mathcal{E} = -E$ and $\Psi = -\Phi$. From this formula it is easy to show that $\rho \propto \Psi^{\beta}$ implies

$$f(\mathcal{E}) \propto \mathcal{E}^{\beta-3/2}. \qquad (3.31)$$

Combining this with equation (3.29) we conclude that for $\beta > 3$ the asymptotic behaviour of a double-power DF is

$$f(\mathbf{J}) = [g(\mathbf{J})]^{-2\beta+3} \text{ as } |\mathbf{J}| \to \infty. \tag{3.32}$$

For the Jaffe and Hernquist models $\beta = 4$, so for these models

$$f(\mathbf{J}) = [g(\mathbf{J})]^{-5} \text{ as } |\mathbf{J}| \to \infty. \tag{3.33}$$

Now that we have the asymptotic behaviour of f in the limits of both small and large $\mathbf{J}$, it is straightforward to devise a suitable form of the DF

$$f(\mathbf{J}) = \frac{M_0}{J_0^3} \frac{[1 + J_0/h(\mathbf{J})]^{(6-\alpha)/(4-\alpha)}}{[1 + g(\mathbf{J})/J_0]^{2\beta-3}}. \tag{3.34}$$

Here M_0 is a constant that has the dimensions of a mass and J_0 is a characteristic action. If the two homogeneous functions are normalised such that $h(\mathbf{J}) \simeq g(\mathbf{J}) \simeq |\mathbf{J}|$, orbits that linger near the break radius r_{b} have $|\mathbf{J}| \simeq J_0$. These conditions ensure that f tends to the required powers of h and g when $|\mathbf{J}| \ll J_0$ and $|\mathbf{J}| \gg J_0$, respectively.

We use different homogeneous functions for the regimes of small and large $\mathbf{J}$ because the frequency ratios in these two regimes will differ. In the Kepler regime, which is handled by g, all frequencies are equal, so if we require an isotropic model we choose

$$g(\mathbf{J}) = J_r + |J_\phi| + J_z. \tag{3.35}$$

In the regime of small $\mathbf{J}$, $\Omega_r > \Omega_\phi = \Omega_z$, and we take h to be of the form (3.10) with a frequency ratio that is less than unity. Unfortunately, in this regime the frequency ratio does vary over a surface of constant energy and an exactly isotropic model cannot be constructed using constant ratios. We simply use $\Omega_\phi/\Omega_r = \Omega_z/\Omega_r = 1/2$, which are the frequency ratios of a harmonic oscillator.

The DF (3.34) is infinite on the orbit $\mathbf{J} = 0$ of a star that is stationary at the model's centre. *Cuspy* models such as the Hernquist, Jaffe and NFW models do have such centrally divergent DFs, while in other *cored* systems the phase space density reaches a finite maximum. Cored systems will be treated in Section 3.4.

3.3.1   Technicalities

Here we touch on some technical issues that arise when one sets out to recover the observable properties of a model from the DF that defines it. The first step is to normalise the DF to the desired total mass by evaluating the integral (3.3). When the DF depends only on the function $h(\mathbf{J})$ defined by equation (3.10) [i.e., the case $g(\mathbf{J}) = h(\mathbf{J})$] with the frequency ratios $\omega \equiv \Omega_\phi/\Omega_r = \Omega_z/\Omega_r$ taken to be constant, it is convenient to change coordinates from (J_r, J_ϕ, J_z) to (J_r, L, J_z) and integrate out J_z, and then to change coordinates to (h, L) and integrate out L. Then one finds

$$\frac{M}{(2\pi)^3} = \int \mathrm{d}h\, f(h) \int_0^{h/\omega} \mathrm{d}L\, L = \frac{1}{2\omega^2} \int_0^\infty \mathrm{d}h\, h^2 f(h). \tag{3.36}$$

Table 3.1: The ratio of the half-mass radius r_h to the scale radius r_0, defined by equation (3.38), for the $f(\mathbf{J})$ Isochrone, $f(\mathbf{J})$ Hernquist and $f(\mathbf{J})$ Jaffe models. For comparison we list also the ratio $r_\mathrm{h}/r_\mathrm{b}$, where r_b is the break radius, of the corresponding classical models.

	Isochrone	Hernquist	Jaffe
r_h/r_0	3.4	2.42	0.76
$r_\mathrm{h}/r_\mathrm{b}$	3.06	2.41	1

In the more general case, when $h(\mathbf{J}) \neq g(\mathbf{J})$, the integral (3.3) cannot be reduced to one-dimension. Equation (3.36) can be written

$$\frac{M}{(2\pi)^3} = M_0 \int \mathrm{d}^3\mathbf{y} \frac{[1 + 1/h(\mathbf{y})]^{(6-\alpha)/(4-\alpha)}}{[1 + g(\mathbf{y})]^{2\beta - 3}}, \tag{3.37}$$

where $\mathbf{y} \equiv \mathbf{J}/J_0$. The integral in equation (3.37) is dimensionless and depends only on the model's parameters α, β and on the forms of the homogeneous functions h and g. It can therefore be computed at the outset. Then the value of M_0 can be set that ensures that the model has whatever mass is required.

The physical scales of the models are determined by the action scale J_0 and by the mass scale M_0, so the natural length scale is

$$r_0 \equiv \frac{J_0^2}{GM_0}. \tag{3.38}$$

In following sections we will present $f(\mathbf{J})$ analogues of three classic models that have a finite mass: the Hernquist, Jaffe and isochrone models. For our analogue models the top row of Table 3.1 gives the ratio r_h/r_0 of half-mass radius to the scale radius defined by equation (3.38). The second row gives for the classical models the ratio of r_h to the break radius, and we see that for the Hernquist model $r_0 = r_\mathrm{b}$ to good precision, while in the other two cases the difference between r_0 and r_b is less than 25 per cent.

Once $f(\mathbf{J})$ has been normalised, we are able to determine the potential $\Phi(\mathbf{x})$ that the model self-consistently generates by the iterative procedure described by Binney (2014).

3.3.2 Worked Examples

3.3.2.a The Hernquist model

The Hernquist (1990) model is an interesting example both because it is a widely used model and because we can derive its ergodic DF as a function of the actions for comparison with the $f(\mathbf{J})$ model given by equation (3.34) with $(\alpha, \beta) = (1, 4)$, which hereafter we refer to as $f(\mathbf{J})$ Hernquist model.

In Appendix A we derive an analytic expression for $J_\mathrm{r} = J_\mathrm{r}(H, L)$ in the spherical Hernquist potential. By numerically inverting this expression, we arrive at $H = H(J_\mathrm{r}, L)$ for the Hernquist sphere. Combining this with the sphere's ergodic DF, which was given already by Hernquist (1990), we have the exact $f = f[H(\mathbf{J})]$. In Fig. 3.1 we show surfaces
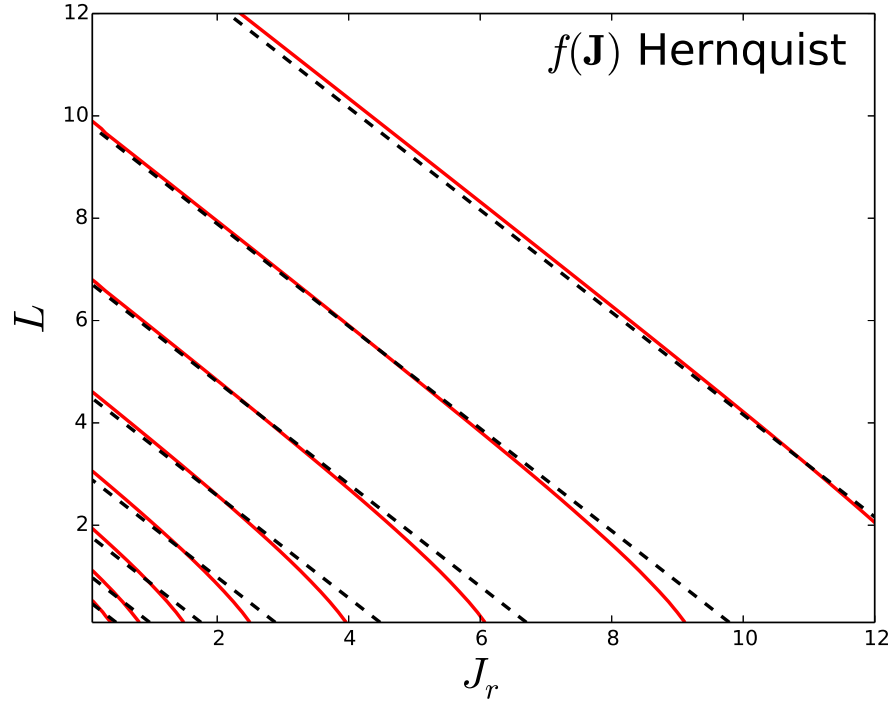
Figure 3.1: The red full curves show surfaces on which the DF of the classical isotropic Hernquist sphere is constant in the (J_r, L) plane of action space, while the black dashed curves show surfaces on which the corresponding $f(\mathbf{J})$ distribution function is constant.

in action space on which this DF is constant together with surfaces on which DF of the $f(\mathbf{J})$ Hernquist model is constant. The differences are small but apparent and arise because the surfaces of constant energy are not exactly planar.

Fig. 3.2 compares the radial profiles of density, circular speed and radial component of velocity dispersion in the exact isotropic model and in the $f(\mathbf{J})$ Hernquist model. The largest discrepancy is in the velocity dispersion and reflects the fact that the model is significantly radially biased around r_0. The long-dashed curve in Fig. 3.3 shows that the $f(\mathbf{J})$ Hernquist model has a slight radial bias at all radii by plotting the anisotropy parameter

$$\beta_{\mathrm{a}} = 1 - \frac{\sigma_\phi^2 + \sigma_z^2}{2\sigma_r^2}. \tag{3.39}$$

By virtue of the adopted form of g (equation 3.35), $\beta_{\mathrm{a}} \to 0$ in the Keplerian regime. Even though the potential is not harmonic at the centre, still the model tends to isotropy also at small radii, which justifies our simple choice for $h(\mathbf{J})$.

3.3.2.b   The Jaffe model

The Jaffe (1983) model behaves as Hernquist's at large radii, while tending to $\rho \propto r^{-2}$ close to the centre. Fig. 3.2 shows the radial profiles of the $f(\mathbf{J})$ Jaffe model defined by
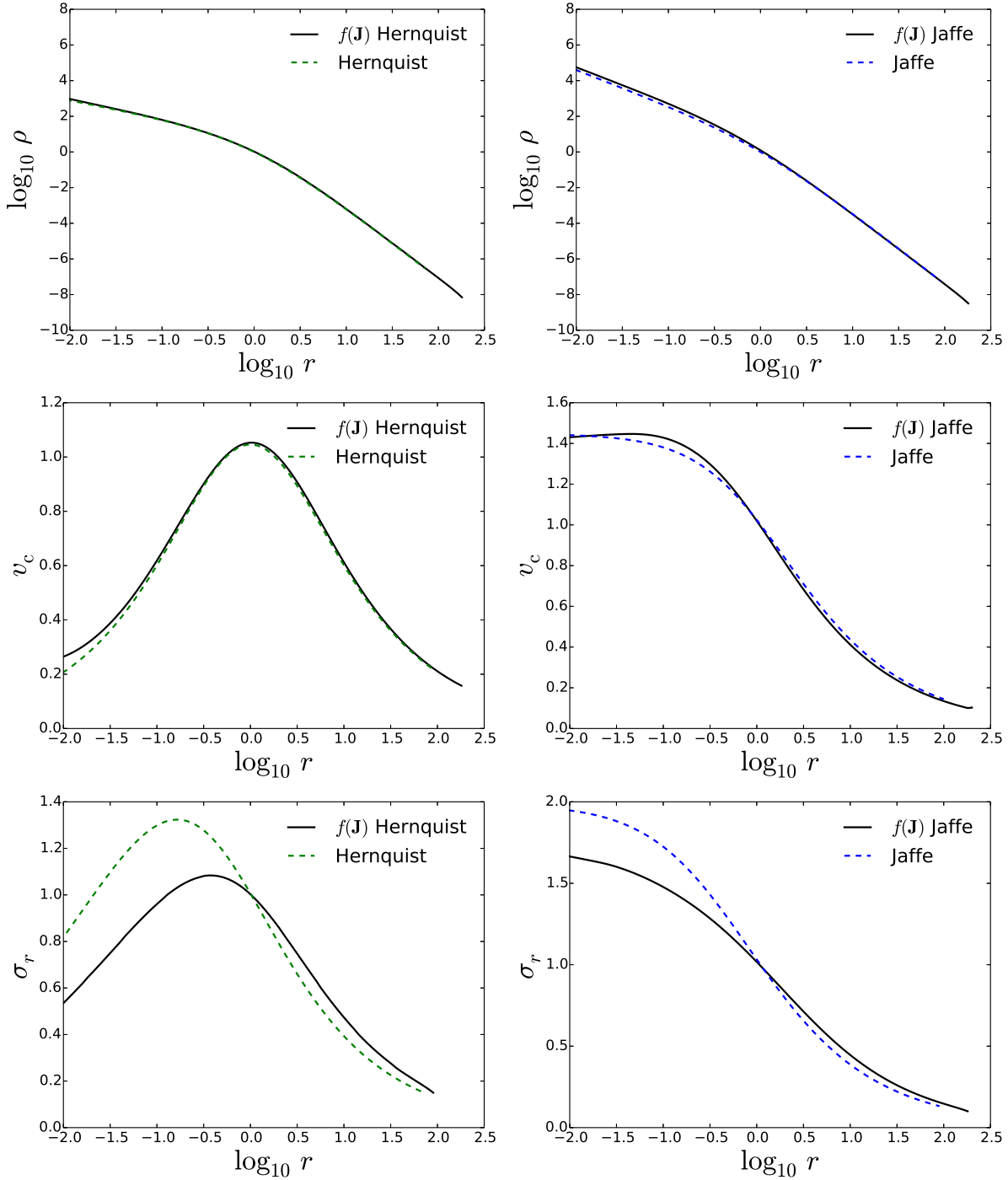
Figure 3.2: Density (top panels), circular velocity (central panels), and radial velocity dispersion (bottom panels) profiles for the classical isotropic Hernquist sphere (normalized to r_{b}, green dashed line) and for the $f(\mathbf{J})$ Hernquist model (normalized to r_0, black solid line) in the left panels and for classical isotropic Jaffe sphere (blue dashed line) and for the $f(\mathbf{J})$ Jaffe model (black solid line).
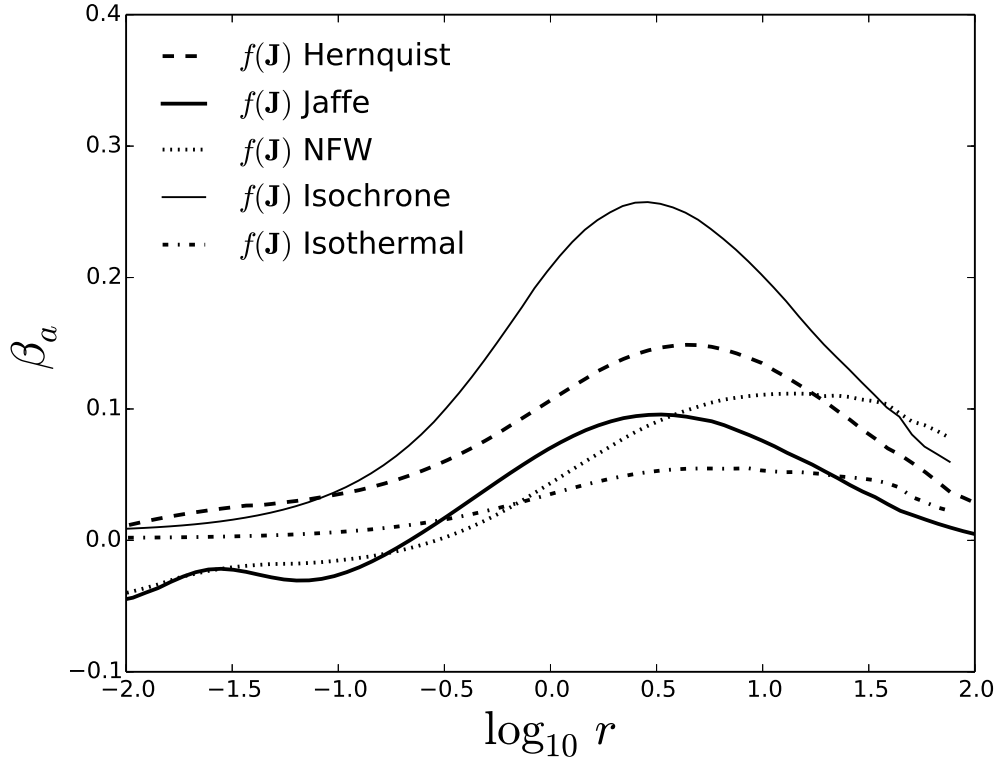
Figure 3.3: Anisotropy profiles for $f(\mathbf{J})$ Hernquist, $f(\mathbf{J})$ Jaffe, $f(\mathbf{J})$ NFW, $f(\mathbf{J})$ isochrone and $f(\mathbf{J})$ isothermal models. The profiles are normalized to r_0 (eq. 3.38).

setting $(\alpha, \beta) = (2, 4)$ in the DF (3.34), and compares them with the classical isotropic model. The discrepancies in σ_r are due to the slight radial bias of the $f(\mathbf{J})$ model around r_0. The full curve in Fig. 3.3 shows that this bias actually quite mild $- |\beta_{\mathrm{a}}| < 0.1$.

3.3.2.c   NFW halo

The NFW model has $\beta = 3$ with the consequence that its mass diverges logarithmically as $r \to \infty$ and its potential is never Keplerian. Consequently, the reasoning used to construct a DF above equation (3.34) does not apply. If we nevertheless adopt equation (3.34) with $(\alpha, \beta) = (1, 3)$, we obtain a DF that implies that as $J \to \infty$ the mass with actions less than J diverges like $\log J$. Asymptotically the circular speed of the standard NFW model is

$$v_{\mathrm{c}} \sim \sqrt{\frac{\log(1 + r/r_0)}{r}}, \tag{3.40}$$

so in this model the action of a circular orbit is $J_\phi \sim \sqrt{r \log r}$. This shows that mass diverging like $\log J$ in action space corresponds, to leading order, to divergence of the mass in real space like $\log r$. Hence it is plausible that the DF (3.34) with $(\alpha, \beta) = (1, 3)$ generates a model similar to the NFW model.

Computation of $\rho(r)$ for the $f(\mathbf{J})$ model with $(\alpha, \beta) = (1, 3)$ bears out this expectation. However the slope of the model's density profile at large r is slightly steeper than
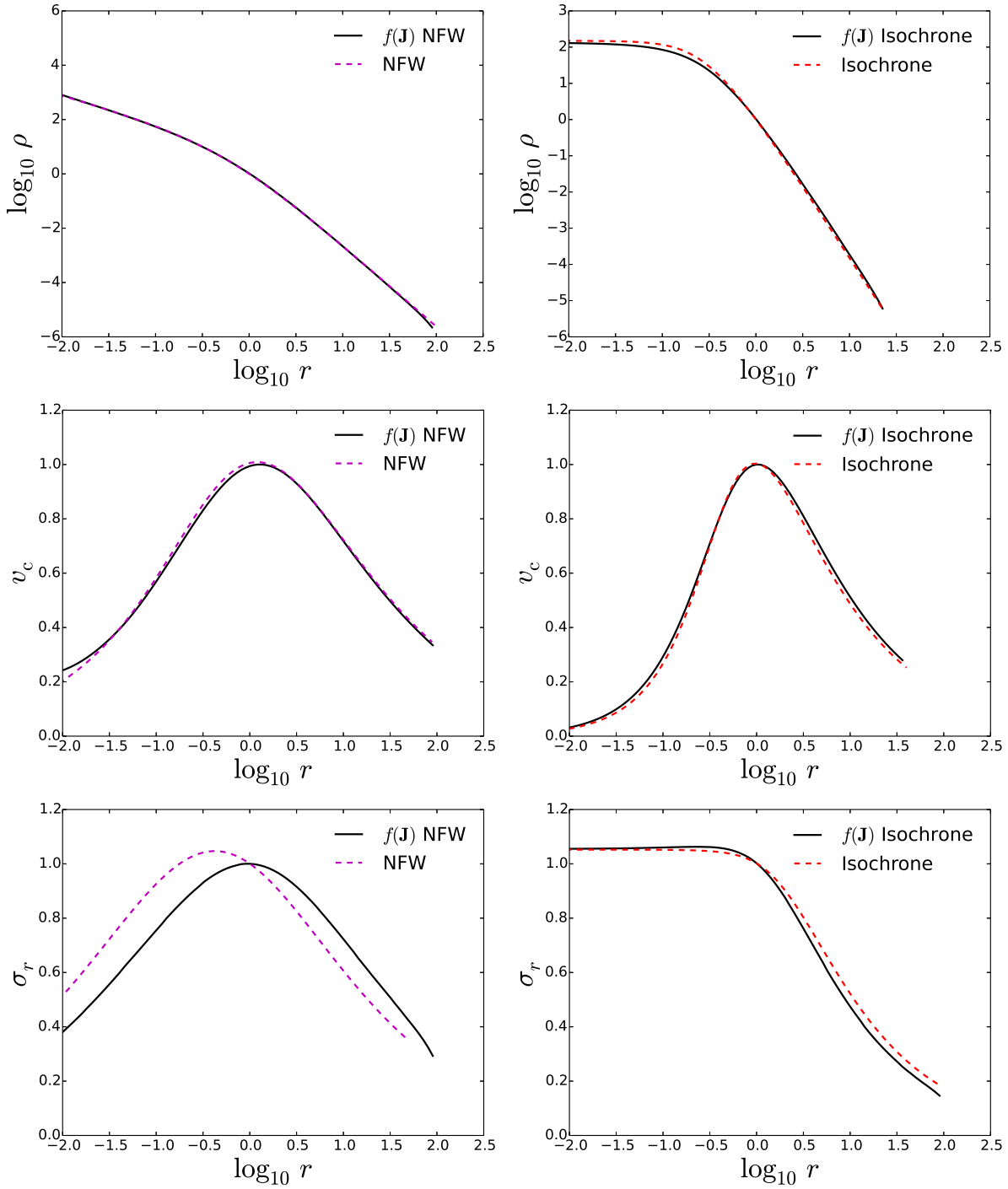
Figure 3.4: Same as Fig.   3.2, but for the classical isotropic NFW sphere and for the $f(\mathbf{J})$ NFW model defined by equation (3.41) on the left panels and for the classical isotropic isochrone sphere and for the $f(\mathbf{J})$ isochrone model on the right panels.

desired, and a better fit to the classical NFW profile is obtained by adopting

$$f(\mathbf{J}) = \frac{M_0}{J_0^3} \frac{[1 + J_0/h(\mathbf{J})]^{5/3}}{[1 + g(\mathbf{J})/J_0]^{2.9}}. \tag{3.41}$$

Fig. 3.4 shows the radial profiles of the classical NFW model and those of the model generated by the DF (3.41), which we shall call $f(\mathbf{J})$ NFW model. The dotted curve in Fig. 3.3 shows that this model is mildly radially biased at radii larger than r_0 and it becomes very slightly tangentially biased for $r < r_0$. These anisotropies account for the difference between the σ_r profiles of the $f(\mathbf{J})$ and classical NFW models.

3.4   Cores and cuts

In the last section we addressed the problematic nature of power-law models – that their mass diverges at either small or large radii – by introducing separate slopes of the dependence of f on $\mathbf{J}$ at small and large $\mathbf{J}$. The recovered models had central density cusps similar to those of the Hernquist, Jaffe and NFW models. If a homogeneous core is required, the natural DF to adopt is

$$f(\mathbf{J}) = \frac{M_0}{J_0^3} \frac{1}{[1 + g(\mathbf{J})/J_0]^{2\beta-3}}, \tag{3.42}$$

for then the phase-space density has the finite value M_0/J_0^3 at the centre of the model, and the asymptotic density profile is expected to be $\rho \propto r^{-\beta}$. For $\beta \leq 3$ the system has infinite mass, so for these models we taper the DF by subtracting a constant from the value given by equation (3.42)

$$f(\mathbf{J}) \mapsto f'(\mathbf{J}) = \max\left[0, f(\mathbf{J}) - f(\mathbf{J}_\mathrm{t})\right], \tag{3.43}$$

where $\mathbf{J}_\mathrm{t}$ is some large action, which defines a truncation radius

$$r_\mathrm{t} = \frac{|\mathbf{J}_\mathrm{t}|^2}{GM}. \tag{3.44}$$

3.4.1   Isochrone model

Fig. 3.4 compares the density profiles of the model equation (3.42) generates for $\beta = 4$ (black curves) with those of the isochrone (Hénon, 1960). The two models are extremely similar, so we shall refer to the model generated by the DF (3.42) when $\beta = 4$ as the $f(\mathbf{J})$ isochrone model. The density profiles of the two models are essentially identical, but at $r \simeq r_0$ σ_r is slightly smaller in the $f(\mathbf{J})$ isochrone than in the classical isochrone because the $f(\mathbf{J})$ isochrone is mildly radially biased near r_0 – the thin full curve in Fig. 3.3 shows $\beta_\mathrm{a}(r)$ for this model. It is non-zero because in action space surfaces of $f(\mathbf{J})$ do not quite coincide with surfaces of constant $H(\mathbf{J})$, as the upper panel of Fig. 3.5 shows by plotting contours of f and H. For the isochrone potential we have an analytic expression for the frequency ratio Ω_ϕ/Ω_r as a function of L. The lower panel of Fig. 3.5
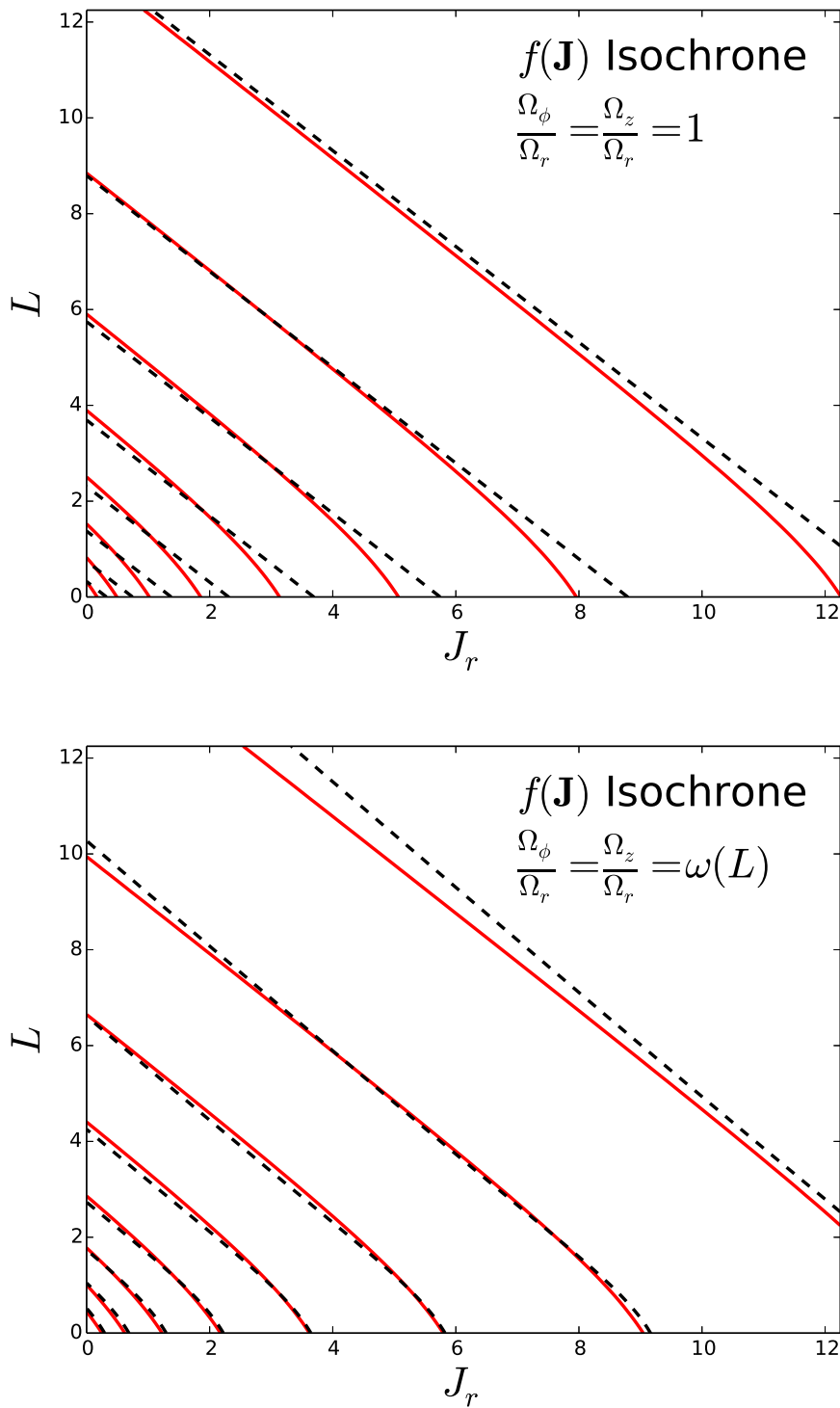
Figure 3.5: Surfaces of constant $H(\mathbf{J})$ (red) and of constant $f(\mathbf{J})$ black in action space for two $f(\mathbf{J})$ isochrone models with different choice of the function g appearing in the DF (3.42). In the upper panel g is $J_r + L$ whereas in the lower panel it is $J_r + (\Omega_\phi/\Omega_r)L$ where the frequency ratio is a function of L.

shows that the constant-energy and constant-DF contours are more closely aligned when the argument of the homogeneous function uses the exact frequency ratio.

Given that the exact DF of the isochrone is a complicated function of $\mathbf{J}$, it is astonishing that the trivial DF (3.42) provides such a good approximation to it.

3.4.2 Cored isothermal sphere

In Section 3.2.1 we derived an approximation (3.24) to the DF of the singular isothermal sphere. Here we modify this model into one that is numerically tractable by (i) adding a core, and (ii) tapering its density at large radii so the model's mass becomes finite. Then the DF is

$$f(\mathbf{J}) = \frac{M_0}{J_0^3} \max\left(0, [1 + J_0/h(\mathbf{J})]^2 - [1 + J_0/h(\mathbf{J}_{\mathrm{t}})]^2\right), \tag{3.45}$$

where $h(\mathbf{J})$ is given by equation (3.10) with both frequency ratios set to $1/\sqrt{2}$ and $\mathbf{J}_{\mathrm{t}} = (0, v_{\mathrm{c}} r_{\mathrm{t}}, 0)$. As full curves in Fig. 3.6 show, this DF generates a model that has a core that extends to r_0 and a density profile that plunges to zero near the truncation radius r_{t}. The short-dashed curve in Fig. 3.3 shows the model's anisotropy parameter β_{a}, which is always small ($|\beta_{\mathrm{a}}| < 0.04$).

An ergodic model with a simple functional form of $\rho(r)$ to which we can compare our $f(\mathbf{J})$ model has

$$\rho(r) = \frac{v_{\mathrm{c}}^2}{2\pi G(r^2 + r_{\mathrm{b}}^2)} \mathrm{e}^{-r^2/r_{\mathrm{t}}^2}. \tag{3.46}$$

The dashed curve in the left panel-hand of Fig. 3.6 shows that the model defined by the DF (3.46) provides an excellent fit to the density profile of our $f(\mathbf{J})$ model. Curiously, in the $f(\mathbf{J})$ model $\sigma_r(r)$ is more nearly constant within r_{t} than in either of the models with analytic density profiles. The dashed curve in the right-hand panel of Fig. 3.6 shows that the model defined by the DF (3.46) has a significantly deeper central depression in σ_r than the $f(\mathbf{J})$ model.

3.5 Conclusions

Studies of both our own and external galaxies will benefit from the availability of a flexible array of *dynamical* models of galactic components such as disc, bulge and dark halo. The construction of general models of this type is rather straightforward when one decides to start from an expression for the component's DF as a function of the action integrals J_i. In this Chapter we have illustrated this fact by deriving simple analytic forms for DFs that self-consistently generate models that closely resemble the isochrone, Hernquist, Jaffe, NFW and truncated isothermal models. In previous papers Binney (2010, 2012b) has given simple analytic DFs that provide excellent fits to the structure of the Galactic disc, so now DFs are available for all commonly occurring galactic components.
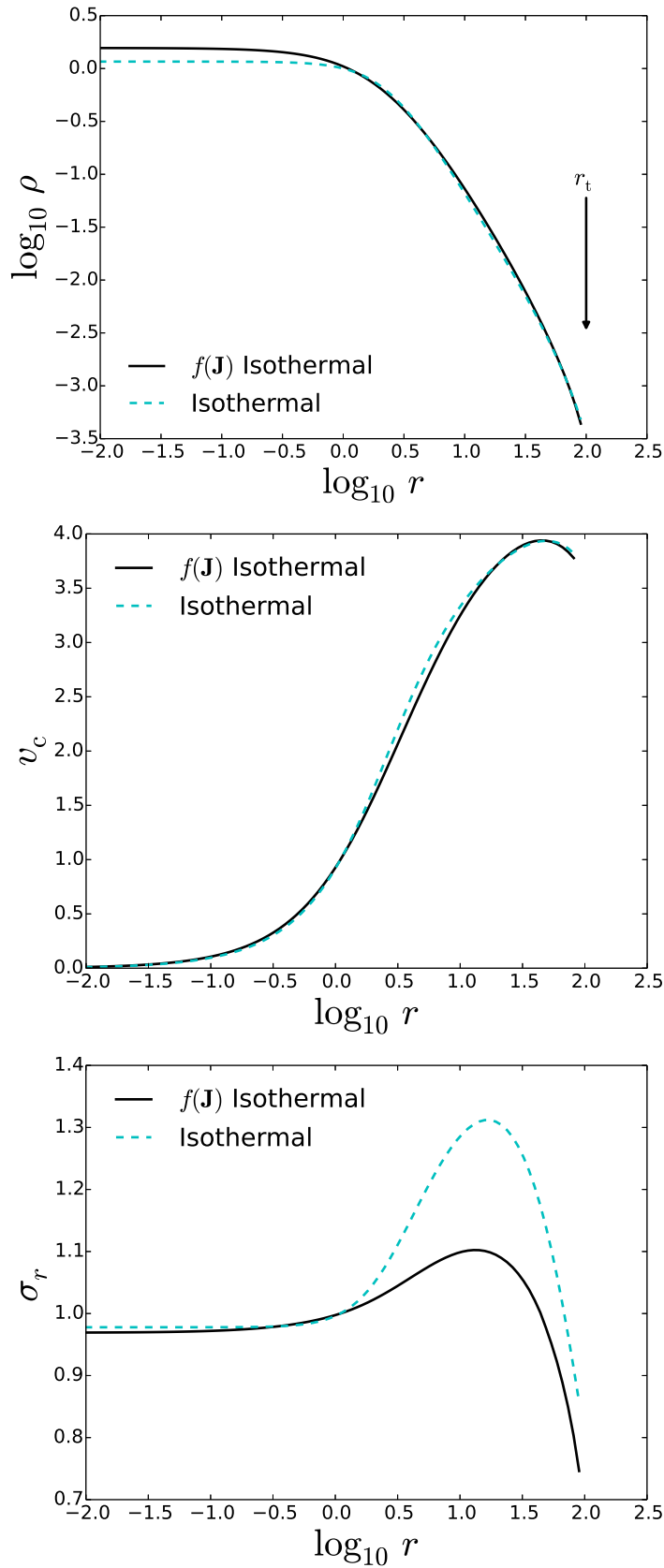
Figure 3.6: Same as Fig. 3.2, but for the truncated isotropic cored isothermal sphere (equation 3.46) and for the $f(\mathbf{J})$ truncated isothermal model (top-left density, top-right circular velocity, bottom radial velocity dispersion). We show the location of the truncation radius defined by equation (3.44).

Our models are tailored to minimise velocity anisotropy at both small and large radii. In all of them the anisotropy parameter $\beta_{\rm a}$ peaks at intermediate radii. The peak is by far sharpest in the $f(\mathbf{J})$ isochrone, but even in this model $\beta_{\rm a}$ stays below 0.25.

Our presentation has been elementary in the sense that we have confined ourselves to spherical, almost isotropic components that live in isolation. However, Binney (2014) showed that given a near-ergodic DF $f(\mathbf{J})$ of a component such as those presented here, it is trivial to modify it so it generates a system that is flattened by velocity anisotropy, or by rotation, or by a combination of the two. Equally important, when the DF of an individual component is given as $f(\mathbf{J})$, it is straightforward to add components. Such addition was exploited by Piffl et al. (2014) in a study of the contribution of dark matter to the gravitational force on the Sun: in that study the models fitted to data comprised a sum of DFs $f(\mathbf{J})$ for the disc and the stellar halo. The dark halo was assigned a density distribution rather than a DF, but Piffl, Penoyre, & Binney (2015) represent the dark halo by the $f(\mathbf{J})$ NFW model, making the Galaxy a completely self-consistent object. A key point for such work is that the mass of each component can be specified at the outset.

Our approach has several points of contact with that of Williams, Evans, & Bowden (2014) and Evans & Williams (2014), who derive approximations to $H(\mathbf{J})$ for models that are defined by DFs of the form $f(E, L)$. In particular, they show that for their models better approximations to the iso-energy surfaces in action space can be obtained if one's homogeneous function has as its argument the sum of a linear function of the actions, as used here, and a small term $\epsilon\sqrt{LJ_r}$. We expect that the anisotropy of our models could be enhanced by adding such a term.

In addition to assisting in the dynamical interpretation of observations of galaxies, the models that the present work makes possible could provide useful initial conditions for N-body simulations. The first step would be the construction of a self-consistent galaxy model from a judiciously chosen DF. Then one could Monte-Carlo sample the action space using the DF as the sampling density, and torus mapping (e.g. Binney & McMillan, 2011) could be used to generate an orbital torus at each of the selected actions. Finally some number n of initial conditions $(\mathbf{x}, \mathbf{v})$ would be selected on each torus, uniformly space in the angles θ_i. The resulting simulation would be in equilibrium to whatever precision had been used in the solution of Poisson's equation, and it would experience a "cold start" (Sellwood, 1987). Moreover, given that it would be possible to evaluate the original DF at any phase-space point, the model would lend itself to the method of perturbation particles (Leeuwin et al., 1993) in which the simulation particles represent the difference between a dynamically evolving model and an underlying equilibrium rather than the whole model. This method has been little used in the past on account of the lack of interesting models with known DFs, which is precisely the need that we have here supplied.

Chapter 4

Self-consistent models for early-type galaxies in the CALIFA Survey

Abstract

A galaxy's mass distribution and orbital anisotropy can be constrained by making use of Integral Field spectroscopy together with state-of-the-art dynamical models. Here we present the first application of self-consistent, continuous models with distribution functions (DFs) depending on the action integrals to a sample of nearby early-type galaxies. Two ellipticals and one lenticular have been selected from the CALIFA survey and we fit their surface-brightness distribution and Integral Field-kinematics to our action-based models. Each one is self-consistent, axisymmetric and produces a unique set of observables by specifying less than ten free parameters. The spatially-resolved kinematics of the CALIFA Survey gives solid constraints in the models' parameter space and we fit the galaxies' surface brightness to within the effective radius, we recover kinematic signatures such as V/σ and we estimate dynamical masses in agreement with other dynamical modelling approaches. For the first time, we self-consistently derive orbital anisotropy profiles for these galaxies. The resemblance of the models' to the galaxies' observables is striking in the round elliptical case and becomes less pronounced as the stellar disc grows importance along the Hubble sequence. As a future improvement of the present study, we will consider more realistic galaxy models by adding a stellar disc and a dark matter halo component for which DFs that are functions of the actions already exist.

4.1   Introduction

The mass of a galaxy is arguably the most important property that shapes the evolutionary path of the galaxy across its lifetime. How mass is distributed in galaxies at each stage of their life is, therefore, one of the main questions of modern astronomy. More massive systems have stronger interactions with the environment which ultimately leads to a larger mass increase via mergers with other collapsed structures and smooth accretion from the cosmic web. The mass distribution of galaxies has historically been measured using spectroscopic observations, since spectroscopy has the unique advantage of tracing the kinematics of the emitters (either gas, stars, planetary nebulae etc.) and hence allowing for a sensible reconstruction of the galaxy's gravitational potential.

The study of the internal dynamics of early-type galaxies has been rejuvenated by the advent of Integral Field spectroscopy, which allows for spatially resolving the projected kinematics of the galaxy on the two-dimensional sky plane. Pioneering projects such as TIGER (Bacon et al., 1995) have led the way for a complete kinematical characterization of early-type galaxies with projects such as SAURON (Bacon et al., 2001) and ATLAS^{3D} (Cappellari et al., 2011a), of a wider sample of galaxies including also gas-rich late-types with projects such as CALIFA (Sánchez et al., 2012), SAMI Galaxy Survey (Bryant et al., 2015) and MaNGA (Bundy et al., 2015), and of distant young galaxies with projects such as SINS (Förster Schreiber et al., 2009) and KMOS^{3D} (Wisnioski et al., 2015). Among these projects, SAURON and ATLAS^{3D} have invested the greatest effort in the accurate characterization of the internal dynamics of early types and on the measurements of fundamental galaxy properties such as mass and mass-to-light ratio. For this purpose, they have explored a wide variety of dynamical models, ranging from one-component axisymmetric models based on the Jeans (1915) equations with constant anisotropy, the so-called "Jeans Anisotropic Multi-Gaussian Expansion" (hereafter JAM models Cappellari, 2008; Scott et al., 2015), to JAM models with the inclusion of a dark matter halo (Cappellari et al., 2013), to Schwarzschild (1979) axisymmetric (Cappellari et al., 2006) and triaxial (van den Bosch et al., 2008) orbit-based models.

All of the state-of-the-art techniques used to generate dynamical models for early types have the common assumption of dynamical equilibrium and that the distribution function (hereafter, DF) depends on three integrals of motion. For instance, observations by Oort (1932) of the vertical kinematics of stars in the solar neighbourhood and kinematic observations along the major- and minor-axis of some nearby bright ellipticals by van der Marel (1991), have built a compelling case for ruling out two-integral DF models, both for the Milky Way and external galaxies. When Integral Field spectroscopy became available, it was soon realized that DFs of the type $f = f(E, L_z)$, where E is the energy and L_z is the component of the angular momentum about the symmetry axis (e.g., Hunter & Qian, 1993; Evans, 1994), do not yield reasonable fits for the observed spatially-resolved line-of-sight velocity distribution of galaxies. Hence, one must allow the DF to depend on a third non-classical integral of motion $I_3(\mathbf{x}, \mathbf{v})$ (see e.g., Emsellem, Dejonghe, & Bacon, 1999). Analytic expressions of I_3 as a function of the phase-space coordinates $(\mathbf{x}, \mathbf{v})$ are generally not known (with notable exceptions e.g., Lynden-Bell, 1962c; de Zeeuw, 1985; Stiavelli & Bertin, 1985; Dejonghe & de Zeeuw, 1988) and numerical approximations must be devised (see classic results e.g., Contopoulos, 1960;

Ollongren, 1965).

Jeans' strong theorem (see Section 2.1.2) binds the DF to depend on the phase-space coordinates only through isolating integrals of motion. If a given potential admits three isolating integrals of motion, then angle-actions coordinates $(\boldsymbol{\theta}, \mathbf{J})$ exist (e.g., Arnold, 1978). $(\boldsymbol{\theta}, \mathbf{J})$ is the only couple of canonical variables for which the conjugate momenta $\mathbf{J}$ are integrals of motion: $\mathrm{d}J_i/\mathrm{d}t = 0$ for $i = 1, 2, 3$. Hence, a physically plausible model will always be generated by employing the action integrals as arguments of the DF. Binney (2010, 2012b) showed that one can use action integrals as arguments of a "quasi-isothermal" DF to generate equilibrium models for our Galaxy and that such models provide excellent fits to a wide range of observables (see e.g., Bovy & Rix, 2013; Piffl et al., 2014). Historically the action integrals of realistic galactic potentials have always been cumbersome to compute, even with advanced calculators. Only recently there have been quite some effort to overcome this obstacle and methods like adiabatic approximation (Binney, 2010), the so-called torus machine (Kaasalainen & Binney, 1994; McMillan & Binney, 2008), the so-called Stäckel Fudge (Binney, 2012a; Sanders & Binney, 2015) and generating function methods (Bovy, 2014; Sanders & Binney, 2014) have finally filled this gap.

Binney (2014) showed that if we know how the Hamiltonian H depends on the actions (e.g., in the case of the isochrone potential, see Hénon, 1959) it is possible to flatten (and set rotating) spherical ergodic systems by simply shuffling orbits on a surface of constant energy in action space. The density distribution of the resulting (rotating) flattened model will be (approximately) the same as that of the parent spherical model. However, precise knowledge of how the Hamiltonian depends on the actions is available only in some specific cases (isochrone and scale-free potentials, see Williams, Evans, & Bowden, 2014) and one may want to use numerical approximations to $H(\mathbf{J})$ as a more general solution (see e.g., Fermani, 2013).

Slightly different is the approach that we used in Chapter 3 of this Thesis to build spherical models for different component of interest in galaxy dynamics (see also Williams & Evans, 2015a). We make the simple ansatz that the DF is a two-power function of the action integrals, so that we have a mathematically simple model, and we justify the ansatz with dimensional arguments. The model parameters can be chosen so to have final density distribution extremely similar to that of e.g., the isochrone, Hernquist (1990) or Navarro, Frenk, & White (1996) spheres. The usefulness of these $f(\mathbf{J})$ models for spheroidal galactic components is two-fold: (i) the action-based formalism makes it easy to generate multi-component self-consistent models, (ii) they are extremely flexible in terms of anisotropy, flattening and rotation. The former arises from the fact that the actions, other than isolating integrals of motion, are also adiabatic invariants; therefore, the functional dependence of the DF on $\mathbf{J}$ will not be altered when adding a new component to the total potential. The latter follows from an orbit-shuffling scheme similar to that of Binney (2014).

This Chapter aims at illustrating the power of such scheme by generating realistic models of early-type galaxies and comparing them with Integral Field observations from the CALIFA survey. Our galaxy models have full control on the density, anisotropy profile and rotation curve. For simplicity we limit ourselves to study one-component self-

consistent axisymmetric models, which we generate by flattening the spherical models presented in Chapter 3. We do not include either a disc or a dark matter halo component, but we do allow for a dark matter distribution which follows that of the galaxy's luminosity density. As a testbed for our action-based models, we have chosen three different early-type galaxies with a different amount of rotational support and disc-to-total ratio, for which we expect a different quality in the final fits to the models. For the present proof of concept we do not employ any automatic best-fitting algorithm, as we obtain reasonable fits to the total galaxy kinematics and brightness by simply "hand-picking" models in the parameter space.

The Chapter is organized as follows: in Section 4.2 we present the family of action-based $f(\mathbf{J})$ models; Section 4.3 presents the sample of galaxies from the CALIFA survey that we consider in this work; in Section 4.4 we derive the models' observables, we discuss the physical meaning of the free parameters and we describe how we generate mock observations; in Section 4.5 we apply the models to the galaxies, first by comparing the light distributions and then the kinematics, and finally we derive some intrinsic properties of our galaxy models, such as mass and anisotropy profiles; Section 4.6 wraps up and concludes.

4.2 Action-based models

In this work we will consider equilibrium models for stellar systems generated by an analytical DF which depends on phase-space coordinates through the three action integrals. They are a generalization of the self-consistent isochrones introduced by Binney (2014) and full details are given in Chapter 3. Similar action-based models have also been independently developed by Williams & Evans (2015a), who later used them to constrain the Milky Way's stellar halo (Williams & Evans, 2015b).

4.2.1 The Distribution Function

A self-consistent, axisymmetric and flattened equilibrium model is generated by the following DF

$$f_+(\mathbf{J}) = \frac{M_0}{J_0^3} \frac{[1 + J_0/h(\mathbf{J})]^A}{[1 + g(\mathbf{J})/J_0]^B}, \tag{4.1}$$

where

$$\begin{aligned} h(\mathbf{J}) &= J_{\mathrm{r}} + \delta_{\mathrm{h},\phi}|J_\phi| + \delta_{\mathrm{h,z}}J_{\mathrm{z}}, \\ g(\mathbf{J}) &= J_{\mathrm{r}} + \delta_{\mathrm{g},\phi}|J_\phi| + \delta_{\mathrm{g,z}}J_{\mathrm{z}}, \end{aligned} \tag{4.2}$$

are two homogeneous functions of degree one with $\delta_{\mathrm{h},\phi}, \delta_{\mathrm{h,z}}, \delta_{\mathrm{g},\phi}, \delta_{\mathrm{g,z}} \geq 0$, $(J_{\mathrm{r}}, J_\phi, J_{\mathrm{z}})$ are respectively the radial, azimuthal and vertical actions, $0 < A < 3$ and $B > 3$ are constants and $M_0 > 0$ and $J_0 > 0$ are respectively a mass and an action scale as in Chapter 3.

The DF (4.1) is an even function of the azimuthal action J_ϕ, which is the component of the total angular momentum in the direction the symmetry axis L_{z}, and thus produces

non-rotating models. Though, rotation can be introduced by adding an odd component $f_-(\mathbf{J})$ to the function $f_+(\mathbf{J})$ (see e.g., Lynden-Bell, 1960). Then the total DF becomes

$$f(\mathbf{J}) = f_+(\mathbf{J}) + kf_-(\mathbf{J}), \tag{4.3}$$

where $0 \leq k \leq 1$ is a constant which specifies the model's level of rotation, from no rotation $k = 0$ to maximally rotating $k = 1$. A natural choice for the odd part is $f_-(\mathbf{J}) = \mathrm{sgn}(J_\phi)f_+(\mathbf{J})$. However, this choice produces a discontinuity for orbits with $J_\phi \to 0$ and completely suppresses counter-rotating orbits even at the centre of the model. So it is more physical to employ a function which smoothly goes from -1 to 1 around the origin, thus allowing for the presence of orbits with $J_\phi < 0$ near the origin, as it should be, physically. In addition, it is expedient to have a tunable parameter that controls the steepness of the slope at $J_\phi = 0$. A function that accomplishes just that is

$$f_-(\mathbf{J}) = \tanh\left(\frac{\chi J_\phi}{J_0}\right) f_+(\mathbf{J}), \tag{4.4}$$

where χ is a free parameter, which specifies the steepness of the rotation curve near the origin: the larger the value, the more steeply the curve rises.

4.3 Data

4.3.1 The CALIFA survey

CALIFA is an Integral Field survey of a sample of up to 600 galaxies of all Hubble types in the local Universe ($0.005 \leq z \leq 0.03$). The main selection criteria is an angular isophotal diameter ($45'' \leq D_{25} \leq 80''$, where D_{25} is the diameter of the isophote at the 25th magnitude in r-band, see Sánchez et al., 2012). The complete sample is representative of galaxies with stellar masses in the range $9.4 \leq \log M_*/M_\odot \leq 11.4$ (the volume-corrected luminosity and mass functions are recovered better than 95%, see Walcher et al., 2014). The Integral Field Unit PMAS/PPaK (Verheijen et al., 2004; Roth et al., 2005) covers a field of view of $74'' \times 64''$ with a hexagonal fibre bundle. The spatial sampling of the instrument is of $1''$, that over-samples the spatial resolution of about a factor of three (see Husemann et al., 2013).

In this work, we have used observations conducted with the instrumental setup which employs the V1200 grating, which is a medium-resolution grating ($R \simeq 1650$ at $\simeq 4500\text{\AA}$) that covers the range $3400-4750\text{\AA}$ and yields high-quality maps of the stellar kinematics.

4.3.2 Sample description

The sample of three galaxies considered in this study is drawn from the public Data Release 2 (DR2) of the CALIFA collaboration (Garcia-Benito et al., 2015). We focus only on early-type galaxies (roughly 20% of the DR2 sample) for which stellar kinematics has been estimated by the CALIFA collaboration using an implementation of the

Table 4.1: Sample of CALIFA galaxies studied in this work. Both the absolute magnitude in r-band $\mathscr{M}_r$ (uncorrected for dust extinction) and the effective radius R_e come from a growth curve analysis of the SDSS r-band image.

Galaxy	Hubble Type	Redshift	R_e [arcsec]	$\mathscr{M}_r$
NGC 6125	E1	0.0158	21.8	−22.86
NGC 2592	E4	0.0066	9.9	−20.72
NGC 6427	S0	0.011	8.3	−21.37

penalized Pixel-Fitting (pPXF) method of Cappellari & Emsellem (2004). Briefly, the spaxels have been re-binned on a Voronoi mesh to achieve a signal-to-noise $\gtrsim 20$ with the method of Cappellari & Copin (2003), the stellar templates are the Indo-U.S. spectral libraries (Valdes et al., 2004) and the penalized likelihood maximization was performed on gaussians line-of-sight velocity distributions (hereafter, LOSVDs). The method is described in detail in Falcòn-Barroso et al. in preparation.

For the purpose of this work, we have chosen to focus on three objects with very different morphology and kinematics:

(i) NGC 6125: E1 morphology, slow rotator,

(ii) NGC 2592: E4 morphology, fast rotator,

(iii) NGC 6427: S0 morphology, fast rotator,

where the distinction between the slow and fast rotators is as in Emsellem et al. (2007, see also Section 4.4.1). With this diverse sample we explore different photometric and kinematic morphologies and we expect different results in the quality of the representation with one-component $f(\mathbf{J})$ models.

In Table 4.1 we give a brief characterization of the sample of three galaxies considered in this work.

4.4 Action-based galaxy models in observable space

In this work, for simplicity, we consider self-consistent *mass-follows-light* models, i.e., we force the total (luminous plus dark-matter) mass to be distributed as the light in the galaxy. Once we have fitted our one-component models to the galaxies described in Section 4.3.2, we would have an estimate of the dynamical mass-to-light ratio. Several previous works (e.g., Cappellari et al., 2013) have argued that such simple models fit kinematical observations of early-type galaxies, typically up to the effective radius, as well as models in which the dark-matter fraction is allowed to vary with radius. However, more realistic models of galaxies should allow for the inclusion of a self-consistent dark halo. The formalism in which one writes down a DF as a function of the actions is ideal to do just that: finding the self-consistent total potential for the two components

is no more difficult than doing it for a one-component system (see Binney & Piffl, 2015). For the scope of the present paper, we prefer to stick with the simpler one-component mass-follows-light models which have a more restricted parameter space.

The parametrization (4.3) of the DF enables one to generate an interestingly large variety of galaxy models. In what follows, we first present and discuss the models and we identify the physical meaning of each free parameter. We describe the procedure used to generate Integral Field-like observables from our continuous models and, then, we discuss the regions of parameter space which are populated by the more realistic galaxy models that DF (4.3) can produce.

Throughout the paper we define the effective radius $R_{\rm e}$ to be the radius of a circular aperture containing half the total light of the system.

4.4.1   From the DF to the observables

Given a DF of the form $f(\mathbf{J})$ the system's mass density is

$$\rho(\mathbf{x}) = \int \mathrm{d}^3\mathbf{v}\, f[\mathbf{J}(\mathbf{x}, \mathbf{v})]. \tag{4.5}$$

Assuming a constant mass-to-light ratio $\Upsilon \equiv M/L$ it follows

$$I(\mathbf{x}_\perp) = \frac{1}{\Upsilon}\Sigma(\mathbf{x}_\perp) = \frac{1}{\Upsilon}\int \mathrm{d}x_\parallel\, \rho(\mathbf{x}), \tag{4.6}$$

where I is the surface brightness, $x_\parallel \equiv \mathbf{x} \cdot \hat{\mathbf{s}}$ is the component of the position vector parallel to the line-of-sight normalized vector $\hat{\mathbf{s}}$, $\mathbf{x}_\perp \equiv \mathbf{x} - x_\parallel\hat{\mathbf{s}}$ is that perpendicular and $\Sigma(\mathbf{x}_\perp)$ is the surface mass density on the sky plane. The first and second velocity moments of the DF projected on the sky plane are (see Binney & Tremaine, 2008, §4.1.2)

$$v_\parallel(\mathbf{x}_\perp) = \frac{\int \mathrm{d}x_\parallel\, \rho(\mathbf{x})\, \hat{\mathbf{s}} \cdot \overline{\mathbf{v}}}{\Sigma(\mathbf{x}_\perp)}, \tag{4.7}$$

$$\sigma_\parallel^2(\mathbf{x}_\perp) = \frac{\int \mathrm{d}x_\parallel\, \rho(\mathbf{x})\, (\hat{\mathbf{s}} \cdot \boldsymbol{\sigma}^2 \cdot \hat{\mathbf{s}} + u^2)}{\Sigma(\mathbf{x}_\perp)}, \tag{4.8}$$

where the bar over the quantity Q means

$$\overline{Q} \equiv \frac{\int \mathrm{d}^3\mathbf{v}\, Q\, f(\mathbf{x}, \mathbf{v})}{\rho(\mathbf{x})}, \tag{4.9}$$

$\overline{\mathbf{v}}$ is the mean velocity, $u \equiv \hat{\mathbf{s}} \cdot \overline{\mathbf{v}} - v_\parallel$ and $\sigma_{i,j}^2(\mathbf{x}) \equiv \overline{v_i v_j} - \overline{v}_i\overline{v}_j$ is the velocity dispersion tensor. Along the same line-of-sight it is possible to compute the probability distribution of the velocities perpendicular to the sky plane

$$P(v_\parallel, \mathbf{x}_\perp) = \frac{\int \mathrm{d}x_\parallel \mathrm{d}^2\mathbf{v}_\perp\, f[\mathbf{J}(\mathbf{x}, \mathbf{v})]}{\Sigma(\mathbf{x}_\perp)}. \tag{4.10}$$

This quantity is the LOSVD, which is also often called line-profile because it gives the Doppler-shifted profile of the line resulting from a system of monochromatic emitters (all with the same emissivity) having DF $f(\mathbf{J})$.

In principle, the LOSVD along a given line-of-sight is the model's quantity closer to the real observable in Integral Field spectroscopy, which is the profile of a given line in the galaxy spectrum. One may be tempted to compare equation (4.10) with the observed line profile, however many authors (see e.g., Cappellari et al., 2013) have noticed that for typical Integral Field observations the spectral resolution is not high enough to get a full characterization of the LOSVD. In particular, for stellar kinematics one gets better results by simply fitting a Gaussian to the LOSVD, instead of performing an expansion in Gauss-Hermite functions (see Gerhard, 1993; van der Marel & Franx, 1993). Moreover, Cappellari et al. (2013) notice that the best empirical approximation to the velocity second moment is often given by the quantity

$$v_{\mathrm{RMS}} \equiv \sqrt{v^2 + \sigma^2}, \tag{4.11}$$

where v and σ are the mean and standard deviation of the Gaussian which best fits the LOSVD. We also define $v_{\mathrm{RMS,e}} = \langle \sqrt{v^2 + \sigma^2} \rangle_{\mathrm{e}}$ and, following Emsellem et al. (2007), the parameter

$$\lambda_{\mathrm{Re}} \equiv \frac{\langle R|v| \rangle_{\mathrm{e}}}{\langle R v_{\mathrm{RMS}} \rangle_{\mathrm{e}}}, \tag{4.12}$$

where $\langle \cdot \rangle_{\mathrm{e}}$ is a light-weighted average within the effective ellipse. λ_{Re} is often used to quantify the rotational support of galaxies and their total angular momentum, and also to separate different kinematic classes, such as fast and slow rotators (see Emsellem et al., 2007).

When measuring line profiles with a telescope, the flux at each location on the sky is influenced also by the neighbouring pixel in such a way that is often parametrized with a so-called Point Spread Function (hereafter PSF). The PSF is a function such that the actual flux measured by the telescope at a given location $\mathbf{x}_\perp$ on the sky is given by the convolution of the intrinsic flux at $\mathbf{x}_\perp$ and the PSF. For a given model, one can take into account such instrumental effect by integrating the light-weighted line profiles within the PSF $\Pi(\mathbf{x}_\perp)$,

$$P_{\mathrm{bs}}(v_\parallel, \mathbf{x}_\perp) = \frac{\int \mathrm{d}^2\mathbf{x}'_\perp \Sigma(\mathbf{x}'_\perp)\, P(v_\parallel, \mathbf{x}'_\perp) \Pi(\mathbf{x}_\perp - \mathbf{x}'_\perp)}{\int \mathrm{d}^2\mathbf{x}'_\perp \Sigma(\mathbf{x}'_\perp)\, \Pi(\mathbf{x}_\perp - \mathbf{x}'_\perp)}. \tag{4.13}$$

Here we have assumed that the PSF is the same at each wavelenght, i.e., Π does not depend on $v_\parallel$, but one can easily relax the assumption by substituting $\Pi(\mathbf{x}_\perp) \mapsto \Pi(v_\parallel, \mathbf{x}_\perp)$. Equation (4.13) includes the effect of beam smearing in equation (4.10).

4.4.2   The physical meaning of the model's parameters

Here we describe how different parameters in our models affect different observables. Even if we find that some degeneracies are still present when comparing $f(\mathbf{J})$ models to observations, we show in the following that it is still possible to constrain different models' parameters with different observables.

4.4.2.a   The radial density profile

The parameters A and B determine the system's density profile: for instance, for spherically symmetric systems with $\rho(r) \propto r^{-\alpha}$ for $r \to +\infty$ and $\rho(r) \propto r^{-\beta}$ for $r \to 0$, we find (see Section 3.3):

$$\begin{aligned} A &= (6 - \alpha)/(4 - \alpha), \\ B &= 2\beta - 3. \end{aligned} \tag{4.14}$$

The reason for this resides in the fact that for an ergodic stellar system, i.e., in which the DF depends only on the orbit's energy, the radial density profile is determined by the number of stars per unit energy (see e.g., Binney & Tremaine, 2008, §4.4). The dependence that the $f(\mathbf{J})$ models have on the action integrals, i.e., via the homogeneous functions h and g in equation (4.2), is so that the (planar) surfaces of equal phase-space density in action space are remarkably close to that of equal-energy, making the system almost ergodic (see Figures 3.1 and 3.5 in Chapter 3).

In addition, the two parameters M_0 and $r_0 \equiv J_0^2/GM_0$ are used to scale up the model to the physical dimensions of each galaxy.

4.4.2.b   Anisotropy and flattening

The parameters $\boldsymbol{\delta} = (\delta_{h,\phi}, \delta_{h,z}, \delta_{g,\phi}, \delta_{g,z})$, which are the coefficients of the actions in the homogeneous functions h and g (4.2), are responsible for populating the system with different kinds of orbits. Close to the system's centre, where $||\mathbf{J}||/J_0$ is large, the actions are typically smaller than J_0 and the probability of finding a star at that location is given by $h(\mathbf{J})$ and is independent of $g(\mathbf{J})$. Viceversa for the system's outskirts. Close to the centre, if one chooses $\delta_{h,\phi} = \Omega_\phi/\Omega_r$ and $\delta_{h,z} = \Omega_z/\Omega_r$, where $\Omega_i \equiv \partial H/\partial J_i$ are the orbital frequencies, the surfaces in action-space where the DF is constant are also isoenergetic. For instance, the models presented in Chapter 3 were constructed by employing constant frequency ratios in both the homogeneous functions h and g and the models they generated were almost ergodic (see Figures 3.1 and 3.5 in Chapter 3).

Here we move from the isotropic and almost ergodic models of Chapter 3 by varying the parameters $\boldsymbol{\delta}$ from the local frequency ratios. We adopt constant $\boldsymbol{\delta}$ so that surfaces of equal-phase space density will still be planar, but typically tilted from the isoenergetic ones. Varying $\delta_{h,\phi}$ and $\delta_{h,z}$ will alter the probability of having e.g., circular over radially oscillating orbits for regions close to the system's centre; viceversa, when varying $\delta_{g,\phi}$ and $\delta_{g,z}$, one will be altering the model's orbital composition at the outskirts. This ultimately translates into modifications of the system's anisotropy: since the DF (4.1) is invariably a decreasing function of the actions[1], $\delta_{h,z} > 1$ will suppress the probability of vertically oscillating orbits close to the system's centre, reducing the vertical pressure

---

[1]

$$\frac{\partial f(\mathbf{J})}{\partial J_i} = -\left[\frac{\frac{\partial g(\mathbf{J})}{\partial J_i}\frac{B}{J_0}}{1 + g(\mathbf{J})/J_0} + \frac{\frac{\partial h(\mathbf{J})}{\partial J_i}\frac{A}{h(\mathbf{J})}}{1 + h(\mathbf{J})/J_0}\right] f(\mathbf{J}) < 0$$

always for $i = r, \phi, z$ and for h and g as in equation (4.2).

and making the model flattened, while $\delta_{\mathrm{h},\phi} < 1$ will enhance the probability of large-angular momentum orbits close to the centre, raising the azimuthal pressure and making the model tangentially biased (see Binney, 2014, Chapter 3).

General choices for the values of $\boldsymbol{\delta}$ tilt the planes defined by $h(\mathbf{J})$ and $g(\mathbf{J})$ with respect to surfaces of constant energy. This, for instance, implies that the model's density profile will depend also on the form of the homogeneous functions h and g. However, we empirically find that deviations in the spherically averaged density profile $\rho(r)$ between models with the same parameters except for $\boldsymbol{\delta}$ are modest.

4.4.2.c　Rotational support

The parameters k and χ govern the model's rotation. k controls the amount of ordered streaming motions in the azimuthal direction and determines the amplitude of the rotation curve, χ controls its shape. Following Binney (2005), one can introduce the quantity

$$
\frac{V}{\sigma} \equiv \left(\frac{\left\langle v_{\|}^2 \right\rangle_{\mathrm{e}}}{\left\langle \sigma_{\|}^2 \right\rangle_{\mathrm{e}}} \right)^{1/2} .
\tag{4.15}
$$

This indicator of the amount of rotational support of galaxies was introduced by Binney (2005) to supersede classical $V/\sigma \equiv v_{\mathrm{max}}/\sigma_{0.5}$, where v_{max} is the peak of the rotation curve and $\sigma_{0.5}$ is the mean line-of-sight velocity dispersion within $R_{\mathrm{e}}/2$ (see e.g., Bertola & Capaccioli, 1975; Illingworth, 1977; Davies et al., 1983). V/σ as in equation (4.15) comes from the Tensor Virial Theorem (e.g., Binney & Tremaine, 2008, §4.8.3) and it is tailored for Integral Field data. The parameters k and χ that control rotation, together with the parameter $\delta_{\mathrm{g},\phi}$ that controls the azimuthal pressure, allow us to adjust the model's V/σ to our liking. Figure 4.1 shows the effect of varying χ for different models which share the other free parameters except $\delta_{\mathrm{g},\phi}$. In order to exemplify the incidence that χ has on the model's rotation curve, we generated three models with the same V/σ by adjusting the amount of azimuthal over radial and vertical pressure, i.e., varying $\delta_{\mathrm{g},\phi}$. Figure 4.1 shows that, for a fixed V/σ, the larger χ, the closer the peak of the projected velocity is to the centre.

Figure 4.2 shows how the line profiles are affected if one sets rotating an azimuthally biased $f(\mathbf{J})$ model in the manner described by equations (4.3)-(4.4). The double peaked line profile, out from the centre, is given by the bias towards more circular orbits (both models shown in Figure 4.2 tend to isotropy to the centre). The rotating model has mean $v_{\|} > 0$ which is due to a dramatic suppression of one of the two peaks of the non-rotating line profile (in particular, the one with approaching velocities) by the tanh function (4.4). The non-Gaussianity of the line profiles at all radii is apparent by the comparison with the best fitting Gaussian and with the expansion in Gauss-Hermite functions (up to order 30, see Gerhard, 1993, and also van der Marel & Franx 1993).
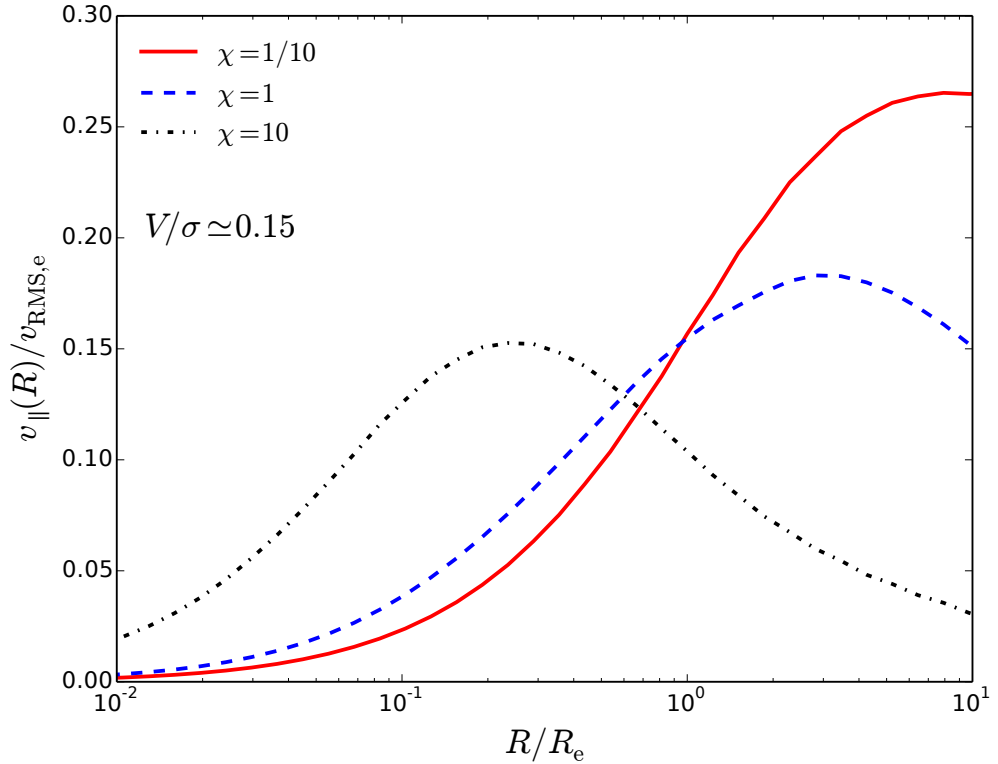
Figure 4.1: Effect of varying χ on $f(\mathbf{J})$ models, while keeping the same radial density profile and a constant $V/\sigma \simeq 0.15$. The plot shows the line-of-sight velocity normalized to the v_{RMS} within the effective radius (edge-on projection) of three $f(\mathbf{J})$ models with $\chi = 1/10$ (red solid line), $\chi = 1$ (blue dashed line) and $\chi = 10$ (black dot-dashed line). For all the models $k = 1$ and we impose $V/\sigma = 0.15$ by varying $\delta_{\mathrm{g},\phi}$, i.e., adjusting the relative amount of azimuthal pressure.

4.4.3 Generating mock data

Since the advent of Integral Field spectrographs, models of early-type galaxies can benefit from the constraints coming from measurements of the spatially resolved stellar kinematics from stellar absorptions lines. Observations such as those of the CALIFA survey give us the ability to characterize the LOSVD at each spatial element (usually referred as spaxel). However, even in bright galaxies it can be hard to characterize the LOSVD since far from the centre the signal-to-noise is typically of the order S/N $\lesssim 10$. So, usually it is preferred to collapse some neighbouring spaxels into a larger spatial bin in order to increase the signal-to-noise, at the expense of the spatial resolution. The most popular method to re-bin an IFU image is that introduced by Cappellari & Copin (2003), who use a Voronoi tessellation to optimally re-bin the IFU spaxels. This method generates a final re-binned grid such that the signal-to-noise in each bin is above an arbitrary threshold.

A direct comparison between our action-based models and Integral Field observations is possible only provided one uses the same methodology and the same assumptions
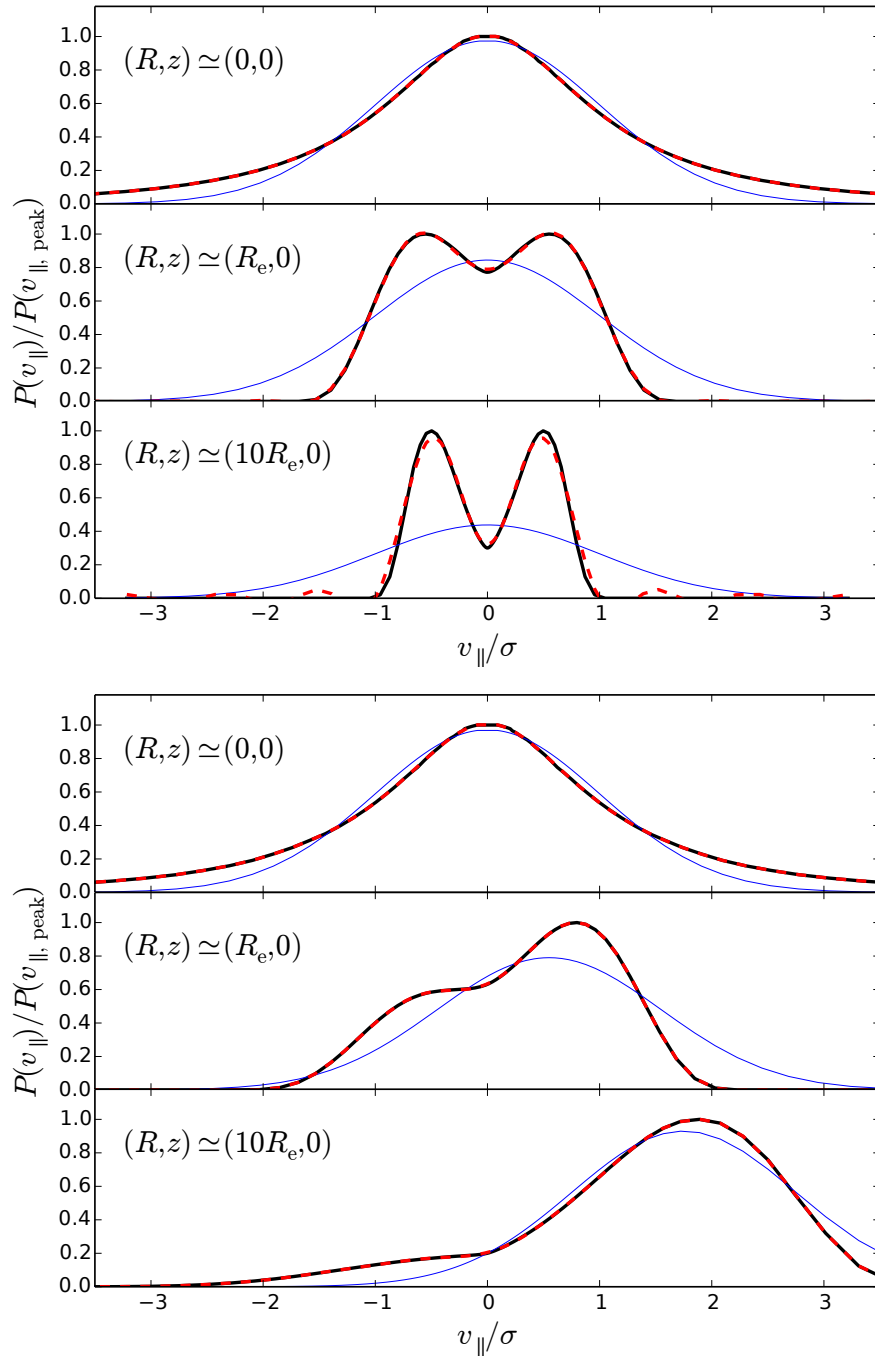
Figure 4.2: Line profiles (equation 4.10) of two flat and tangentially biased $f(\mathbf{J})$ models (with the same $A, B, \boldsymbol{\delta}$). We have projected both the models edge-on and we have computed the line profiles at three different locations on the equatorial plane $z \simeq 0$: at $R \simeq 0$, $R \simeq R_{\mathrm{e}}$ and $R \simeq 10R_{\mathrm{e}}$. The top panel is for the non-rotating model, while the bottom panel is for the rotating model. In both panels, the black solid curves are the model's line profiles, the blue thin curve is the best Gaussian fit, while the dashed red line is the best fit with Gauss-Hermite functions up to order 30 (see Gerhard, 1993). For reference, the rotation curve of the latter model is not much different from the blue dashed line in Figure 4.1.

as the observers do to get their results. In this spirit, we applied Cappellari & Copin (2003) method to bin our smooth projections of the DF moments (4.6)-(4.8), assuming a Poissonian noise on the intensity maps. Figure 4.3 shows line-of-sight velocity and velocity dispersion Voronoi re-binned maps for representative $f(\mathbf{J})$ models in the parameter space $(\delta_{g,\phi}, \delta_{g,z})$. The models have the same $(A, B, \delta_{h,\phi}, \delta_{h,z}, \chi, k) = (5/3, 5, 1/2, 1/2, 1, 1)$ and their location on the plane corresponds to the model's $(\delta_{g,\phi}, \delta_{g,z})$. For the purpose of showing the effect of varying $(\delta_{g,\phi}, \delta_{g,z})$ on the models' observable kinematics, we have also fixed the inclination of the line-of-sight to be 90°, i.e., an edge-on projection. We construct the re-binned grid from the surface brightness map (equation 4.6), light average the first and second projected moments (equations 4.7-4.8) and normalize to the model's v_{RMS} within the effective radius. We also overplot isophotal contours equally spaced in logarithm.

Flattened models require $\delta_{g,z} > \delta_{g,\phi}$ (see also Binney, 2014) so that the DF deters orbits with large vertical excursion, while typically $\delta_{g,z} < \delta_{g,\phi}$ produces prolate models. For maximally rotating configurations ($k = 1$) with fixed shape of the velocity curve (here $\chi = 1$), V/σ increases as the azimuthal pressure increases and the models become tangentially biased, i.e., $\delta_{g,\phi} \to 0$. For a fixed value of $\delta_{g,\phi}$, models with smaller $\delta_{g,z}$ tend to suppress very radial orbits, resulting in a net increase of the model's V/σ. While for very low V/σ models ($\delta_{g,\phi}, \delta_{g,z} \to +\infty$) the shape of the iso-$\sigma_\parallel$ contours closely follows that of the isophotes, for fast rotating models $\sigma_\parallel$ falls off further away from the symmetry axis, where $v_\parallel$ is large. Hence, the iso-$\sigma_\parallel$ contours tend to be prolate even for systems with oblate light distribution.
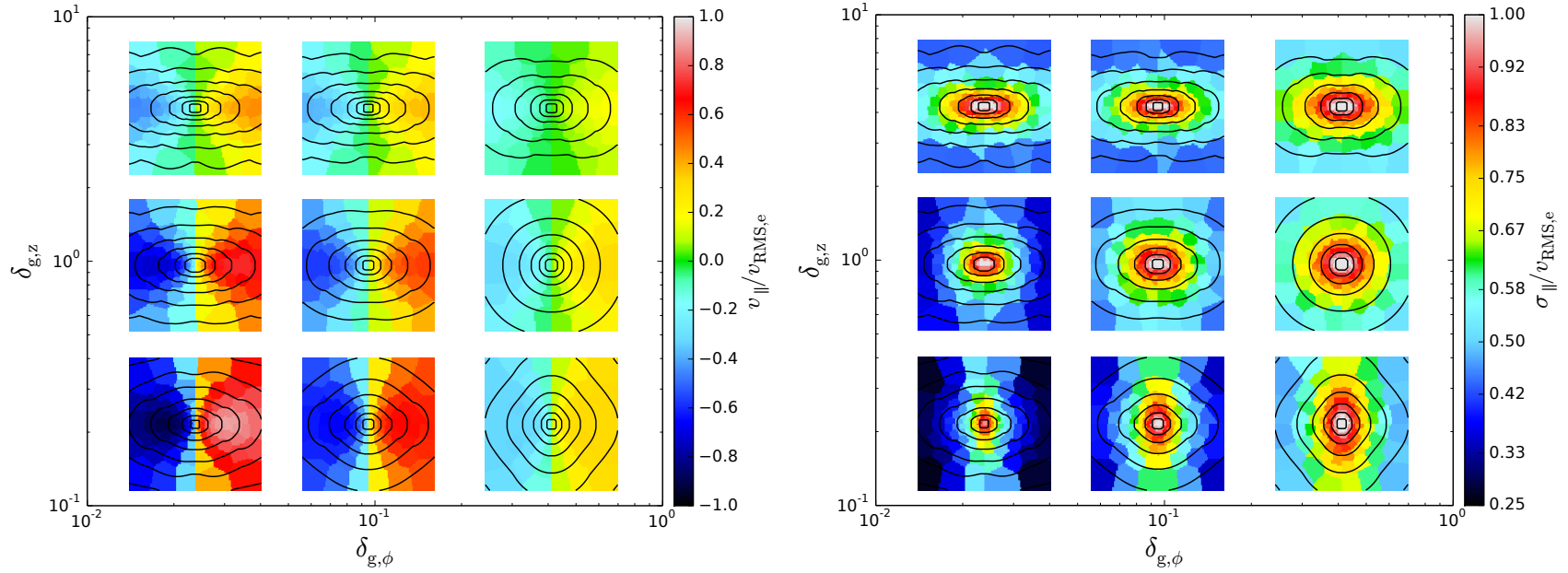
Figure 4.3: Mock observations of $f(\mathbf{J})$ models as in equations (4.1)-(4.3) with fixed $(A, B, \delta_{\mathrm{h},\phi}, \delta_{\mathrm{h},\mathrm{z}}, \chi, k) = (5/3, 5, 1/2, 1/2, 1, 1)$ and inclination of $90°$ (edge-in projection). The model's location on the plane is given by its $(\delta_{\mathrm{g},\phi}, \delta_{\mathrm{g},\mathrm{z}})$. Line-of-sight velocity (left) and velocity dispersion (right) Voronoi re-binned maps are shown with superposed isophotal contours equally spaced in logarithm. The velocity maps are normalized to $v_{\mathrm{RMS},\mathrm{e}}$, i.e., the light-averaged v_{RMS} within the effective radius. The colour maps extend from $-2R_{\mathrm{e}}$ to $+2R_{\mathrm{e}}$.

4.5 Applications

In this Section we present the comparison between the data and the models' observables. The stellar kinematics data for the three galaxies is from the CALIFA collaboration, the photometric data that we use to constrain the models' light distribution is from r-band SDSS images. We estimate the galaxies' inclination from the observed global isophotal ellipticity $\epsilon \equiv 1 - \sqrt{\langle y^2 \rangle / \langle x^2 \rangle}$ (see e.g., Emsellem et al., 2007) by assuming that the distribution of intrinsic axis ratio $q \equiv b/a$ for both fast and slow rotators is a Gaussian with mean and standard deviation $(\mu, \sigma) = (0.25, 0.14)$ for fast rotators and $(\mu, \sigma) = (0.63, 0.09)$ for slow rotators (see Weijmans et al., 2014). For oblate galaxies the inclination angle i w.r.t. the symmetry axis, the intrinsic axis ratio q and the observed ellipticity ϵ satisfy (e.g., Binney & Merrifield, 1998)

$$(1 - \epsilon)^2 = \cos^2 i + q^2 \sin^2 i. \tag{4.16}$$

With equation (4.16) it is possible to estimate the probability distribution of seeing a galaxy at a given inclination i, given the observed ellipticity and the distribution of intrinsic axis ratios for a large sample of fast and slow rotators (e.g., that of the ATLAS$^{\text{3D}}$sample in Weijmans et al., 2014). In Appendix C we show the resulting full probability distribution of inclinations for each galaxy. Here we are interested in the most probable values: $i \simeq 20°$ for NGC 6125, $i \simeq 40°$ for NGC 2592 and $i \simeq 70°$ for NGC 6427. For our models we assumed inclination values of, respectively, $i = 20°$, $i = 40°$ and $i = 90°$ (in the models for the lenticular galaxy NGC 6427 we explored edge-on projections in order to maximize the effect of flattening and rotation).

The general procedure that we use to find the best model candidate to represent each galaxy is the following:

(i) we assume a given inclination and, for simplicity, we use models that tend to be isotropic in the centre, i.e., $\delta_{\text{h},\phi} = \delta_{\text{h},z} = 1/2$,

(ii) we look for the best A and B parameters to represent the surface brightness profile,

(iii) we adjust the parameters $\delta_{\text{g},\phi}, \delta_{\text{g},z}$ to match the isophotes' flattening at large radii,

(iv) we set k and χ accordingly to the galaxy's rotation curve,

(v) we go back to step (iii) and adjust $\delta_{\text{g},\phi}, \delta_{\text{g},z}$ again to get the best match with the kinematic 2D maps and the isophotal shape.

We do not employ any automatic best-model finding scheme: the aim of this work is to show that models with a DF $f(\mathbf{J})$ are able to generate realistic observables that closely match galaxy observations. In a future work, we will set up an automatic best-fitting algorithm, but for the moment we decided to "hand-pick" models in the multi-dimensional parameter space using the steps described above. It has been possible to reach such a quality in matching the data because of the simple connections that exists among the model's parameters and observables (see Section 4.4.2).

The main limitation of the models here presented is the fact that they are a one-component bulge-like stellar distribution. However, most of the fast rotating ellipticals

show strong evidence of having two kinematically distinct stellar components: a bulge and a disc. A separate DF (likely of the form *quasi-isothermal*, e.g., Binney, 2012b) should be added to the DF (4.3) in order to improve the comparisons. In fact, Piffl, Penoyre, & Binney (2015) and Binney & Piffl (2015) already showed the ease with which stellar components can be added in a self-consistent fashion if one uses $f(\mathbf{J})$ DFs: this is because the functional form of the DF does not change as one adds components.

The best models' parameters can be found in Table 4.2.

4.5.1   Light distribution

Using SDSS r-band images, we derived the galaxies' surface-brightness profile via growth-curve analysis employing circular apertures (as in Lyubenova et al. in preparation). The background contamination is computed from a sample of pixels uniformly scattered over the whole image, for which the mode is estimated after clipping the high and low tails of the pixels' intensity distribution. After flux-calibration, we integrate the light coming from circular apertures centred on the brightest pixel and we stop integrating where the flat part of the growth curve is reached, which we consider the edge of the galaxy (typically at $\simeq 10R_e$). Figure 4.4 shows the agreement between the surface brightness distribution of the three galaxies with their respective best $f(\mathbf{J})$ models. The isophotal shape is matched to good accuracy, though by construction the models are not able to catch non axisymmetric features such as the position angle variations (isophotal twisting) in the inner $20 - 10$ arcsec for NGC 2592 and NGC 6427. NGC 6125's photometry, morphologically classified as E1, is unsurprisingly well matched by the $f(\mathbf{J})$ model: indeed, the normalized light profiles agree within 20% up to $\sim R_e$, though more flux seem to be present at larger radii in the observed profile (maybe due to some contamination, see residuals plot in Figure 4.4).

We are able to get a fairly realistic representation of the fast rotating E4 galaxy NGC 2592 in terms of both isophotal shape and light profile (within 20% up to $\sim R_e$). This is the best case to study how realistic Binney (2014) flattening scheme is: the quality of the agreement with our hand-picked model demonstrates the usefulness of such method. However, the disky isophotes of the fast rotating S0 galaxy NGC 6427 unsurprisingly pose an extreme challenge for two-power $f(\mathbf{J})$ DF: the lack of circular orbits for $R \gtrsim R_e$ in our models makes it difficult to reproduce the isophotes of a very flattened S0 galaxy. Nonetheless, we are still able to find a very good agreement between the surface-brightness profiles (within $30 - 40\%$ up to $\sim 3 - 4R_e$).

Table 4.2: Parameters of the best models. The set of DF parameters used to fully specify the models, as in equations (4.1)-(4.3); we also specify the inclination which we define as the angle between the line-of-sight w.r.t. the symmetry axis (in degrees, 0 is face-on, 90 is edge-on).

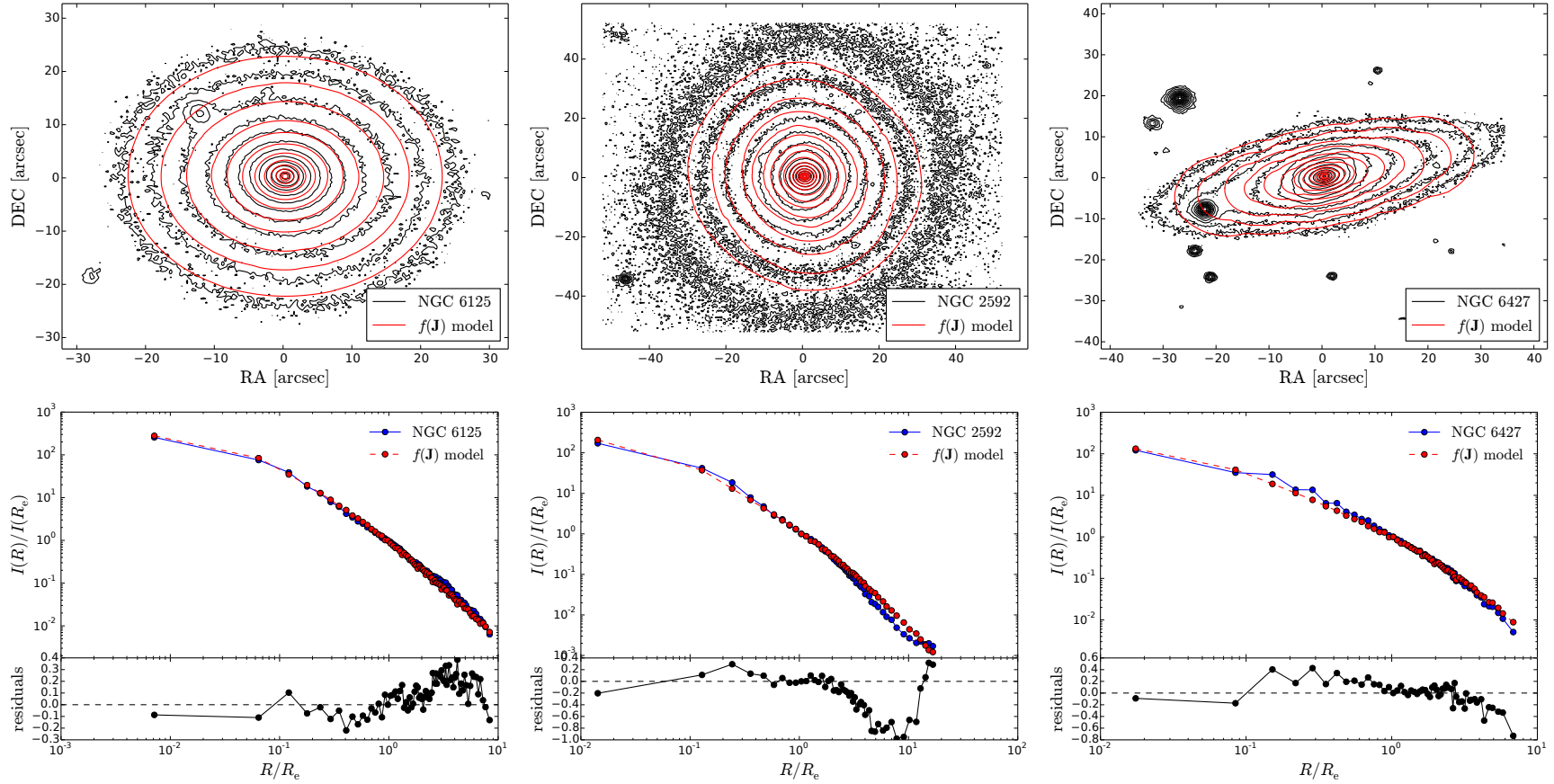| Model name	A	B	$\delta_{h,\phi}$	$\delta_{h,z}$	$\delta_{g,\phi}$	$\delta_{g,z}$	χ	k	$M_0/M_\odot$	r_0/kpc	inclination
			Dimensionless DF parameters						Scale parameters		Projection
$f(\mathbf{J})$ NGC 6125	9/5	11/2	1/2	1/2	1/2	1/2	4	4/5	2.14×10^9	9.48	20°
$f(\mathbf{J})$ NGC 2592	2	5	1/2	1/2	10^{-2}	1	1	1	2.57×10^7	0.5	40°
$f(\mathbf{J})$ NGC 6427	5/3	5	1/2	1/2	10^{-4}	1/2	1/2	1	1.53×10^8	0.34	90°

Figure 4.4: *Top row:* SDSS r-band surface-brightness contours for the three galaxies in the sample (from left to right, NGC 6125, NGC 2592 and NGC 6427, black lines) compared with that of the best $f(\mathbf{J})$ models (red lines). Both the data and the model's contours are spaced by 0.5 mag arcsec^{-2}. *Bottom row:* surface brightness profiles, normalized to the effective radius, for the three galaxies in the sample (blue solid line), compared to that of the best $f(\mathbf{J})$ models (red dashed line). Both profiles have been obtained performing a growth-curve analysis. We compute the residuals of the surface brightness profile as (data - model)/data. In all the panels we have convolved the models' surface brightness distribution with a Gaussian PSF with FWHM=1 arcsec.

4.5.2 Kinematics

The CALIFA collaboration's pipeline extracts first and second moment of the LOSVD from stellar absorption lines over a Voronoi re-binned grid. We use this information to compute $v_\parallel$ and $\sigma_\parallel$ for our models using the same re-binned grid. We estimate the galaxy's kinematic axis using the method of Krajnović et al. (2006) which efficiently computes the kinematic position angle[2]. Along the galaxy's major axis we extract $v_\parallel$ and we estimate the systemic velocity so to symmetrize the peaks of the velocity curve's approaching and receding sides. We compare the $v_\parallel$ and $\sigma_\parallel$ profiles along the major axis to that of the model: Figure 4.5 shows such comparison. When observing with a given spatial resolution, the system's rotation and velocity dispersion will be effectively averaged over a region larger than the actual spatial resolution because of beam smearing. This typically results in a smaller estimate of the velocity and a larger one of the velocity dispersion (see e.g., Epinat et al., 2010). To mimic such effect, we convolved our models' kinematic maps with a Gaussian Point Spread Function (PSF) having a Full Width at Half Maximum (FWHM) of $\simeq 2.7$ arcsec (see Garcia-Benito et al., 2015).

We scale the models' profile so to match $v_{\mathrm{RMS,e}}$. This match defines a scale of velocity v_u for the model. Together with the spatial scale R_u given by the match between the model's and galaxy's effective radius, we define the model's mass scale as

$$M_u = \frac{R_u v_u^2}{G}. \tag{4.17}$$

Figure 4.6 shows the comparison between the two-dimensional line-of-sight velocity and velocity dispersion maps, with also the residuals maps, for the three CALIFA galaxies and the corresponding best $f(\mathbf{J})$ models. For the sake of clarity, we plot the isophotes coming from a Multi Gaussian Expansion (MGE) over the observed maps, instead of the r-band SDSS contours. Our best models do a very good job at reproducing the galaxies' kinematics, with the largest errors on $v_\parallel$ and $\sigma_\parallel$ maps of the order of 50 km s^{-1}. The largest discrepancy here is due to some asymmetries in the galaxies' dispersion maps, e.g., the north-east bins of NGC 6125. Apart from these small non-axisymmetric deviations, it is safe to say that axisymmetric single-component action-based models can fit to good accuracy the kinematics of these galaxies.

---

[2]We acknowledge use of the routine `fit_kinematic_pa` in `http://www-astro.physics.ox.ac.uk/~mxc/software`.
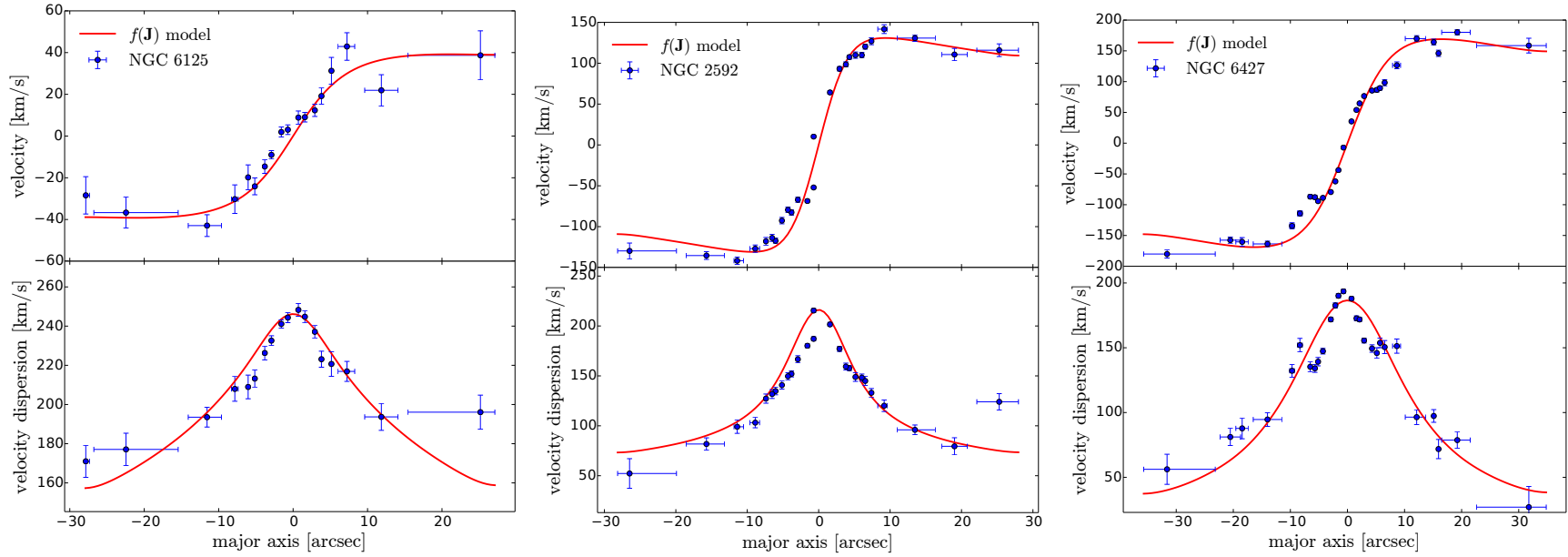
Figure 4.5: *Top row:* profiles of mean line-of-sight velocity along the major axis for the three galaxies in the sample (from left to right, NGC 6125, NGC 2592 and NGC 6427, red points) compared to that of the best $f(\mathbf{J})$ models (blue points). The models' profile are matched so that $v_{\mathrm{RMS,e}}$ is the same as that of the galaxies. *Bottom row:* same as the top row, but for the line-of-sight velocity dispersion. In deriving all the profiles for the models we have applied a correction that mimics the effect of the so-called *beam smearing* in the IFU observations, that is we have convolved the synthetic velocity maps with a Gaussian symmetric PSF having a FWHM$\simeq 2.7$ arcsec.
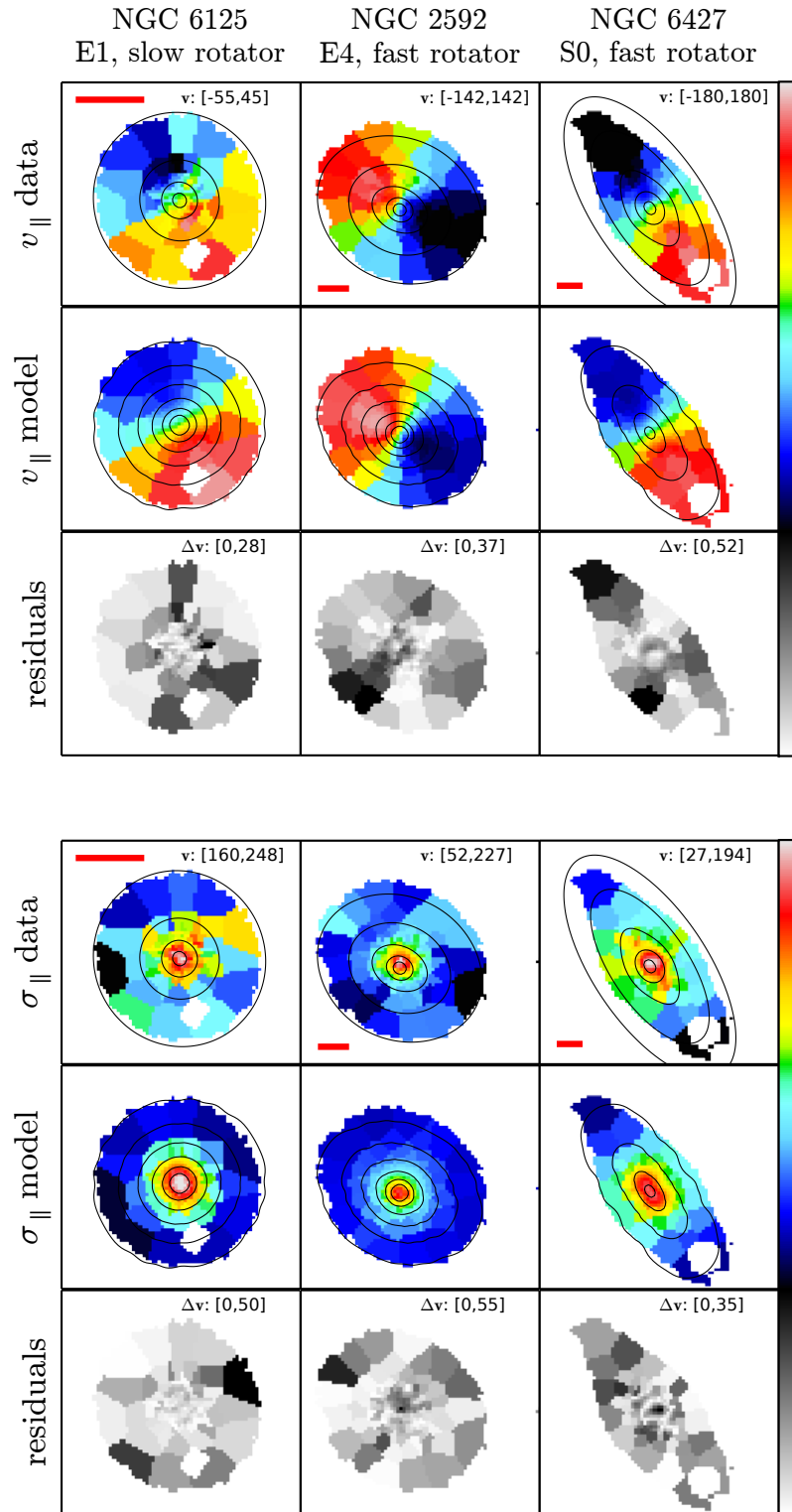
Figure 4.6: Kinematic comparison of galaxies and $f(\mathbf{J})$ models. The panels are arranged as follows: each column is for a given galaxy and the two nine-panels blocks refer to the maps of the line-of-sight velocity (top) and velocity dispersion (bottom). In each block, the top row shows the kinematic maps of the galaxies, with overplotted MGE contours of their surface brightness; the central row shows the kinematic maps of the models, with overplotted isophotal contours; while the bottom row shows the corresponding residuals maps. The red segment on the top row panels is of the same size of R_{e} of the galaxies. We use two color scales, one for the residuals maps (grey) and one for the $v_{\parallel}$ and $\sigma_{\parallel}$ maps (blue-red), with minimum and maximum values in km/s written for each galaxy.

Table 4.3: Results table. (i) $M_{f(\mathbf{J})}$ is the total mass of the $f(\mathbf{J})$ model. (ii) $\Upsilon_{\mathrm{r},f(\mathbf{J})}$ is the ratio between $M_{f(\mathbf{J})}$ and the total r-band luminosity of the galaxy computed from the absolute magnitudes in r-band (see Table 4.1) and assuming $\mathscr{M}_r^{\odot} = 4.64$ (see Blanton & Roweis, 2007). (iii) M_{vir} is the virial mass estimator as in equation (4.19). (iv) $\lambda_{\mathrm{Re},f(\mathbf{J})}$ is the angular momentum parameter (4.12) for the $f(\mathbf{J})$ models. (v) $(V/\sigma)_{f(\mathbf{J})}$ is equation (4.15) for the $f(\mathbf{J})$ models. (vi) $\lambda_{\mathrm{Re,obs}}$ is the same as (iv) but for the observed galaxies. (vii) $(V/\sigma)_{\mathrm{obs}}$ is the same as (v) but for the observed galaxies.

Galaxy Model	$M_{f(\mathbf{J})}$ $[M_{\odot}]$	$\Upsilon_{\mathrm{r},f(\mathbf{J})}$ $[(M/L_{\mathrm{r}})_{\odot}]$	M_{vir} $[M_{\odot}]$	$\lambda_{\mathrm{Re},f(\mathbf{J})}$	$(V/\sigma)_{f(\mathbf{J})}$	$\lambda_{\mathrm{Re,obs}}$	$(V/\sigma)_{\mathrm{obs}}$
$f(\mathbf{J})$ NGC 6125	3.5×10^{11}	3.7	4×10^{11}	0.09	0.09	0.1	0.09
$f(\mathbf{J})$ NGC 2592	6×10^{10}	4.3	5.6×10^{10}	0.4	0.37	0.43	0.43
$f(\mathbf{J})$ NGC 6427	1.1×10^{11}	4.34	6.5×10^{10}	0.43	0.42	0.37	0.36

4.5.3 Models' intrinsics

4.5.3.a Mass

The spherically-averaged total dynamical mass profiles that we infer for the three galaxies in our sample are shown in Figure 4.7. Under the assumption of mass-follows-light models, we can compute the model galaxy's mass profile up to about ten effective radii, where the relative mass increase begins to be negligible as a function of radius. We compare with total stellar mass estimates by González Delgado et al. (2015) for which the entire wavelength range observed by the CALIFA collaboration is used ($3650 - 7300$Å). Our estimated total mass is always significantly larger than the stellar mass of about a factor $1.5 - 2$, meaning that the contribution of dark matter to the total mass is non-negligible. This is a robust result of our work since the errors in the stellar masses estimated by González Delgado et al. (2015) take into account several unknowns typical of stellar population analysis, for instance the stellar Initial Mass Function.

The mass, size and velocity dispersion of a virialized galaxy are related by the Scalar Virial Theorem (SVT) as

$$M = K \frac{R_{\mathrm{e}} \sigma_{\mathrm{e}}^2}{G}. \tag{4.18}$$

Here K is a structural parameter which is generally different from galaxy to galaxy. A simple estimate of the total mass of a galaxy can be obtained with some assumptions on the parameter K: the most simple and common choice is to set a constant $K = 5$ for all galaxies (see e.g., Cappellari et al., 2013), but other choices are possible (see e.g., Peralta de Arriba et al., 2014). We shall therefore use the following definition for the virial mass estimator:

$$M_{\mathrm{vir}} = 5 \frac{R_{\mathrm{e}} \sigma_{\mathrm{e}}^2}{G}. \tag{4.19}$$

We find that the total masses of our model galaxies are very similar to those computed with such a virial estimator: indeed they are all within a factor ~ 1.7 from the corresponding M_{vir}.

We also compare our mass estimates with those obtained with orbit-based two-component (dark matter + stars) Schwarzschild (1979) models for the same objects (see Zhu et al. in preparation). These models give excellent fits to the galaxies' kinematics and the total dynamical mass within the effective radius is in very good agreement with our estimate based on $f(\mathbf{J})$ models (the worst case is the S0 galaxy, NGC 6427, for which the masses agree within 50%).
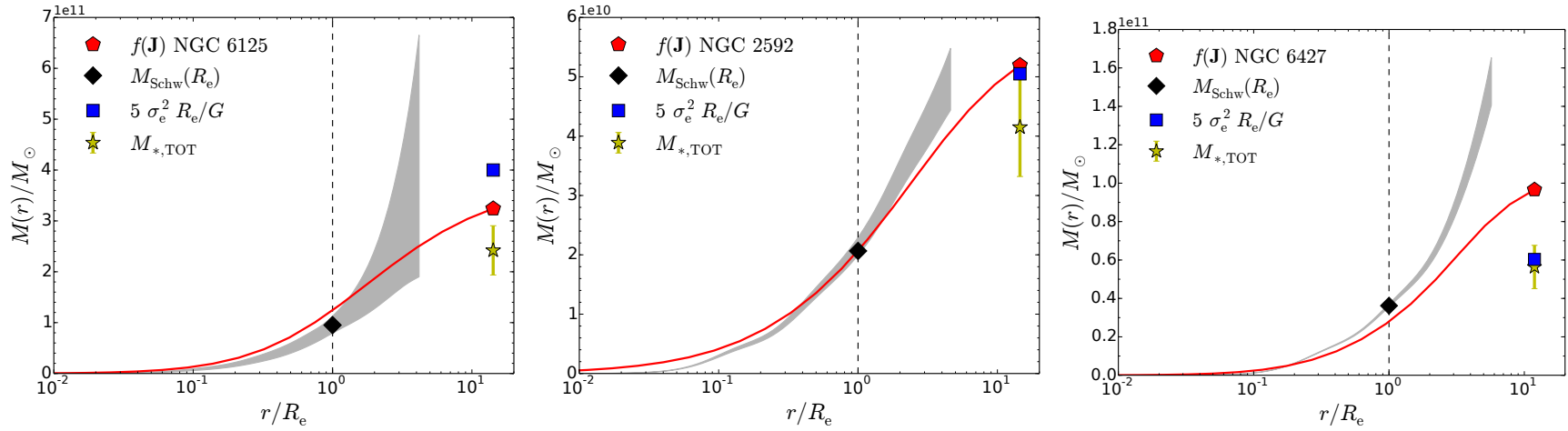
Figure 4.7: Total mass of the best $f(\mathbf{J})$ models for the three galaxies as a function of radius in units of the models' effective radii. The red solid line shows the mass enclosed within the spherical radius r of the three galaxies, the black diamond is the mass enclosed within R_e estimated with Schwarzschild (1979) models and the grey band is the corresponding mass profile with 1-σ error, the yellow star is the total stellar mass given by the SED fitting with errorbars accounting for differences in the stellar population analysis (including stellar Initial Mass Function variations, see González Delgado et al., 2015), the blue square is the virial estimate (4.19) of the total mass.
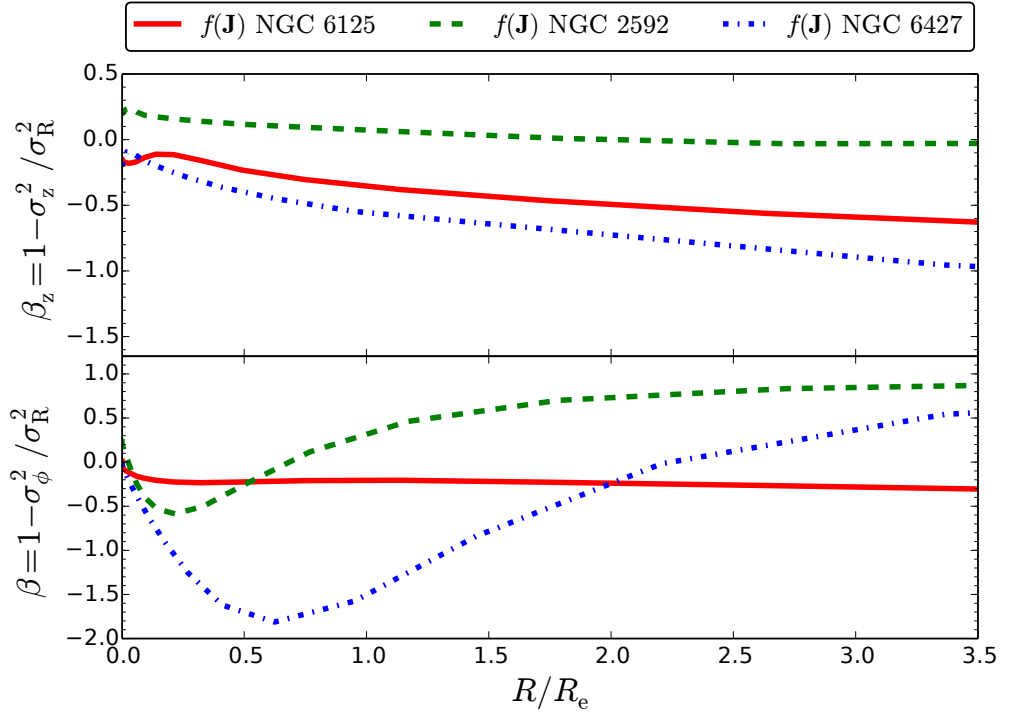
Figure 4.8: Vertical, $\beta_{\mathrm{z}} = 1 - \sigma_{\mathrm{z}}^2/\sigma_{\mathrm{R}}^2$, and tangential, $\beta = 1 - \sigma_\phi^2/\sigma_{\mathrm{R}}^2$, anisotropy parameters in the equatorial plane, as a function of the cylindrical radius for the models described in Table 4.2.

4.5.3.b Anisotropy

Figure 4.8 shows the profiles of the anisotropy parameter on the equatorial plane of the three best $f(\mathbf{J})$ models. We adopt two definitions of the anisotropy in our axisymmetric models: the ratio between tangential and radial dispersion $\beta = 1 - \sigma_\phi^2/\sigma_{\mathrm{R}}^2$ and the ratio between vertical and cylindrical radial dispersion $\beta_{\mathrm{z}} = 1 - \sigma_{\mathrm{z}}^2/\sigma_{\mathrm{R}}^2$. Close to the centre, all the models tend to isotropy, except for $f(\mathbf{J})$ NGC 2592 which has some mild radial bias. In this model, the vertical pressure is always small compared to the radial, while at radii of the order of the effective radius there is significant azimuthal pressure which tangentially biases the model's orbital distribution (within $R_{\mathrm{e}}/2$) and contributes to the model's rotation. At large radii the vertical pressure starts dominating significantly over the radial pressure the models $f(\mathbf{J})$ NGC 6125 (up to $\beta_{\mathrm{z}} \sim -0.5$) and $f(\mathbf{J})$ NGC 6427 (up to $\beta_{\mathrm{z}} \sim -1$). Similarly, the model with the most pronounced rotational support, i.e., $f(\mathbf{J})$ NGC 6427, has significant azimuthal bias out to about $2R_{\mathrm{e}}$. The models of the two fast rotating galaxies have a sharp decline in σ_ϕ w.r.t. σ_{r} for $r > R_{\mathrm{e}}$, since almost all the motion in the azimuthal direction gets ordered by the effect of the parameters k and χ (see Section 4.4.2). For the model of the slow rotator the azimuthal dispersion always slightly dominates over the radial, but almost never over the vertical. In Appendix B we show the velocity ellipsoids of the best $f(\mathbf{J})$ models in Table 4.2.

4.6   Summary and Conclusions

We have generated self-consistent axisymmetric and rotating models with DFs depending on the action integrals for three early-type galaxies in the CALIFA Survey. We have modeled three galaxies different in morphology (E1, E4 and S0) and in kinematics (both slow and fast rotators) so to prove the flexibility of the $f(\mathbf{J})$ family of models. We match the observed light distribution (in r-band) and spatially-resolved kinematics (up to $\sim 2 - 3R_{\mathrm{e}}$) with a typical mismatch of $10 - 20\%$. With the ansatz that the mass-to-light ratio is constant with radius, we derive intrinsic properties for the three galaxies such as total mass distribution and anisotropy. Our estimates of the dynamical mass enclosed within the effective radius are in agreement with orbit-based discrete models for the same galaxies and both yield mass-to-light ratios of about $\Upsilon_{\mathrm{r}} \sim 4$. Our galaxy models are, by construction, isotropic close to the centre and their rotation is supported by a substantial tangential bias in their orbital distribution further out. For the purpose of showing the potential of modeling stellar systems with action-based DFs, we did not go through a quest for the best model in our multi-dimensional parameter space, but instead we showed how easy it is to get reasonable fits by understanding which parameter has the major effects on which observable. In this sense, the models that we addressed as "best models" should be intended as locating a neighbourhood in the parameter space on which a proper systematic search of the best-fitting model must be run if one wants an accurate characterization of the galaxies.

This study sets as a benchmark for distribution function models of external galaxies and shows how closely one could match observables with one-component models. Unsurprisingly, we find a very different quality in the fits for the round E1 and for the lenticular S0 since, by construction, the models presented here do not contain a stellar disc. Such an addition is prompt and easy in the $f(\mathbf{J})$ formalism, as several works have already proved (see Piffl, Penoyre, & Binney, 2015; Binney & Piffl, 2015). Even though the match to the spatially-resolved kinematics of the S0 galaxy NGC 6427 is remarkable considering that the best model is a flattened rotating bulge, adding a quasi-isothermal DF (see Binney, 2010) to that of $f(\mathbf{J})$ NGC 6427 will lead to better fits of especially the light distribution. The only issue is that one has to perform a clever and systematic search through a parameter space which has several additional dimensions with the one considered in this work (e.g., as done by Binney & Piffl, 2015). More realistic models of galaxies should allow also for a general dark matter distribution, which should be as well modeled as an independent $f(\mathbf{J})$ component (see Chapter 3 and Piffl, Penoyre, & Binney, 2015). This will allow for a self-consistent characterization of the galaxy's dark halo and provide an independent test for the estimates of mass-to-light ratios within R_{e} obtained with orbit-based discrete models and with moment based models (see Cappellari et al., 2006, 2013). We hope to report soon on such an extension of the present application.

A great advantage of generating dynamical models by specifying the DF is that the full LOSVD can be modeled, instead of fitting just its first and second moments. In the context of local early-types whose stellar kinematics is traced by Integral Field spectroscopy, the data quality is typically not high enough to give significant constraints on further moments of the LOSVD and often just the first two are used (e.g., Cappellari

et al., 2013). Hence, in this work we did not exploit the power of equation (4.10) and we adopted a similar approach to that of Cappellari et al. (2006, 2013), i.e., fitting $v_\parallel$ and $\sigma_\parallel$ maps. However, three-integral $f(\mathbf{J})$ DFs would be very useful for instance for recovering masses of supermassive black holes at the centres of massive galaxies, where very high resolution spectra give considerable constraints on the non-Gaussianity of the lines. In that context, $f(\mathbf{J})$ models are handy since (i) the system's total mass can be specified at the outset (see Chapter 3), (ii) the addition of an external source of gravity at the centre (e.g., a black hole) does not alter the functional form of the DF. On the contrary, DFs depending on energy and angular momentum are modified by the addition of external potentials (e.g., van der Marel et al., 1994).

A sensible step forward in the present work will be generating a synthetic data-cube which accounts for the LOSVD of the model at each location on the sky. An effect that is still poorly understood in the context of stellar kinematics with Integral Field units is the beam smearing. $f(\mathbf{J})$ models can be used to study what is the contribution to the line's broadening (and shift) coming from stars orbiting nearby and falling within the PSF at a given location on the sky. If not properly taken into account, one could mis-interpret very broadened lines as due to a large stellar velocity dispersion, without considering the contribution from stars at different speeds within the same aperture. This could be critical especially for low spatial resolution (see e.g., Epinat et al., 2010).

DF models are a valid alternative to the more popular Schwarzschild (1979), made-to-measure (M2M, Syer & Tremaine, 1996) and JAM (Cappellari, 2008) models since they are self-consistent and allow for general anisotropy, unlike JAM, and they are continuous and characterized by only a handful of free parameters, unlike Schwarzschild or M2M. The field of investigating the dynamics of galaxies by specifying a mathematical form for the DF is now rejuvenated by the use of action integrals as arguments for the DF. This work adds nearby early-type galaxies to the list of systems that can be potentially modeled with great accuracy with $f(\mathbf{J})$ DFs.

Chapter 5

Dynamical evolution of early-type galaxies and their haloes

Abstract

Early-type galaxies (ETGs) are observed to be more compact, on average, at $z \gtrsim 2$ than at $z \simeq 0$, at fixed stellar mass. Recent observational works suggest that such size evolution could reflect the similar evolution of the host dark matter halo density as a function of the time of galaxy quenching. We explore this hypothesis by studying the distribution of halo central velocity dispersion (σ_0) and half-mass radius (r_h) as functions of halo mass M and redshift z, in a cosmological Λ-CDM N-body simulation. In the range $0 \lesssim z \lesssim 2.5$, we find $\sigma_0 \propto M^{0.31-0.37}$ and $r_\mathrm{h} \propto M^{0.28-0.32}$, close to the values expected for homologous virialized systems. At fixed M in the range $10^{11} M_\odot \lesssim M \lesssim 5.5 \times 10^{14} M_\odot$ we find $\sigma_0 \propto (1+z)^{0.35}$ and $r_\mathrm{h} \propto (1+z)^{-0.7}$. We show that such evolution of the halo scaling laws is driven by individual haloes growing in mass following the evolutionary tracks $\sigma_0 \propto M^{0.2}$ and $r_\mathrm{h} \propto M^{0.6}$, consistent with simple dissipationless merging models in which the encounter orbital energy is accounted for. We compare the N-body data with ETGs observed at $0 \lesssim z \lesssim 3$ by populating the haloes with a stellar component under simple but justified assumptions: the resulting galaxies evolve consistently with the observed ETGs up to $z \simeq 2$, but the model has difficulty reproducing the fast evolution observed at $z \gtrsim 2$. We conclude that a substantial fraction of the size evolution of ETGs can be ascribed to a systematic dependence on redshift of the dark matter haloes structural properties.

5.1   Introduction

Since early studies in the '70s, we know that early-type galaxies (ETGs) adhere to some empirical scaling relations, such as the luminosity-velocity dispersion (Faber & Jackson, 1976), size-surface brightness (Kormendy, 1977), Fundamental Plane (Djorgovski & Davis, 1987; Dressler et al., 1987), black-hole mass-bulge mass (Magorrian et al., 1998), black-hole mass-velocity dispersion (Ferrarese & Merritt, 2000; Gebhardt et al., 2000) and black-hole mass-Sérsic index (Graham et al., 2001; Graham & Driver, 2007) relations. Such correlations, some of which were first used as distance estimators to help building the distance scale ladder, have given the astrophysical community important clues about the possible scenarios of galaxy formation (e.g., Ciotti, 2009). In this respect, the stellar mass-size relation has currently a special role, because galaxy sizes and masses can be measured out to $z \simeq 2.5 - 3$. With such data available, different authors found indications that the population of ETGs undergoes a significant size evolution from $z \simeq 3$ to $z \simeq 0$, such that present-day galaxies have, on average, significantly larger sizes than higher z galaxies of similar stellar mass (see e.g., Stiavelli et al., 1999; Ferguson et al., 2004; Daddi et al., 2005; Trujillo et al., 2006; Cimatti et al., 2008; van der Wel et al., 2008; van Dokkum et al., 2008; Saracco, Longhetti, & Andreon, 2009; Cassata et al., 2011; Damjanov et al., 2011; Krogager et al., 2013). For the current galaxy formation models it is still challenging and non-trivial to explain such behaviour of massive ETGs. Various mechanisms have been proposed to explain the observed size evolution, including dry (i.e., dissipationless) major and minor merging (see Khochfar & Silk, 2006; Nipoti et al., 2009b; Naab, Johansson, & Ostriker, 2009; Hopkins et al., 2009b; López-Sanjuan et al., 2012; Laporte et al., 2013; Sonnenfeld, Nipoti, & Treu, 2013) and feedback-driven expansion (see e.g., Fan et al., 2008, 2010; Ragone-Figueroa & Granato, 2011; Ishibashi, Fabian, & Canning, 2013). Currently, the issue is far from being resolved and further observations, together with more comprehensive theoretical models, are desirable.

Recently, Carollo et al. (2013, see also Poggianti et al. 2013) argued that the median size growth of ETGs of stellar mass $10^{10.5} M_{\odot} \leq M_* \leq 10^{11} M_{\odot}$ could be due to the dilution of the sample of galaxies quenched at early times in a population of bluer and larger galaxies that have been quenched much later. In the sample of ETGs with $M_* > 10^{11} M_{\odot}$ the same authors find indications of intrinsic size evolution, which can not be explained with the dilution of the population. In other words, Carollo et al. (2013) find evidence that not all the progenitors of local quenched-ETGs can be identified with the compact quiescent ETGs observed at $z \simeq 1 - 2$, because a substantial fraction of present-day ETGs have stopped forming stars much later than the higher-z ETGs. An interesting conclusion of Carollo et al. (2013) is that the stellar density of ETGs scales with the mean density of the Universe *at the time of quenching*. This suggests that the host halo evolution could be the main driver of the galaxy evolution, in the sense that the redshift-dependence of the properties of an ETG results similar to that of its host halo (see also Stringer et al., 2014).

The natural tool to explore such halo-galaxy connection would be a large-scale, high-resolution, cosmological simulation jointly following the evolution of dark matter (hereafter DM) and baryons, including star formation and feedback. However, given

the well known uncertainties and technical issues still present in this method (see e.g., Kereš et al., 2012; Vogelsberger et al., 2012; Hopkins, Narayanan, & Murray, 2013), we adopt here a simpler approach, trying to extract useful information on the evolution of ETGs studying the behaviour of a population of DM haloes in a DM-only cosmological simulation. We focus our attention on the scaling laws of DM haloes in a Λ-CDM Universe and in particular on their size and velocity dispersion evolution. Our aim is trying to understand whether the evolution of the haloes is somehow similar to that of ETGs which are expected to be hosted in such haloes. Therefore, we will also try to compare our N-body data with available observations of ETGs, populating haloes with galaxies under simple but justified assumptions.

This Chapter is organized as follows: in Section 5.2 we present the methods of our investigation and we set the stage with all the definitions and simple theoretical expectations; in Section 5.3 we show our results on the scaling relations of the dark-halo population; in Section 5.4 we trace the merger histories of individual haloes which are representative for the entire population; in Section 5.5 we link the dark-halo properties with those of the ETGs and compare the predicted size and velocity dispersion evolution with recent observations; Section 5.6 summarizes and concludes.

5.2 Methods and definitions

5.2.1 Computational tools

We performed a cosmological N-body simulation with the publicly available code GADGET-2 (Springel, 2005, see also Springel, Yoshida, & White 2001) in a standard Λ-CDM flat Universe where the matter density, dark-energy density and Hubble constant are, respectively, $\Omega_{0,m} = 0.28$, $\Omega_{0,\Lambda} = 0.72$ and $H_0 = 70\,\mathrm{km\,s^{-1}\,Mpc^{-1}}$. In the run we simulated the evolution of $512^3 \simeq 1.3 \times 10^8$ particles of mass $M_{\mathrm{part}} \simeq 1.5 \times 10^9 M_\odot/h$, from $z = 99$ to $z = 0$, in a cosmological comoving box of side $l = 128\,\mathrm{Mpc}/h$, where h is the reduced Hubble constant $h = H_0/100\,\mathrm{km\,s^{-1}\,Mpc^{-1}}$. The initial conditions of the simulation were generated using a modified version of the publicly available code GRAFIC2 (see Bertschinger, 2001). We used a softening length of $\sim 1\,\mathrm{kpc}/h$ throughout the simulation. The simulation was run on 72 cores on the UDF Linux cluster at STScI (Baltimore) and took about 6 days to complete. We produced 16 snapshots equally spaced in $\log a$, where $a(t) = (1 + z)^{-1}$ is the cosmic scale factor, from $z \simeq 2.5$ to $z = 0$.

5.2.2 Definitions of the structural and kinematical properties of dark matter haloes

In this Section we define the fundamental structural and kinematical properties of the simulated DM haloes, such as the mass M, the size r and the velocity dispersion σ. There is not a unique method to identify a DM halo in a cosmological N-body simulation, because, as for every non-truncated and non-isolated particle system, it is not trivial to define the set of particles that belong to the object: various techniques have been proposed in the astrophysical literature (e.g., friends-of-friends or spherical overdensity

algorithms[1]; see Efstathiou et al., 1985; Davis et al., 1985; Lacey & Cole, 1993; Evrard et al., 2008). The problem is relevant, because different sets of particles can lead to different estimates of the properties of the object.

In this work, we adopted the conventions of Knollmann & Knebe (2009) and we have used their AHF finding code. The haloes are identified from the peaks of a three dimensional density field calculated in a grid with Adaptive Mesh Refinement (AMR). The spherical region of radius r_Δ, which is centred at the centre of mass of the particles in the highest refinement level of the AMR grid, defines the set of particles that belong to the DM halo[2] (see Knollmann & Knebe, 2009). We use a standard definition of a halo as a certain spherical top-hat overdensity, via the formula

$$\frac{3M}{4\pi r_\Delta^3} = \Delta_c(z)\rho_c(z), \tag{5.1}$$

where $\rho_c(z) = 3H^2(z)/8\pi G$ is the critical density of the Universe at redshift z, $\Delta_c(z)$ is the overdensity value at the same time, $H(z)$ is the Hubble parameter and G is the gravitational constant. We adopt the following definition of the critical overdensity in a flat Universe with negligible radiation energy density:

$$\Delta_c(z) = 18\pi^2 + 82\left[\Omega(z) - 1\right] - 39\left[\Omega(z) - 1\right]^2, \tag{5.2}$$

where $\Omega(z) = \Omega_{0,m}(1+z)^3/E(z)^2$ and $E(z)^2 = \Omega_{0,m}(1+z)^3 + \Omega_{0,\Lambda}$, such that the haloes identified are expected to be close to equilibrium (see Lacey & Cole, 1993; Bryan & Norman, 1998).

Given the velocities of all particles belonging to the halo, we compute the *virial velocity dispersion* of the system

$$\sigma_V = \left[\sum_{i=1}^{N}\sum_{j=1}^{3}\frac{(v_{i,j} - \bar{v}_j)^2}{N}\right]^{1/2}, \tag{5.3}$$

where N is the number of particles in the halo, $v_{i,j}$ is the j-th component of the i-th particle's velocity and $\bar{v}_j$ is the j-th component of the average velocity.

The definition of the halo size is also non-trivial, since it is intimately affected by the choice of the spherical overdensity. As a matter of fact the definition of r_Δ via equation (5.1) is based on the idea that the material surrounding the overdensity is bound to the halo if the dynamical time of the particle is less than the Hubble time at that redshift, so one can reasonably expect the halo of size r_Δ to be in equilibrium. For this reason, r_Δ is often, but improperly, called *virial radius* and, in any case, in the following we will adopt such convention. However, other definitions of the halo size are possible: for example, the gravitational radius (i.e., the true virial radius)

$$r_g \equiv \frac{GM}{\sigma_V^2} \tag{5.4}$$

---

[1] For a brief review of different methods see Knebe et al. (2011).
[2] An *unbinding procedure* is also run on the haloes in order to remove the gravitationally unbound particles inside the spherical region (see Knollmann & Knebe, 2009).

and the half-mass radius $r_{\rm h}$, i.e., the radius of the sphere enclosing half the total mass of the halo, $M(< r_{\rm h}) = M/2$.

We also employ a definition of the halo velocity dispersion alternative to $\sigma_{\rm V}$: we compute the velocity dispersion profile $\sigma(< r)$ in the same fashion as the mass profile, where the velocity dispersion is calculated as in equation (5.3) and the sum is only on the particles within the spherical region of radius r. From the $\sigma(< r)$ profile, we then estimate the *central velocity dispersion*

$$\sigma_0 \equiv \sigma\left(< r_{\rm h}\right). \tag{5.5}$$

We define our sample of DM haloes by selecting those for which $r_{\rm h} > 2r_{\rm conv}$, where $r_{\rm conv}$ is the convergence radius in the sense of Power et al. (2003), i.e., the radius within which the two-body collisions dominate the orbital motions of the particles integrated by the code and the density estimates are therefore unreliable. We verified that, for our sample, the mass contained within the convergence radius is typically a small fraction of that contained within the half-mass radius, so our measurement of σ_0 should be robust. The sample selected with the above criterion is made of ≈ 11000 DM haloes, with a lower limit in mass $M_{\rm lower} \simeq 1.3 \times 10^{11} M_\odot$.

5.2.3 Behaviour of the different size and velocity dispersion proxies

In this section we discuss the relations between different size and velocity dispersion estimators, in particular how the *virial* proxies (r_Δ, $\sigma_{\rm V}$) compare to the *central* ones ($r_{\rm h}$, σ_0).

In this work we use σ_0 and $r_{\rm h}$ (see Section 5.2.2) to characterize the haloes because it is reasonable to expect that the stellar central velocity dispersion σ_* and the effective radius $R_{\rm e}$ of the galaxies inside such haloes are more related to the halo central quantities than to the halo virial quantities. However, different choices would be possible. For instance, a tight correlation between r_Δ and $R_{\rm e}$ has been suggested, both theoretically (see Mo, Mao, & White, 1998) and using abundance matching techniques (see Kravtsov, 2013). In addition, it is well known that the ratio $r_{\rm g}/r_{\rm h}$ depends only weakly on the density profile (see Binney & Tremaine, 2008; Ciotti, 1991; Nipoti, Londrillo, & Ciotti, 2003). It is therefore interesting to verify how the different proxies correlate in our sample of haloes and how their values depend on the choice of the critical overdensity $\Delta_{\rm c}$.

In Fig. 5.1 we show the dependence of r_Δ, $r_{\rm g}$ and $r_{\rm h}$ on $\Delta_{\rm c}$ at $z = 0$ for a representative halo with $M \simeq 10^{13} M_\odot$. As expected from equation (5.1), the virial radius has a perfect $r_\Delta \propto \Delta_{\rm c}^{-1/3}$ scaling. We note that also the gravitational radius scales roughly as $r_{\rm g} \propto \Delta_{\rm c}^{-1/3}$ and this is because it depends only on virial quantities (see equation 5.4), while the half-mass radius has slightly less steep dependence on $\Delta_{\rm c}$, namely $r_{\rm h} \propto \Delta_{\rm c}^{-0.22}$. This is an additional reason to prefer $r_{\rm h}$ to r_Δ in the present context. Formally, also the quantity $\sigma_{\rm V}$, and so σ_0, depends on $\Delta_{\rm c}$, but the dependence is weak: the variation is no more than 10% in $\sigma_{\rm V}$, when varying $\Delta_{\rm c}$ by an order of magnitude.
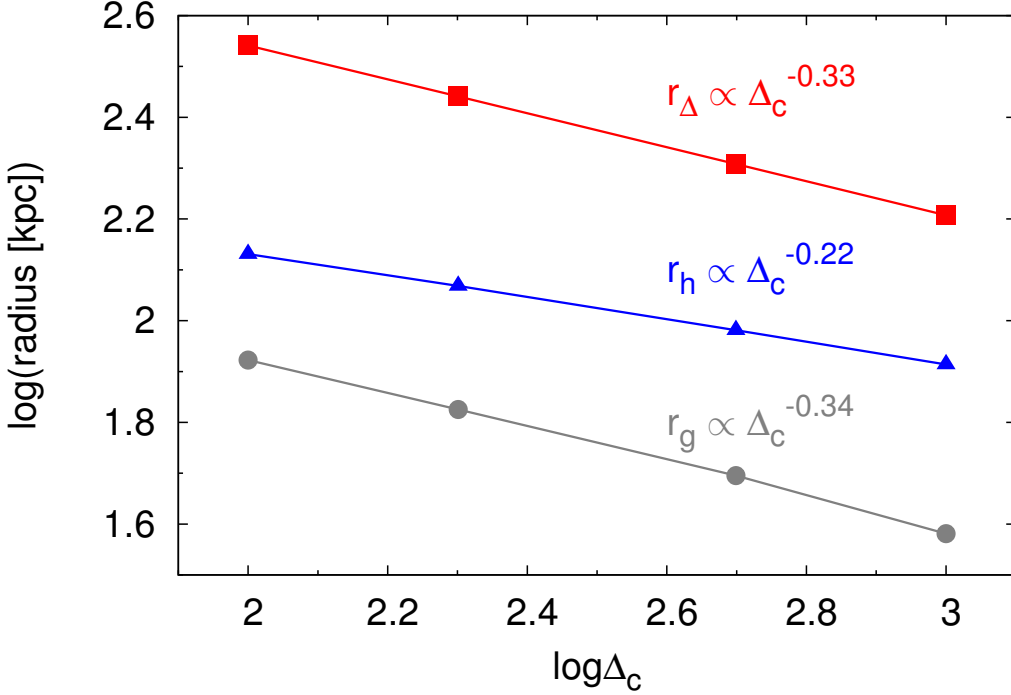
Figure 5.1: Virial radius (red squares, see equation 5.1), gravitational radius (gray circles, see equation 5.4) and half-mass radius (blue triangles) as functions of the critical overdensity Δ_c for a $M \simeq 10^{13} M_\odot$ halo, taken from the $z = 0$ snapshot of the simulation.

In Fig. 5.2 we show the distributions of the halo population at $z = 0$ in the $\sigma_0 - \sigma_V$, $r_h - r_\Delta$ and $r_g - r_\Delta$ planes. We find that in all cases a linear correlation is in good agreement with the distribution of the haloes in the three planes; fitting with power laws we get $\sigma_0 \propto \sigma_V^{0.97\pm0.01}$, $r_h \propto r_\Delta^{0.96\pm0.01}$ and $r_g \propto r_\Delta^{1.1\pm0.01}$. Interestingly, for a given halo, the ratio σ_0/σ_V is very close to unity: the average ratio in our sample is $\langle\sigma_0/\sigma_V\rangle = 1.01$. We recall that it is not a priori expected that the central quantities correlate linearly with the virial ones. This finding indicates that the DM haloes are not systematically non-homologous: in other words, more massive haloes are, on average, just rescaled versions of less massive haloes (at least, as far as the relation between virial and central quantities is concerned). The scatter around the linear relations in Fig. 5.2 can be ascribed to some degree of non-homology at a given halo mass or to the fact that some haloes are not completely virialized. We note also that Diemer, Kravtsov, & More (2013) recently found that there is a remarkable homology in their cluster-sized haloes sample: they argued that a tight relation exists between the mass and velocity dispersion profiles of DM haloes. Moreover, they claimed that the mass-velocity dispersion relation of the halo sample is almost insensitive to the size definition (in the range $100 < \Delta_c < 2500$ in equation 5.1) because of such homology in the radial profiles.

For the purposes of this work, given that, on average, the central quantities (σ_0, r_h) scale linearly with the virial quantities (σ_V, r_Δ), our results would be virtually unchanged if we adopted σ_V, instead of σ_0, and r_Δ or r_g, instead of r_h, to characterize our haloes.
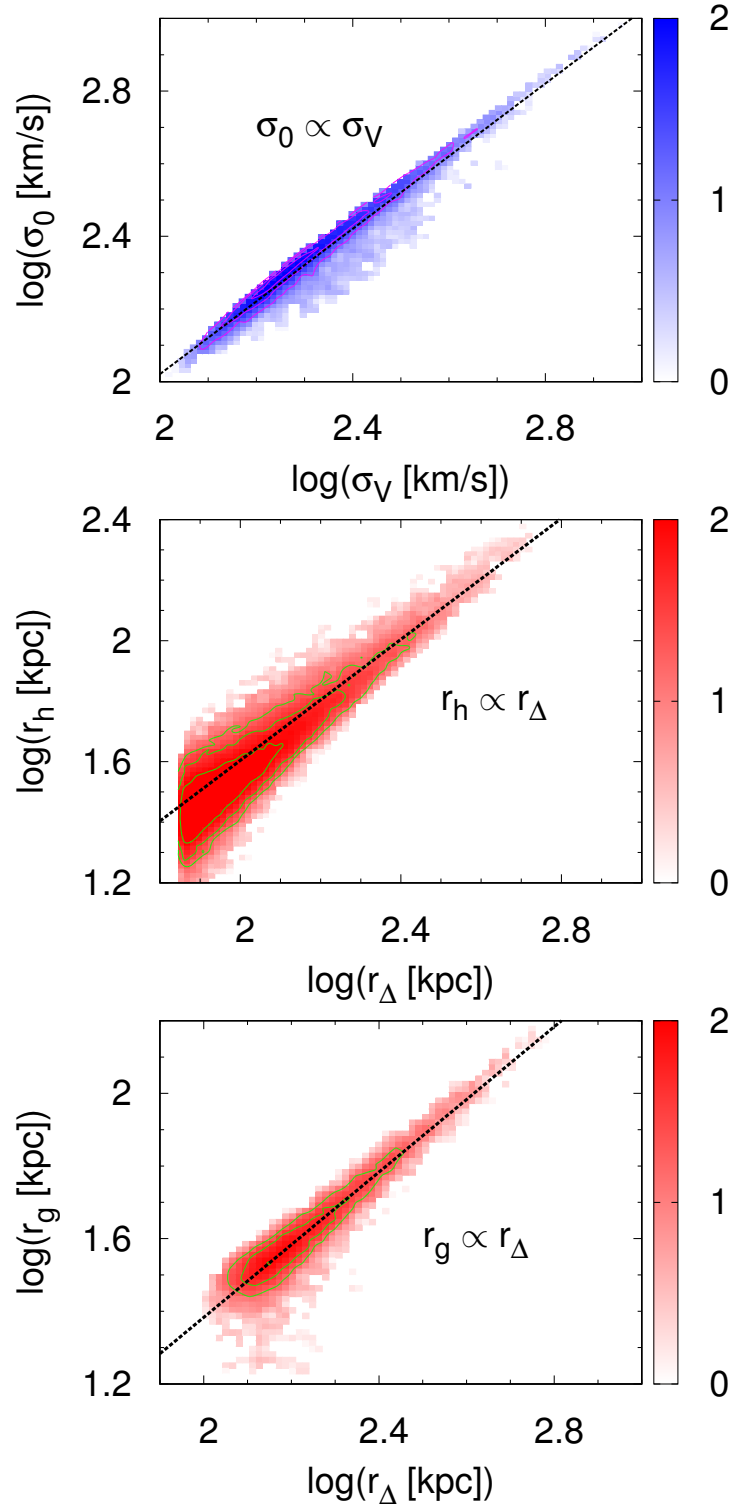
Figure 5.2: Distributions of the simulated haloes at $z = 0$ in the $\sigma_0 - \sigma_V$ (left-hand panel), $r_h - r_\Delta$ (central panel) and $r_g - r_\Delta$ (right-hand panel) planes. In each panel, the black short-dashed line is the *linear* best-fit to the distribution.

5.2.4 Virial expectations for the halo mass-velocity dispersion and mass-size relations

With the adopted halo definition (equation 5.2) we expect the DM haloes to be virialized in every snapshot of the simulation from $z \simeq 2.5$ to $z \simeq 0$. It follows that, some well known scaling laws are expected for the dark-halo population: from equation (5.4), under the assumption of a linear proportionality between the virial radius (equation 5.1) and the gravitational radius (equation 5.4) it follows (e.g., Lanzoni et al., 2004) that for haloes in equilibrium

$$M \propto \sigma_V^3. \tag{5.6}$$

The correlation is expected to depend on redshift as

$$\sigma_V \propto [E(z)\,M]^{1/3} \tag{5.7}$$

(see e.g., Evrard et al., 2008). Using equation (5.1) to define the haloes and the definition of the critical density $\rho_c = 3H^2/8\pi G$, for a flat Universe we get

$$r_\Delta = \left[2GM\,\Delta_c(z)^{-1}\,H(z)^{-2} \right]^{1/3}, \tag{5.8}$$

where $H(z) = H_0 E(z)$. Assuming a linear dependence of the form $r_\Delta = \xi r_g$, where ξ is a dimensionless constant, then the virial velocity dispersion can be written as $\sigma_V^2 = GM\xi/r_\Delta$, implying

$$\sigma_V = \xi^{1/2} \left(\frac{GM}{\sqrt{2}} \right)^{1/3} \Delta_c(z)^{1/6} H(z)^{1/3}. \tag{5.9}$$

We have seen in Section 5.2.3 that $\sigma_0 \propto \sigma_V$, so also the mass and redshift dependence of σ_0 is expected to be given by equation (5.9). Under the assumption that r_h and r_g scale linearly with r_Δ (see Section 5.2.3), from equation (5.8) we have that a fixed z

$$r_h \propto r_g \propto M^{1/3}. \tag{5.10}$$

The z-dependence of the other size proxies are also given by equation (5.8), as $r_g \propto r_\Delta$ and $r_h \propto r_\Delta$ (see Section 5.2.3).

5.3 Scaling relations of dark matter haloes as functions of redshift

Here we present the distributions of the size and the velocity dispersion as functions of mass and redshift for our sample of ~ 11000 DM haloes (see Section 5.2.2) in the mass range $10^{11} M_\odot \leq M \leq 5.5 \times 10^{14} M_\odot$. We adopt the same lower mass limit in all the snapshots of our simulation, while we do not restrict the upper mass limit, which varies from $M \simeq 2.67 \times 10^{13} M_\odot$ at $z \simeq 2.5$ to $M \simeq 5.5 \times 10^{14} M_\odot$ at $z = 0$.
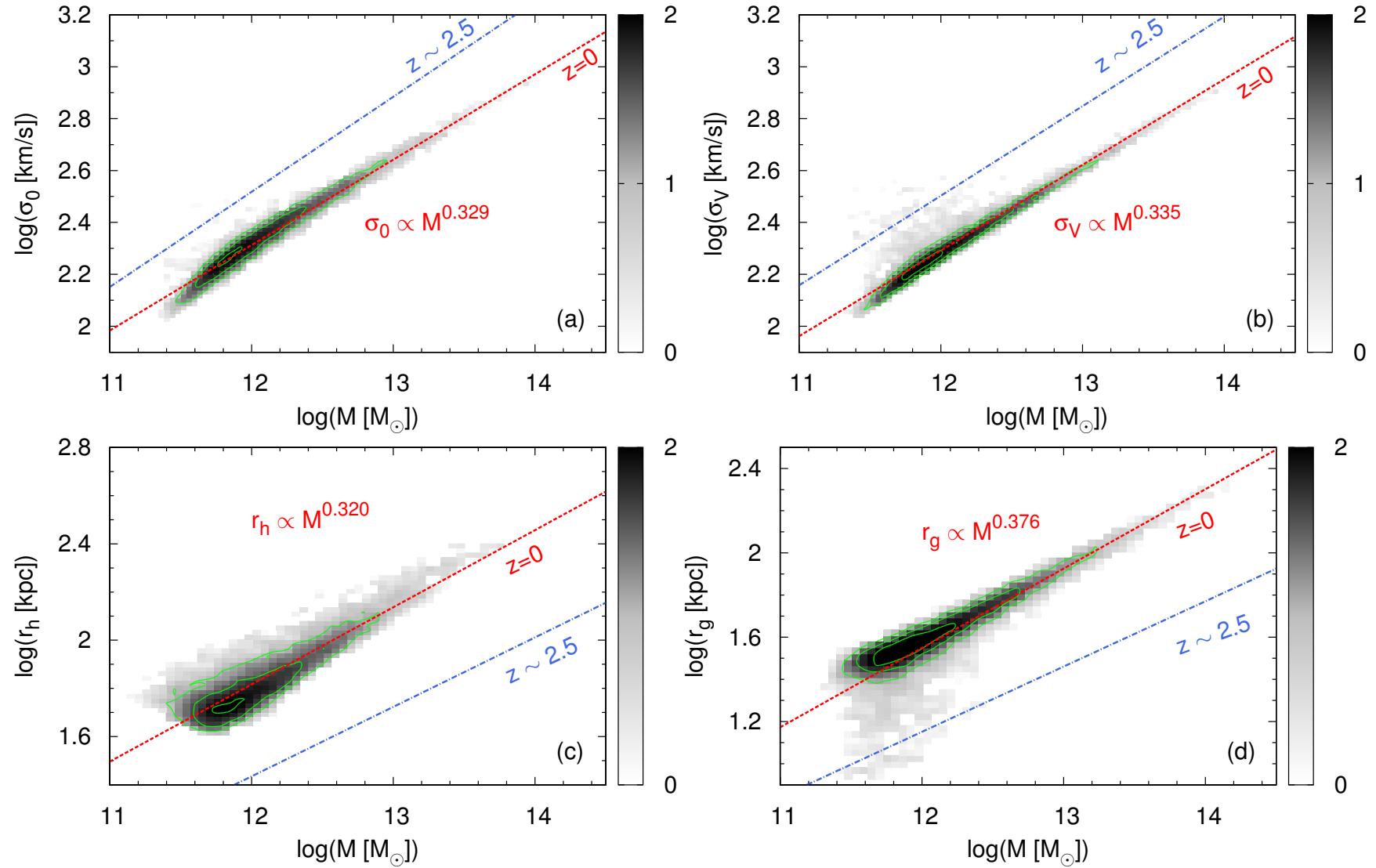
Figure 5.3: Distributions at $z = 0$ of the simulated haloes in the planes $M - \sigma_0$ (panel a), $M - \sigma_V$ (panel b), $M - r_h$ (panel c) and $M - r_g$ (panel d). In each panel, the plane has been binned in cells and the gray scale represents the logarithm of the counts of haloes in each cell. The red dotted lines are the best-fits at $z = 0$ ($\sigma_0 \propto M^{0.329}$, $\sigma_V \propto M^{0.335}$, $r_h \propto M^{0.320}$ and $r_g \propto M^{0.376}$); for comparison, the best-fits at $z \simeq 2.5$ are plotted as blue dot-dashed lines.

5.3.1 Mass-velocity dispersion: the measured correlation and evolution

The simulated DM halo population is well represented by the following best-fit relation:

$$\log\left(\frac{\sigma_0}{\text{km/s}}\right) = \gamma \log\left(\frac{M}{M_\odot}\right) + b, \tag{5.11}$$

where

$$\begin{aligned}
\log\gamma &= (0.103 \pm 0.008)\log(1+z) - (0.49 \pm 0.002), \\
\log b &= (0.163 \pm 0.02)\log(1+z) + (0.179 \pm 0.006).
\end{aligned} \tag{5.12}$$

In Fig. 5.3(a) we show the distribution of the sample in the $M - \sigma_0$ plane at $z = 0$ and we find a best-fit correlation of the type $M \propto \sigma_0^{3.04 \pm 0.01}$ (i.e. $\gamma \simeq 0.32$). For comparison we also show the best-fit correlation at $z \simeq 2.5$: the slope is slightly larger than that at $z = 0$, i.e., $\gamma \simeq 0.37$, whereas the normalization is significantly higher: as we expected, at fixed mass higher z haloes have higher velocity dispersion.

Assuming $\sigma_0 \propto \sigma_V$ (see Section 5.2.3), we can compare our results with both theoretical expectations, e.g., equation (5.6), and previous findings. At fixed mass $M = 10^{12} M_\odot$ we find a good agreement with equation (5.7): i.e., our sample follows[3] $\sigma_{0,12} \propto E(z)^{0.36}$. In the top panel of Fig. 5.4 we show the evolution of the central velocity dispersion at $M = 10^{12} M_\odot$ in the redshift range $0 \lesssim z \lesssim 2.5$. We have chosen $M = 10^{12} M_\odot$ as a reference mass, since it is roughly the mean mass in our sample at $z = 0$ and it is still well resolved (about 8×10^2 particles). As expected from cosmological predictions (equation 5.7), $\sigma_{0,12}$ decreases with time. We find a power-law best-fit evolution of the type $\sigma_{0,12} \propto (1+z)^{0.35}$ and also a better representation (about two orders of magnitude in the reduced χ^2) of the results via the fitting formula $\log\sigma_0 = 0.29\,x^2 + 0.2\,x$, where $x \equiv \log(1+z)$. We comment here that fixing a typical mass, say $M = 10^{12} M_\odot$ as in Fig. 5.4, means that we are analysing different haloes at different z, unlike fixing a halo and focusing on its evolution.

To further compare the results of our simulation with theoretical predictions and previous works, we have analysed the correlation between the mass and the virial velocity dispersion σ_V. In Fig. 5.3(b) we plot the distribution of the DM haloes in the $M - \sigma_V$ plane. In general, there is a very good agreement with the theoretical expectation (5.6) derived from the equilibrium assumption: the best-fit relation corresponds to $M \propto \sigma_V^{2.97 \pm 0.01}$. Other authors found similar results from independent simulations (see e.g., Evrard et al., 2008; Stanek et al., 2010; Munari et al., 2013; Diemer, Kravtsov, & More, 2013). We fitted the evolution of the normalization, at $M = 10^{12} M_\odot$, of the $M - \sigma_V$ correlation for our simulated haloes as a function of $E(z)$. We find that from $z \simeq 2.5$ to $z \simeq 0$ the normalization at $M = 10^{12} M_\odot$ follows $\sigma_{V,12} \propto E(z)^{0.33}$, which is in remarkably good agreement with theoretical expectations (equation 5.7). We compare also our results with previous findings: for $M = 10^{14} M_\odot$ Stanek et al. (2010) estimate an evolution $\sigma_{V,14} \propto E(z)^{0.34}$ and we find $\sigma_{V,14} \propto E(z)^{0.35}$; for $M = 10^{14.3} M_\odot$ Lau, Nagai, & Kravtsov (2010) find $\sigma_{V,14.3} \propto (1+z)^{0.49}$ in their non radiative case (with fixed $\Delta_c = 500$) and we find $\sigma_{V,14.3} \propto (1+z)^{0.36}$.

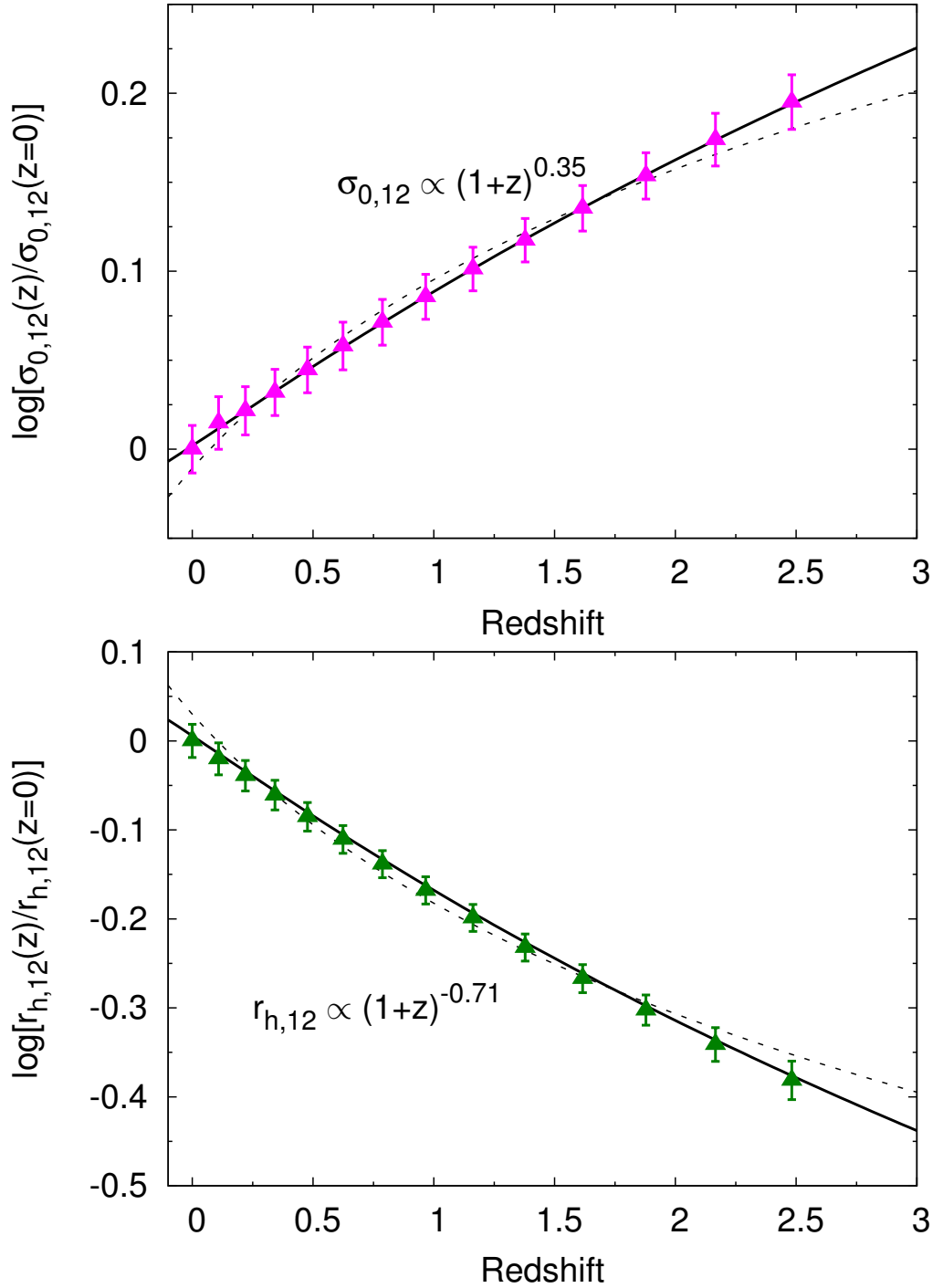[3] We define $A_{X,Y} \equiv A_X(M = 10^Y M_\odot)$.

Figure 5.4: Top panel: halo central velocity dispersion at fixed $M = 10^{12} M_\odot$ as a function of redshift. The black dashed line is the power-law best-fit to the points, while the black solid line is a fit quadratic in logarithm (see text). Bottom panel: same as top panel but for the half-mass radius at fixed $M = 10^{12} M_\odot$.

5.3.2   Mass-size: the measured correlation and evolution

The simulated DM halo population is well represented by the following best-fit relation:

$$\log \left(\frac{r_\mathrm{h}}{\mathrm{kpc}} \right) = \gamma \log \left(\frac{M}{M_\odot} \right) + b, \tag{5.13}$$

where

$$\begin{aligned} \log \gamma &= (-0.069 \pm 0.01) \log(1+z) + (-0.489 \pm 0.003), \\ \log b &= (0.02 \pm 0.02) \log(1+z) + (0.312 \pm 0.004). \end{aligned} \tag{5.14}$$

The measured correlation for the simulated haloes is shown in Fig. 5.3(c). The best-fit relation computed for this sample at $z = 0$ is $M \propto r_\mathrm{h}^{3.12 \pm 0.02}$ (i.e. $\gamma \simeq 0.32$). For comparison, we also plot here the $z \simeq 2.5$ best-fit correlation: the slope is slightly decreasing with redshift, down to $\gamma \simeq 0.28$ and the normalization in this mass range gets lower at later times. As we expected, at fixed mass higher z haloes have smaller size, i.e., they have higher density.

We then fit the evolution of the normalization at $M = 10^{12} M_\odot$ of the $M - r_\mathrm{h}$ correlation as a function of redshift in the range $0 < z < 2.5$: we find an evolution of the type $r_{\mathrm{h},12} \propto E(z)^{-0.65}$, which is in good agreement with the expectations given by equation (5.8). In the bottom panel of Fig. 5.4 our findings on the evolution in time of $r_{\mathrm{h},12}$ are shown: as expected (equation 5.8), we find that $r_{\mathrm{h},12}$ increases with time. We find a power-law best-fit $r_\mathrm{h} \propto (1+z)^{-0.71}$ and also that a better representation of the results is given by $\log r_\mathrm{h} = -0.53\,x^2 - 0.41\,x$, where $x \equiv \log(1+z)$.

In Fig. 5.3(d) we plot the distribution of the DM haloes in the $M - r_\mathrm{g}$ plane. Also in this case we find a reasonably good agreement with the virial expectation (5.10), with a best-fit correlation $M \propto r_\mathrm{g}^{2.71 \pm 0.02}$. We notice here that the somehow steeper slope than expected in Fig. 5.3(d) is due to a *tail* of the distribution composed of low mass haloes ($M < 10^{12} M_\odot$) with small r_g: this feature can be due to the fact that some DM haloes are not in equilibrium, for instance, because they could have experienced a recent major merger, and so virialization is not a good assumption for such objects.

5.4   Evolution of individual haloes

5.4.1   Evolution of simulated dark haloes in the mass-velocity dispersion and mass-size planes

According to the halo definition here adopted (equation 5.1) the halo mass increases monotonically with time, so studying a property of a halo as a function of its mass is equivalent to studying the time-evolution of the same property. Here we present the time-evolution of σ_0 and r_h for some individual representative haloes in our simulation, by tracking them in the planes $\sigma_0 - M$ and $r_\mathrm{h} - M$. In Fig. 5.5 we plot the evolutionary tracks followed by a representative halo with mass $M \simeq 5.5 \times 10^{14} M_\odot$ at $z = 0$: we reconstruct the growth in velocity dispersion (top panel) and size (bottom panel) as the halo gets more massive. It is apparent that neither in the $M - \sigma_0$ nor in the $M - r_\mathrm{h}$
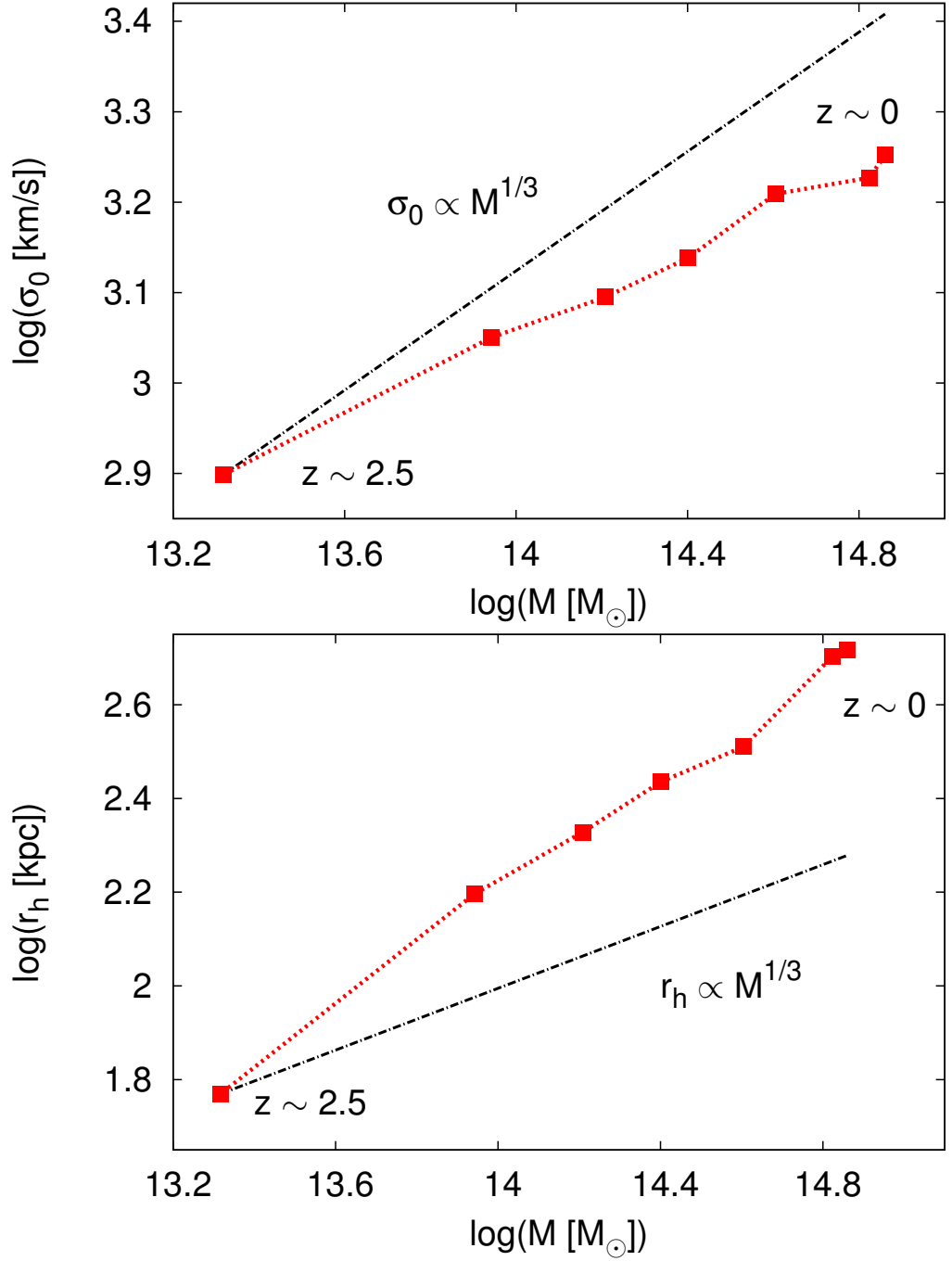
Figure 5.5: Top panel: evolution of a DM halo of mass $M(z = 0) \simeq 5.5 \times 10^{14} M_\odot$ in the $M - \sigma_0$ plane from $z \simeq 2.5$ to $z = 0$ (red squares). Here, mass traces time: the least massive point is the one at highest z. The black dot-dashed line is a power law of index 1/3, plotted for comparison. Bottom panel: same as top panel, but in the $M - r_{\rm h}$ plane.

plane the halo evolves along the scaling law of slope $\approx 1/3$. The actual evolution experienced by the halo in Fig. 5.5 is significantly shallower in the $M - \sigma_0$ plane, with best-fit $\sigma_0 \propto M^{0.2}$, and steeper in the $M - r_{\mathrm{h}}$ plane, with best-fit $r_{\mathrm{h}} \propto M^{0.6}$., consistent with the results of previous works on binary dissipationless mergers (see e.g., Nipoti, Londrillo, & Ciotti (2003); Boylan-Kolchin, Ma, & Quataert, 2005; Hopkins et al., 2009a; Hilz et al., 2012; Hilz, Naab, & Ostriker, 2013).

Figure 5.6 gives an overall picture of the evolution in the $M - \sigma_0$ (upper panel) and $M - r_{\mathrm{h}}$ (lower panel) planes of the whole halo population. In particular, we follow the evolution from $z \simeq 2.5$ of three objects, having $M \simeq 10^{13} M_{\odot}$, $M \simeq 10^{14} M_{\odot}$ and $M \simeq 5.5 \times 10^{14} M_{\odot}$ at $z = 0$, representative of an ETG sized halo, a group sized halo and a cluster sized halo, respectively. Figure 5.6 indicates that the evolutionary tracks of the whole population of DM haloes in the simulation reflect that of the halo shown in the of Fig. 5.5, therefore we do not find clear indications of mass-dependent evolution. In other words, the velocity dispersion grows weakly and the half-mass radius grows strongly independently of the halo mass. The fact that the individual haloes experience an evolution in σ_0 with a shallower slope than the global $\sigma_0 \propto M^{1/3}$ correlation (and viceversa for the evolution in r_{h}) is responsible for the z-evolution of the normalization of the $\sigma_0 - M$ correlation, such that at fixed mass σ_0 is smaller at lower z. Similarly, the z-evolution of the normalization of the $r_{\mathrm{h}} - M$ correlation is such that at fixed mass r_{h} is larger at lower z.

5.4.2   Comparison with simple dry merger models

In a hierarchical context, the evolution and mass assembly of haloes is often decomposed it two main processes: diffuse accretion and mergers (e.g. Fakhouri, Ma, & Boylan-Kolchin, 2010). According to the halo definition here adopted (equation 5.1), the halo mass can grow in principle even in an isolated and static configuration, just because the critical density of the Universe decreases with time (see e.g., Diemer, More, & Kravtsov, 2013). However, in a realistic cosmological context a halo experiences several mergers in its lifetime and in many cases they dominate its mass assembly. In the following, we will consider the case in which merging is the driving process for the structural evolution of individual haloes and we will compare our results with predictions of simple dry merging models.

5.4.2.a   Analytic arguments

Here we present some of the analytic arguments one can use to describe the evolution of the velocity dispersion and size of a halo which grows mainly via mergers with other haloes. If both the mass loss in the collision and the orbital energy of the encounter are negligible, in an equal-mass merger scenario the halo is expected to grow in size linearly with mass, while its velocity dispersion is expected to remain constant (see e.g., Nipoti, Londrillo, & Ciotti, 2003). Under the same hypothesis, if the evolution is dominated by accretion of many satellites much less massive than the main halo, the velocity dispersion is expected to *decrease* linearly with the mass, while the size would grow quadratically with mass (see e.g., Naab, Johansson, & Ostriker, 2009). In a realistic merging history
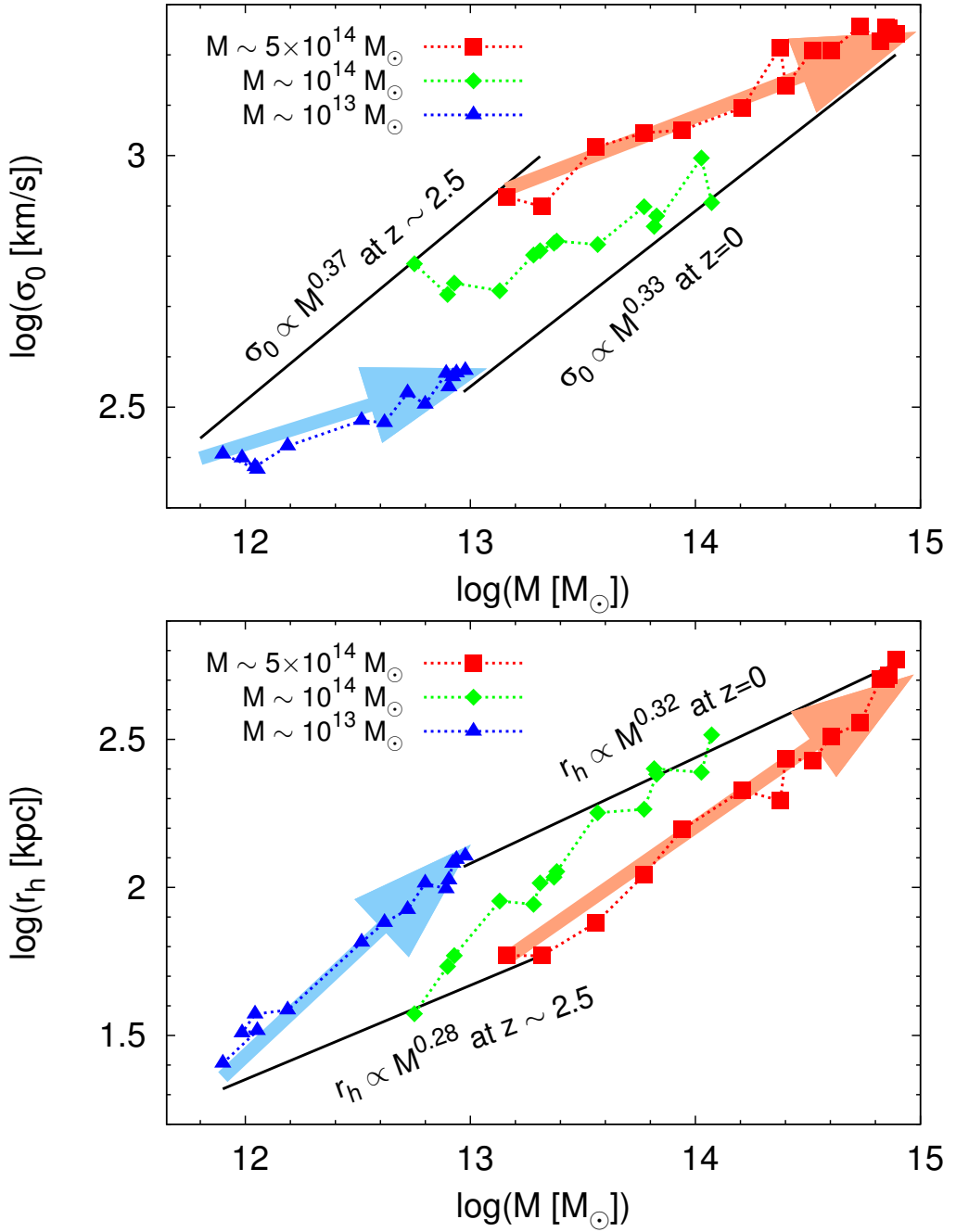
Figure 5.6: Top panel: evolution in the $M - \sigma_0$ plane of three representative haloes in our simulation. The red filled squares refer to a cluster-sized halo of mass $M(z = 0) \simeq 5.5 \times 10^{14} M_\odot$ (the same halo as in Fig. 5.5, but with a finer sampling), the green filled diamonds refer to a group-sized halo of mass $M(z = 0) \simeq 10^{14} M_\odot$, while the blue filled triangles refer to a early-type galaxy-sized halo of mass $M(z = 0) \simeq 10^{13} M_\odot$. The two black solid lines are the best-fit $M - \sigma_0$ correlation for the whole population at $z = 0$ and at $z \simeq 2.5$. The big blue and red arrows represent a schematic view of the evolutionary track in the $M - \sigma_0$ plane for, respectively, the low-mass and high-mass haloes. Bottom panel: same as top panel, but in the $M - r_{\rm h}$ plane.

consisting of both major and minor mergers, we expect the behaviour of $r_{\rm h}$ and σ_0 to be in between those predicted by the two extreme cases illustrated above.

However the assumptions of zero orbital energy and negligible mass loss are not necessarily realistic. Some authors have shown how the effect of mass loss could play an important role in the evolution of the velocity dispersion and of the size of an object (see e.g., Nipoti, Londrillo, & Ciotti (2003); Hilz et al., 2012). Also the effect of the orbital energy on the evolution of σ_0 and $r_{\rm h}$ can be non-negligible (Nipoti, Treu, & Bolton, 2009a; Nipoti et al., 2012, hereafter Nipoti et al. (2012)), even if there are indications that most halo encounters are on orbits close to parabolic (see e.g., Khochfar & Burkert, 2006). In this section we attempt to study the effect of orbital energy using the data of our simulation.

If we know the orbital energy, we can predict analytically the merger-driven evolution of the virial velocity dispersion $\sigma_{\rm V}$: the dissipationless merging of two virialized systems, which have kinetic energies respectively $T_1 = M_1\sigma_{\rm V,1}^2/2$ and $T_2 = M_2\sigma_{\rm V,2}^2/2$, on a barycentric orbit of energy $E_{\rm orb}$, results in a system that, when in equilibrium, has virial velocity dispersion (see Nipoti, Londrillo, & Ciotti, 2003)

$$\sigma_{\rm V,f}^2 = \frac{M_1\sigma_{\rm V,1}^2 + M_2\sigma_{\rm V,2}^2}{M_1 + M_2} - 2\frac{E_{\rm orb}}{M_1 + M_2}, \tag{5.15}$$

assuming no mass loss (the subscript f indicates the final value). As long as $\sigma_0 \propto \sigma_{\rm V}$ (see Section 5.2.3), equation (5.15) can be used to predict also the evolution of σ_0.

Similarly, one can predict how the size of the halo is evolving in the merging process: assuming a linear proportionality $r_{\rm h} \propto r_{\rm g}$ (see Section 5.3.2 and Fig. 5.2), we have that $r_{\rm h} \propto M/\sigma_{\rm V}^2$. We can use equation (5.15) to make predictions in the context of a simple dry merging model: we calculate the half-mass radius of the halo at a given redshift, then we predict its evolution calculating the ratio

$$\frac{r_{\rm h,f}}{r_{\rm h,1}} = \frac{M_1 + M_2}{M_1}\frac{\sigma_{\rm V,1}^2}{\sigma_{\rm V,f}^2}, \tag{5.16}$$

where $\sigma_{\rm V,f}^2$ was calculated through equation (5.15) and we have taken halo 1 as reference progenitor.

5.4.2.b   Orbital parameters

To account for the contribution of $E_{\rm orb}$ in the evolution of σ_0 and $r_{\rm h}$ for our haloes (i.e to apply equation 5.15), we need to extract the merger orbital parameters from our simulation. We have reconstructed the merger histories of the haloes and then calculated the orbital parameters of the encounters in the point-mass approximation (hereafter PMA) of the progenitors (i.e., approximating every merging halo as a point located in its centre of mass and having the same mass as the object; see e.g., Khochfar & Burkert, 2006; Wetzel, 2011).

As well known, the orbit of a collision is completely characterized by two parameters, for instance the orbital energy and the orbital angular momentum or the eccentricity
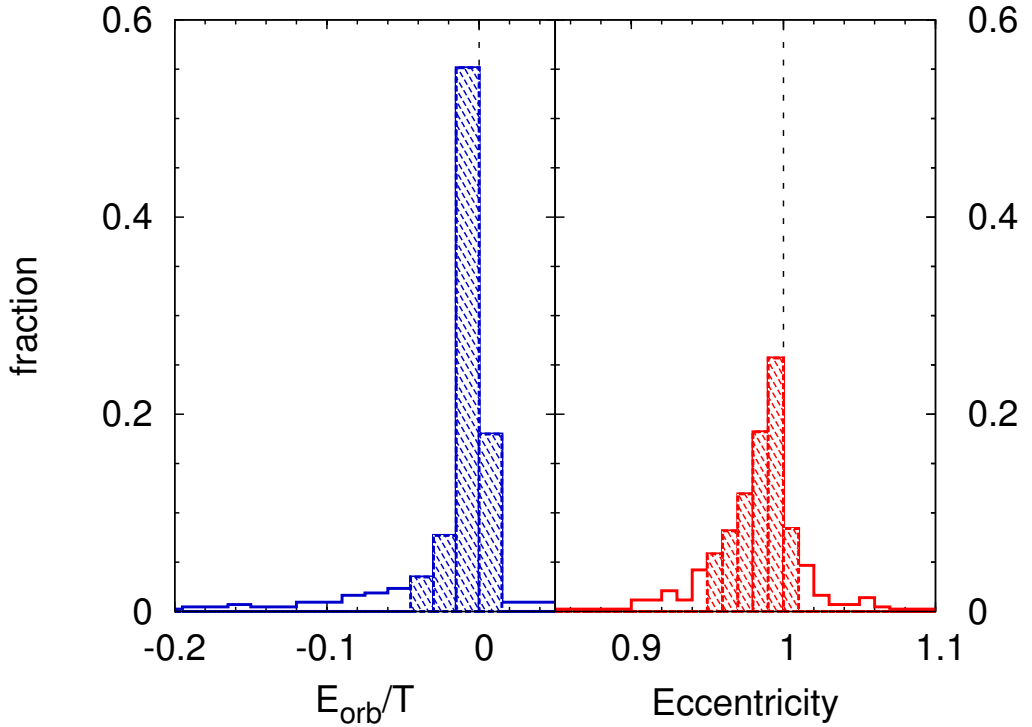
Figure 5.7: Histograms of the orbital energies (left-hand panel) and of the eccentricities (right-hand panel), computed in the PMA, of the mergers experienced by a $M(z = 0) \simeq 5.5 \times 10^{14} M_{\odot}$ DM halo, from $z \simeq 2.5$ to $z = 0$. The orbital energies are normalized to the internal energy $T = M\sigma_V^2/2$ of the reference halo. The dashed area, centred on the median value, contains 80% of the counts, so that each tail of the distribution accounts only for 10%.

and the pericentric radius. Here we find convenient to characterize the orbits of our mergers with the orbital energy E_{orb} and the eccentricity

$$e = \sqrt{1 + \frac{2E_{\text{orb}}L_{\text{orb}}^2}{\mu(GM_1M_2)^2}}, \tag{5.17}$$

where M_1 and M_2 are the masses of the two colliding systems, L_{orb} is the norm of the barycentric orbital angular momentum and $\mu \equiv M_1M_2/(M_1 + M_2)$ is the reduced mass. In Fig. 5.7 we plot the histograms of E_{orb} and e (computed in the PMA) of the encounters experienced by a $M(z = 0) \simeq 5.5 \times 10^{14} M_{\odot}$ DM halo in our simulation from $z \simeq 2.5$ to $z = 0$. We find that the distribution of the orbital energies has a clear peak at $E_{\text{orb}} \simeq 0$ (left-hand panel of Fig. 5.7) and that of the eccentricities has a clear peak at $e \simeq 1$ (right-hand panel of Fig. 5.7), with both distributions having non-negligible tails both at bound orbits ($e < 1$ and $E_{\text{orb}} < 0$) and unbound orbits ($e > 1$ and $E_{\text{orb}} > 0$). Overall, our findings are in agreement with those of Khochfar & Burkert (2006): the large majority of the mergers happen on orbits close to parabolic.

The orbital potential energy computed in the PMA ($U_{\text{orb,PMA}}$) is always larger (in modulus) than the actual orbital potential energy U_{orb}, computed for the extended objects. As an example, one can think of a toy model in which the two particle systems

are initially very far away, where the PMA is justified, and then they start to get nearer and nearer up to the limit in which the centres of mass of the two system coincide: in this limit the orbital potential U_{orb} in the PMA diverges, while that of the extended system is still finite.

We tried to obtain a better estimate of the orbital energy by empirically correcting $U_{\mathrm{orb,PMA}}$ as follows. We computed the relative distance d_{rel} of a merger as the distance of the centres of the haloes in the snapshot before of the merging, i.e., is the latest snapshot in which the two haloes are distinct. Calculating the distribution of d_{rel} of the collisions in our simulation, we find that it peaks at $d_{\mathrm{rel}} \simeq r_\Delta$ of the biggest merging halo. Assuming an NFW (see Navarro, Frenk, & White, 1997) profile for the dark haloes, we made some experiments in order to evaluate the overestimate of $|U_{\mathrm{orb}}|$ in the PMA varying the parameters of the haloes (such as mass ratio, size ratio and concentration) and, most important, the relative distance between their centres of mass. We used GADGET-2 to calculate the U_{orb} of the encounter between the two systems and we compared it to that calculated in the PMA. We find that, quite independently of the structural parameters of the haloes, in a range of relative distances consistent with that measured in our simulation, $U_{\mathrm{orb}} \simeq U_{\mathrm{orb,PMA}}/2$.

5.4.2.c   Application to N-body data

In the hypothesis that mergers are the driving mechanism for halo evolution, it is possible, with equation (5.15), to predict the evolutionary track of a halo in the $M - \sigma_0$ plane across different snapshots in the simulation. For a given halo, starting from M and σ_0 of the most massive progenitor, we considered one at a time every merger in the halo merger tree and we used for each of them equation (5.15) to predict the evolution of σ_0 after the collisions. In Fig. 5.8 (top panel) we show the evolution of a representative halo in the $\sigma_0 - M$ plane and we compare it with the predictions of three dry-merging models based on equation (5.15): the parabolic-merger model (i.e. $E_{\mathrm{orb}} = 0$), the PMA model ($E_{\mathrm{orb}} = E_{\mathrm{orb,PMA}}$, where $E_{\mathrm{orb,PMA}}$ is the orbital energy computed in the PMA) and the corrected PMA model ($U_{\mathrm{orb}} = U_{\mathrm{orb,PMA}}/2$; see Section 5.4.2.b). The relative errors of the models with respect to the N-body data (bottom panel of Fig. 5.8) indicate that in the majority of the cases, the parabolic merger approximation tends to underestimate the σ_0 evolution by a factor $\approx 20 - 30\%$, while $E_{\mathrm{orb}} = E_{\mathrm{orb,PMA}}$ model tends to overestimate its growth up to $\approx 80\%$, probably due to the overestimate of $|U_{\mathrm{orb}}|$ introduced by the PMA. When we apply the empirical correction we find a much better agreement with the N-body data. We have checked that the resulting behaviour is fairly independent of the halo considered (i.e., on the halo mass at $z \sim 0$).

Using equation (5.16), where we compute $\sigma_{\mathrm{V,f}}$ as in equation (5.15), we are able to predict also the evolution in size of the halo. The results are summarized in Fig. 5.9. The parabolic merging model always tends to overestimate the actual size growth of the halo: such trend is in agreement with the analytical expectation of strong growth of the halo size (see Section 5.4.2.a). On the other hand, the $E_{\mathrm{orb}} = E_{\mathrm{orb,PMA}}$ model is underestimating the r_{h} evolution. Applying the empirical correction to the orbital energy in the PMA, we find a much better representation of the N-body data with respect to previous cases (see the bottom panel of Fig. 5.9).
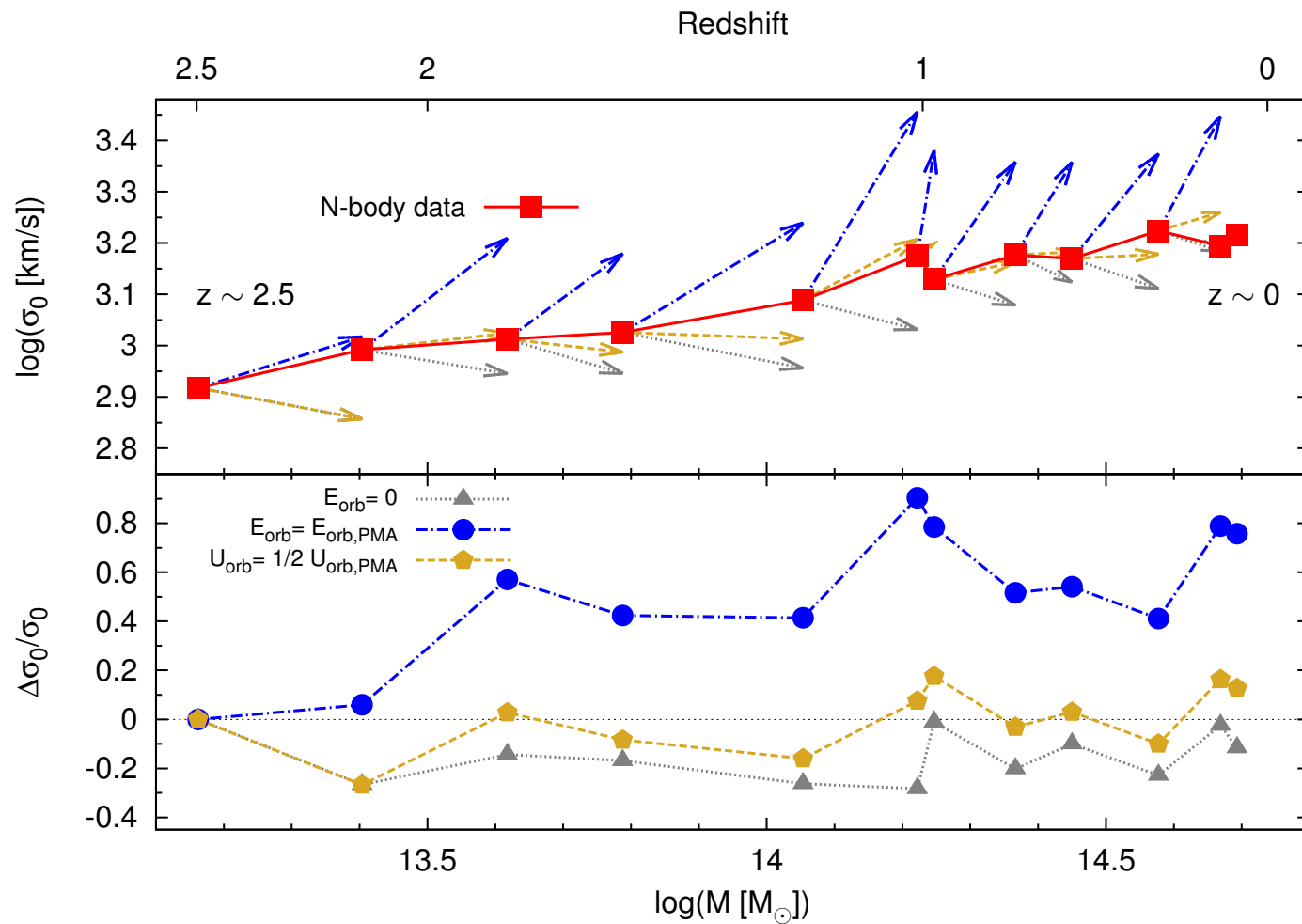
Figure 5.8: Top panel: evolution of a $M(z = 0) \simeq 5.5 \times 10^{14} M_\odot$ halo in the $M - \sigma_0$ plane from $z \simeq 2.5$ to $z \simeq 0$ (red filled squares). The different arrows represent the predictions of the σ_0 in the different models, starting from the reference point which is (M, σ_0) of the halo measured at the previous snapshot: gray dotted arrows are in the parabolic ($E_{\rm orb} = 0$) model, the blue dot-dashed arrows in the $E_{\rm orb} = E_{\rm orb, PMA}$ model, in which the orbital energy is computed in the PMA, while the golden short-dashed arrows are in the $U_{\rm orb} = U_{\rm orb, PMA}/2$ model, in which the orbital potential energy is half that in the PMA (see text). Bottom panel: relative deviations of the model predictions from the measured N-body data.
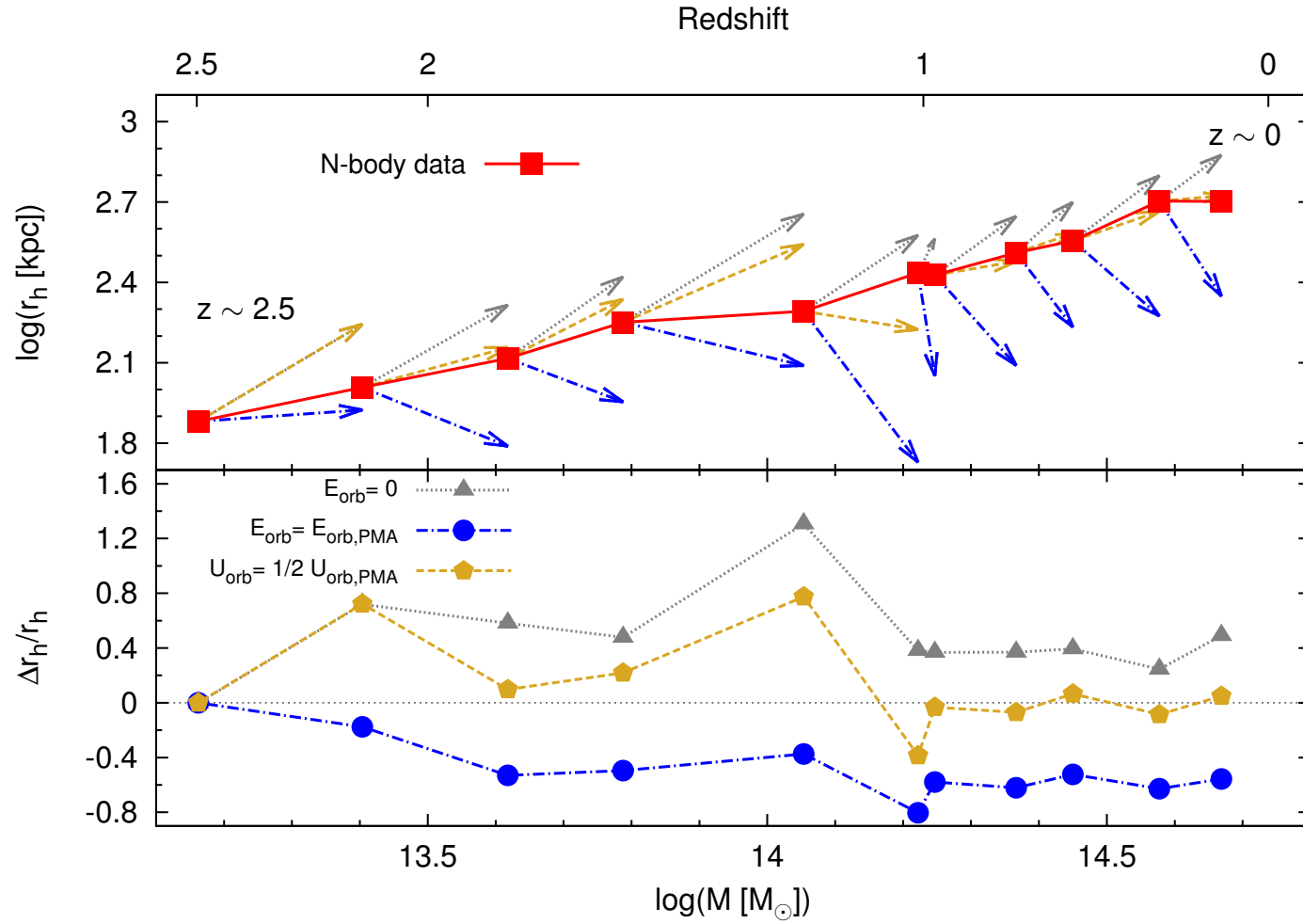
Figure 5.9: Same as Fig. 5.8, but for the evolution in the $M - r_h$ plane.

The results above deserve a further comment: since in the code we are using energy is conserved (see Springel, 2005), in principle, if we took into account all the possible complications to the merging model we would reproduce the actual measured evolution. Here we focus on the effect of one of these possible complications, namely the orbital energy. Other authors have used this approach before, studying for example the effect of escapers (see e.g., Nipoti, Londrillo, & Ciotti (2003); Hilz et al., 2012): in particular, Hilz et al. (2012) found that mass loss can be very important in reproducing the size growth of collisionless systems in binary mergers simulations. Our effort is complementary to such works: we added a detailed study of the importance of the orbital energy, finding that taking into account such effect in a simple dry merging model can be *crucial* in order to reproduce the halo evolution in a cosmological context.

5.5 Implications for the size evolution of early-type galaxies

In the previous sections we have described the evolution in size and velocity dispersion of the population of DM haloes. This evolution is qualitatively similar to that of the observed population of ETGs. The aim of this section is to compare quantitatively our N-body data to observations. Since there are no baryons in the simulation, we need to populate our DM haloes with galaxies, by assigning the stellar mass M_* and the stellar effective radius R_e, which can be done using currently available prescriptions for the stellar-to-halo mass relation (SHMR) and the stellar-to-halo size relation (SHSR).

5.5.1 The stellar-to-halo mass relation (SHMR)

A critical point in this work is the assignment of stellar masses to the dark haloes of our N-body simulation. To do so, we need to assume a SHMR, i.e., a function that associates a stellar mass M_* to each given halo mass M at a given redshift z. Many prescriptions are available at the time of this writing for this function (see e.g., Behroozi, Conroy, & Wechsler, 2010; Wake et al., 2011; Leauthaud et al., 2012; Moster, Naab, & White, 2013), but the detailed properties of the SHMR are still uncertain and debated.

In order to account for the uncertainties in the SHMR, we use two different models of SHMR: Model 1, adopting the prescription of Behroozi, Conroy, & Wechsler (2010, hereafter Behroozi, Conroy, & Wechsler, 2010) and Model 2, adopting the prescription of Leauthaud et al. (2012, hereafter Leauthaud et al. (2012)). A graphical representation of such models can be found in Fig. 5.10: the SHMR is plotted in different colours in the redshift range $0 \leq z \leq 4$. The functional forms and parameters of the two prescriptions used here are summarized in section 3.2.1 of Nipoti et al. (2012). Throughout the paper we adopt a Chabrier (2003) initial mass function. As in Nipoti et al. (2012), for simplicity, we do not take into account the scatter of the SHMR: to each halo we assign an M_* which is the mean value of the distribution.

We consider a subset of the DM halo population presented in Section 5.2.2. We cut our sample of objects to have a stellar mass $\log M_*/M_\odot \geq 10.5$ and such that no
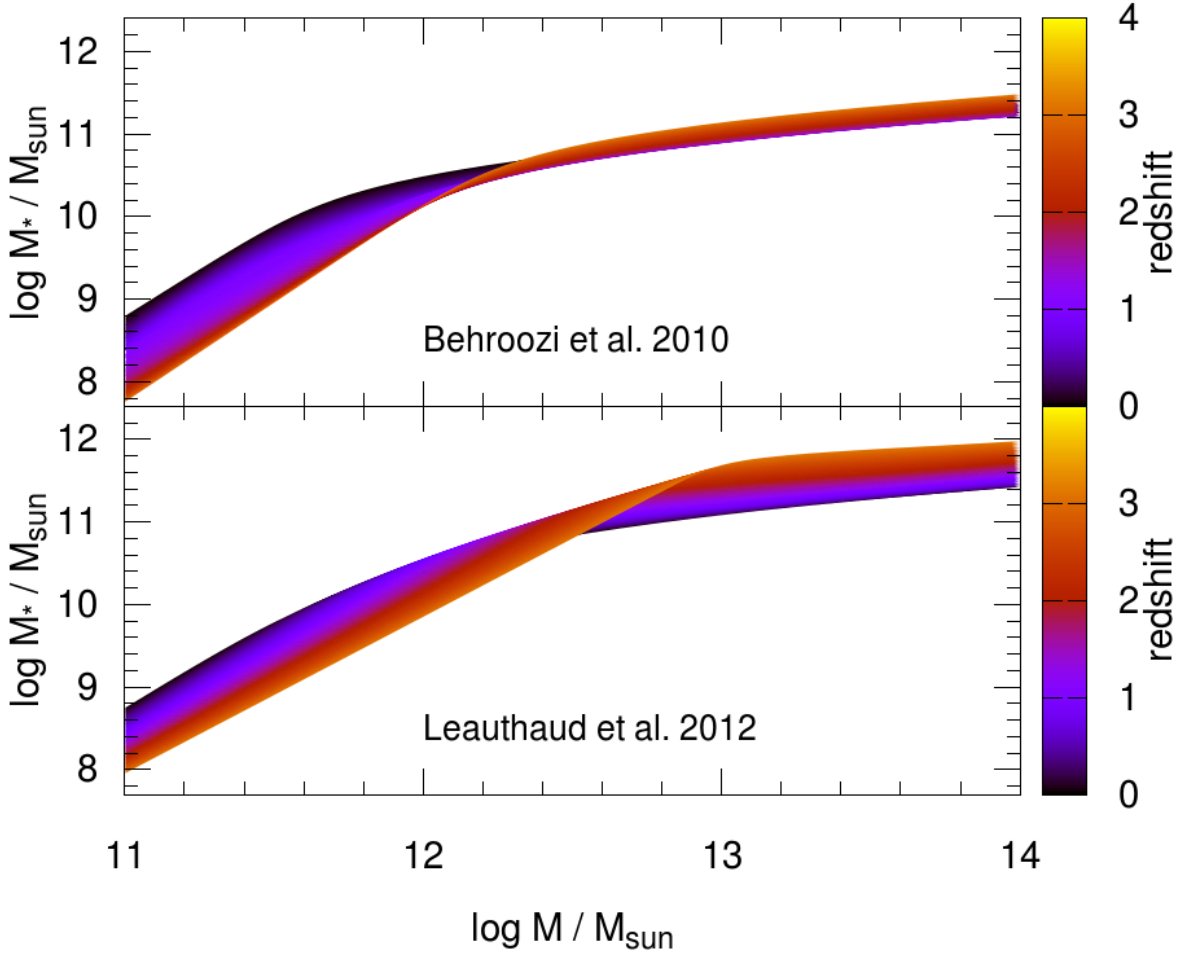
Figure 5.10: Stellar mass M_* as a function of the halo mass M and redshift according to the prescriptions of Behroozi, Conroy, & Wechsler (2010) (top panel; here used in Model 1) and Leauthaud et al. (2012) (bottom panel; here used in Model 2).

halo exceeds $M \simeq 4 \times 10^{13} M_\odot$. The stellar mass lower limit is so that the population is dominated by ETGs, since at high stellar mass the fraction of ETGs over the total number of galaxies is larger. The halo mass upper limit is motivated by the fact that DM haloes with mass larger than $M = 4 \times 10^{13} M_\odot$ are more likely to host groups of galaxies than single ETGs. We notice here that even if the two models have the same upper limit in halo mass, they have a different upper limit in stellar mass, because of the different model of SHMR used: Model 2 has a steeper slope and a higher normalization at the high-mass end, resulting in more massive galaxies associated to the same halo mass with respect to Model 1. The stellar mass ranges used here are: $3.2 \times 10^{10} M_\odot \leq M_* \leq 1.4 \times 10^{11} M_\odot$ (corresponding to $8.5 \times 10^{11} M_\odot \leq M \leq 4 \times 10^{14} M_\odot$ in halo mass) for Model 1 and $3.2 \times 10^{10} M_\odot \leq M_* \leq 2 \times 10^{11} M_\odot$ (corresponding to $9 \times 10^{11} M_\odot \leq M \leq 4 \times 10^{14} M_\odot$ in halo mass) for Model 2.

5.5.2   The stellar-to-halo size relation (SHSR)

After having characterized every DM halo with a stellar mass under the assumption of a SHMR, the second step is to assign a size, namely an effective radius R_e, to the stellar component. Assuming a reasonable form for the SHSR is not trivial and at this time there is not yet a prescription that can be taken as a reference.

However, recently Kravtsov (2013, following the theoretical work of Mo, Mao, & White 1998 and Fall & Efstathiou 1980) argued that such relation can be measured over a wide range of stellar masses, using abundance matching techniques to derive a functional form. Kravtsov (2013) finds that the relation between the virial radius r_Δ of the host halo and the effective radius R_e of the galaxy is linear. Such result confirms the theoretical predictions (see Mo, Mao, & White, 1998) that the virial radius of the halo is linearly proportional to the size of the galactic disk and that the constant of proportionality depends of the spin parameter $\lambda = L\,|E|^{1/2}G^{-1}M^{-5/2}$, where L is the norm of the angular momentum of the halo, E is the total energy of the halo and G is the gravitational constant. Moreover, the fact that both early-type and late-type galaxies follow this linear SHSR with a scatter of $\sim 20\%$ (see Kravtsov, 2013) can be interpreted as the fact that the Mo, Mao, & White (1998) model not only works for disk galaxies, but it represents a general behaviour of all types of massive galaxies.

Here we assume $R_e \propto r_h$, where r_h is the halo half-mass radius, defined in Section 5.2.2. However, in Section 5.2.3 we showed that $r_h \propto r_\Delta$, on average, so our assumption is consistent with the results of Kravtsov (2013). As a check to this hypothesis, we compare the stellar mass-effective radius correlation for our model galaxies (i.e., $M_* - R_e$) at $z = 0$ with that observed in the local Universe, taking as reference the $M_* - R_e$ correlation of the ETGs in the Sloan Digital Sky Survey (SDSS; Shen et al., 2003). In Fig. 5.11 we plot the distribution of the effective radius as a function of the stellar mass for our model galaxies in Models 1 and 2 (see Section 5.5.1), and we compare it to the best-fit relation of Shen et al. (2003). In particular, we have used $R_e/r_h = 0.031$ for Model 1 and $R_e/r_h = 0.042$ for Model 2, which are in reasonable agreement with the expectations of Mo, Mao, & White (1998) and the results of Kravtsov (2013), given that on average we find $r_h/r_\Delta \simeq 0.82$ in the simulated haloes. Overall, Fig. 5.11 shows that the distribution of the $z \simeq 0$ model galaxies in the $R_e - M_*$ plane is consistent with that of SDSS galaxies. In more detail, Model 2, with a best-fit $R_e \propto M_*^{0.64}$, appears to reproduce better the SDSS data (best-fit $R_e \propto M_*^{0.56}$) than Model 1 (best-fit $R_e \propto M_*^{0.84}$).

When comparing our models to observations (see Section 5.5.3) we will assume that the ratio R_e/r_h is independent of M and z. We will study only the redshift evolution of size ratios [namely, $R_e(z)$ normalized to $R_e(z \simeq 0)$], so the results are independent of the actual value of R_e/r_h. We note that an underlying assumption of our models is that baryons do not affect substantially the structural evolution of DM haloes. Though the stellar and DM components are expected to affect each other significantly, even in dissipationless mergers (see e.g., Hilz, Naab, & Ostriker, 2013). However, our results are not sensitive to this effect as long as it is independent on halo mass.
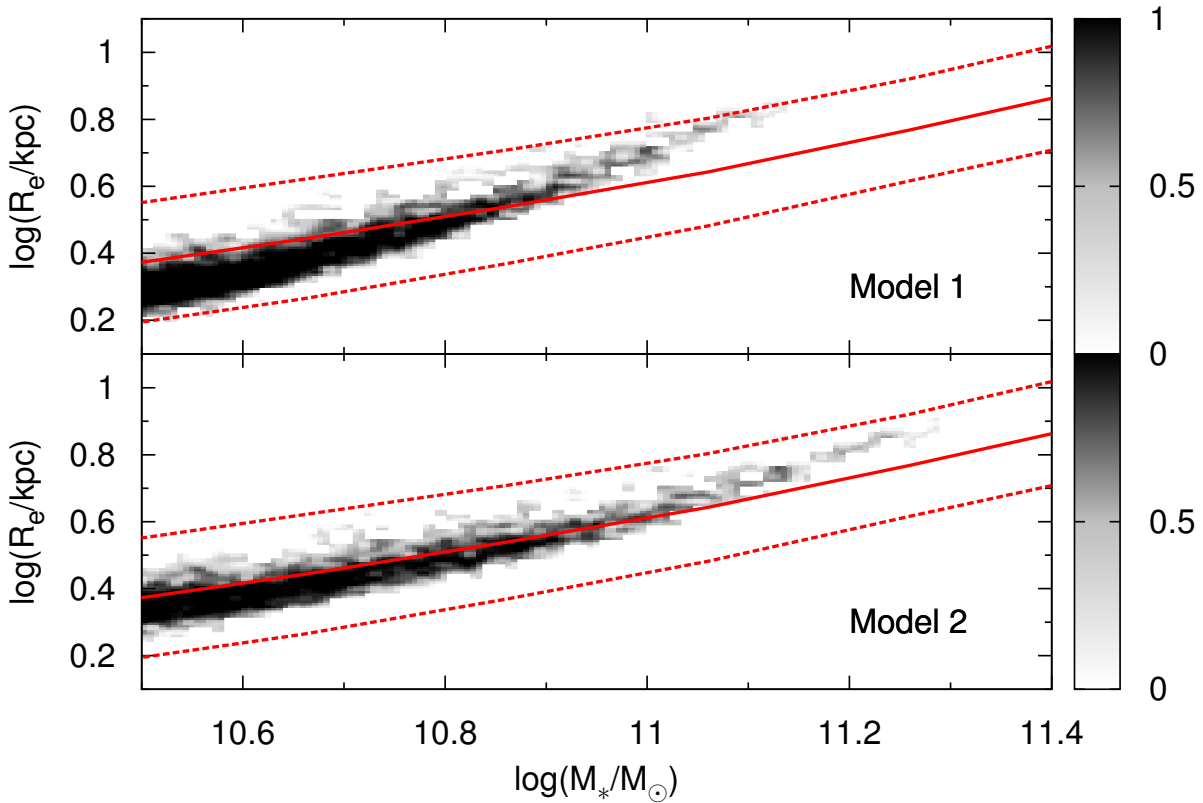
Figure 5.11: Distribution in the plane stellar mass-effective radius of the sample of model galaxies obtained by populating the $z \simeq 0$ simulated DM haloes according to Model 1 (top panel) and Model 2 (bottom panel). In both panels, the gray scale is proportional to the logarithm on the number counts of haloes in the binned plane and the solid line is the best-fit relation of Shen et al. (2003), for SDSS galaxies, with the corresponding 1σ scatter (dashed lines).

5.5.3 Size evolution of early-type galaxies: comparing models with observations

Here we compare the size evolution of our model galaxy sample (built from the N-body data as described in Sections 5.5.1 and 5.5.2) with that of the observed population of ETGs. In particular, we take as reference observational sample the collection of ETGs in the redshift range $0 \lesssim z \lesssim 3$ presented by Cimatti, Nipoti, & Cassata (2012, hereafter Cimatti, Nipoti, & Cassata (2012)). We show such comparison in Fig. 5.12: we compute the average size of the model galaxy sample at different times (16 snapshots of the N-body simulation in the range $0 \leq z \leq 3$) and we normalize it to that at the mean redshift of the SDSS. Following Cimatti, Nipoti, & Cassata (2012), we plot the evolution in three different mass bins. In Fig. 5.12 we are showing a sort of *backward* evolution: we are normalizing our models to be in agreement with the data at $z \simeq 0$ and we follow the evolution of the average size of the model galaxies at higher redshift. Our choice is motivated by the fact that we anchor the models to observations in the local Universe, which are more numerous with respect to $z \simeq 2.5 - 3$ data.
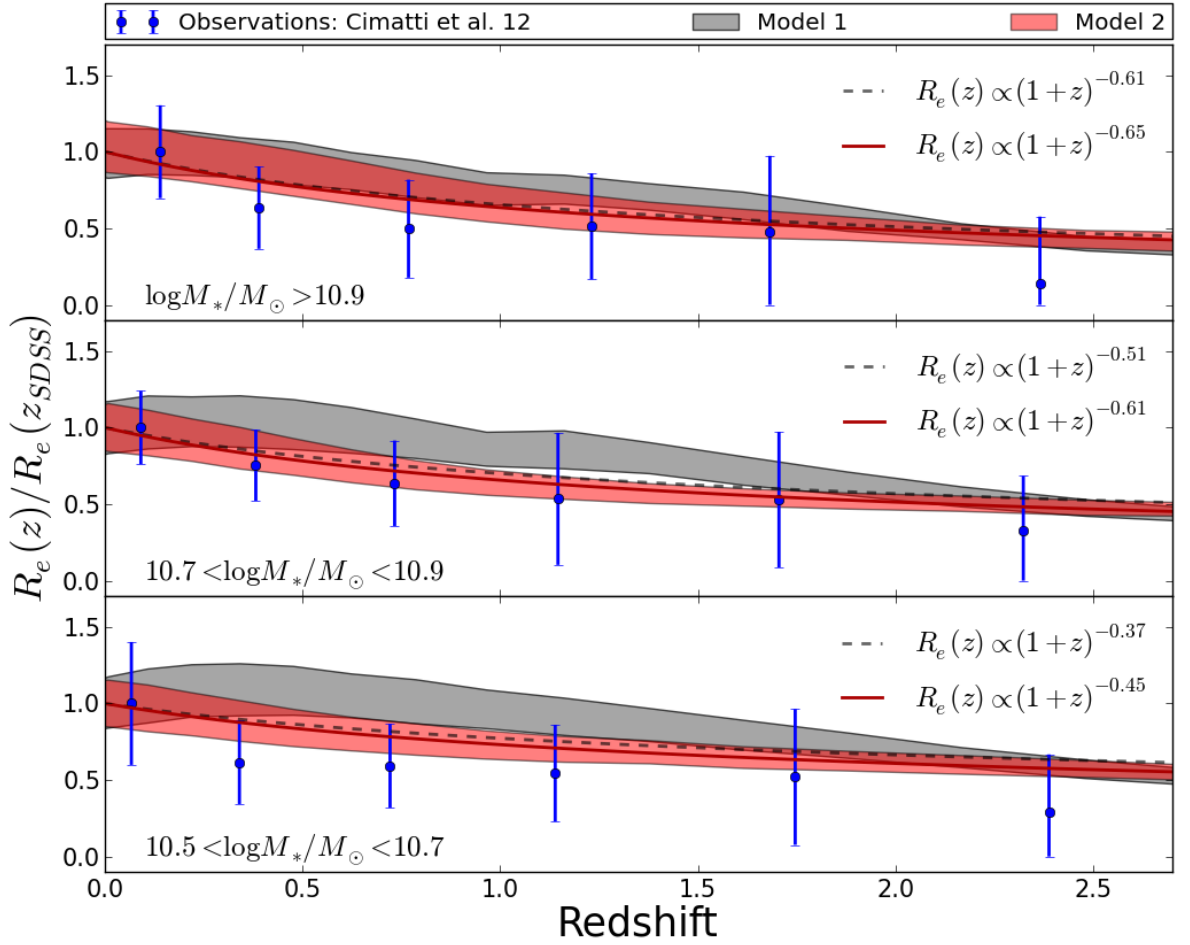
Figure 5.12: Average effective radius R_e as a function of redshift for simulated galaxies of Model 1 (gray bands) and Model 2 (red bands) of the present work and for observed ETGs of Cimatti, Nipoti, & Cassata (2012) (blue filled circles). Overplotted are also the best-fit power-laws $R_e \propto (1+z)^\gamma$ to Model 1 (gray dashed line) and Model 2 (red solid line). Each panel refers to the indicated stellar mass interval and the radii are normalized to the average R_e of SDSS galaxies in that mass interval. The models are anchored to the lowest-z (i.e. SDSS) observational points (see text). The vertical bars and the widths of the bands indicate one standard deviation.

The distribution of our model galaxies significantly overlaps with that of the observed ETGs of Cimatti, Nipoti, & Cassata (2012), but the models suffer from a systematic underestimate of the size growth in all the mass bins, in particular at $z > 2$. At $z < 2$ the models (especially Model 2, which is based on Leauthaud et al., 2012) are consistent within the scatter with the observational data, suggesting that the host haloes actually left their footprint in the stellar density at the time of galaxy quenching and that the after-quenching evolution of the galaxies mimicked that of the haloes. To give reference numbers, for both models, we computed the ratio $R_e(z \simeq 2.5)/R_e(z \simeq 0)$ in the three different mass bins finding that from $z \simeq 2.5$ to $z \simeq 0$ the average effective radius increases of roughly a factor of ≈ 2 in the lowest mass bin ($\log M_*/M_\odot < 10.7$) and a

factor of ≈ 3 in the highest one ($\log M_*/M_\odot > 10.9$). For comparison, most observational data agree on an evolution of the average effective radius of the ETG population of a factor $2 - 5$ from $z \gtrsim 2$ to the present (see e.g., Cimatti, Nipoti, & Cassata, 2012).

In Table 5.1 we report the best-fit values of γ, where $R_\mathrm{e} \propto (1+z)^\gamma$, for both models in the range $0 \lesssim z \lesssim 2.5$ and in the three mass bins. We find values of γ similar to those in Cimatti, Nipoti, & Cassata (2012) when they exclude the $z > 2$ data, while the models fail at reproducing the observed slopes which take into account also the higher redshift points.

Our analysis shows that, provided that the galaxy formation process produces a linear SHSR, the observed size evolution of the population of ETGs up to $z \simeq 2$ could be explained by the underlying size evolution of the halo population, in the sense that quiescent galaxies mimic the host halo evolution. At $z > 2$ the average size of the observed population of ETGs evolves significantly faster than predicted by our simple models (in agreement with Cimatti, Nipoti, & Cassata (2012); Nipoti et al., 2012). This difference at $z \gtrsim 2$ can possibly give us some insights into the role dissipative effects, such as star formation or active galactic nuclei (AGN) feedback: it might not be a mere coincidence that at $z \approx 2$ there are the peaks of the cosmic star formation rate (Madau et al., 1996; Lilly et al., 1996) and of AGN activity (see e.g., Merloni & Heinz, 2008; Gruppioni et al., 2011).

Overall, our results are in agreement with those of previous investigations (Cimatti, Nipoti, & Cassata (2012); Nipoti et al. (2012); Newman et al., 2012), which are in a sense complementary to the present work. For instance, we note that the approach used here is different from that of Cimatti, Nipoti, & Cassata (2012), who (following Nipoti et al. (2012)) treat in their model only the evolution of individual galaxies and do not include the contribution of galaxies that have become quiescent at relatively low redshift. In other words, when comparing models to observations, Cimatti, Nipoti, & Cassata (2012) do not try to account for the so-called progenitor bias (see e.g., Saglia et al., 2010; Carollo et al., 2013) because they assume that the observed population of high-z ETGs is representative of the progenitors of present-day ETGs. Our approach, though simple, should be more robust against the progenitor bias: in our sample of simulated objects, at any redshift, we can have in principle both galaxies that have just stopped forming stars (and that are identified for the first time as ETGs) and galaxies that became quiescent much earlier. However, it must be stressed that our model is limited by the fact that we are assuming that galaxies grow in size and mass so that the SHMR and SHSR are reproduced at all redshifts, without having specified any underlying physical model for such growth. In this respect, a more physically justified approach is that of Cimatti, Nipoti, & Cassata (2012) and Nipoti et al. (2012), who assume that the size and mass growth of ETGs is driven by dry mergers, finding that, under this hypothesis, the SHMR inferred from observations is not necessarily reproduced (see Nipoti et al. (2012)). In summary, our results, combined with those of similar previous works, suggest a scenario in which, at least up to $z \simeq 2$, the observed growth of ETGs reflects the underlying growth of their host DM haloes.
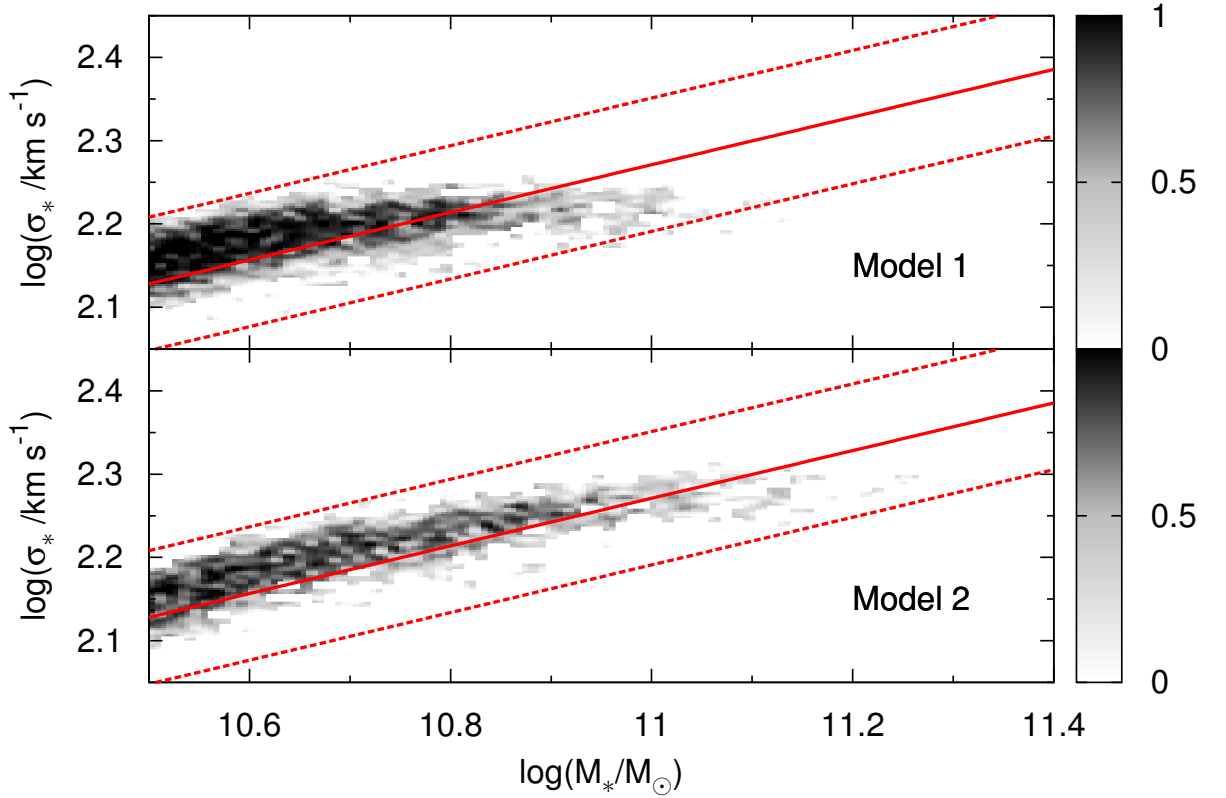
Figure 5.13: Same as Fig. 5.11, but in the stellar mass-velocity dispersion plane. In both panels, the solid line is the best-fit relation of Hyde & Bernardi (2009), for SDSS galaxies, with the corresponding 1σ scatter (dashed lines).

5.5.4 Velocity dispersion evolution of early-type galaxies: comparing models with observations

In this Section we compare the stellar velocity dispersion evolution of our model ETGs with that observed up to $z \simeq 2$. For such comparison we rely on the data collection of ETGs from Belli, Newman, & Ellis (2013) and van de Sande et al. (2013). We use a very simple recipe to get the stellar velocity dispersion of the model galaxies: consistent with our choice for the assignment of R_e (i.e., $R_e \propto r_h$), we assume a scaling with the halo properties of the form $\sigma_*^2 \propto M_*(M)/R_e(r_h)$, where we use the SHMR (Section 5.5.1) and SHSR (Section 5.5.2) from Model 1 and 2.

We check this recipe for ETGs at $z \simeq 0$: in Fig. 5.13 it is plotted the stellar mass-velocity dispersion relation at $z \simeq 0$ for our model ETGs which we compare to SDSS observations data from Hyde & Bernardi (2009). Overall, both models are able to represent fairly well the SDSS data within their uncertainties. However, we notice that Model 2 works systematically better than Model 1 in reproducing the observed $M_* - \sigma_*$: Model 1 is best-fitted by $\sigma_* \propto M_*^{0.11}$, while for Model 2 we find $\sigma_* \propto M_*^{0.2}$, closer to the Hyde & Bernardi (2009) relation $\sigma_* \propto M_*^{0.286}$.

Figure 5.14 shows the average velocity dispersion (*backward*) evolution of our model galaxies in the redshift range $0 \lesssim z \lesssim 2$. We compute the average σ_* as a function
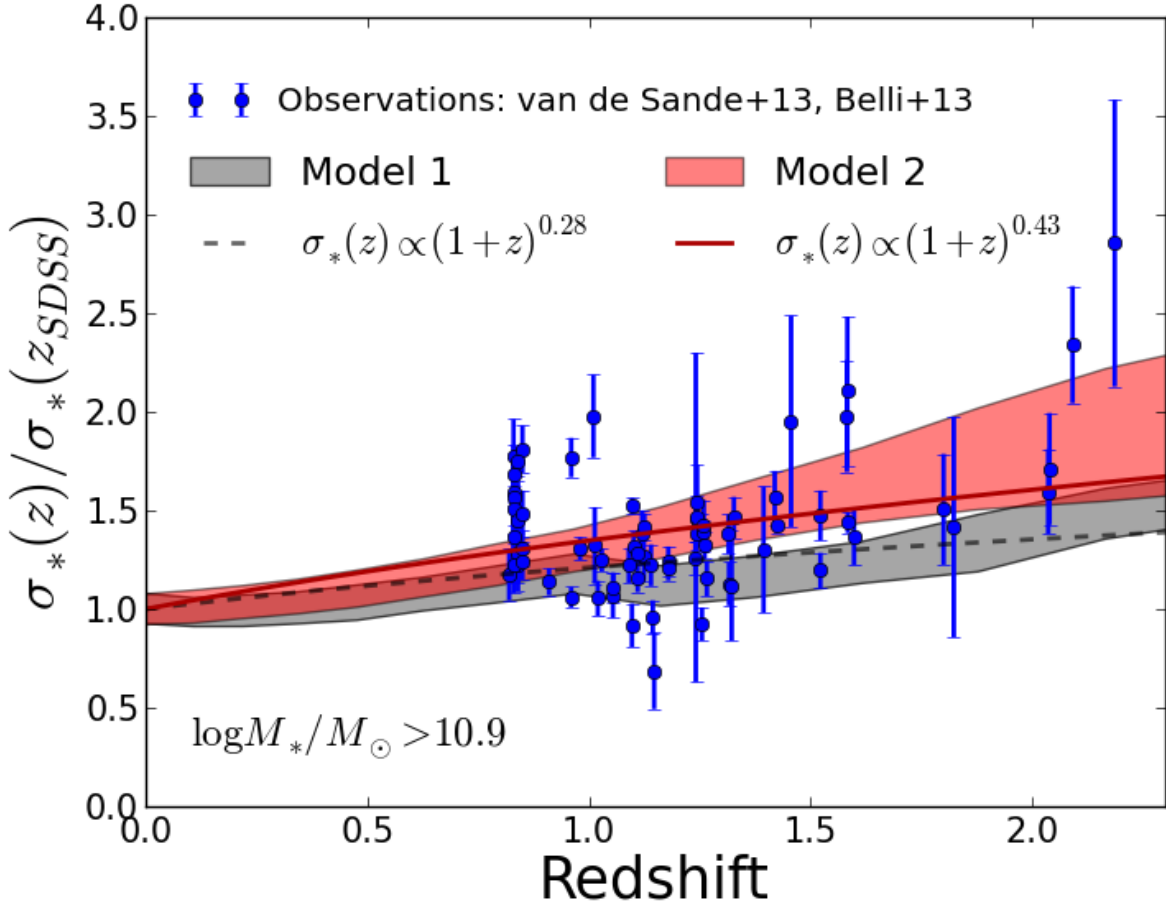
Figure 5.14: Average velocity dispersion σ_* as a function of redshift for simulated galaxies of Model 1 (gray bands) and Model 2 (red bands) of the present work and for observed ETGs of van de Sande et al. (2013) and Belli, Newman, & Ellis (2013) (blue filled circles). Here we restrict to stellar masses $\log M_*/M_\odot > 10.9$. Overplotted are also the best-fit power-laws $\sigma_* \propto (1+z)^\delta$ (gray dashed line and red solid line, respectively to Model 1 and Model 2). The models are anchored to the lowest-z (i.e. SDSS) observational points (see text), as in Fig. 5.12. The vertical bars and the widths of the bands indicate one standard deviation.

of redshift, we anchor the data from Belli, Newman, & Ellis (2013) and van de Sande et al. (2013) to a reference value for the local Universe taken from Hyde & Bernardi (2009) and we directly compare the backward evolution with data available for individual ETGs. Qualitatively we find a reasonable agreement with observations of high-mass (i.e., $\log M_*/M_\odot > 10.9$) passive galaxies up to $z \simeq 2$. The predictions, expecially those of Model 2, are able to reproduce the evolutionary trend in the observations, even though there is significant scatter. Quantitavely, we find that Model 2 evolution is well fitted by $\sigma_* \propto (1+z)^\delta$, with $\delta = 0.43 \pm 0.07$, while for Model 1 we find $\delta = 0.28 \pm 0.05$. For comparison, fitting the individual observations with a similar power-law evolution gives us $\delta = 0.36 \pm 0.02$, which is consistent within the uncertainties at least with Model 2. The model galaxies have decreased on average their velocity dispersion by a factor $\sigma_*(z \simeq 2)/\sigma_*(z \simeq 0) \approx 1.4 - 1.8$, for comparison van de Sande et al. (2013) quote an

Table 5.1: Summary of the best fitting power-laws $R_{\rm e}(z) \propto (1+z)^\gamma$ and $\sigma_*(z) \propto (1+z)^\delta$ to our models in the range $0 \lesssim z \lesssim 2.5$, for different stellar mass bins (see Section 5.5.3 and 5.5.4).

Stellar mass	Model 1		Model 2	
	γ	δ	γ	δ
$\log M_*/M_\odot > 10.9$	-0.61 ± 0.07	0.28 ± 0.05	-0.65 ± 0.09	0.43 ± 0.07
$10.7 < \log M_*/M_\odot < 10.9$	-0.51 ± 0.06	0.18 ± 0.05	-0.61 ± 0.06	0.20 ± 0.06
$10.5 < \log M_*/M_\odot < 10.7$	-0.37 ± 0.06	0.04 ± 0.05	-0.45 ± 0.06	0.01 ± 0.05

evolution in their sample of data of a factor $\approx 1.4 - 1.7$.

In Table 5.1 we summarize the results of fitting the velocity dispersion evolution in both models with simple power-laws, in the range $0 \lesssim z \lesssim 2.5$ and in the three stellar mass bins considered in Section 5.5. The numbers reported in Table 5.1 and the trends shown by Fig. 5.12 and 5.14 are also in good agreement with previous results of the *average* size and velocity dispersion evolution of stellar systems in hydrodynamical cosmological simulations (see e.g., Oser et al., 2012).

The above results on the velocity-dispersion evolution depend on the assumed assignement of σ_* to haloes (i.e., $\sigma_*^2 \propto M_*/R_{\rm e}$). A different choice could be $\sigma_* \propto \sigma_0$ (where σ_0 is the halo velocity dispersion); however, we have verified that assuming a scaling of that type leads to a very poor comparison of the $M_* - \sigma_*$ relation with data for the local Universe. This suggests that the evolution of the velocity dispersion of the stellar component is somewhat decoupled from that of the dark component: while σ_0 increases with time for individual haloes in our sample (see Fig. 5.6), viceversa σ_* of individual model galaxies tends to decrease as a function of time, if one assumes $\sigma_*^2 \propto M_*/R_{\rm e}$.

The same trend of velocity dispersion decreasing with time for individual galaxies is found in the cosmological hydrodynamical simulations of Oser et al. (2012, Oser private communication). However, it must be noted that Dubois et al. (2013), who also studied the evolution of early-type galaxies using cosmological hydrodynamical simulations, found that the velocity dispersion of individual galaxies increases with time.

5.6   Summary and Conclusions

Motivated by the observational finding that ETGs are, on average, more compact at higher redshift, we have explored the hypothesis that such evolution is mainly driven by the systematic redshift-dependence of the structural properties of their host DM haloes. Using a cosmological N-body simulation, we have followed the evolution of the structural and kinematical properties of a DM halo population in the Λ-CDM framework, focusing on the halo mass range $10^{11} \lesssim M/M_\odot \lesssim 5 \times 10^{14}$. Starting from a sample of simulated haloes, we have built a sample of model ETGs and we have compared the redshift evolution of their sizes with that of observed galaxies.

The main results can be summarized as follows:

- At $z = 0$ the haloes are well represented by $\sigma_0 \propto M^{0.329 \pm 0.001}$ and $r_{\rm h} \propto M^{0.320 \pm 0.002}$ at $z = 0$, where $r_{\rm h}$ is the half-mass radius and σ_0 is the central velocity dispersion. These global correlations are remarkably similar to those predicted for the virial quantities of the haloes (namely, $M \propto \sigma_{\rm V}^3$ and $M \propto r_\Delta^3$), meaning that there is not significant non-homology in the halo population.

- The slopes of the $M - \sigma_0$ and $M - r_{\rm h}$ correlations depend only slightly on z, but their normalizations evolve significantly with z in the sense that, at fixed mass, higher-z haloes have smaller $r_{\rm h}$ and higher σ_0. For instance, at fixed $M = 10^{12} M_\odot$ we find $\sigma_0 \propto (1 + z)^{0.35}$ and $r_{\rm h} \propto (1 + z)^{-0.71}$.

- The redshift evolution of the halo scaling laws is driven by individual haloes growing in mass following evolutionary tracks $\sigma_0 \propto M^{0.2}$ and $r_{\rm h} \propto M^{0.6}$. So, while individual haloes grow in mass, their velocity dispersions increase slowly and their sizes grow rapidly.

- The size and velocity dispersion evolution of individual haloes is successfully described by simple dissipationless merging models, in which a key ingredient is the (typically negative) orbital energy of the encounters.

- We compare our N-body data with observations of ETGs in the redshift range $0 \lesssim z \lesssim 3$, by populating the DM haloes with galaxies assigning to each halo a stellar mass, an effective radius and a stellar velocity dispersion. We find that the size and velocity dispersion evolution of our model galaxies is in reasonable agreement with the evolution observed for ETGs at least up to $z \simeq 2$. At $z > 2$ the observed size growth is stronger than predicted by our simple models.

The above findings suggest a scenario in which the size and velocity dispersion scaling laws of ETGs derive from underlying scaling laws of the DM haloes. Overall, the results of the present work give further support to the idea of a halo-driven evolution of ETGs: galaxy structural and dynamical properties are related to that of their haloes at the time of quenching and the further ETG evolution mimics that of haloes. Of course, the present approach is limited by the fact that we do not include a self-consistent treatment of baryonic physics. In a forthcoming study, we plan to investigate this problem by adding the baryonic evolution in the simulations.

Chapter 6

Conclusions & Future prospects

In this Thesis I have investigated some important aspects of the dynamics and evolution of early-type galaxies. The way in which the luminous and dark matter are distributed in galaxies has a major role in determining the galaxy's dynamics and evolution in time. Observationally, the dynamics can be probed by spectroscopy, that allows for the reconstruction of the galaxy's kinematics, while galaxy evolution by deep photometric and high-resolution spectroscopic observations, so that large catalogs of the progenitors of early-types at high redshift can be made. This Thesis focuses on some theoretical aspects that aim at reproducing and, possibly, explaining such observations.

In the following, I will separately discuss the main conclusions and prospects for future research for i) the equilibrium dynamical models and ii) the structural evolution of the galaxy population.

6.1   Dynamical models

Dynamical models in which the distribution function is a specified analytic functions are, in principle, superior to any other alternative since they always generate physical models for which any desirable information on e.g., how the mass and/or the velocities are distributed, are at hand. Models based on the Jeans equations give typically reasonable fits to observations of a wider class of objects (see e.g., MGE and JAM models in Section 2.3.1), but there is no guarantee that the best fitting model is physical (it may may not have an underlying positive-definite DF) and even if a model which fits nicely the observations is found, other more general classes of models can not be excluded. Particle-based and orbit-based models have typically millions/thousands of free parameters (the particle/orbit weights); observables can constrain such parameters, but

obvious degeneracies are difficult to break and often the solution is strongly dependent on e.g., the orbital library chosen.

Action-based DF models can be used as a testbed for other popular dynamical models. The dependence of the DF on the three action integrals make the models extremely flexible since their orbital distribution can be arbitrarily chosen by re-distributing the probability of orbits with the same energy (see Section 2.2.4.b) and since it is easy to generalize them to multiple components (because actions are adiabatic invariants and because the mass of each component is computed upfront). In Chapter 3 I introduced the $f(\mathbf{J})$ and in Chapter 4 I showed that their flexibility allows one to find remarkable fits with the spatially resolved kinematics of nearby massive early-type galaxies. Comparisons of action-based models for these galaxies with orbit-based and moment-based (e.g., JAMs) models have proved promising: the different techniques are in qualitatively good agreement. An interesting check on JAM models can be provided for instance by comparing their velocity ellipsoids, which are cylindrically aligned by construction, and that of the $f(\mathbf{J})$ DF models (see Appendix B), as it has been recently suggested (see Evans et al., 2015). Conversely, Schwarzschild models generate velocity distributions and also a sort of "discretized DF" which can be both directly compared with those of $f(\mathbf{J})$ models.

A very well-known problem of most dynamical models is the so-called *mass-anisotropy degeneracy*, namely that a set of kinematic observables can be equally fit with a self-consistent isotropic model in which the mass-to-light ratio is a function of position or with one that has a constant mass-to-light ratio, but an anisotropy (β eq. 2.14) which is a function of position (see e.g., Illingworth, 1981; Binney & Mamon, 1982). This degeneracy strongly biases results of Jeans models for which some priors on the velocity-dispersion tensor must be assumed. A partial break of the degeneracy is achieved when using non-Gaussian LOSVDs to fit the data, so that also velocity-moments of order higher than two are considered (e.g., van der Marel & Franx, 1993). The best possible approach is, therefore, to employ a model which predicts full LOSVDs and is always physical, in the sense that the DF is positive-definite. Three-integral DF models, such as the action-based $f(\mathbf{J})$ models, are perfectly suitable to do so.

6.1.1 Application to massive galaxies

In Chapter 4 I showed that dynamical models in which the DF depends on the action integrals can successfully reproduce the observed kinematics of some early-type massive galaxies. The models I presented are made of a stellar spheroidal component and a dark-matter component whose distribution follows that of the stars, i.e., the models have a mass-to-light ratio constant with radius. While the presented models yield a reasonably good representation of the surface brightness and spatially-resolved kinematics of roundish galaxies (e.g., NGC 6125 and NGC 2592), the quality of best-fit achieved is sensibly lower in the case of disc-like systems (e.g., NGC 6427). The natural way to extend the present work is to self-consistently add galaxy components such as bulge, stellar disc and dark-matter halo and repeat the present analysis with such more realistic models. The advantage of having DFs which take actions as arguments is that it is feasible to compute the self-consistent total galaxy potential of all the components together.

Multi-component systems when the DF of each component is known, can be generated in an iterative way (e.g., Prendergast & Tomer, 1970; Rowley, 1988). Consider a DF which depends on the energy amongst other integrals of motion and a star with a given energy in the self-consistent one-component case. Now, when another component is added the iterative algorithm tries to compute the self-consistent potential, but at each iteration the energy of that star will change, since the potential changes, and therefore the DF will weight that orbit differently. The advantage of the action integrals is that they are adiabatic invariants and hence they are less sensitive to (small) changes of the potential: the DF will weight the orbit equally at each step and the iterative algorithm is more likely to reach convergence. If one has prescriptions to specify the DFs of the two components as a function of the actions, the self-consistent total potential can be robustly found by iterations. Luckily we are now living in a moment in which action-based DFs for all the major galaxy components are available: the quasi-isothermal DFs of Binney (2010) for the stellar discs and the work of Chapter 3 for the bulge, stellar and dark-matter haloes. In particular, the latter have greatly widened the range of spheroidal $f(\mathbf{J})$ by generalizing the self-consistent isochrones of Binney (2014) to any two-power density distribution.

The works in Chapters 3-4 lead the way to a systematic study of massive systems, observed with Integral Field Units, ranging from round elliptical to spirals. Cappellari et al. (2011b) proposed a morphological classification of galaxies different from the classical Hubble (1936) tuning fork: the basic quantity that drives their classification is the bulge fraction. Two-component bulge+disc $f(\mathbf{J})$ models are ideal to further study the variation of the bulge-to-disc ratio across the "ATLAS^{3D} sequence" (see also van den Berg, 1976) as they could provide consistency checks to the JAMs used to model such galaxies.

6.1.2 Application to other systems

The applicability of $f(\mathbf{J})$ models is not limited only to the study of massive galaxies, but comprises also for instance

- *adiabatic contraction*: Blumenthal et al. (1986) pioneered the study of this phenomenon, namely the response of the dark-matter halo subsequent to the infall of baryons (see Gnedin et al., 2004, for an improved model). Multi-component (halo+stars) $f(\mathbf{J})$ models allow for much a general study of the contraction of dark-matter haloes as a response to condensation of baryons onto different final configurations (e.g., discs, spheroids): simple analytic recipes proposed in literature often assume special geometry and/or of the orbital distribution of the system; instead, much more general distributions are generated by $f(\mathbf{J})$ DFs for both the dark and the baryonic components and the contraction of the system in the total potential is mediated by the actions which are adiabatic invariants. For instance, this methodology have already been used to quantify the amount of contraction (and flattening induced by the stellar disc) in the dark-matter halo of the Milky Way (see Piffl, Penoyre, & Binney, 2015; Binney & Piffl, 2015).

- *dark matter haloes*: the phase-space structure of dark-matter haloes has been

widely investigated, but still a definitive answer is lacking (see e.g., Sharma & Steinmetz, 2006; Vogelsberger et al., 2008; Wojtak et al., 2008). Recently Pontzen & Governato (2013) argued that actions can be of use in determining whether the haloes form through a violent relaxation phase. This is because actions are adiabatic invariants and are (approximately) conserved during the violent relaxation process. The $f(\mathbf{J})$ formalism would improve their results by e.g., generalizing to axisymmetric models the dark haloes and allowing for a wider range of density profiles.

- *dwarf galaxies*: low mass galaxies, such as dwarf spheroidals, can as well be modeled with action-based DFs. Typically these are very dark-matter dominated systems ($M/L_V \sim 100$) and it is therefore crucial to have a self-consistent multi-component dynamical model to compare with kinematic observations. Cored isothermal truncated model (see Section 3.4.2) can be taken as a reference one-component model, then an NFW dark halo (see Section 3.3.2.c) can be easily added and finally the free parameters of the whole system are sought to best represent the data. For gas rich systems, such as some dwarf irregulars (e.g., Leo T, Ryan-Weber et al., 2008), an additional external potential due to the gaseous disc can be considered.

- *globular clusters*: evidences that some globular clusters, such as ω-Centauri (e.g., Ferraro et al., 2006) and NGC 2419 (e.g., Dalessandro et al., 2008), may have a two-body relaxation timescale of the order of their age have been proposed. If this is the case, then collisionless DFs can be of use in modeling their dynamics. A King (1966) profile is, to first order, similar to that of the cored and truncated isothermal in Section 3.4.2 and can be used to model such systems.

- *super-massive black-holes*: historically one of the most common method to estimate the masses of the super-massive black-holes at the centre of galaxies is by fitting dynamical models to the reproduce especially the galaxy's kinematics at the centre. For these studies it is crucial to have models that can make accurate predictions on the shapes of the line profiles. $f(\mathbf{J})$ models for the bulge with an additional contribution to the gravitational field from the black hole yield predictions for self-consistent systems that are directly comparable to the observations.

- *intermediate-mass black-holes*: there is growing interest on accurately measuring the central kinematics of crowded stellar systems such as globular clusters, since from the Magorrian et al. (1998) relation they are expected to host black-holes of masses between $10^2 - 10^4 M_\odot$ (e.g., van der Marel & Anderson, 2010). A common way to estimate the masses of such objects is by measuring the line-of-sight velocities of stars in the (croweded) central field and using them to sample the line-of-sight velocity distribution, though some biases may be present (see e.g., Lützgendorf et al., 2013; Lanzoni et al., 2013). Usually, only the first two velocity moments are used, but there are also some indications that higher-moments may be non-negligible (see Lützgendorf et al., 2012). Typically, spherical isotropic Jeans models are used to determine the dynamical mass-to-light ratio and it is not

clear whether more general models (i.e., axisymmetric and anisotropic) may give more robust estimates. Moreover, one could exploit also proper motion measurements that, coupled with the line-of-sight velocities, give constraints on the full three-dimensional velocity distribution of the system, which can be modeled with e.g., DF and orbit-based models, but not with moment-based ones.

6.1.3   Other applications

Models in which the DF is a function of the action integrals can be used also for other studies, including

- *non-equilibrium*: states out of equilibrium are best studied by perturbation theory starting from equilibria configurations. DF as a function of actions are ideal for such analysis since angle-action variables are the natural coordinate system of perturbation theory. For instance, Gerhard & Saha (1991) and Kaasalainen (1994) use perturbed Hamiltonians as a function of the actions to study orbits and resonances in different galaxy potentials. Now that some more knowledge has been added on how the Hamiltonian (e.g., Williams, Evans, & Bowden, 2014) and the DF of realistic galaxy potentials (see Chapters 3-4) can be written as a function of the actions, there is ample room for improvement.

- *stability*: models which are radially biased close to the centre can be subject to bar formation and radial orbit instability (see e.g., Fridman & Polyachenko, 1984). It is interesting to study whether any threshold in the parameters of $f(\mathbf{J})$ models exists which separates stable and unstable configurations. In particular, generalizations of the present models to triaxial symmetry (e.g. Sanders & Evans, 2015) are ideal to study in detail if and where in the parameter space some unstable modes can be generated and amplified.

- *N-body simulations*: any equilibrium DF can be used as a probability density from which to draw a discrete realization in configuration space. This technique is especially useful to build N-body models in equilibrium which can be used as intial conditions for simulations. One way to efficiently sample the probability distribution is by sample in action space using $f(\mathbf{J})$ to get the probability of the orbit and then map the actions into positions and velocities, i.e., $\mathbf{J} \mapsto (\mathbf{x}, \mathbf{v})$, by torus mapping (e.g., McMillan & Binney, 2008).

- *perturbation particles*: Leeuwin et al. (1993) introduced an N-body method in which the masses of the particles are variable and represent the difference between the model's time-evolving state and an unperturbed equilibrium state. The typical fluctuations in the gravitational potential are much smaller than that in conventional N-body models (especially close to equilibrium), since the system is always close to equilibrium, and small perturbation are best studied. Now that equilibrium configurations that are of practical interest in galaxy dynamics can be realized with axisymmetric (Chapter 3) and triaxial (Sanders & Binney, 2015) symmetry, it makes sense to adopt this method to numerically study deviations from such interesting equilibrium states.

6.2   Galaxy evolution

Models for the evolution of galaxies can not disregard the evolution of their host dark-matter halo. Both the infall of baryons and the merger history of the galaxy are mediated by their dark halo; therefore, it is resonable to expect that the dark halo population (in a statistical sense) may leave their imprint in the evolution of the host galaxies. In Chapter 5, I argued that indeed their evolution typically follows similar paths in terms of average size and velocity dispersion, and in terms of evolutionary tracks in the mass-size and mass-velocity dispersion planes. This, ultimately, can be explained as the fact that the stellar density of passively-evolving systems reflects the mean density of the Universe at the time of quenching (i.e., when the passive phase in the galaxy's evolution began, see e.g., Carollo et al., 2013). In this scenario, both the stellar-to-halo mass relation and the stellar-to-halo size relation are tightly correlated and one may argue that the properties of the stellar component derive simply from the size of the dark-matter halo and from angular momentum conservation (Mo, Mao, & White, 1998; Stringer et al., 2014). Moreover, since stars and dark matter share the same potential well, it is natural to think that the velocity dispersion of dark-matter particles is not much different from that of the stars in the galaxy. A linear correlation between the velocity dispersions of the two components is, therefore, to be expected. As a result of these arguments, the average density of the dark-matter haloes at fixed mass drives the evolution of the average density of passive galaxies in time, which is observed as trends in the average size and velocity dispersion of galaxy populations at different redshifts.

6.2.1   The role of dark haloes in centrals and satellites

The environment in which galaxies live has a substantial impact on the evolution of the galaxies. In particular, galaxies living at the centre of very large dark-matter haloes, such as those of galaxy clusters or galaxy groups, typically have an evolution which is much more active dynamically w.r.t. the majority of galaxies. In fact, dynamical friction is especially efficient and brings massive non-central galaxies to the centre which merge with the central galaxy. It is, therefore, interesting to assess the question whether centrals and satellites, i.e., galaxies not at the centre of their host halo, experience a substantially different evolution.

Vulcani et al. (2014) uses samples of early-types selected in galaxy clusters at different redshifts (from nearby Universe to $z \simeq 1$) and study the average size evolution of two separate populations of central and satellite galaxies. They find that the centrals experience a much stronger evolution, as they are systematically more expanded in nearby clusters w.r.t. to satellites at that redhsift, while both the populations lie on the same mass-size relation at higher redshift. A tempting way to interpret these observations is that centrals experience many more mergers than satellites and, on average, the growth of their dark-matter halo would be much stronger than that of satellites. The technique deloped in Chapter 5 can be directly applied to test this speculation, since it is sufficient to correctly identify central haloes, i.e., that of the whole galaxy clusters, and sub-haloes, i.e., that of satellite galaxies, and compute the evolution of the model galaxies as in Section 5.5. Currently, many robust methods exist to consistently

identify haloes and sub-haloes in cosmological N-body simulations (see Onions et al., 2012), therefore the results of such analysis would robustly quantify what is the imprint of dark-matter on the evolution of the two galaxy populations.

6.2.2   Model galaxy formation

A natural improvement of the work I presented in Chapter 5 is including a consistent physical treatment of the baryon physics in the N-body simulation. The condensation of baryons is known to have important effects on the evolution of dark-matter haloes (e.g., Blumenthal et al., 1986; Schaller et al., 2015), which typically leads to more concentrated haloes more conspicuously at halo masses of about $10^{12} - 10^{13} M_\odot$, where the star formation is more prominent. The issue here is, of course, that baryonic physics is still poorly understood and the phenomenological models used in state-of-the-art cosmological simulations are usually fine tuned to reproduce a given set of observables. This ultimately leads to predictions that depend on the implementation of the hydrodynamics and of the small scale baryon physics in the numerical code, and convergence amongst different methods is usually a mirage.

Nevertheless, the currently most detailed simulations of structure formation do reproduce a remarkable set of observables on different dynamical scales (see e.g., the Illustris simulation, Vogelsberger et al. 2014, and the EAGLE simulation, Schaye et al. 2015). It is, therefore, interesting to compare the expectations resulting from their numerical models with simpler analytic estimates of the galaxy growth from the cosmological background evolution (see e.g., Wellons et al., 2015; Furlong et al., 2015). If, for instance, their simulated galaxies experience the same size and velocity dispersion evolution as real galaxy do from $z \simeq 2$ to $z \simeq 3$, where models based on dry mergers fail, then perhaps we would have some insights on which dissipational process play a key role in the evolution of massive galaxies at very early times.

Bibliography

Abazajian K. N., et al., 2009, ApJS, 182, 543

Abel N. H., 1826, Journal für die reine und angewandte Mathematik, 1, 153-157

Arnold V.I., 1978, The Mathematical Methods of Classical Mechanics, Springer, New York

Arnold R., 1995, MNRAS, 276, 293

Bacon R., et al., 1995, A&AS, 113, 347

Bacon R., et al., 2001, MNRAS, 326, 23

Bacon R., et al., 2010, SPIE, 7735, 773508

Barnes J., Hut P., 1986, Nature, 324, 446

Behroozi P. S., Conroy C., Wechsler R. H., 2010, ApJ, 717, 379 (B10)

Belli S., Newman A. B., Ellis R. S., 2013, arXiv, arXiv:1311.3317

Bendinelli O., 1991, ApJ, 366, 599

Bertin G., Saglia R. P., Stiavelli M., 1988, ApJ, 330, 78

Bertola F., Capaccioli M., 1975, ApJ, 200, 439

Bertschinger E., 2001, ApJS, 137, 1

Blumenthal G. R., Faber S. M., Flores R., Primack J. R., 1986, ApJ, 301, 27

Binney J., 1978, MNRAS, 183, 501

Binney, J. 1982a, MNRAS, 201, 15

Binney, J. 1982b, ARA&A, 20, 399

Binney J., 1987, ASIC, 207, 399

Binney J., 2005, MNRAS, 363, 937

Binney J., 2010, MNRAS, 401, 2318

Binney J., 2012a, MNRAS, 426, 1324

Binney J., 2012b, MNRAS, 426, 1328

Binney J., 2014, MNRAS, 440, 787

Binney J., & Spergel D. 1982, ApJ, 252, 308

Binney J., Mamon G. A., 1982, MNRAS, 200, 361

Binney J. J., Davies R. L., Illingworth G. D., 1990, ApJ, 361, 78

Binney J., & Merrifield M. 1998, Galactic Astronomy, Princeton Univ. Press, Princeton, NJ

Binney J., & Tremaine S. 2008, Galactic Dynamics, 2nd edn. Princeton Univ. Press, Princeton, NJ

Binney J., McMillan P.J., 2011, MNRAS, 413, 1889

Binney J., et al., 2014, MNRAS, 439, 1231

Binney J., Piffl T., 2015, arXiv, arXiv:1509.06877

Birkinshaw M., 1999, PhR, 310, 97

Bissantz N., Debattista V. P., Gerhard O., 2004, ApJ, 601, L155

Blanton M. R., Roweis S., 2007, AJ, 133, 734

Bolton A. S., Burles S., Koopmans L. V. E., Treu T., Moustakas L. A., 2006, ApJ, 638, 703

Boylan-Kolchin M., Ma C.-P., Quataert E., 2005, MNRAS, 362, 184

Bovy J., Rix H.-W., 2013, ApJ, 779, 115

Bovy J., 2014, ApJ, 795, 95

Bryan G. L., Norman M. L., 1998, ApJ, 495, 80

Bryant J. J., et al., 2015, MNRAS, 447, 2857

Bundy K., et al., 2015, ApJ, 798, 7

Byrd P.F., Friedman M. D., 1971, Handbook of elliptic integrals for engineers and scientists, Springer-Verlag, Berlin

Cappellari M., 2002, MNRAS, 333, 400

Cappellari M., 2008, MNRAS, 390, 71

Cappellari M., Copin Y., 2003, MNRAS, 342, 345

Cappellari M., Emsellem E., 2004, PASP, 116, 138

Cappellari M., et al., 2006, MNRAS, 366, 1126

Cappellari M., et al., 2007, MNRAS, 379, 418

Cappellari M., et al., 2011a, MNRAS, 413, 813

Cappellari M., et al., 2011b, MNRAS, 416, 1680

Cappellari M., et al., 2012, Nature, 484, 485

Cappellari M., et al., 2013, MNRAS, 432, 1709

Carollo C. M., et al., 2013, ApJ, 773, 112

Cassata P., et al., 2011, ApJ, 743, 96

Chabrier G., 2003, PASP, 115, 763

Cimatti A., et al., 2008, A&A, 482, 21

Cimatti A., Nipoti C., Cassata P., 2012, MNRAS, 422, L62 (CNC12)

Ciotti L., 1991, A&A, 249, 99

Ciotti L., 1996, ApJ, 471, 68

Ciotti L., 2009, NCimR, 32, 1

Contopoulos G., 1960, ZA, 49, 273

Contopoulos G., 1963, AJ, 68, 1

Cortesi A., et al., 2013, A&A, 549, A115

Côté P., McLaughlin D. E., Cohen J. G., Blakeslee J. P., 2003, ApJ, 591, 850

Courteau S., et al., 2014, RvMP, 86, 47

Cretton N., van den Bosch F. C., 1999, ApJ, 514, 704

Croom S. M., et al., 2012, MNRAS, 421, 872

Daddi E., et al., 2005, ApJ, 626, 680

Dalessandro E., Lanzoni B., Ferraro F. R., Vespe F., Bellazzini M., Rood R. T., 2008, ApJ, 681, 311

Damjanov I., et al., 2011, ApJ, 739, L44

Das P., et al., 2008, AN, 329, 940

Das P., Gerhard O., Churazov E., Zhuravleva I., 2010, MNRAS, 409, 1362

Davies R. L., Efstathiou G., Fall S. M., Illingworth G., Schechter P. L., 1983, ApJ, 266, 41

Davis M., Efstathiou G., Frenk C. S., White S. D. M., 1985, ApJ, 292, 371

de Blok W. J. G., Walter F., Brinks E., Trachternach C., Oh S.-H., Kennicutt R. C., Jr., 2008, AJ, 136, 2648

de Lorenzi F., Debattista V. P., Gerhard O., Sambhus N., 2007, MNRAS, 376, 71

de Vaucouleurs G., 1948, AnAp, 11, 247

Deason A. J., Belokurov V., Evans N. W., McCarthy I. G., 2012, ApJ, 748, 2

Dehnen W., 1993, MNRAS, 265, 250

Dehnen W., 2009, MNRAS, 395, 1079

Dehnen W., 1995, MNRAS, 274, 919

Dejonghe H., 1986, PhR, 133, 217

Dejonghe H., 1989, ApJ, 343, 113

Dejonghe H., de Zeeuw T., 1988, ApJ, 333, 90

Dejonghe H., Laurent D., 1991, MNRAS, 252, 606

de Zeeuw T., 1985, MNRAS, 216, 273

Dickson L.E., 1914, Elementary Theory of Equations, J. Wiley & Sons Incorporated, Hoboken, New Jersey, USA

Diemer B., More S., Kravtsov A. V., 2013a, ApJ, 766, 25

Diemer B., Kravtsov A. V., More S., 2013b, ApJ, 779, 159

Djorgovski S., Davis M., 1987, ApJ, 313, 59

Dressler A., Lynden-Bell D., Burstein D., Davies R. L., Faber S. M., Terlevich R., Wegner G., 1987, ApJ, 313, 42

Dubois Y., Gavazzi R., Peirani S., Silk J., 2013, MNRAS, 433, 3297

Dumas, H. S., & Laskar, J. 1993, Physical Review Letters, 70, 297

Eddington A. S., 1916, MNRAS, 76, 572

Emsellem E., Monnet G., Bacon R., 1994, A&A, 285, 723

Emsellem E., Dejonghe H., Bacon R., 1999, MNRAS, 303, 495

Emsellem E., et al., 2004, MNRAS, 352, 721

Emsellem E., et al., 2007, MNRAS, 379, 401

Emsellem E., et al., 2011, MNRAS, 414, 888

Efstathiou G., Davis M., White S. D. M., Frenk C. S., 1985, ApJS, 57, 241

Epinat, B., Amram, P., Balkowski, C., & Marcelin, M. 2010, MNRAS, 401, 2113

Evans N. W., de Zeeuw P. T., Lynden-Bell D., 1990, MNRAS, 244, 111

Evans N. W., 1994, MNRAS, 267, 333

Evans N. W., Williams A. A., 2014, MNRAS, 443, 791

Evans N. W., Sanders J. L., Williams A. A., An J., Lynden-Bell D., Dehnen W., 2015, arXiv, arXiv:1509.08794

Evrard A. E., et al., 2008, ApJ, 672, 122

Faber S. M., Jackson R. E., 1976, ApJ, 204, 668

Fakhouri O., Ma C.-P., Boylan-Kolchin M., 2010, MNRAS, 406, 2267

Fall S. M., Efstathiou G., 1980, MNRAS, 193, 189

Fan L., Lapi A., De Zotti G., Danese L., 2008, ApJ, 689, L101

Fan L., Lapi A., Bressan A., Bernardi M., De Zotti G., Danese L., 2010, ApJ, 718, 1460

Ferguson H. C., et al., 2004, ApJ, 600, L107

Fermani F., 2013, DPhil Thesis, University of Oxford

Fermi-LAT Collaboration, 2015, arXiv, arXiv:1503.02641

Ferrarese L., Merritt D., 2000, ApJ, 539, L9

Ferraro F. R., Sollima A., Rood R. T., Origlia L., Pancino E., Bellazzini M., 2006, ApJ, 638, 433

Förster Schreiber N. M., et al., 2009, ApJ, 706, 1364

Frenk C. S., White S. D. M., Davis M., Efstathiou G., 1988, ApJ, 327, 507

Fricke W., 1952, AN, 280, 193

Fridman A. M., Polyachenko V. L., 1984, Physics of Gravitating Systems. Springer, New York

Furlong M., et al., 2015, arXiv, arXiv:1510.05645

Garcia-Benito R., et al., 2015, A&A, 576, A135

Gantmacher F.R., 1959, The Theory of Matrices Vol.2, American Mathematical Society, Providence, Rhode Island, USA

Gebhardt K., et al., 2000, ApJ, 539, L13

Gerhard O. E., 1993, MNRAS, 265, 213

Gerhard O., 2013, IAUS, 295, 211

Gerhard O.E., Saha P., 1991, MNRAS, 251, 449

Giavalisco M., et al., 2004, ApJ, 600, L93

Gnedin O. Y., Kravtsov A. V., Klypin A. A., Nagai D., 2004, ApJ, 616, 16

González Delgado R. M., et al., 2015, A&A, 581, A103

Gott R. J., III, 1973, ApJ, 186, 481

Graham A. W., Erwin P., Caon N., Trujillo I., 2001, ApJ, 563, L11

Graham A. W., Driver S. P., 2007, ApJ, 655, 77

Gruppioni C., Pozzi F., Zamorani G., Vignali C., 2011, MNRAS, 416, 70

Hénon M., 1959, AnAp, 22, 126

Hénon M., 1960, AnAp, 23, 474

Hernquist L., 1990, ApJ, 356, 359

Hilz M., Naab T., Ostriker J. P., Thomas J., Burkert A., Jesseit R., 2012, MNRAS, 425, 3119

Hilz M., Naab T., Ostriker J. P., 2013, MNRAS, 429, 2924

Hockney R. W., Eastwood J. W., Computer Simulation using Particles, 1981, McGraw-Hill, New York

Hopkins P. F., Lauer T. R., Cox T. J., Hernquist L., Kormendy J., 2009a, ApJS, 181, 486

Hopkins P. F., Bundy K., Murray N., Quataert E., Lauer T. R., Ma C.-P., 2009b, MNRAS, 398, 898

Hopkins P. F., Narayanan D., Murray N., 2013, MNRAS, 432, 2647

Hubble E. P., 1936, Realm of the Nebulae. Yale Univ. Press, New Haven

Humphrey, P. J., Buote, D. A., Gastaldello, F., et al. 2006, ApJ, 646, 899

Hunter C., 1975, AJ, 80, 783

Hunter C., Qian E., 1993, MNRAS, 262, 401

Husemann B., et al., 2013, A&A, 549, A87

Hyde J. B., Bernardi M., 2009, MNRAS, 394, 1978

Illingworth G., 1977, ApJ, 218, L43

Illingworth G., 1981, seng.proc, 27

Ishibashi W., Fabian A. C., Canning R. E. A., 2013, MNRAS, 431, 2350

Jaffe W., 1983, MNRAS, 202, 995

Jeans J. H., 1915, MNRAS, 76, 70

Jeans J. H., 1919, Phil. Trans. R. Soc. London, 218 (157-210)

Jørgensen I., Chiboucas K., Flint K., Bergmann M., Barr J., Davies R., 2006, ApJ, 639, L9

Kaasalainen M., Binney J., 1994, MNRAS, 268, 1033

Kaasalainen M., 1994, MNRAS, 268, 1041

Kapteyn J. C., 1922, ApJ, 55, 302

Kereš D., Vogelsberger M., Sijacki D., Springel V., Hernquist L., 2012, MNRAS, 425, 2027

Khochfar S., Burkert A., 2006, A&A, 445, 403

Khochfar S., Silk J., 2006, ApJ, 648, L21

King, I. R. 1966, AJ, 71, 64

Knebe A., et al., 2011, MNRAS, 415, 2293

Knollmann S. R., Knebe A., 2009, ApJS, 182, 608

Kormendy J., 1977, ApJ, 218, 333

Kravtsov A. V., 2013, ApJ, 764, L31

Krajnović D., Cappellari M., de Zeeuw P. T., Copin Y., 2006, MNRAS, 366, 787

Krogager J.-K., Zirm A. W., Toft S., Man A., Brammer G., 2013, arXiv, arXiv:1309.6316

Kronawitter A., Saglia R. P., Gerhard O., Bender R., 2000, A&AS, 144, 53

Kuijken K., 1995, ApJ, 446, 194

La Barbera F., Busarello G., Merluzzi P., Massarotti M., Capaccioli M., 2003, ApJ, 595, 127

Lacey C., Cole S., 1993, MNRAS, 262, 627

Lambas D. G., Maddox S. J., Loveday J., 1992, MNRAS, 258, 404

Landau, L. D., & Lifshitz, E. M. 1969, Course of Theoretical Physics Vol 1: Mechanics, Oxford: Pergamon Press, 1969, 2nd ed.,

Lanzoni B., Ciotti L., Cappi A., Tormen G., Zamorani G., 2004, ApJ, 600, 640

Lanzoni B., et al., 2013, ApJ, 769, 107

Laporte C. F. P., White S. D. M., Naab T., Gao L., 2013, MNRAS, 435, 901

Larson R. B., 1975, MNRAS, 173, 671

Laskar, J. 1990, Icarus, 88, 266

Lau E. T., Nagai D., Kravtsov A. V., 2010, ApJ, 708, 1419

Leauthaud A., et al., 2012, ApJ, 744, 159 (L12)

Leeuwin F., Combes F., Binney J., 1993, MNRAS, 262, 1013

Lilly S. J., Le Fevre O., Hammer F., Crampton D., 1996, ApJ, 460, L1

Liouville J., 1838, Journal de Mathématiques Pures et Appliquées, Série I, 3 (342)

Long R. J., Mao S., 2010, MNRAS, 405, 301

López-Sanjuan C., et al., 2012, A&A, 548, A7

Lützgendorf N., Kissler-Patig M., Gebhardt K., Baumgardt H., Noyola E., Jalali B., de Zeeuw P. T., Neumayer N., 2012, A&A, 542, A129

Lützgendorf N., et al., 2013, A&A, 552, A49

Lynden-Bell D., 1960, MNRAS, 120, 204

Lynden-Bell D., 1962a, MNRAS, 123, 447

Lynden-Bell D., 1962b, MNRAS, 124, 1

Lynden-Bell D., 1962c, MNRAS, 124, 95

Lynden-Bell D., 1967, MNRAS, 136, 101

Madau P., Ferguson H. C., Dickinson M. E., Giavalisco M., Steidel C. C., Fruchter A., 1996, MNRAS, 283, 1388

Magorrian J., Binney J., 1994, MNRAS, 271, 949

Magorrian J., et al., 1998, AJ, 115, 2285

McMillan P. J., Binney J. J., 2008, MNRAS, 390, 429

Méndez, R. H., Riffeser, A., Kudritzki, R.-P., et al. 2001, ApJ, 563, 135

Merloni A., Heinz S., 2008, MNRAS, 388, 1011

Merritt D., 1985, AJ, 90, 1027

Merritt D., 1993, ApJ, 413, 79

Merritt D., 1996, AJ, 112, 1085

Merritt D., 1997, AJ, 114, 228

Michie R. W., 1963, MNRAS, 125, 127

Mo H. J., White S. D. M., 1996, MNRAS, 282, 347

Mo H. J., Mao S., White S. D. M., 1998, MNRAS, 295, 319

Mo H., van den Bosch F. C., White S., 2010, Galaxy Formation and Evolution, Cambridge University Press, Cambridge, UK

Monnet G., Bacon R., Emsellem E., 1992, A&A, 253, 366

Moster B. P., Naab T., White S. D. M., 2013, MNRAS, 428, 3121

Munari E., Biviano A., Borgani S., Murante G., Fabjan D., 2013, MNRAS, 430, 2638

Naab T., Johansson P. H., Ostriker J. P., 2009, ApJ, 699, L178

Napolitano N. R., Pota V., Romanowsky A. J., Forbes D. A., Brodie J. P., Foster C., 2014, MNRAS, 439, 659

Navarro J. F., Frenk C. S., White S. D. M., 1996, ApJ, 462, 563

Navarro J. F., Frenk C. S., White S. D. M., 1997, ApJ, 490, 493

Newman A. B., Ellis R. S., Bundy K., Treu T., 2012, ApJ, 746, 162

Nipoti C., Londrillo P., Ciotti L., 2003, MNRAS, 342, 501

Nipoti C., Treu T., Bolton A. S., 2009a, ApJ, 703, 1531

Nipoti C., Treu T., Auger M. W., Bolton A. S., 2009b, ApJ, 706, L86

Nipoti C., Treu T., Leauthaud A., Bundy K., Newman A. B., Auger M. W., 2012, MNRAS, 422, 1714

Ollongren A., 1962, BAN, 16, 241

Ollongren A., 1965, ARA&A, 3, 113

Onions J., et al., 2012, MNRAS, 423, 1200

Oort J. H., 1932, BAN, 6, 249

Oser L., Naab T., Ostriker J. P., Johansson P. H., 2012, ApJ, 744, 63

Osipkov, L. P. 1979, Pisma v Astronomicheskii Zhurnal, 5, 77

Papastergis E., Cattaneo A., Huang S., Giovanelli R., Haynes M. P., 2012, ApJ, 759,

138

Peng Y.-j., et al., 2010, ApJ, 721, 193

Peralta de Arriba L., Balcells M., Falcón-Barroso J., Trujillo I., 2014, MNRAS, 440, 1634

Piffl T., et al., 2014, MNRAS, 445, 3133

Piffl T., Penoyre Z., Binney J., 2015, MNRAS, 451, 639

Planck Collaboration, et al., 2014, A&A, 571, A1

Plummer, H. C. 1911, MNRAS, 71, 460

Poggianti B. M., Moretti A., Calvi R., D'Onofrio M., Valentinuzzi T., Fritz J., Renzini A., 2013, arXiv, arXiv:1309.2427

Pontzen A., Governato F., 2013, MNRAS, 430, 121

Posti L., Nipoti C., Stiavelli M., Ciotti L., 2014, MNRAS, 440, 610

Posti L., Binney J., Nipoti C., Ciotti L., 2015, MNRAS, 447, 3060

Power C., Navarro J. F., Jenkins A., Frenk C. S., White S. D. M., Springel V., Stadel J., Quinn T., 2003, MNRAS, 338, 14

Prendergast K.H., Tomer E., 1970, AJ, 75, 647

Ragone-Figueroa C., Granato G. L., 2011, MNRAS, 414, 3690

Richstone D. O., 1982, ApJ, 252, 496

Rix H.-W., de Zeeuw P. T., Cretton N., van der Marel R. P., Carollo C. M., 1997, ApJ, 488, 702

Romanowsky A. J., Strader J., Spitler L. R., Johnson R., Brodie J. P., Forbes D. A., Ponman T., 2009, AJ, 137, 4956

Roth M. M., et al., 2005, PASP, 117, 620

Rowley G., 1988, ApJ, 331, 124

Ryan-Weber E. V., Begum A., Oosterloo T., Pal S., Irwin M. J., Belokurov V., Evans N. W., Zucker D. B., 2008, MNRAS, 384, 535

Saglia R. P., et al., 2010, A&A, 524, A6

Sánchez S. F., et al., 2012, A&A, 538, A8

Sanders J. L., Binney J., 2014, MNRAS, 441, 3284

Sanders J. L., Binney J., 2015, MNRAS, 447, 2479

Sanders J. L., Evans N. W., 2015, MNRAS, 454, 299

Saracco P., Longhetti M., Andreon S., 2009, MNRAS, 392, 718

Sarazin C. L., 1986, RvMP, 58, 1

Satoh C., 1980, PASJ, 32, 41

Schaller M., et al., 2015, MNRAS, 451, 1247

Schaye J., et al., 2015, MNRAS, 446, 521

Schwarzschild M., 1979, ApJ, 232, 236

Scott N., et al., 2015, MNRAS, 451, 2723

Sellwood J.A., ARA&A, 25, 151

Sérsic J. L., 1963, BAAA, 6, 41

Sharma S., Steinmetz M., 2006, MNRAS, 373, 1293

Sharma S., et al., 2014, ApJ, 793, 51

Sharples R., et al., 2013, Msngr, 151, 21

Shen S., Mo H. J., White S. D. M., Blanton M. R., Kauffmann G., Voges W., Brinkmann J., Csabai I., 2003, MNRAS, 343, 978

Sonnenfeld A., Nipoti C., Treu T., 2013, arXiv, arXiv:1310.3280

Springel V., Yoshida N., White S. D. M., 2001, NewA, 6, 79

Springel V., 2005, MNRAS, 364, 1105

Springel V., Frenk C. S., White S. D. M., 2006, Natur, 440, 1137

P. Stackel, 1890, Mathematische Annalen, 35, 91-103

Stanek R., Rasia E., Evrard A. E., Pearce F., Gazzola L., 2010, ApJ, 715, 1508

Stiavelli M., Bertin G., 1985, MNRAS, 217, 735

Stiavelli M., et al., 1999, A&A, 343, L25

Stringer M. J., Shankar F., Novak G. S., Huertas-Company M., Combes F., Moster B. P., 2014, MNRAS, 441, 1570

Sunyaev R. A., Zeldovich Y. B., 1970, CoASP, 2, 66

Syer, D., & Tremaine, S. 1996, MNRAS, 282, 223

Thomas J., Saglia R. P., Bender R., Thomas D., Gebhardt K., Magorrian J., Richstone D., 2004, MNRAS, 353, 391

Trujillo I., et al., 2006, ApJ, 650, 18

Tully R. B., Fisher J. R., 1977, A&A, 54, 661

Valdes F., Gupta R., Rose J. A., Singh H. P., Bell D. J., 2004, ApJS, 152, 251

van Albada T. S., 1982, MNRAS, 201, 939

van Albada T. S., Bahcall J. N., Begeman K., Sancisi R., 1985, ApJ, 295, 305

van de Sande J., et al., 2013, ApJ, 771, 85

van de Ven G., Hunter C., Verolme E. K., de Zeeuw P. T., 2003, MNRAS, 342, 1056

van de Ven G., de Zeeuw P. T., van den Bosch R. C. E., 2008, MNRAS, 385, 614

van den Bosch F. C., 2002, MNRAS, 331, 98

van den Bosch R. C. E., van de Ven G., Verolme E. K., Cappellari M., de Zeeuw P. T., 2008, MNRAS, 385, 647

van den Bergh S., 1976, ApJ, 206, 883

van der Marel R. P., 1991, MNRAS, 253, 710

van der Marel R. P., Franx M., 1993, ApJ, 407, 525

van der Marel, R. P., Evans, N. W., Rix, H.-W., White, S. D. M., & de Zeeuw, T. 1994, MNRAS, 271, 99

van der Marel R. P., Cretton N., de Zeeuw P. T., Rix H.-W., 1998, ApJ, 493, 613

van der Wel A., Holden B. P., Zirm A. W., Franx M., Rettura A., Illingworth G. D., Ford H. C., 2008, ApJ, 688, 48

van der Marel R. P., Anderson J., 2010, ApJ, 710, 1063

van Dokkum P. G., et al., 2008, ApJ, 677, L5

Verheijen M. A. W., Bershady M. A., Andersen D. R., Swaters R. A., Westfall K., Kelz A., Roth M. M., 2004, AN, 325, 151

Vogelsberger M., White S. D. M., Helmi A., Springel V., 2008, MNRAS, 385, 236

Vogelsberger M., Sijacki D., Kereš D., Springel V., Hernquist L., 2012, MNRAS, 425, 3024

Vogelsberger M., et al., 2014, Natur, 509, 177

Voit G. M., 2005, RvMP, 77, 207

Vulcani B., et al., 2014, ApJ, 797, 62

Wake D. A., et al., 2011, ApJ, 728, 46

Walcher C. J., et al., 2014, A&A, 569, A1

Weijmans A.-M., et al., 2014, MNRAS, 444, 3340

Wellons S., et al., 2015, arXiv, arXiv:1507.02291

Wetzel A. R., 2011, MNRAS, 412, 49

White S. D. M., 1978, MNRAS, 184, 185

White S. D. M., Rees M. J., 1978, MNRAS, 183, 341

Williams A. A., Evans N. W., Bowden A. D., 2014, MNRAS, 442, 1405

Williams A. A., Evans N. W., 2015a, MNRAS, 448, 1360

Williams A. A., Evans N. W., 2015b, arXiv, arXiv:1508.02584

Wilson C.P., 1975, ApJ, 80, 175

Wisnioski E., et al., 2015, ApJ, 799, 209

Wojtak R., Łokas E. L., Mamon G. A., Gottlöber S., Klypin A., Hoffman Y., 2008, MNRAS, 388, 815

Analytical expression for the radial action in the Hernquist sphere

The radial action is defined as

$$
J_{\mathrm{r}} = \frac{1}{2\pi} \oint p_r \mathrm{d}r = \frac{1}{\pi} \int_{r_1}^{r_2} \mathrm{d}r \sqrt{2E - 2\Phi(r) - \frac{L^2}{r^2}}, \tag{A.1}
$$

where $\Phi(r) = -GM/(r + r_{\mathrm{b}})$ and r_1, r_2 are the pericentric and apocentric radii for the given energy E and angular momentum L, i.e., the two roots of the integrand in equation (A.1). Introducing the dimensionless quantities $s \equiv r/r_{\mathrm{b}}$, $\mathcal{E} \equiv -Er_{\mathrm{b}}/GM$ and $l = L/\sqrt{2GMr_{\mathrm{b}}}$, equation (A.1) can be rewritten get

$$
J_{\mathrm{r}} = \frac{\sqrt{2GMr_{\mathrm{b}}}}{\pi} \int_{s_1}^{s_2} \mathrm{d}s \sqrt{-\mathcal{E} + \Psi(s) - \frac{l^2}{s^2}}, \tag{A.2}
$$

where $\Psi(s) \equiv 1/(1 + s)$ is the relative dimensionless potential. We now change the integration variable variable from $s = (1 - \Psi)/\Psi$ to Ψ (Ciotti, 1996), and have

$$
J_{\mathrm{r}} = \frac{\sqrt{2GMr_{\mathrm{b}}}}{\pi} \int_{\Psi_2}^{\Psi_1} \mathrm{d}\Psi \frac{\sqrt{\mathcal{P}(\Psi)}}{(1 - \Psi)\Psi^2}, \tag{A.3}
$$

where $\Psi_1 \equiv \Psi(s_1)$, $\Psi_2 \equiv \Psi(s_2)$ and

$$
\mathcal{P}(\Psi) = -\mathcal{E}(1 - \Psi)^2 + \Psi(1 - \Psi)^2 - l^2\Psi^2 \tag{A.4}
$$

is a cubic in Ψ, the roots of which can be found by standard methods (e.g., Dickson, 1914). Ψ_1, Ψ_2 are two roots in the physical range $0 \le \Psi \le 1$. Let A be the third real root, so

$$
\mathcal{P}(\Psi) = (\Psi_1 - \Psi)(\Psi - \Psi_2)(A - \Psi). \tag{A.5}
$$

While it is physically obvious that two of the three real solutions of equation (A.4) are in the range $(0, 1)$ and the remaining one is outside ($A > 1$), we remark that the same conclusion can be reached by purely algebraic arguments by using the Routh-Hurwitz

theorem (see e.g., Gantmacher, 1959). By evaluating equations (A.4) and (A.5) at $\Psi = 0$ one gets $A = \mathcal{E}/\Psi_1\Psi_2 > 0$. By splitting into its partial fractions the integrand in equation (A.3), it is possible to express the integral for J_{r} in terms of complete elliptic integrals (see Byrd and Friedman , 1971):

$$
\begin{aligned}
J_r = \frac{\sqrt{2GMa}}{\pi} D_5 \left[D_1\Pi\left(\alpha_1, k^2\right) + D_2\mathrm{E}\left(k^2\right) + \right. \\
\left. + D_3\mathrm{K}\left(k^2\right) + D_4\Pi\left(\alpha_2, k^2\right) \right],
\end{aligned}
\tag{A.6}
$$

where $\mathrm{K}, \mathrm{E}, \Pi$ are respectively the complete elliptic integral of the first, second and third kind,

$$
\alpha_1 \equiv \frac{\Psi_1 - \Psi_2}{\Psi_2}, \quad \alpha_2 \equiv \frac{\Psi_1 - \Psi_2}{1 - \Psi_2}, \quad k^2 \equiv \frac{\Psi_1 - \Psi_2}{A - \Psi_2}
\tag{A.7}
$$

and finally

$$
\begin{aligned}
D_1 &= [(1 - 2\Psi_1)\Psi_2 + \Psi_1]A + \Psi_1\Psi_2, \\
D_2 &= \Psi_2(\Psi_2 - A), \\
D_3 &= \Psi_2(A - 2), \\
D_4 &= 2\Psi_2(A - 1)(\Psi_1 - 1), \\
D_5 &= -\sqrt{A - \Psi_2}/D_2.
\end{aligned}
\tag{A.8}
$$

We have tested the formula (A.6) for consistency by numerically integrating equation (A.1) for a large set of orbits at different (E, L) and the numerical and analytical results agree within the error of the employed routine.

Velocity ellipsoids of the galaxy models in Chapter 4

In Figure B.1 we show the velocity ellipsoids of the $f(\mathbf{J})$ models described in Chapter 4 on the meridional plane. Those of $f(\mathbf{J})$ NGC 6125 and $f(\mathbf{J})$ NGC 6427 align with the spherical coordinates, while those of $f(\mathbf{J})$ NGC 2592 tend to align more closely to the cylindrical coordinates at small radii, $r \lesssim r_{\mathrm{half}}$ where r_{half} is the half-mass radius. For the latter model, the radial dispersion is larger than the vertical on the equatorial plane up to about $2R_{\mathrm{e}}$ (see Figure 4.8), while along the symmetry axis the vertical dispersion is always dominant. This model has $\delta_{\mathrm{z}} = 1$ which implies that the DF assigns the same probability to orbits with large vertical action and to those with large radial action.
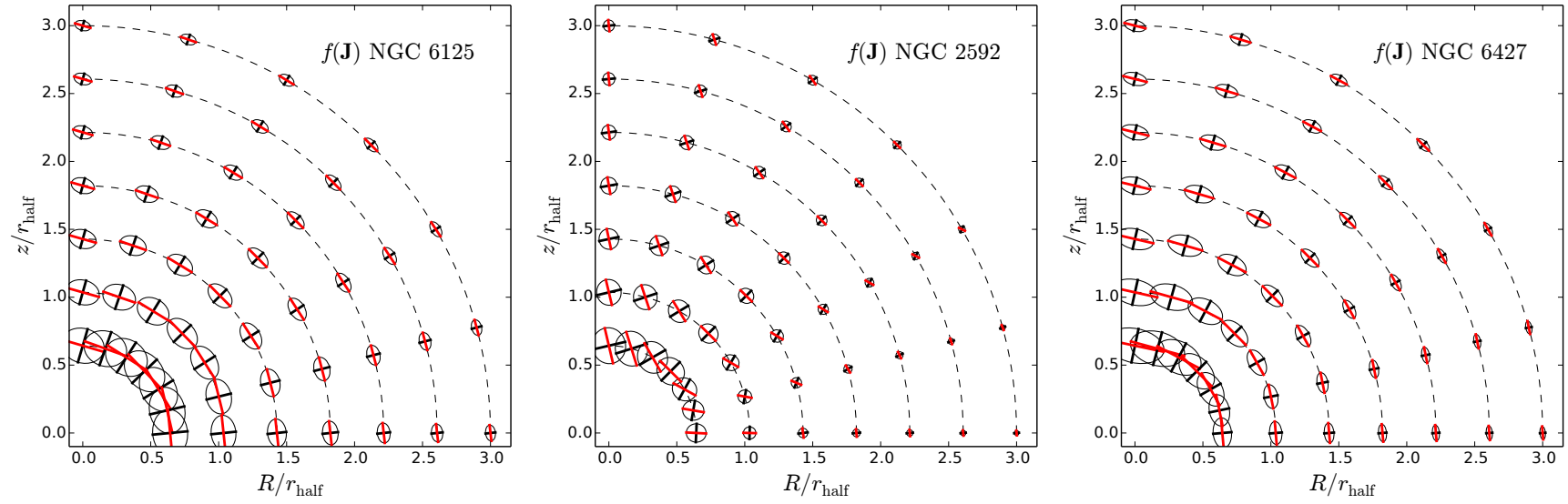
Figure B.1: Velocity ellipsoids in the meridional plane for the three models in Table 4.2. In each panel the major axis and the minor axis of the ellipsoid are indicated respectively with a red and black segment, whose length is proportional to the local amount of velocity dispersion.

Appendix C

Galaxies' inclination

Here we present the derivation of the probability distribution of galaxies' inclination, given the observed ellipticity. In general, the problem of deriving the galaxy's inclination from the observables is degenerate with the knowledge of its intrinsic shape. Hence, for general configurations it is not possible to derive neither the inclination nor the intrinsic shape from the flattening of the isophotes projected on the sky. Only for special cases in which the intrinsic shape is known, such as discs, one is able to measure accurately the object's inclination. Both for axisymmetric and for triaxial galaxies, dynamical models can be fitted to the galaxies, provided that some constraints on their kinematics is available, and the inclination is usually a free parameter that enters the fitting routine. The obvious drawback is that this would be severely model dependent and that the degeneracies with other model parameters are often difficult to handle.

A possible approach that one can use is a statistical one: by selecting a large sample of similar galaxies (e.g., in morphology, in kinematics) one can recover the probability distribution of intrinsic shape with some simple assumptions on the galaxy's symmetry. Early works of e.g., Lambas, Maddox, & Loveday (1992) who divided galaxies in classes of morphological Hubble types, were recently revised by the ATLAS^{3D} collaboration with the critical addition of a well defined distinction between kinematic classes of fast and slow rotators. From the volume limited sample of early-type galaxies of that survey, Weijmans et al. (2014) estimated the probability distribution function $P(q)$ of the intrinsic axis ratios $q \equiv b/a$ for that sample. They were able to compute $P(q)$ from the observed $P(\epsilon)$, being ϵ the ellipticity, by numerically inverting the relation between the conditional probability $P(\epsilon|q)$ and the marginalized $P(\epsilon)$, $P(q)$ and by assuming random orientations. Their result is that the fast and slow rotator population can be distinguished by having separate distributions of intrinsic axis ratios: they found that the fast rotating galaxies are distributed as a Gaussian with mean and standard deviation of $(\mu, \sigma) = (0.25, 0.14)$, while the slowly rotating galaxies as a Gaussian with $(\mu, \sigma) = (0.63, 0.09)$.

Following Weijmans et al. (2014), we assume that the galaxies are oblate spheroids, so that the rotation axis is the minor axis. Hence, it follows that the observed ellipticity ϵ, the intrinsic axis ratio q and the galaxy's inclination w.r.t. the rotation axis i satisfy

$$(1-\epsilon)^2 = \cos^2 i + q^2 \sin^2 i. \tag{C.1}$$

We used the work hypothesis that the fast rotators and slow rotators in our sample
are drawn from $P(q)$ estimated by Weijmans et al. (2014) and that $P(\epsilon)$ for the single
galaxy is a Gaussian centred in the measured value of $\epsilon \equiv 1 - \sqrt{\langle y^2 \rangle / \langle x^2 \rangle}$ with a standard
deviation of the order of the measurement error ($\sigma \sim 0.01$). Hence, from equation (C.1)
it follows that the cumulative probability of the inclinations $F(\sin i)$ is

$$F(\sin i) = \int_0^{\sin i} \mathrm{d}(\sin i)\, P(\sin i) = \int_\Omega \mathrm{d}\epsilon \mathrm{d}q\, P(\epsilon)\, P(q), \qquad (\text{C.2})$$

where $\Omega = \left\{ (\epsilon, q) \in \mathbb{R}^2 : (1 - \epsilon)^2 - 1 = \sin^2 i (q^2 - 1) \right\}$. Then, the probability distribu-
tion of the galaxy's inclination $P(i)$ is readily obtained by derivation of (C.2). In Figure
C.1 we show the resulting probability distribution of inclination angles for the three
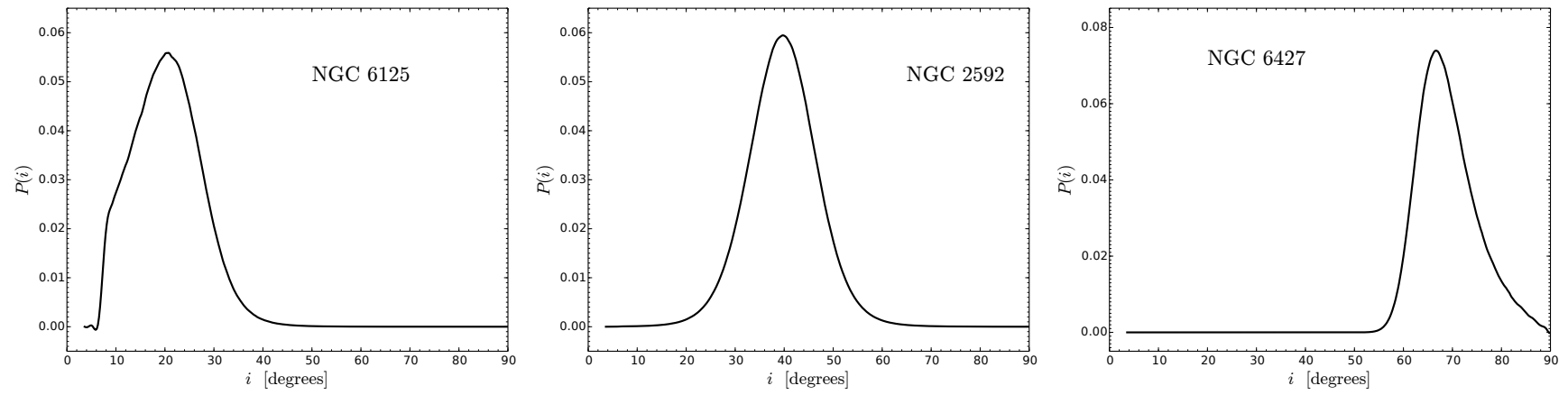galaxies considered in this work.

Figure C.1: Probability distribution of inclinations for the three galaxies.

LIST OF PUBLICATIONS

Publications related to this Thesis

▶ **L. Posti**, C. Nipoti, M. Stiavelli & L. Ciotti, 2014:
"*The imprint of dark matter haloes on the size and velocity dispersion evolution of early-type galaxies*"
MONTHLY NOTICES OF THE ROYAL ASTRONOMICAL SOCIETY, 440, 610

▶ **L. Posti**, J. Binney, C. Nipoti & L. Ciotti, 2015:
"*Action-based distribution functions for spheroidal galaxy components*"
MONTHLY NOTICES OF THE ROYAL ASTRONOMICAL SOCIETY, 447, 3060

▶ **L. Posti**, G. van de Ven, J. Binney, C. Nipoti, L. Ciotti et al. in preparation:
"*Self-consistent models for early-type galaxies in the CALIFA Survey*"

Publications unrelated to this Thesis

▶ C. Nipoti & **L. Posti**, 2013:
"*Thermal stability of a weakly magnetized rotating plasma*"
MONTHLY NOTICES OF THE ROYAL ASTRONOMICAL SOCIETY, 428, 815

▶ C. Nipoti & **L. Posti**, 2014:
"*On the Nature of Local Instabilities in Rotating Galactic Coronae and Cool Cores of Galaxy Clusters*"
THE ASTROPHYSICAL JOURNAL, 792, 21

▶ C. Nipoti, **L. Posti**, S. Ettori and M. Bianconi, 2015:
"*Magnetorotational instability in cool cores of galaxy clusters*"
JOURNAL OF PLASMA PHYSICS, 81, 5